

ECOLE DOCTORALE D'ASTRONOMIE ET D'ASTROPHYSIQUE D'ÎLE DE FRANCE

THÈSE DE DOCTORAT

présentée par

Clément BARUTEAU

pour obtenir le grade de
docteur de l'Observatoire de Paris
en Astronomie et Astrophysique

VERS DES SCÉNARIOS PRÉDICTIONNELS DE LA MIGRATION PLANÉTAIRE

dirigée par

Frédéric MASSET

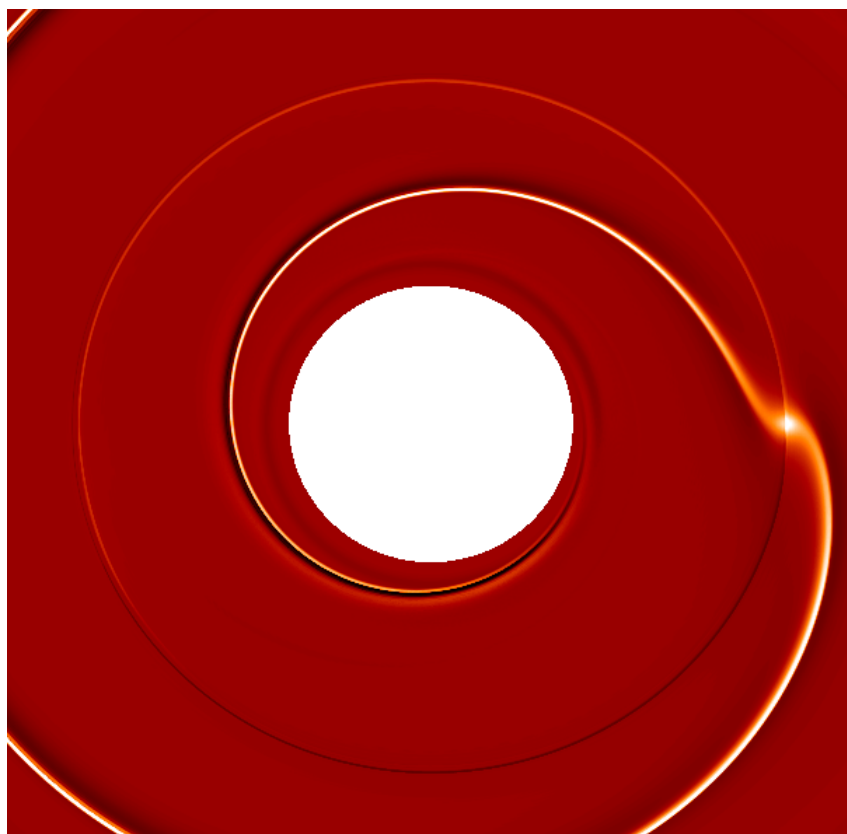
et soutenue le 02 octobre 2008
devant la commission composée de

Dr. Gennaro D'ANGELO rapporteur
Prof. Jean-Marc HURÉ examinateur
Prof. Wilhelm KLEY rapporteur
Prof. Douglas LIN rapporteur
Dr. Frédéric MASSET directeur de thèse
Prof. Bruno SICARDY examinateur, président du jury
Prof. Caroline TERQUEM examinatrice

Service d'Astrophysique du CEA Saclay
clement.baruteau@cea.fr

Clément BARUTEAU

Toward predictive scenarios of planetary migration



– CEA Saclay –

Cover page :

The perturbed surface density of a gaseous protoplanetary disc, obtained from a two-dimensional hydrodynamic calculation. The white circle at the center of the picture encloses the central star and the disc parts close to the star. The protoplanetary disc is perturbed by a low-mass planet (the brightest point on the right-hand side of the picture) that excites a spiral-shaped wake propagating in the disc. The planet induces an additional perturbation in a narrow annulus located close to the star-planet separation.

Remerciements / Acknowledgments

Je tiens d'abord à remercier Pierre-Olivier LAGAGE pour m'avoir accueilli dans son service lors de ma thèse. Je lui suis reconnaissant, ainsi qu'à la direction de l'IRFU, de m'avoir permis de séjourner au Mexique, d'avoir assuré les frais de trajet et de mission sur place. J'espère que le présent manuscrit, et le travail réalisé durant ces trois ans de thèse, auront été à la hauteur de la confiance qui m'a été accordée.

Un grand merci aux personnes du service qui m'ont aidé à avancer au cours de ces trois ans. A Michel TAGGER pour ses conseils sur l'auto-gravité. A Romain TEYSSIER et Thierry FOGLIZZO pour leurs explications et intuitions sur les discontinuités de contact. A Edouard AUDIT pour sa patience quant à mon utilisation surintensive de Godunov. Un remerciement plus particulier à Sébastien FROMANG pour ses conseils précieux et avisés sur des points aussi variés que la conception d'un poster, la rédaction de dossiers pour les offres de postdocs ou la préparation de la soutenance de thèse.

L'avancée a aussi été humaine, ainsi j'adresse aux étudiants (et assimilés!) mes plus sincères vœux de bonheur et de réussite : notre spécialiste ès kouign amann Alain GUEGUEN, Ana PALACIOS, Matthias GONZALEZ y el amigo Fabio ACERO con los que fue un placer hablar español, Anaëlle MAURY, Mickaël CORIAT, Lionel PRAT, sans qui j'aurais eu du mal à assister à la conférence en Chine, Jérôme GUILLET, Benjamin BRACONNIER, mes super cobureaux Yohan DUBOIS et Benoît COMMERÇON, que je remercie d'avoir relu le premier chapitre de ce manuscrit, Estelle DEAU, notre coureur Henri TRIOU, Ivan DEBONO, Savita MATHUR, Julien SALMON, Médéric BOQUIEN, Laurène JOUVE, Lilia SOLOVYEVA, Guillaume LOISEL, Pierrick ABRIAL, Joël BERGE, Sandrine PIRES, Vincent DUEZ, Nazirah JETHA, Arnaud WOISSELLE. Un petit mot enfin pour Jules CASOLI, compagnon d'aventures mexicaines, à qui je souhaite une thèse brillante avec Frédéric.

I wish to thank the following people for their help and comments on my research work. A special thank to Takayuki MUTO and Sijme-Jan PAARDEKOOPEL for insightful comments on the corotation torque calculation in adiabatic discs. Aurélien CRIDA for clarifying remarks on the migration of massive planets. Alessandro MORBIDELLI for a thorough reading of the two articles written during my thesis. Andres CARMONA for an illuminating question about self-gravity during the IAU meeting in Suzhou.

It was my honor to have them as committee members. Gennaro D'ANGELO for a detailed reading of the manuscript, and for insightful comments and questions I appreciated much. Jean-Marc HURÉ qui a révélé en moi un goût certain pour les simulations hydrodynamiques. Wilhelm KLEY for fruitful discussions during the conferences I attended to. Douglas LIN for his reading of the manuscript, and for having quickly enrolled me as a postdoc at UCSC! Bruno SICARDY pour m'avoir passionné pour les résonances de Lindblad lors de son cours de Master, et pour m'avoir inspiré un travail sur la capture en résonance de Pluton. Et enfin Caroline TERQUEM pour ses commentaires avisés sur les disques radiatifs.

J'en viens à rendre hommage à mes amis. Aux complices Guilhem LAVAUX, Elisabetta MICELOTTA, Gwenaël BOUÉ, que je remercie d'avoir relu les deux premiers chapitres de ce manuscrit, Isabelle et Sébastien ESNAULT, Hervé BOISSON et sa famille. Une pensée toujours émue à notre promotion du Master de l'Observatoire : Kevin BAILLIE, Virginie BATISTA, Gwenaël BOUÉ, encore lui, Josselin DESMARS, Jordi FONTDECABA I BAIG, Julie GAYON,

Magali MAROCCIA, Arielle MOULLET, Christophe OUZEAU et Arianne SAUVENIER. Viennent encore Aurélien BENOIT-LEVY, Kumiko KOTERA, Elisabete DA CUNHA, Sara CAUCCI, pour son cours d'italien, la famille RIMADA pour son accueil chaleureux au Mexique et la famille HURPIN. A tous je souhaite mes plus vifs vœux de bonheur.

Une pensée chaleureuse à ma famille d'hier, d'aujourd'hui et de demain : Catherine, Georges, Maurice, Nicole, Claire, Camille, François, Gabriel, Hélène, Gerald, Agnès, Stefan, Alice, Matthieu, et Sarah, *mi vida*.

Peut-être les thèses se suivent et se ressemblent. Comme toi, j'ai gardé le meilleur pour la fin. A toi, Frédéric MASSET, mon directeur de thèse, pour m'avoir aiguillé sur le chemin de la recherche. Travailler avec toi a été une expérience enthousiasmante et ô combien enrichissante. Je mesure la chance que j'ai eue de pouvoir bénéficier de tes intuitions, de tes commentaires et discussions éclairés, de ta disponibilité à toute épreuve, même à l'autre bout de la Terre. Merci aussi pour ta relecture de ce manuscrit. Comme le jour de la soutenance, je vais te vieillir un peu : j'espère être comme toi dans quinze ans !

Vers des scénarios prédictifs de la migration planétaire

La détection récente des exoplanètes a fourni un formidable laboratoire d'expérimentation des théories de formation et d'évolution planétaire. Un résultat troublant est la proportion de planètes géantes situées plus près de leur étoile que ne l'est Mercure de notre Soleil! Si, comme il est admis, ces planètes se sont formées à plus grande distance de l'étoile dans le disque protoplanétaire, il reste à expliquer comment elles ont pu s'en rapprocher. Remarquablement, une telle théorie est apparue bien avant la découverte de la première exoplanète. Elle explique que sous l'interaction avec le disque protoplanétaire, les planètes se rapprochent de leur étoile en spiralant. On parle de migration planétaire. De nombreuses études ont montré que le temps de migration des planètes de faible masse est bien plus court que le temps de dissipation du disque. Toutes les planètes devraient avoir migré jusqu'à leur étoile! Ce qui est déjà remis en cause par notre Système Solaire. Afin d'inscrire la migration planétaire dans un scénario prédictif de formation et d'évolution planétaire, il est primordial d'affiner notre compréhension de l'interaction disque-planète. La prise en compte de l'auto-gravité du disque est un exemple de progrès en ce sens. Je montre que négliger l'auto-gravité conduit à surestimer significativement le couple différentiel de Lindblad. Une autre branche explorée dans cette thèse est l'impact des processus thermiques sur la migration. Je montre que l'évolution thermodynamique du disque génère une contribution supplémentaire au couple de corotation, capable de ralentir considérablement, voire de renverser, la migration des planètes de faible masse.

Mots clé : migration planétaire, disques protoplanétaires, hydrodynamique, analyse linéaire, simulations numériques

Toward predictive scenarios of planetary migration

The recent detection of extrasolar planets has provided an exciting opportunity to test our theories of planet formation and evolution. An impressive result is the significant proportion of giant planets located much closer to their star than Mercury is from our own Sun! These planets should have formed further out in the protoplanetary disc, thus one needs to explain how they could move closer to their host star. Remarkably enough, such an explanation was proposed well before the discovery of the first exoplanet. It considered the interaction between a planet and the protoplanetary disc, which leads to a decrease of the planet's semi-major axis. This is known as planetary migration. Many studies have shown that the migration timescale of low-mass planets is much shorter than the lifetime of the disc. All planets should therefore have migrated to the vicinity of their host star! This is at least in contradiction with the locations of the planets in our Solar System. In order to elaborate predictive scenarios of planet formation and evolution, it is of primary interest to refine our understanding of disc-planet interactions. The inclusion of the disc self-gravity is an illustration of this. With analytical and numerical arguments, I show that discarding the self-gravity leads to a significant overestimate of the differential Lindblad torque for migrating low-mass planets. Another aspect explored in this thesis is the impact of the gas thermodynamics on migration. I show that the thermodynamic evolution of the disc induces an additional contribution to the corotation torque, which may dramatically slow down or even reverse the migration of low-mass planets.

Keywords: planetary migration, protoplanetary discs, hydrodynamics, linear analysis, numerical simulations

Contents

1	Other Solar Systems in the Universe!	1
1.1	The wealth of the Solar System	2
1.1.1	Guided tour	2
1.1.2	Did you say “planet”?	3
1.2	Extrasolar Planets	4
1.2.1	Detection methods	4
1.2.2	Statistical properties	9
1.3	Planetary formation	10
1.3.1	A byproduct of stellar formation	10
1.3.2	Core-accretion model	11
1.3.3	Formation of giant planets by gravitational instabilities	13
1.4	Concluding remarks	14
2	Planetary Migration	15
2.1	Introduction	16
2.2	Protoplanetary discs: an overview	16
2.3	Migration of low-mass planets: type I migration	18
2.3.1	Torque at Lindblad resonances	19
2.3.2	Torque at corotation resonances	24
2.3.3	Any ideas to slow down type I migration ?	30
2.4	Transition to the non-linear regime	32
2.5	Migration in a gap: type II migration	36
2.6	Runaway migration: type III migration	36
2.7	Concluding remarks	38
3	Disc-planet interactions: numerical calculations	41
3.1	The FARGO code	42
3.1.1	Initialization	43
3.1.2	Courant limit evaluation	44
3.1.3	Planet update	47
3.1.4	Gas update	47
3.1.5	Output step	50
3.1.6	Code units	50
3.2	Implementation of the self-gravity	50
3.2.1	Introduction	50
3.2.2	Implementation in the FARGO code	55
3.2.3	Test problems	57
3.2.4	Domain decomposition	59
3.3	Implementation of an energy equation	61

3.3.1	Thermodynamic background	61
3.3.2	Heat transport equation	62
3.3.3	Contact discontinuities	63
3.3.4	Implementation in the FARGO code	64
3.3.5	Test problems	65
3.4	Appendix: wave propagation properties	69
4	Type I planetary migration in a self-gravitating disc	73
4.1	Introduction	74
4.2	Numerical method	74
4.3	Physical model	75
4.4	Unexpected results without self-gravity	77
4.4.1	Inward shift of Lindblad resonances	77
4.4.2	Torque discrepancy	79
4.5	Inclusion of the disc self-gravity	82
4.5.1	Axisymmetric self-gravitating calculations	82
4.5.2	Fully self-gravitating calculations	83
4.5.3	Comparison with analytical results	86
4.6	The anisotropy model	89
4.6.1	Motivation	89
4.6.2	Validity	91
4.7	Corotation torque issues	92
4.8	Conclusions	94
5	On the corotation torque in adiabatic discs	97
5.1	Introduction	98
5.2	Linear analysis at an isolated resonance	98
5.3	Corotation torque	100
5.3.1	Limit of a cold disc	102
5.3.2	General case	104
5.4	Numerical study of an isolated corotation resonance	106
5.4.1	Numerical method	106
5.4.2	Results	107
5.4.3	Dynamics of the corotation region	110
5.5	Conclusions	113
6	Type I planetary migration in a radiative disc	115
6.1	Excess of corotation torque in an adiabatic disc	116
6.1.1	An illustrative example	116
6.1.2	Connection with analytics	122
6.1.3	Beyond linear analysis: the horseshoe model	125
6.1.4	Dependence on the entropy gradient	127
6.1.5	Impact of the softening length	129
6.1.6	Impact of the adiabatic index	130
6.1.7	Vortensity - entropy coupling	132
6.2	Desaturation of the corotation torque in a radiative disc	133
6.2.1	Saturation issues	133
6.2.2	A simple temperature prescription	137
6.2.3	Heat diffusion in the disc mid-plane	139
6.3	Concluding remarks	140

6.4 Appendix: estimate of the horseshoe U-turn time	140
7 Conclusions and perspectives	143
Bibliography	146
Refereed publications	152
On the Corotation Torque in a Radiatively Inefficient Disk	152
Type I Planetary Migration in a Self-Gravitating Disk	167
Curriculum Vitæ	182

Chapter 1

Other Solar Systems in the Universe!

THIS CHAPTER describes the current paradigm of planet formation. We start with a brief presentation of the planets in the Solar System in section 1.1. In section 1.2, we review the detection methods and the statistical properties of the extrasolar planets orbiting Sun-like stars. We describe in section 1.3 how far the discovery of exoplanets altered our models of planet formation. We address in section 1.4 some concluding remarks setting the outline of this manuscript.

Contents of this chapter

1.1	The wealth of the Solar System	2
1.1.1	Guided tour	2
1.1.2	Did you say “planet”?	3
1.2	Extrasolar Planets	4
1.2.1	Detection methods	4
1.2.2	Statistical properties	9
1.3	Planetary formation	10
1.3.1	A byproduct of stellar formation	10
1.3.2	Core-accretion model	11
1.3.3	Formation of giant planets by gravitational instabilities	13
1.4	Concluding remarks	14

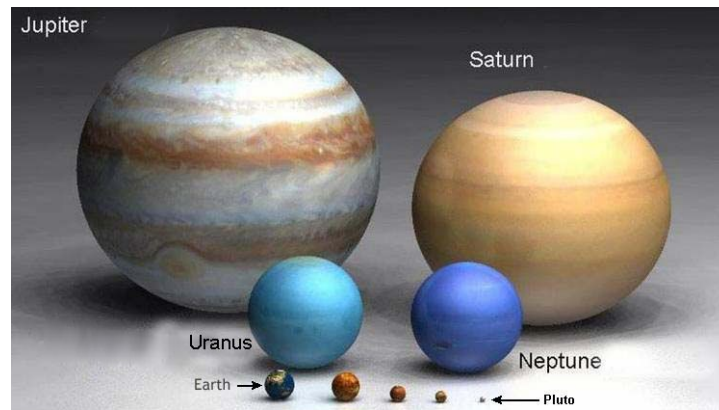


FIGURE 1.1: *The main protagonists of the Solar system.*

1.1 The wealth of the Solar System

1.1.1 Guided tour

The Solar System is an extraordinary laboratory for celestial mechanics. The least we can say is that it does not lack of diversity. Basically, its main protagonists, depicted in figure 1.1, divide between rocky planets close to the Sun, giant gaseous ones further out, and *fallen* Pluto, recently retrograded as dwarf planet after the recent revision of the planet definition in 2006 (see section 1.1.2). The Solar System also contains many small bodies: satellites, asteroids, Kuiper belt objects, or comets traveling from Oort's cloud. Recent mission Cassini-Huygens reported fascinating results concerning Saturn's world of satellites and rings, which is a bit like a Solar System in miniature. In addition, most planets exhibit odd features in their rotation properties, or their long-term evolution. Mercury rotates three times on its axis for every two orbits around the Sun. Contrary to all other planets of the Solar System, Venus rotates clockwise. The presence of the Moon is likely to have stabilized Earth's obliquity, thereby preventing dramatic changes in climate (Laskar et al. 1993). Eventually, recent studies are about to explain why Uranus' axis of rotation nearly lies on the Ecliptic plane (Boué, 2008, priv. comm.).

The link between mankind and planets has been marked by a subtle blending of observation, religion and myths. And when it comes to interpreting observations, myths are never too far. Even recently, Mars provides a good example. The planet has long stirred curiosity, because of its similarities with the Earth: a comparable size, a rather red aspect recalling of Earth deserts, the presence of ice caps, similar to Antarctic, and that of greenish regions, a bit like our forests. In 1925, an article reported by the french encyclopedia *Larousse* pretended to give a complete knowledge of the planet. It is worth translating. *"Some results can be considered as definitely established. The most interesting of them is the identification of vast forests covering a major part of the planet, and which had been confounded with seas, because of their dark aspect."* Later on, we learn that *"some astronomers had claimed that Martian vegetables were red. They were not totally exact, but had just seen a part of the truth..."* !

In a joint effort of observations and of theoretical works, our knowledge of Mars and of the rest of the Solar System has considerably increased. As we will see in section 1.3, the current paradigm of planet formation states that planets did not form where they are observed. This has important consequences for the planets evolution itself, to know in particular if other planets might have harbored life in the past, but also for the dynamics of the small objects in the Solar System. This may account for instance for the capture in mean-motion resonance¹ of many

¹Two objects are in Mean-Motion Resonance (MMR) if the ratio of their orbital period is a rational number.

objects belonging to the asteroid belts and to the Kuiper belt.

1.1.2 Did you say “planet”?

In 2006, the International Astronomical Union has revised the definition of a planet. Shall be called planet any object orbiting a central object (the Sun in the case of our Solar System), having sufficient mass to be in hydrostatic equilibrium (and thus having a nearly round shape) and to clear its neighborhood of small bodies. The astrophysicist Hal Levison has proposed a simple way to quantify the latter criterion, depending on the mass and on the location of the object within the planetary system. His arguments are as follows. Consider a system containing a central star of mass M_* , a single planet of mass M_p on a circular orbit of radius a_p , and a number of small bodies on planet-crossing orbits. In this system, the planet can remove the small bodies nearby it if:

- (1) It can gravitationally *eject* them from the planetary system. As a small body interacts with the planet, it undergoes a random walk in orbital energy. The planet can eject a small body in the age of the planetary system (t^*) if it is able to change the body's orbital energy by an amount at least equal to its original value. [Tremaine \(1993\)](#) shows that this occurs if:

$$\frac{M_p}{M_\oplus} \gtrsim \left(\frac{M_*}{M_\odot} \right)^{3/4} \left(\frac{1\text{Gyr}}{t^*} \right)^{1/2} \left(\frac{a_p}{1\text{AU}} \right)^{3/4}, \quad (1.1)$$

where 1 AU (Astronomical Unit) corresponds to the Sun-Earth distance, and where M_\odot and M_\oplus respectively denote the mass of the Sun and of the Earth.

- (2) or it can *accrete* all of them. Assuming a typical inclination for the bodies and a representative volume density near the planet location, Levison showed that for a planet to accrete all bodies nearby its orbital radius, its mass must satisfy:

$$\frac{M_p}{M_\oplus} \gtrsim \begin{cases} 4.4 \times 10^{-3} \left(\frac{4\text{Gyr}}{t^*} \right)^{3/2} \left(\frac{a_p}{1\text{AU}} \right)^{21/4} & \text{if } M_p < M_t, \\ 5.5 \times 10^{-2} \left(\frac{4\text{Gyr}}{t^*} \right)^{3/4} \left(\frac{a_p}{1\text{AU}} \right)^{15/8} & \text{otherwise,} \end{cases} \quad (1.2)$$

where $M_t = 0.7M_\oplus (a_p/1\text{AU})^{-3/2}$ is a transition mass such that if $M_p > M_t$ the gravitational focusing of the planet on nearby bodies is important.

An object of orbital radius a_p is defined as a planet if its mass M_p satisfies at least one of the two equations (1.1) and (1.2). These two criteria are depicted in figure 1.2, in the case of the Solar System ($M_* = M_\odot$, $t_* \sim 4.5$ Gyr). The eight planets of the Solar System and Pluto are represented with green circles, with their *current* mass and semi-major axis. The purple circle shows the asteroid Ceres. Any object above the blue line will eject the small bodies of its neighborhood, while any object above the two-pieces red line will accrete them. Anything above either line being a planet, there are therefore eight planets in the Solar System. Objects below both curves are called *dwarf planets* if they have a round shape (e.g. Pluto or Ceres, the only dwarf planet of the asteroid belt), or *small bodies* otherwise (all other asteroids). As we shall see later, the semi-major axis of the planets should have changed with time. For low-mass planets like Mars, we expect that it decreased with time. Assuming that Mars built up at larger distance from the Sun then leads to the intriguing conclusion that it might have satisfied none of the above criteria for planet definition before moving to its present location.

For Neptune and Pluto, this ratio is very close to 3/2: after three revolutions of Neptune, Pluto has performed two.

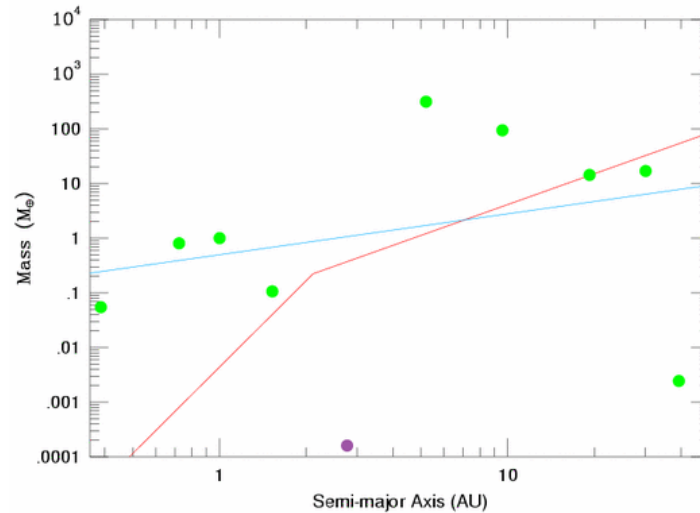


FIGURE 1.2: Planet mass - semi-major axis diagram illustrating the two criteria of Levison to define a planet. The green circles represent the nine 'classical' planets of the Solar System, with their current mass and location. The purple one shows Ceres. The blue line depicts the ejection condition of equation (1.1), whereas the two-pieces red line displays the accretion criterion of equation (1.2). From [Levison \(2006\)](#).

1.2 Extrasolar Planets

The very first planet discovered outside the Solar System was detected in 1992 around the millisecond pulsar PSR1257+12a ([Wolszczan & Frail 1992](#)). Three planets were actually detected, of 0.02, 4.3 and 3.9 Earth masses, respectively orbiting at 0.19, 0.36 and 0.46 AU from the pulsar. Planets orbiting pulsars are thought to be byproducts of the supernova explosion that gave origin to the pulsar, rather than bodies already existing by the time of the explosion. They are thus unlikely to harbor life, and researchers have rather concentrated on finding planets around Sun-like stars. After years of efforts, the first extrasolar planet around a Sun-like star, 51 Pegasus b, was reported in 1995 by [Mayor & Queloz \(1995\)](#), and immediately confirmed by [Marcy & Butler \(1995\)](#). This detection came as a real surprise, as one would not have imagined a Jovian mass planet orbiting its parent star in only 4 days! And being about 100 times closer to its star than is Jupiter from the Sun. Thirteen years after the detection of 51 Pegasus b, more than 300 exoplanets have been discovered, and the hunt for new worlds is getting faster and faster. There are currently 95 ongoing programs or future projects devoted to the search for extrasolar planets, 15 of them are space missions ([The Extrasolar Planets Encyclopedia](#), <http://extrasolar.eu>). A striking result of the exoplanets detected so far is their huge variety of characteristics. Planet searches have revealed giant planets with orbital periods as short as 1.1 days (e.g. WASP-12 b), or as long as ~ 10 years (e.g. HD 187123 c). Some exoplanets have an eccentricity comparable to that of the comets in our Solar System (like HD 20782 b, with $e \sim 0.92$), while some others have nearly circular orbits (e.g. HD 189733 b). Not all exoplanets are found in multiple planetary systems (only $\sim 15\%$ of them). Extrasolar planets are definitely very different from their Solar System counterparts.

1.2.1 Detection methods

We review in this paragraph the main detection methods of extrasolar planets. Our motivation is to give a physical, intuitive approach of these methods. We especially focus on the radial velocity technique, since it has contributed to the vast majority of the detections to date.

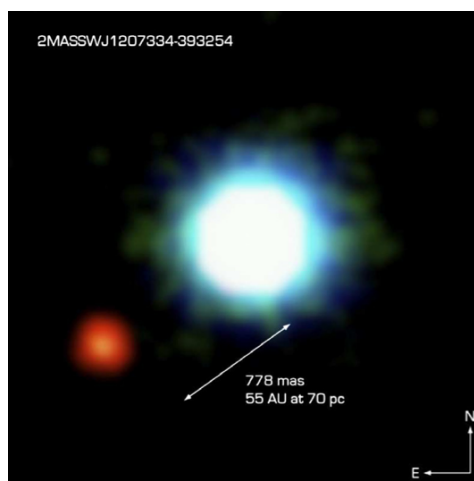


FIGURE 1.3: Composite infrared image of brown dwarf 2M1207 and its companion, as viewed by the Very Large Telescope. The primary and secondary have masses of 25 and 5 times the mass of Jupiter, and are distant of ~ 55 AU, suggesting it is a binary brown dwarf. Image taken from [Chauvin et al. \(2004\)](#).

Direct imaging

A natural method to detect exoplanets is to point a telescope toward a nearby star and search for a planetary companion around. It suffers however from two major difficulties: an extremely small angular separation, and a very high star to planet flux ratio. For example, the Sun-Jupiter system located at 10 parsecs would be seen with an angular separation of $0.5''$, with a stellar to planet flux ratio of $\sim 10^9$ in optical wavelengths, and of $\sim 10^5$ in the infrared. The direct detection was still a fiction's quest a few years ago. And yet, spectacular progress in adaptive optics have already given us a few images of companions to close-by young stars, like the one depicted in figure 1.3. The improvement of interferometry, in particular the use of nulling techniques to block the light coming from the star (like the coronagraph) gives a promising future to this technique. Despite the fast improvements in this field, detecting exoplanets with direct imaging remains a very intricate task. From now on, only five candidates have been reported, most of them are brown dwarfs at large distance from their primary. Within the next decade, space based projects, like Darwin or Terrestrial Planet Finder, might be able to detect Earth-like planets in habitable zones², and to perform spectroscopic observations of their atmospheres.

Radial velocity measurement

To overcome the difficulty of a direct detection, there exists an elegant solution, based on detecting exoplanets *indirectly*. If a planet orbits its parent star, the two-body problem tells us that the star rotates around the center-of-mass of the star and the planet. Measuring a periodic perturbation of the star's motion may therefore betray the presence of a companion. This recalls the discovery of Neptune³. The perturbed motion of the star is evaluated by the Doppler

²The concept of habitable zone has regained interest since the discovery of the first exoplanets. For a planet to be in a habitable zone, and presumably to harbor life, several conditions are required. Among them, the planet should be reasonably close to its parent star so that its surface temperature might maintain liquid water. Furthermore, the planetary system it belongs to should be reasonably close to the galactic center, so that, in its early stages, it contained enough heavy elements to favor the formation of rocky planets.

³The observed orbit of Uranus differing from ephemerides, Urbain Le Verrier and John Couch Adams independently predicted in 1845 the existence of a eighth planet in the Solar System, perturbing the movement of Uranus. This was confirmed observationally in 1846.

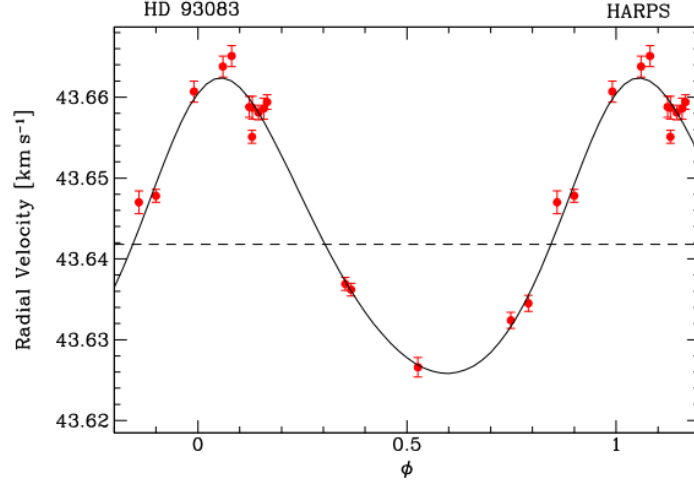


FIGURE 1.4: Radial velocity signal for HD 93083 (circles). The phase Φ in abscissa evolves linearly with time. The solid curve shows the result of the best fit obtained with the least squares technique. Companion HD 93083b has a minimum mass comparable to that of Saturn, and its eccentricity is $e \sim 0.14$. From [Lovis et al. \(2005\)](#).

shift measurement of many absorption lines in its spectrum. This gives the velocity of the star projected along the line of sight, or *radial velocity*. It is this technique that led to the discovery of 51 Pegasus b by [Mayor & Queloz \(1995\)](#). By measuring the radial velocity of star 51 Pegasus at many different times, the authors obtained a signal similar to that depicted in figure 1.4. The signal is usually adjusted assuming that only one prograde companion orbits the star. The radial velocity v_{rad} thus takes the form: $v_{\text{rad}} = v_0 + Kf(t)$, where v_0 is the velocity of the center-of-mass, f is a periodic function of time with zero mean, and where

$$K = \left(\frac{2\pi\mathcal{G}}{P} \right)^{1/3} \frac{1}{\sqrt{1-e^2}} \frac{M_p \sin(i)}{(M_\star + M_p)^{2/3}} \quad (1.3)$$

is called the semi-amplitude of the radial velocity. It features the gravitational constant \mathcal{G} , the orbital period P , the companion eccentricity e , the mass M_\star of the star, that M_p of the planet, and the inclination i between the line of sight and the perpendicular to the orbital plane. The best fit of the radial velocity signal is obtained by adjusting v_0 , K and f through the least squares technique. The main orbital elements of the companion are then deduced, among them: e , P , the semi-major axis a and the minimal mass $M_p \sin(i)$. We comment that:

- Measuring the projected velocity can only lead to an estimate of the *projected* mass of the companion, $M_p \sin(i)$. In other words, only a *lower limit* of the planet mass can be determined, which is *a priori* a strong limitation for this technique. Assuming an isotropic distribution for the orbital inclinations, it can be shown that the minimum masses should actually be close to the real masses ([Jorissen et al. 2001](#)). Nonetheless, the unambiguous determination of the companion mass is possible only if the inclination is evaluated independently (e.g. through an astrometric detection), or in the particular case of a photometric transit (see below).
- Equation (1.3) shows that $K \propto M_p \sin(i) P^{-1/3}$. The radial velocity is therefore biased toward the detection of massive exoplanets with short periods. Since the fit of the orbital elements requires the monitoring of a full orbital period, it is the duration of the surveys that limits the maximum semi-major axis of the exoplanets detected so far.

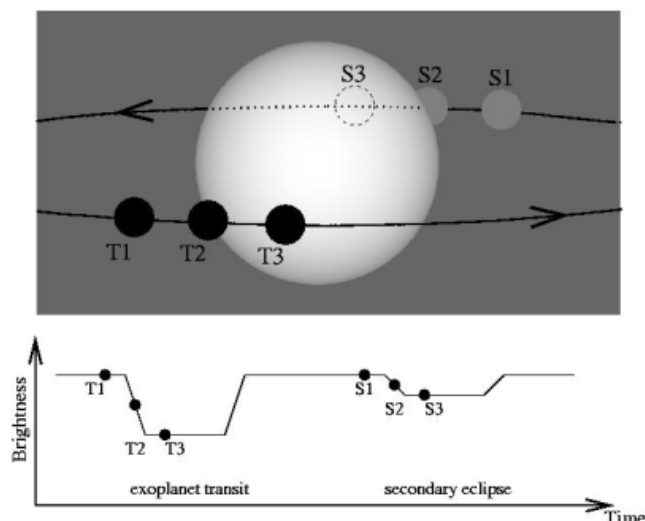


FIGURE 1.5: *Illustration of a transit signal. The relative variation of the stellar flux is depicted as a function of time. The different stages of the exoplanet transit, and those of the secondary eclipse (when the planet passes behind the star) are explicated with the above picture. Illustration from I. Snellen.*

- The radial velocity signal may be much more intricate than the one depicted in figure 1.4. This happens for instance when several planets orbit the star. In this case, the same method as above is applied for each hypothetical companion, assuming coplanar orbits. This approach led for instance to the discovery of a second planet orbiting Gliese 876 (Marcy et al. 2001). When several planets orbit the star, the dynamics of the system can provide additional constraints on the fit of the orbital elements. In particular, the least squares technique and the requirement for stable orbits on the long term may provide different solutions for the planetary system (Correia et al. 2005). Regarding the case of multiple exoplanets, we mention the recent work of Gayon & Bois (2008) who showed that planetary systems with counter-revolving orbits (e.g. two planets with one retrograde and one prograde) are likely to be more stable on the long term.

Since the discovery of 51 Pegasus b, the radial velocity technique has been the most productive in detecting exoplanets. As of today (July, 14th 2008), 290 out of the 307 exoplanets known have been reported with this method. Currently, the most accurate instrument is the HARPS spectrograph (Mayor et al. 2003), which can achieve a long-term precision better than 1 m.s⁻¹. The hunt for earth-like planets, requiring an accuracy of ~ 0.1 m.s⁻¹, is about to begin. However, it will become more and more difficult to extract the planetary signal from the noise generated for instance by dark spots at the stellar surface, or by atmospheric vibrations due to acoustic modes, all inducing radial velocity amplitudes of a few m.s⁻¹.

Photometric transits

Another way of detecting exoplanets indirectly is to search for transits, that is for stellar occultations by a planetary companion. The first transit of an exoplanet (HD 209458b) was detected in 1999 by Charbonneau et al. (2000). As the exoplanet had already been discovered by the radial velocity technique, this detection proved beyond doubt that the Doppler shift was indeed caused by a planet. The transit detection consists in measuring the stellar flux variation with time, an illustration of which is displayed in figure 1.5. It shows that two occultations occur: when the planet passes in front of the star (exoplanet transit), and then behind it (secondary eclipse). We note in passing that the flux emitted by the planet may be evaluated by difference.

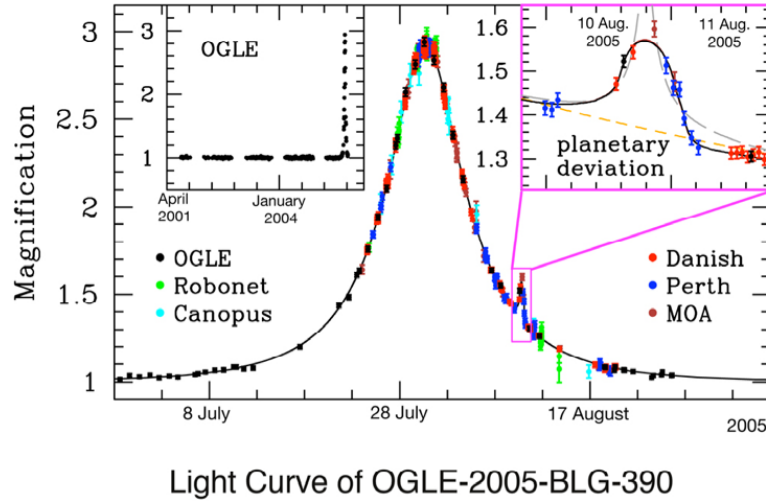


FIGURE 1.6: Magnification variation with time of OGLE-2005-BLG-390. The largest peak corresponds to the magnification due to the lens star, the second peak is due to a low-mass planet orbiting the lens star. From [Beaulieu et al. \(2006\)](#).

During the exoplanet transit, the maximum variation of the stellar flux F_\star is connected with the planet radius R_p as:

$$\left(\frac{\Delta F_\star}{F_\star}\right)_{\max} = \left(\frac{R_p}{R_\star}\right)^2, \quad (1.4)$$

where R_\star denotes the star radius, which can be determined with the other characteristics of the transit (its shape and duration). From equation (1.4), assuming the star has a solar radius, $\Delta F_\star/F_\star$ is $\sim 10^{-2}$ for a Jupiter-like planet, while it amounts to $\sim 10^{-4}$ for a Earth-like planet. While the technique accuracy from the ground is about 10^{-3} , it can reach 10^{-6} from space, where the transit detection of terrestrial planets should not be a problem. This motivated the development of two space missions. The first is COROT⁴, which has recently detected extremely faint signals that, if confirmed, could indicate the existence of an exoplanet with a radius as small as 1.7 times Earth's radius. The next step in the hunt for rocky exoplanets is KEPLER, which will be launched in February 2009. Its precision is one order of magnitude better than that of COROT, and it is expected to find at least 50 terrestrial planets.

The transit detection supposes an inclination i very close to $\pi/2$. It is thus an interesting complementary approach to the radial velocity measurement. Combining both approaches gives indeed the true mass of the planet, as $\sin(i) \approx 1$, and its radius. The mean density of the planet can therefore be deduced. Moreover, detecting the transit in different wavelengths can provide information on the exoplanets atmospheres ([Charbonneau et al. 2002](#), [Vidal-Madjar et al. 2004](#)). The transit detection opens many possibilities to confront the observed properties of exoplanets (inner structure, atmosphere composition) with those predicted by theoretical models.

Microlensing

The microlensing technique involves two stars: a background star as a source of light, and a foreground star as a gravitational lens. When it passes in front of the source star, the lens star causes the latter to suddenly brighten by several orders of magnitude, for several days or months. The increase of the source brightness is called magnification. Of particular interest is the case where the lens star has a planetary companion, which induces a smaller and shorter magnification

⁴COROT is a french mini-satellite devoted to asteroseismologic and photometric studies of stars.

of the source star. We display in figure 1.6 the magnification variation with time of OGLE-2005-BLG-390. The second peak, better seen in the close-up, is the magnification induced by a planet of mass $M_p \sim 5.5M_\oplus$, located at ~ 2.6 AU from the lens star (Beaulieu et al. 2006). This is one of the least massive exoplanets so far detected. The microlensing technique is complementary to the other detection methods, as it is well suited to detect terrestrial planets at distance between 1 and 5 AU from their parent star, hence in habitable zones.

1.2.2 Statistical properties

Thirteen years after the discovery of 51 Pegasus b, more than 300 exoplanets have been reported, about 95% of them by the radial velocity technique. Their statistical properties reveal a number of surprising results and provide important constraints for the scenarios of planetary formation, as we shall see later. The projected mass of the known exoplanets is displayed as a function of their semi-major axis in the left panel of figure 1.7. For comparison, some of the planets of the Solar System are also depicted. The most striking observation is the vast number of high-mass planets at very small separations: about 80 exoplanets with a minimum mass larger than $\sim 0.05M_{\text{Jup}}$ (which is about the mass of Uranus, the lightest giant planet of the Solar System) are detected at separations smaller than 0.1 AU! Much smaller than the Mercury-Sun distance! Among them, those having a minimum mass comparable to that of Jupiter are usually called the *Hot Jupiters*. None of these planets were supposed to exist according to the theories of planetary formation at the time of the first detections. The temperatures at these low distances are so high that the material needed to build the core of such planets cannot be found in a solid phase there. Planets must therefore have built up further out before moving closer to the central star. Remarkably enough, *orbital migration* of planets had been predicted about 15 years before the discovery of the first exoplanet. We will describe the planetary migration process in details in chapter 2. The large amount of high-mass planets at small separations is certainly due to the intrinsic biases of the radial velocity technique (see section 1.2.1). Nevertheless, the above diagram reveals a significant deficit of very massive companions ($M_p \sin(i) \gtrsim 4M_{\text{Jup}}$) at small semi-major axis ($a \lesssim 0.4$ AU). As we will see later, this result is compatible with the predictions of the planetary migration theory, which states that when the planet becomes more massive than the local disc (with which the planet is interacting), the migration speed decreases with the planet mass. We eventually stress that no exoplanets are found at $a \lesssim 0.02$ AU.

In the right panel of figure 1.7, we display the eccentricities of the exoplanets as a function of their semi-major axis. The first six planets of the Solar System are also represented. The smaller the semi-major axis, the smaller the eccentricity, which is consistent with the expected tidal circularization due to the host star. For $a \gtrsim 0.5$ AU, the exoplanets eccentricity varies from 0 to more than 0.9. This is again in sharp contrast with the planets of our Solar System, which are on nearly circular orbits. Note that higher eccentricities seem to be obtained for more distant planets. We also mention that there is no significant difference between the eccentricity distributions of planets in multiple planets systems and in single systems.

Another unexpected property of the exoplanets is the rather high metallicity of their host star. More than 20% of stars having a metallicity twice the solar value harbor a *giant* planet, while this ratio decreases to $\sim 3\%$ for stars with solar metallicity (Santos 2008). Interestingly, this metallicity-planet correlation tends to disappear for stars hosting lower planet masses (Udry et al. 2006). Decreasing the metallicity renders the formation of planetary cores less effective. Thus, protoplanets may not achieve enough mass to start forming a gas envelope by runaway accretion of gas (see section 1.3), thus keeping a mass of a few times that of the Earth.

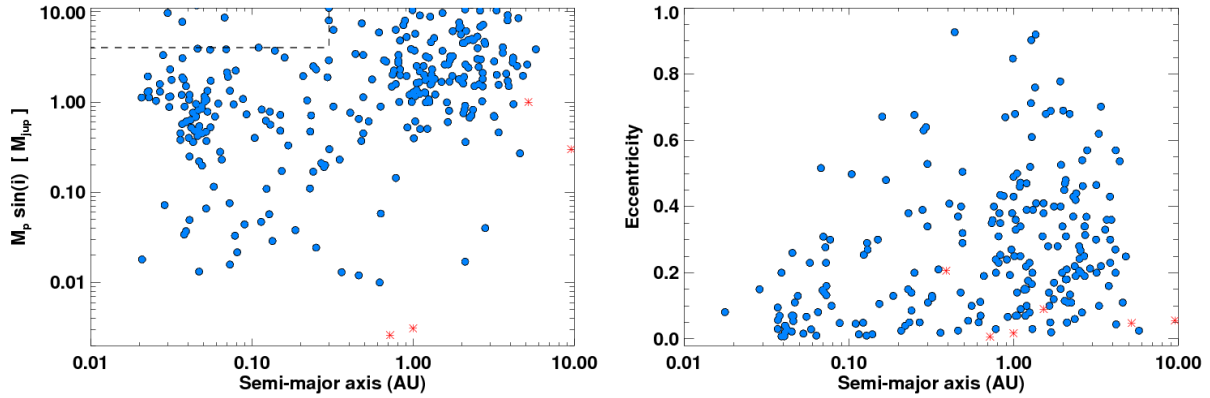


FIGURE 1.7: Left: projected mass, expressed in jovian mass, as a function of the semi-major axis (in AU), for the 307 exoplanets known to date (blue circles). For comparison, some planets of the Solar System are represented with red stars. The rectangle delimited by the dashed lines shows that there is a deficit of very high-mass planets (projected mass larger than $\sim 4M_{\text{jup}}$) at short separation from their host star (smaller than $\sim 0.3\text{AU}$). Right: eccentricity versus semi-major axis (in AU). The six first planets of the Solar System appear with red stars. The data used to build these plots were exported from *The Extrasolar Planets Encyclopedia*.

1.3 Planetary formation

Before the early 1990's, our understanding of planet formation relied on several centuries of observation of the planets in the solar system. In particular, theories of planet formation intended to reproduce the dichotomy of the Solar System, with terrestrial planets in its inner parts, and giant gaseous planets in its outer parts. A few years of exoplanets detections have been enough to significantly renew our formation models, and have revealed that our Solar System may only be a very particular system.

1.3.1 A byproduct of stellar formation

The first theories of planetary formation emerged in the eighteenth century under the impulse of the philosopher Kant (1755) and of the scientist Laplace (1796). They independently proposed that the Solar System formed from a cold disc of gas and dust rotating around the Sun, and that planets were the byproducts of the star and disc formation. Two centuries later, their pioneering ideas are the basis of the standard model for stellar formation. According to this model, stellar formation begins with the collapse of a massive, rotating molecular cloud. The pressure and temperature at the cloud center increase dramatically. Soon, the first nuclear reactions occur and a protostar is produced. Due to the conservation of angular momentum, the cloud progressively collapses into a disc of gas and grains orbiting the nascent star, in about 10^5 yrs. The disc vertical extent is 10 to 30 times smaller than its horizontal extent. Its mass, which is dominated by the gas component, is 10 to 1000 times smaller than the mass of the star. Although the solid component is much less massive, it contributes to the formation of the planetesimals, which are the brick elements of the planet cores. During its early stages, the disc contains dust grains with a size ranging from 0.1 to 1 micron, which is the typical size of grains in the interstellar medium. Due to their interaction with the gas, grains sediment toward the disc mid-plane, and ballistic collisions between them lead to the formation of dust aggregates of centimeter to meter size. This process is however particularly sensitive to the level of turbulence in the gas, which tends to spread grains in the entire vertical extent of the disc (see e.g. [Fromang & Papaloizou 2006](#)). The growth of these particles into km-sized planetesimals is

still unclear, more especially in the context of a turbulent disc. Accumulation of dust particles through collisions may not be efficient enough to prevent their destruction through collisional fragmentation and their rapid drift toward the central star (Brauer et al. 2008). The recent work of Johansen et al. (2007) may bring a solution to this lingering issue. The authors showed that an efficient gravitational collapse of dust particles can be achieved in high-pressure regions in the gas, which act as particle traps. Kilometer-sized boulders may be rapidly formed, depending upon the mechanisms sustaining turbulence in the disc. Accretion of planetesimals can then lead to planet formation, as will be described in section 1.3.2. In the following, we will refer to *protoplanetary disc* as the disc of gas and of planetesimals surrounding the central star.

1.3.2 Core-accretion model

The core-accretion model is a unified theory for the formation of both terrestrial and giant gaseous planets. The basics of this model were introduced in the early 1960's by Safronov as an attempt to explain the dichotomy of the Solar System. This model has been recently revisited by Pollack et al. (1996), whose results showed that the formation of giant planets may be divided into three parts, as illustrated in figure 1.8. The protoplanetary core is first formed by runaway accretion of the planetesimals (~ 1 km-sized objects) located in the planet's *feeding zone*. The extent of the latter is typically a few times the planet's Hill radius⁵. The core's growth ends as the planet has severely depleted its feeding zone of planetesimals. Its duration relies on the planet's initial location in the protoplanetary disc. Fast growth is thought to occur preferentially beyond the so-called *snow line*, where the disc is cold enough for ices to condensate, thereby maximizing the density of solids available for accretion (Ida & Lin 2004a). For Sun-like stars, the snow line is typically located around 3 AU. Within the snow line, the core's growth is too slow to induce significant gas accretion, and a terrestrial planet is formed. Above the snow line, the growth is rapid (~ 0.5 Myr for Jupiter, see figure 1.8), and the forming planet may enter a long stage (here between 0.5 and ~ 7.5 Myr, the planet mass is slightly larger than 10 Earth masses) when its mass increase is essentially due to the slow accretion of gas in its envelope. As the envelope mass grows up, the extent of the feeding zone rises as well, and more planetesimals are accreted. The energy gained by the accretion of planetesimals is balanced by the energy radiated away by the gaseous envelope, so the latter maintains quasi-static equilibrium. However, when the envelope mass approximately reaches the accumulated solid mass, the radiative losses can no longer be compensated for by the accretion, and the envelope starts to contract. This contraction increases the gas accretion rate, which increases the radiative losses and the process undergoes a runaway. The final mass of the planet will depend on the amount of gas that can be supplied by the circumplanetary disc. The runaway stage occurs for a critical solid mass ranging from 10 to 15 Earth masses, which is in roughly good agreement with the estimated mass of ice and rocks for the giant planets of the Solar System.

In the core-accretion model, the timescale for giant planet formation is essentially limited by the slow accretion of gas in the second phase. Its duration is particularly sensitive to the initial surface density of planetesimals in the feeding zone (Pollack et al. 1996), and to the grain opacities in the planet's envelope (Hubickyj et al. 2005). With the surface density considered in figure 1.8, Jupiter can be formed in about 8 Myrs. Reducing the initial surface density of solids by a 25% factor increases the formation timescale to nearly 50 Myrs! For some opacities, the

⁵The planet's Hill radius R_H is the distance from the planet below which the gravity of the planet prevails over the gravity of the star and the centrifugal force. Its expression is:

$$R_H = a_p \left(\frac{M_p}{3M_\star} \right)^{1/3}.$$

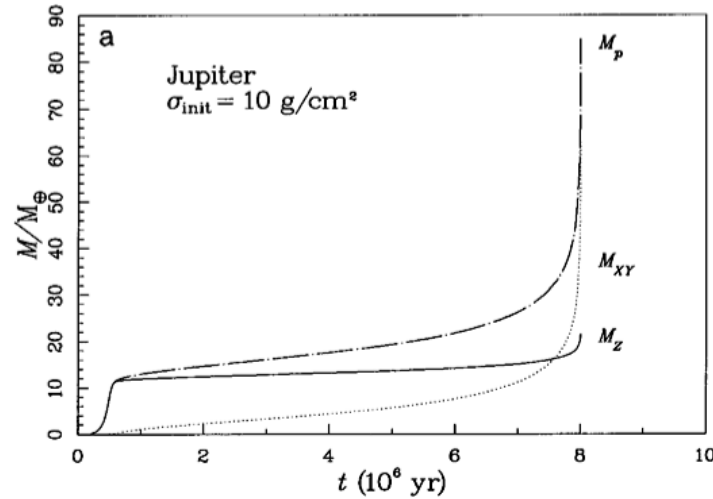


FIGURE 1.8: Time evolution of Jupiter’s mass, predicted by the J1 model of [Pollack et al. \(1996\)](#). The planet remains fixed at 5.2 AU, and the initial surface density of the protoplanetary disk is 10 g.cm^{-2} . The solid line shows accumulated solid mass, the dotted line accumulated gas mass, and the dot-dashed line the total mass of the planet. Figure taken from [Pollack et al. \(1996\)](#).

formation of Jupiter can occur within 2 Myrs! The formation timescale is uncomfortably long compared to the lifetime of protoplanetary discs, which should range between 1 and 10 Myrs ([Cieza et al. 2007](#), [Hillenbrand 2008](#)). This *timescale problem* led to the hypothesis that another faster mechanism might be at work to explain the formation of giant planets. One possibility is that gravitational instabilities in protoplanetary discs could enhance giant planet formation ([Boss 1997](#)). We will discuss this model in section 1.3.3.

There is another issue regarding the core-accretion model. As stated above, a giant planet can be formed provided its core’s growth is sufficiently rapid, which supposes that the core builds up at large separations from the star. However, we have seen in section 1.2.2 that exoplanets with minimum mass of about Jupiter’s mass are commonly found at separations of a few 0.1 AU. We have already concluded in this section that planets should have formed much further in the disc, and then have *migrated* toward their current location. Planetary migration is one consequence of the interaction between the planet and the gaseous protoplanetary disc, so it occurs as long as gas is present in the disc. Furthermore, low-mass planets are predicted to migrate very fast (type I migration), in typically $10^4 - 10^5$ yrs ([Tanaka et al. 2002](#)), which is much faster than the giant planet formation process predicted by [Pollack et al. \(1996\)](#), and much faster than the observed disc lifetimes. [Alibert et al. \(2005\)](#) therefore revisited the core-accretion model, including planetary migration and disc evolution. To prevent the rapid migration of planet cores toward the vicinity of the star, the authors assumed a migration rate that is 10 to 100 times smaller than that predicted by the analytical estimate of [Tanaka et al. \(2002\)](#), yet in good agreement with the results of disc-planet numerical simulations (see e.g. [D’Angelo et al. 2002](#)). Within this strong limitation, they found a significant reduction of the timescale for giant planet formation, now of ~ 1 Myr. The reason for this speed up is that the planet’s feeding zone is continuously regenerated with fresh planetesimals as the planet migrates. The accretion of gas is not necessary anymore to extent the feeding zone, and the tedious second stage of Pollack’s model is suppressed. This extended version of the core-accretion model now successfully explains the formation of giant planets within disc lifetimes, provided that type I migration be much slower than expected.

The improvements of the core-accretion model and the growing number of exoplanets detected has raised the possibility to build population synthesis, in an attempt to reproduce the

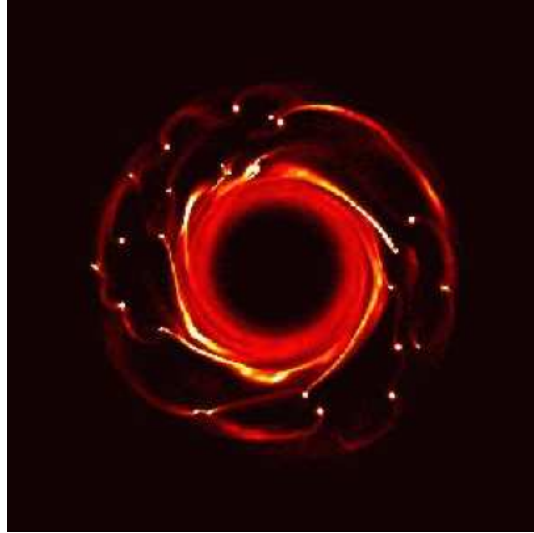


FIGURE 1.9: Typical shape of the surface density in the mid-plane of a fragmenting protoplanetary disc. At the outermost parts of the disc, high-density clumps form that may supply adequate conditions for the formation of gaseous planets. Taken from [Durisen et al. \(2007\)](#).

observed properties of exoplanets. Using an alternative core-accretion model, which lacks however the migration process of low-mass planets, [Ida & Lin \(2004b\)](#) found that the formation probability of gas giant planets increases rapidly with the metallicity of their host stars, and predicted a metallicity distribution for stars bearing giant planets that is in quantitative agreement with the observed one. Including the migration of low-mass planets, the same authors stress that the mass and semi-major axis distributions of extrasolar giant planets could be reproduced if, again, the migration rate of low-mass planets was an order of magnitude smaller than predicted by analytic estimates ([Ida & Lin 2008](#)).

1.3.3 Formation of giant planets by gravitational instabilities

Gravitational instabilities have been reexamined by [Boss \(1997\)](#) as an alternative model to explain the formation of giant planets, at a time when the standard core-accretion model led to a formation timescale comparable to if not larger than disc lifetimes. If the protoplanetary disc is massive enough, the propensity of the fluid elements to interact gravitationally and merge together can no longer be compensated for by the disc rotation and the pressure force. This is quantitatively controlled by the Toomre parameter Q of the disc. Its expression will be given by equation (4.12). Parts of the disc where Q is smaller than ~ 1 become gravitationally unstable, and rapidly lead to the formation of clumps. This is illustrated in figure 1.9. Clumps are high-pressure *cocoons* trapping solid particles, which may ultimately give rise to giant planets. This is conditioned by the clumps survival, which occurs if the latter radiate away their thermal energy efficiently. When the two conditions ($Q \lesssim 1$ and efficient cooling) are satisfied, giant planets can be formed in a dynamic timescale, hence in about $10^1 - 10^2$ yrs, depending on the location in the disc. This is the main success of this model. The actual timescale for giant planet formation therefore relies on the time required for the disc to reach fragmentation conditions. This is the main issue of this model. It is still unclear indeed whether these conditions are satisfied in realistic models of protoplanetary discs. On the one hand, the work done by Boss (e.g. [Boss 2008](#)) essentially shows that fragmentation is very likely to occur at separations smaller than ~ 50 AU, and that it does not significantly depend on the star metallicity (in contradiction with the probability detection of giant planets, as seen in section 1.2.2). On the other hand, work done

for instance by [Boley et al. \(2007\)](#) reveals opposite results: fragmentation would occur under exceptional (unphysical) conditions, and metallicity would matter. These opposite statements might depend upon the details of the algorithms used to perform numerical simulations. Even if the conditions for fragmentation are not fulfilled, protoplanetary discs should remain marginally unstable, and spiral waves should develop. These waves induce local high-pressure regions that favor the accumulation of solid particles, which may render the core-accretion process easier. Any other mechanism generating local pressure maxima could enhance planet formation. This has been suggested by [Varnière & Tagger \(2006\)](#) with the formation of Rossby vortices, which has been recently confirmed by [Lyra et al. \(2008\)](#).

1.4 Concluding remarks

After thirteen years of observations, over three hundred exoplanets orbiting Sun-like stars have been discovered. Despite the biases inherent to the detection methods, the statistical properties of the exoplanets reveal that the Solar System should be better seen as an exception rather than an illustrative example of planetary systems. Our theories of planetary formation, which were before 1995 dedicated to reproducing the Solar System, have been deeply revisited. Of particular importance, the discovery of the Hot Jupiters has turned planetary migration into a key ingredient of the formation models. Taking the planet migration and the disc evolution into account, the core-accretion model succeeds in explaining the formation of giant planets within the observed disc lifetimes. We have seen that this model may be sustained by any mechanism yielding high-pressure regions in the gaseous protoplanetary disc. Population synthesis based on the extended core-accretion model tend to reproduce the observed properties of the extrasolar planets, and provide exciting predictions for the future. One may be optimistic. Even the lingering issue of the planetesimals formation is in good way to be solved. A coherent scenario describing each stage of the planet formation, from micron-sized grains to giant planets, may not be so idealistic. Nonetheless, the extended core-accretion model requires a timescale for type I migration that is at least one order of magnitude smaller than the accepted value. Predictive scenarios of planetary formation therefore require a mechanism, or additional physics, that may slow down type I migration. This is what the following chapters of this thesis are about.

Chapter 2

Planetary Migration

THE INTERACTION BETWEEN A PLANET AND A PROTOPLANETARY DISC is described in this chapter. We show that the disc exerts a torque on the planet that generally reduces the planet's semi-major axis, causing the planet to progressively spiral toward the central star. This is known as planetary migration. After a brief overview on protoplanetary discs in section 2.2, we review the different types of planetary migration through sections 2.3 to 2.6.

Contents of this chapter

2.1	Introduction	16
2.2	Protoplanetary discs: an overview	16
2.3	Migration of low-mass planets: type I migration	18
2.3.1	Torque at Lindblad resonances	19
2.3.2	Torque at corotation resonances	24
2.3.3	Any ideas to slow down type I migration ?	30
2.4	Transition to the non-linear regime	32
2.5	Migration in a gap: type II migration	36
2.6	Runaway migration: type III migration	36
2.7	Concluding remarks	38

2.1 Introduction

We have given in last chapter a short introduction on the extrasolar planets, in particular how their remarkable properties jeopardized our models of planet formation. Many mechanisms have been proposed to reproduce the great diversity of the exoplanets orbital elements:

- *Gas-planet interaction.* A planet embedded in a protoplanetary gaseous disc experiences a torque from the disc which leads in general to its orbital decay toward the central object (Ward 1997). Recall that the variation of the planet's semi-major axis is referred to as the *planet migration*. There are several migration regimes that mainly differ from the ranges of planet and disc masses to which they apply. Type I migration is related to low-mass planets, whose perturbation on the disc is described by a linear analysis - see section (2.3). If the planet is massive enough, it can build a gap on the disc and its migration, referred to as type II migration, is severely slowed down - see section (2.5). For intermediate planet masses evolving in massive disc, the migration process can undergo a runaway. This is type III migration - see section (2.6). Another migration regime concerns low to intermediate planet masses in turbulent discs (such as discs invaded by the Magneto-Rotational Instability, described in section 2.2). In this case, planetary migration is much like a random-walk, so it is usually referred to as stochastic migration - see section (2.3.3). In a global way, the gas-planet interaction can efficiently alter the planets' semi-major axis. Conversely, the gas damps the planets' eccentricity, so the gas-planet interaction alone cannot reproduce the large dispersion of the exoplanets eccentricities.
- *Planetesimals-planet interaction.* Interactions between planets and planetesimals may also significantly alter the planets orbital elements, in particular when the gaseous protoplanetary disc is dissipated. The change in the planets semi-major axis through this interaction is called *planetesimal-driven migration*. It has been particularly investigated for the Solar System, where Jupiter might have slightly drifted inwards, whereas Saturn, Uranus and Neptune might have significantly migrated outwards. This mechanism was proposed to explain the current location of the Kuiper Belt (Levison & Morbidelli 2003), or the capture in mean-motion resonances of many of the Kuiper belt objects, like Pluto (Malhotra 1995). It also gives an elegant explanation for the Late Heavy Bombardment of the terrestrial planets (Tsiganis et al. 2005, Gomes et al. 2005).
- *Planet-planet interaction.* When planets migrate, be it due to their interaction with the gas or with planetesimals, they may lock into mean-motion resonance (MMR, see chapter 1). In the Solar System, Jupiter and Saturn are very close to a 5 : 2 MMR, while $\sim 20\%$ of the exoplanets in multiple planetary systems are found in MMR. The lock into mean-motion resonance provides a significant increase of the planets eccentricities, to values that typically range between 0.2 and 0.6 (Rasio & Ford 1996). Higher eccentricities may be induced by the Kozai resonance (Takeda & Rasio 2005), when a high-inclination binary companion secularly perturbs the planet orbit.

In this thesis, we only focus on the interaction of a planet with its parent gaseous disc, we discard planet-planet and planet-planetesimals interactions. Studying the gas-planet interaction first requires to be familiar with the properties of protoplanetary discs.

2.2 Protoplanetary discs: an overview

Protoplanetary discs correspond to the early stages of the disc evolution process described in section 1.3.1. It orbits a pre-main sequence star, also called T Tauri star. The disc is essentially

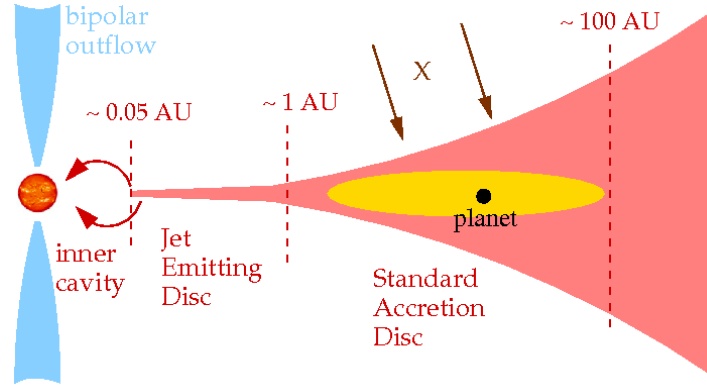


FIGURE 2.1: Schematic representation of a protoplanetary disc around a T Tauri star.

made of gas (mainly hydrogen and helium), the solid component (dust at early times) represents only a tiny fraction of the disc mass ($\sim 1\%$). The disc to primary mass ratio typically ranges from 10^{-3} to 10^{-1} . While the disc's radial extent can reach a few hundreds of AU, its vertical extent is much smaller: the pressure scale height to radius ratio, H/r , also called the *disc aspect ratio*, typically varies from 0.03 to 0.1. As already mentioned in section 1.3.2, the disc lifetime, which is also the timescale over which disc-planet interactions occur, is approximately between 10^6 and 10^7 yrs. An oversimplified, schematic representation of a protoplanetary disc, seen edge-on, is proposed at figure 2.1. The disc is basically separated into a Jet Emitting Disc¹, which is optically thin, and a Standard Accretion Disc, rather optically thick. The latter may be divided into the irradiated disc photosphere, if any (darkest filled region) and the disc mid-plane (lightest filled region), where the planets are supposed to form. In the context of disc-planet interactions, the gas in the disc mid-plane is usually assumed to be locally isothermal (the temperature is constant with time), and its self-gravity is neglected. We will revisit these assumptions in chapters 4 to 6.

Protoplanetary discs are accretion discs. Gas is continuously falling from the inner edge of the disc onto the surface of the star, with a typical accretion rate of 10^{-9} to $10^{-8} M_{\odot} \cdot \text{yr}^{-1}$. The molecular viscosity is about 10 orders of magnitude too small to account for the disc accretion rates. Nonetheless, the inward drift of the gas is usually modeled with an effective viscosity. [Shakura & Sunyaev \(1973\)](#) proposed a phenomenological approach where the kinematic viscosity of accretion discs takes the form:

$$\nu = \alpha c_s H, \quad (2.1)$$

with c_s the local sound speed, and α a numerical constant that typically amounts from 10^{-5} to 10^{-1} , as we shall see below. This approach is known as the α -model. The most probable mechanism leading to accretion is *turbulence*. Turbulence may originate from hydrodynamic instabilities, such as the Rossby-wave instability ([Lovelace et al. 1999a](#), [Li et al. 2000a; 2001](#)), the global baroclinic instability ([Klahr & Bodenheimer 2003](#)), or the Kelvin-Helmholtz instability, triggered by the vertical shear of the gas as dust settles in the mid-plane ([Johansen et al. 2006](#)). Another source of turbulence is the so-called Magneto-Rotational Instability (MRI, [Balbus & Hawley 1991](#)). This instability relies on the coupling of the ionized gas to the weak magnetic field of the disc. Ionization may occur in the vicinity of the central object due to the star irradiation, or further out in the disc layers, most probably through the UV background or cosmic rays. The ionization state of the disc mid-plane, where protoplanets build up and migrate, is rather unclear. It is still a matter of debate whether the disc mid-plane

¹We point out that not all protoplanetary discs harbor a jet emitting disc (not all T Tauri stars emit jets).

should be ionized as well, or if it remains neutral, being *shielded* by the layers. In any case, its ionization state may significantly evolve with time (Ilgner & Nelson 2008). The gas near the mid-plane that is not sufficiently ionized to couple to the magnetic field, and to be invaded by the turbulence triggered by the MRI, is usually called a *dead zone*. In contrast, the ionized parts of the disc that are unstable to the MRI are called *active zones*. Numerical simulations show that, in active zones, typical α values are in between 10^{-3} and 10^{-1} , depending on the geometry of the magnetic field (see e.g. Fromang & Papaloizou 2007). Even if the MRI only develops in the disc layers, turbulence may be *induced* in the dead zone (Fleming & Stone 2003). The authors estimated that the α parameter in the dead zone might be at least one order of magnitude smaller than in the active layers. Values of α in the range $10^{-5} - 10^{-4}$ might thus be relevant in dead zones. So far only the MRI has been shown to be robust in generating turbulence in protoplanetary discs. In addition to that, it may have important consequences for planet formation - see section 1.3.1 - and migration, as we will see below.

Before going on, we specify some notations used in the rest of this chapter. We will mainly consider two-dimensional discs, which are naturally described by the set of polar coordinates: r (the distance to the central star) and φ (the azimuth). The disc's rotation profile is Ω . Two useful quantities we will largely refer to are the second Oort's constant, defined by:

$$B = \frac{1}{2r} \frac{d(r^2\Omega)}{dr}, \quad (2.2)$$

and the horizontal epicyclic frequency κ , given by $\kappa = (4\Omega B)^{1/2}$. It is the frequency at which an eccentric test particle describes an epicycle about its guiding center, which has a uniform circular trajectory. In addition, the disc sound speed c_s is connected to the pressure scale height H by $c_s = H\Omega$. Recall that the disc aspect ratio h is defined by $h = H/r$. The disc surface density and temperature are respectively denoted by Σ and T . We will assume that they have a power-law dependence on r . Regarding the planet, we denote by M_p its mass and we will often mention the planet to primary mass ratio, $q = M_p/M_\star$. We will only consider planets on circular orbits, for which the semi-major axis a and the separation r from the star are identical. Eventually, any disc quantities calculated at the planet location will be written with a p subscript. For instance, the disc aspect ratio at the planet location is h_p .

2.3 Migration of low-mass planets: type I migration

We study in this section the interaction between a low-mass planet and its parent gaseous disc. By low-mass planet, we mean that the disc response to the planet potential is linear, and can thus be studied with a linear analysis. We will largely comment on the validity of the linear assumption in section 2.4. The disc is assumed to be two-dimensional, non self-gravitating, and to have a fixed temperature profile (the disc is locally isothermal). The planet describes a circular orbit at $r = r_p$. Studying the linear response of the disc to the forcing potential of the planet relies on the linearization of the hydrodynamic equations modeling the disc evolution. For a detailed illustration of this, the reader is referred to section 5.2, where the energy equation of the disc is also taken into account. The planet potential Φ , as well as all disc quantities, is expressed as a Fourier series of azimuthally periodic components characterized by m , the inverse of the wavenumber in the azimuthal direction. Since the planet has a circular orbit, each component Φ_m of the potential rotates with the planet's angular velocity Ω_p and has the same phase (which we arbitrarily take equal to zero). We therefore have:

$$\Phi_m(r, \varphi, t) = \Phi_m(r) \cos [m(\phi - \Omega_p t)], \quad (2.3)$$

where $\Phi_m(r)$ is a real function of r that represents the amplitude of the m th component of the planet potential.

Before going further, we assume that the disc is simply made of particles, with no pressure support, no viscosity, and no self-gravity (the disc is therefore strictly Keplerian). Goldreich & Tremaine (1979) showed that the planet and the disc exchange angular momentum only at precise locations in the disc referred to as resonances. Denoting by $\tilde{\omega}(r) = m[\Omega_p - \Omega(r)]$ the perturbing frequency of the planet seen in the matter frame, two kind of resonances can be defined:

- the *Lindblad resonances*, which satisfy $\tilde{\omega} = \pm\kappa$. It is straightforward to derive their location for a Keplerian disc, where κ reduces to the angular velocity Ω . Depending of the sign of $\tilde{\omega}$, hence on the locations of the resonances with respect the planet's orbit, we define the Inner and Outer Lindblad Resonances, usually denoted by ILR and OLR. Their locations are respectively given by:

$$r_{\text{ILR}} = r_p \left(\frac{m}{m-1} \right)^{-2/3} \quad \text{and} \quad r_{\text{OLR}} = r_p \left(\frac{m}{m+1} \right)^{-2/3}. \quad (2.4)$$

We note that there is no ILR associated with $m = 1$, and that the resonances converge toward the planet location in the limit $m \rightarrow \infty$. In this simple configuration, Lindblad resonances correspond to the $m : m \pm 1$ mean-motion resonances with the planet.

- the *Corotation resonances*, for which $\tilde{\omega} = 0$. Particles in corotation resonances therefore rotate at the planet frequency, so they are usually called co-orbital corotation resonances. For the disc of particles we consider, they are located exactly at the planet orbital radius.

The exchange of angular momentum at the resonances corresponds to a torque exerted by the planet on the disc, or to a torque of the disc on the planet, according to Newton's third law. Whenever the term "torque" is mentioned, it will refer to the torque *of* the disc *on* the planet. It dictates the migration rate \dot{a} of the planet as follows. Let J be the planet's angular momentum. Its time variation \dot{J} matches the torque Γ exerted on the planet. The planet having a circular orbit, $J = M_p a^2 \Omega$ and $\dot{J} = 2Ba\dot{a}M_p = \Gamma$, where B is the second Oort's constant, given by equation (2.2) (notice that $B = \Omega/4$ for a Keplerian disc). Thus, a negative torque causes the planet to migrate inwards, whereas a positive torque implies outward migration. We now describe the main properties of the torque exerted at the Lindblad and corotation resonances.

2.3.1 Torque at Lindblad resonances

Using the Wentzel-Kramers-Brillouin (WKB) approximation, Goldreich & Tremaine (1979) derived the expression of the torque at a Lindblad resonance, or *Lindblad torque*. It decomposes as the sum over m of the torque components Γ_m , expressed as:

$$\Gamma_m = m\pi^2 \left(\frac{\Sigma_m}{r dD/dr} \left[r \frac{d\Phi_m}{dr} + \frac{2\Omega}{\Omega - \Omega_p} \Phi_m \right]^2 \right)_{r=r_L}, \quad (2.5)$$

with Σ_m the m th component of the disc surface density, and r_L the location of Lindblad resonances. The quantity $D(r) = \kappa^2(r) - \tilde{\omega}^2$, which vanishes at $r = r_L$, is called the distance to the resonance. The sign of Γ_m is that of the quantity rdD/dr . For a Keplerian disc, $rdD/dr = 3\Omega^2(\pm m - 1)$, where the upper (lower) sign applies for the ILR (OLR). The torque on the perturber is therefore positive at the ILR, and negative at the OLR. It scales with the square of the planet's potential, hence the square of the planet mass. Apart from the surface density, to which it is proportional, and the angular velocity, the torque displays no explicit

dependence on other disc parameters. In the simplest case that we have considered, namely that of a pressureless, inviscid disc without self-gravity, angular momentum exchange occurs at the Lindblad resonances and it accumulates at their exact locations. Any additional physical process, like pressure, viscosity or self-gravity, removes the angular momentum deposited at the resonances, and a steady state exchange of angular momentum can therefore be achieved. Remarkably, [Meyer-Vernet & Sicardy \(1987\)](#) showed that the underlying physics modifies the location, shape and width of the resonant region, but the torque *expression* is independent of the physical processes at work in the disc. In the following, we go back to our case of interest, namely that of a gaseous, pressure-supported disc.

Impact of the gas pressure

In a gaseous disc, angular momentum is removed away from Lindblad resonances by pressure waves. Their propagation satisfies the WKB dispersion relation $\tilde{\omega}^2 = \kappa^2 + k^2 c_s^2$, where k is the wave vector of the perturbations, and $c_s(r)$ is the local sound speed. [Artymowicz \(1993\)](#) showed that pressure affects the evaluation of the Lindblad torque in two ways. First, it shifts Lindblad resonances. Their *effective* location², which are the radii r satisfying the above dispersion relation, are given by:

$$r_L \approx r_p \left(1 + \epsilon \sqrt{1 + m^2 h_p^2 / m} \right)^{2/3}, \quad (2.6)$$

with $\epsilon = +1$ for the OLR, -1 for the ILR. In the limit $m \rightarrow \infty$, Lindblad resonances are located at $\pm 2hr_p/3$ from the planet, a finite distance which causes the forcing potential to decrease abruptly with m ($\Phi_m \propto e^{-2mh/3}$, see [Artymowicz \(1993\)](#)). Whereas $\Gamma_m \propto m^2$ at low m , this *sharp cutoff* of the potential components ensures that Γ_m tends rapidly to zero above a certain m , so the total torque summed over m reaches a finite value. Furthermore, the inclusion of pressure yields non-WKB effects that introduce a *mild cutoff* term in the expression of [Goldreich & Tremaine \(1979\)](#). As inferred from the denominations "sharp" and "mild", it can be shown that the latter effect is of marginal impact compared to the former one, induced by the shift of the Lindblad resonances, and the statements of [Meyer-Vernet & Sicardy \(1987\)](#) therefore prevail. From these results, [Ward \(1997\)](#) produced the most accurate expression for the Lindblad torque (see his equation 8). Note that it scales with $\Sigma M_p^2 h^{-3}$.

We display in the left panel of figure 2.2 the disc response to the $m = 3$ component of a perturbing potential, corotating with the material at $r = 1$. The perturbed radial velocity of the disc is depicted. The response was calculated with a two-dimensional hydrodynamic calculation. The dashed lines in the figure show the location of the ILR and OLR, whereas the corotation radius is indicated with the dotted line. The figure illustrates that the wave response of the disc is launched at the Lindblad resonances. However, between the Lindblad resonances, the perturbation displays no winding and seems to be evanescent. This can be understood by the above dispersion relation, which shows that inside a band centered on the corotation (where $\tilde{\omega} = 0$) and bounded between the Lindblad resonances, the radial wave vector is purely imaginary. Inside this band, the disturbance has indeed no winding, and its amplitude decays exponentially over a length scale that depends on its separation from the corotation radius. At corotation, this length scale is equal to the pressure scale height.

In the right panel of figure 2.2, we show the components (in absolute value) of the inner (outer) Lindblad torque, defined as the torque evaluated at the inner (outer) Lindblad resonances. The torque components are calculated with two different aspect ratios, namely $h = 0.03$ and $h = 0.07$. The figure illustrates the torque cutoff at high- m , which starts at $m \sim 8 - 9$ for $h = 0.07$, and at $\sim 21 - 22$ for $h = 0.03$. The sum of the inner and outer torques peaks at

²This denomination is used to distinguish with the locations of the resonances without pressure support, called *nominal* location.

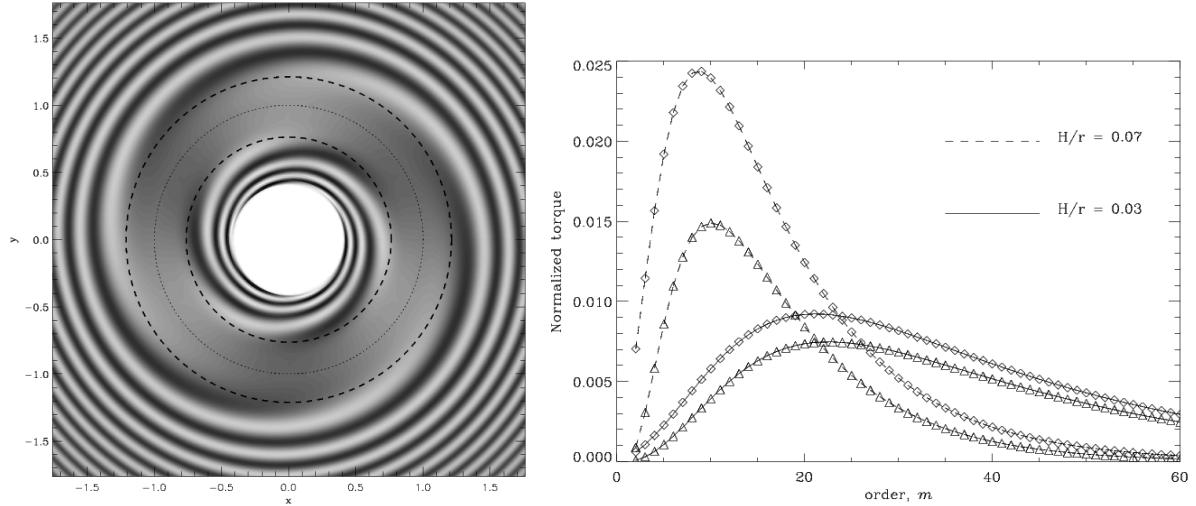


FIGURE 2.2: Left: radial velocity perturbation due to a $m = 3$ -armed potential rotating at $r = 1$. The wave response of the disc is launched at the inner and outer Lindblad resonances (dashed lines). Waves hardly propagate inside the forbidden band, which is the band centered on the corotation radius (dotted line) and inserted between the Lindblad resonances. Taken from [Masset \(2008\)](#). Right: absolute values of the torque components Γ_m evaluated at ILR (triangles) and at OLR (diamonds), for two different aspect ratios: $h = 0.03$ (solid line) and $h = 0.07$ (dashed line). Figure also taken from [Masset \(2008\)](#), which reproduces the results of [Ward \(1997\)](#).

$m \sim (2h)^{-1}$ ([Goldreich & Tremaine 1980](#)). We note furthermore that, whatever m , the amplitude of the outer torque is systematically larger than that of the inner torque. There are several reasons for that. One of them is that the outer Lindblad resonance is slightly closer to the orbit than the inner resonance (this is shown in particular by [Ward \(1997\)](#), whose calculation of the resonances locations is more precise than that used to derive equation (2.6)). This result is relatively robust against a change of the disc parameters ([Ward 1997](#)). The *total* torque exerted on the planet at Lindblad resonances is always negative, and it causes the planet to migrate toward the central object.

The planet wake

We contemplate in this paragraph the global disc response to the planet potential, which corresponds to the sum of the wave responses related to each component of the potential. [Ogilvie & Lubow \(2002\)](#) showed that all these waves constructively interfere and yield a one-armed trailing³ spiral wave. This spiral wave is called the *planet wake*, it rotates at the planet's angular velocity. The authors provide the parametric equation of the wake, which reads:

$$\phi_{r < r_p}^{r > r_p} = \pm \frac{2}{3} h(r)^{-1} \left[\left(\frac{r}{r_p} \right)^{3/2} - \frac{3}{2} \ln \left(\frac{r}{r_p} \right) - 1 \right], \quad (2.7)$$

where $h(r)$ denotes the local aspect ratio of the disc (in the original work of [Ogilvie & Lubow \(2002\)](#), the disc aspect ratio was taken uniform). The radial variation of the wake phase ϕ is faster for a disc with low aspect ratio, hence low sound speed. Thus, the smaller the sound speed, the more tightly wound the wake. Similarly, the phase varies faster far from the planet location. The wake therefore becomes more and more tightly wound as it recedes from the planet orbit.

³A trailing wave is a wave such that $k_r \times k_\varphi$ is negative, where k_r and k_φ denote the radial and azimuthal components of the wave vector. For a leading wave, the previous product is positive.

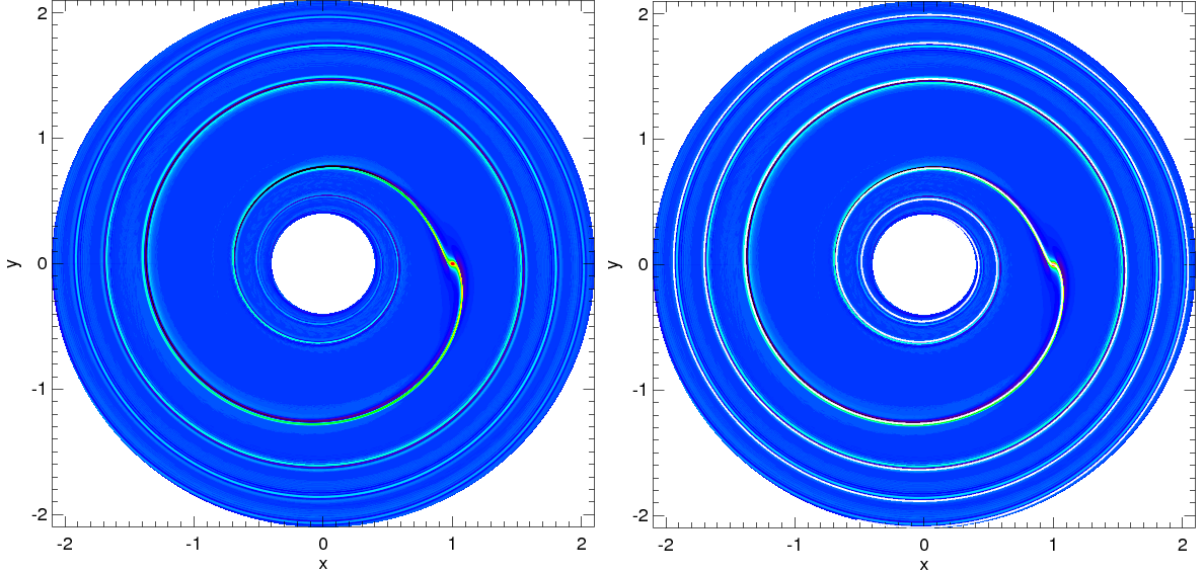


FIGURE 2.3: Left: disc surface density perturbation obtained with a $q = 6 \times 10^{-6}$ planet to primary mass ratio, with $h = 0.03$. The planet is located at $x = 1, y = 0$. Right: same as in the left panel, but the location of the wake given by equation (2.7) is superimposed.

This is clearly illustrated in figure 2.3, where we display the disc response to a $M_p = 6 \times 10^{-6} M_\star$ planet mass (this corresponds to a 2 Earth mass planet if the central star has a solar mass). The left panel shows the relative perturbation of the disc surface density obtained with a numerical simulation assuming a uniform disc aspect ratio $h(r) = 0.03$. It takes the form of a one-armed spiral wave propagating in the disc from the planet, rotating at $r = 1$. On the right panel, the parametric equation of the wake, given by equation (2.7), is superimposed. The wake locations obtained in both panels are in very good agreement.

Differential Lindblad torque

The total torque exerted by the disc on the planet is the sum of each torque component Γ_m at both ILR and OLR. This defines the *differential Lindblad torque*, which we denote by $\Delta\Gamma_{\text{LR}}$. Tanaka et al. (2002) have provided the most accurate analytic estimate of the differential Lindblad torque, both in two- and three-dimensions, assuming the disc has a uniform temperature. Their estimate reads:

$$\Delta\Gamma_{\text{LR}} = -C_{\text{LR}} q^2 \Sigma_p \Omega_p^2 r_p^4 h_p^{-2}, \quad (2.8)$$

with:

$$C_{\text{LR}} = 2.340 - 0.099\sigma \text{ in 3D, } C_{\text{LR}} = 3.200 + 1.468\sigma \text{ in 2D,} \quad (2.9)$$

where σ denotes the power-law index of the surface density profile ($\sigma = -d \log \Sigma / d \log r$). We comment that both estimates have the same dependence with the planet mass and with the disc parameters. The scaling with $\Sigma_p q^2$ was already apparent in the torque expression of Goldreich & Tremaine (1979), given by equation (2.5). However, the differential Lindblad torque scales as h^{-2} , whereas the inner and outer Lindblad torques scale as h^{-3} (see above). This is explained by Ward (1997), who showed that the relative difference of (the absolute values of) the inner and outer torques, that is the quantity $|\Delta\Gamma_{\text{LR}}/\Gamma_{\text{LR}}|$, scales with h . This result is clearly visible in the right-hand panel of figure 2.2. We point out that, since the disc sound speed c_s scales with h , the differential Lindblad torque decreases as c_s decreases.

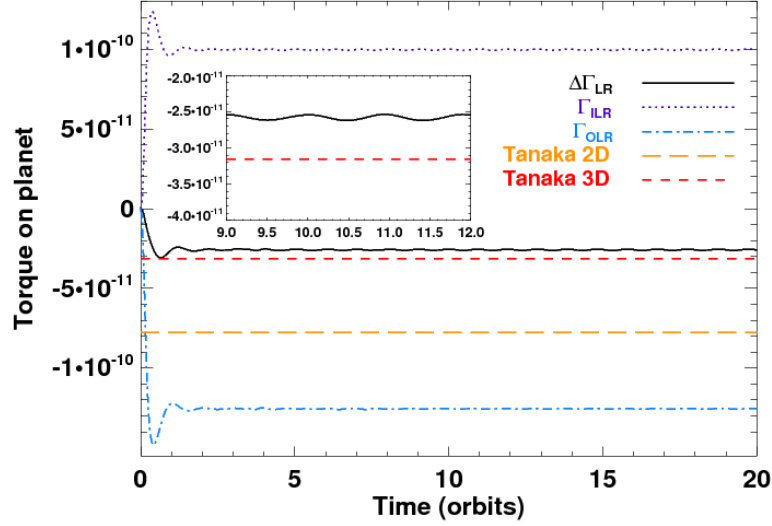


FIGURE 2.4: Result of a two-dimensional calculation with a $q = 6 \times 10^{-6}$ planet to primary mass ratio, a surface density decreasing as $r^{-1.5}$, and a uniform temperature profile. We display the time variations of the inner Lindblad torque (dotted curve), the outer Lindblad torque (dash-dotted curve) and the differential Lindblad torque (solid curve). The two- and three-dimensional analytic estimates of the differential Lindblad torque of Tanaka et al. (2002), given by equations (2.8) and (2.9), are displayed respectively with long-dashed and dashed lines. The close-up shows a zoom on the differential Lindblad torque and on the 3D analytic estimate.

An example of two-dimensional calculation results is displayed in figure 2.4. The torque exerted on a $M_p = 6 \times 10^{-6} M_\star$ planet mass is depicted as a function of time (the units in which the results are expressed will be detailed in section 3.1.6). For this calculation, the surface density profile decreases as $r^{-1.5}$ and the temperature profile is taken uniform. This choice ensures that the corotation torque cancels out in a locally isothermal disc, as will be shown in section 2.3.2. The torque evaluated with our calculation therefore only accounts for the differential Lindblad torque. Its evaluation is simply given by:

$$\int_{\text{disc}} (\mathbf{r}_p \times d\mathbf{F}_{\text{disc} \rightarrow \text{planet}}) \cdot \mathbf{e}_z, \quad (2.10)$$

where $d\mathbf{F}_{\text{disc} \rightarrow \text{planet}}$ stands for the gravitational force exerted by each fluid element on the planet, and \mathbf{e}_z is the unit vector along the direction perpendicular to the disc plane. The figure illustrates the torque properties aforementioned: the inner torque Γ_{ILR} is positive, whereas the outer torque Γ_{OLR} is negative. Their sum, the differential Lindblad torque $\Delta\Gamma_{\text{LR}}$, is negative. Note that the torques reach a steady-state very rapidly, after only $\sim 1 - 2$ orbits of the planet (Meyer-Vernet & Sicardy 1987). The 2D and 3D estimates of Tanaka et al. (2002), given by equations (2.8) and (2.9), are superimposed for comparison. The torque given by our calculation is at least three times smaller than the 2D analytic estimate. This reduction stems from the use in numerical simulations of a softening length for the planet potential, which reads:

$$\Phi = -\frac{\mathcal{G}M_p}{\sqrt{\|\mathbf{r} - \mathbf{r}_p\|^2 + \varepsilon^2}}, \quad (2.11)$$

with ε the softening length over which the potential is smoothed. Its value is a fraction of the disc scale height at the planet location that typically varies from 0.3 to 0.8. Its choice is generally motivated to get a numerical torque as close as possible of the 3D analytical estimate. The softening length we considered for this calculation, namely $\varepsilon = 0.6H(r_p)$, is in good agreement with the 3D estimate of the differential Lindblad torque.

Migration timescale

Although the total torque on the planet also includes the corotation torque, it is instructive to derive an order of magnitude estimate of the type I migration timescale, with *only* the differential Lindblad torque. For a locally isothermal disc, the amplitude of the corotation torque is indeed smaller than that of the differential Lindblad torque (see section 2.3.2). The conservation of the planet's angular momentum therefore reads $2Ba\dot{a}M_p = \Delta\Gamma_{\text{LR}}$ (where we recall that $\dot{a} = da/dt$ denotes the planet's migration rate). We define the migration timescale τ_1 by $\dot{a} = -a/\tau_1$. Assuming the central star has a solar mass, we find:

$$\tau_1[\text{yrs}] \sim \frac{7 \times 10^5}{C_{\text{LR}}} \left(\frac{\Sigma}{1 \text{ g.cm}^{-2}} \right)^{-1} \left(\frac{r}{1 \text{ AU}} \right)^{-1/2} \left(\frac{M_p}{M_\star} \right)^{-1} \left(\frac{H}{r} \right)^2, \quad (2.12)$$

where C_{LR} is given by equation (2.9). Let us consider the case of a 10 Earth mass planet embedded in the Minimum Mass Solar Nebula (MMSN) at 5 AU ($\Sigma \sim 150 \text{ g.cm}^{-2}$ and $\sigma = 1.5$), with $h = 0.07$. Equation (2.12) gives $\tau_1 \sim 6 \times 10^4$ yrs with the 2D estimate, and $\tau_1 \sim 1.5 \times 10^5$ yrs with the 3D estimate. This order of magnitude estimate does not change much as the planet migrates inwards. As stated above, the inclusion of the corotation torque will not significantly alter this estimate. It means that the protoplanet requires only $\mathcal{O}(10^5)$ yrs to reach the very vicinity of the central star, which is at least one order of magnitude smaller than the timescale for giant planet formation predicted by the extended core-accretion model (see section 1.3.2). While it may account for the detection of the Hot Jupiters, the formation (and thus the detection) of giant planets somewhat further out in the disc, which shall be called *Cold Jupiters*, appears to be very unlikely. Many recent studies on disc-planet interactions have therefore investigated processes that may slow down type I migration. We will review them in section 2.3.3.

Recent studies on the differential Lindblad torque

The properties of the differential Lindblad torque have recently been revisited by a few studies, who added still more complexity to the original physical problem. Among them, [Menou & Goodman \(2004\)](#) considered realistic models of T Tauri α -discs instead of the customary power law models, and found that type I migration can be significantly slowed down at opacity transitions in the disc. The impact of the magnetic field has also been investigated, by [Terquem \(2003\)](#) for a toroidal field, and by [Muto et al. \(2008\)](#) for a poloidal field. In both situations, Lindblad resonances are shifted away from the orbit as the *effective* sound speed is larger: c_s is substituted by $(c_s^2 + v_A^2)^{1/2}$, with v_A the Alfvén speed, proportional to the magnetic field. Compared to the case of an unmagnetized disc, the differential Lindblad torque is therefore reduced, and this reduction increases with the strength of the magnetic field. Note that the inclusion of magnetic field introduces new resonances, where angular momentum is exchanged. This gives rise to additional torque contributions, which may prevail over the differential Lindblad torque. Eventually, the impact of the disc self-gravity has been studied by [Pierens & Huré \(2005\)](#). The authors calculated the shift of the Lindblad resonances due to the self-gravity, and predicted an increase of the torque. This prediction has been confirmed with numerical simulations by [Baruteau & Masset \(2008b\)](#), as we will see in chapter 4.

2.3.2 Torque at corotation resonances

The disc and the planet can also exchange angular momentum at the corotation resonances, which all share the same location in the disc. This location, called the *corotation radius*, matches the planet's orbital radius in the particular case of a pressureless disc. We have seen in section 2.3.1 that the planet excites pressure waves that are able to remove the angular momentum

deposited at Lindblad resonances. These waves being evanescent between Lindblad resonances, they cannot remove the angular momentum deposited at corotation. Another difference is that the gas pressure significantly alters the expression of the corotation torque. Using a linear analysis, and under the WKB approximation, Tanaka et al. (2002) showed that the m th component of the corotation torque, exerted on the perturber by an *isothermal* disc, reads:

$$\Gamma_{C,m} = -\frac{m\pi^2}{2} \left[\frac{|\Phi_m + \Psi_m|^2}{d\Omega/dr} \frac{d}{dr} \left(\frac{\Sigma}{B} \right) \right]_{r_c}, \quad (2.13)$$

where Ψ_m is the m th component of the perturbed gas enthalpy⁴. In the particular case where $|\Psi_m| \ll |\Phi_m|$, equation (2.13) reduces to the torque expression of Goldreich & Tremaine (1979) (their equation 56). This occurs in gaseous discs where the thermal energy is a small amount of the total energy, depending on the gas temperature and on the strength of the perturbing potential. For typical disc and planet parameters, this approximation is incorrect (Korycansky & Pollack 1993, Tanaka et al. 2002). In equation (2.13), r_c denotes the location of the corotation radius, which satisfies $\Omega(r) = \Omega_p$. Assuming power-law functions for the density and temperature profiles, namely $\Sigma(r) \propto r^{-\sigma}$ and $T(r) \propto r^{-1+2f}$ (see section 3.1.1), we have:

$$r_c \approx r_p [1 - (\sigma + 1 - 2f)h^2/3]. \quad (2.14)$$

Assuming the pressure p decreases with r ($\sigma + 1 - 2f > 0$, as p satisfies $p \propto \Sigma T$), r_c is slightly smaller than r_p . Furthermore, we stress that the sign of $\Gamma_{C,m}$ is that of the gradient of Σ/B , where B , the second Oort's constant, scales as $r^{-3/2}$ for a Keplerian disc. The corotation torque, which is the sum over m of $\Gamma_{C,m}$, is therefore proportional to $(3/2 - \sigma)$ for an isothermal disc. This indicates that, contrary to the differential Lindblad torque, the corotation torque can be positive or negative, depending on the power-law index of the density profile. Note that, with previous assumptions, the corotation torque cancels out for the surface density profile of the MMSN, for which $\sigma = 3/2$. It is also worth mentioning that, since B is half the vertical component ω of the flow vorticity, the corotation torque scales with the gradient of (the inverse of) the flow *vortensity* ω/Σ . The vortensity is one of the key quantities in hydrodynamics. Another one is the entropy, to which we will mainly refer when we take the gas thermodynamics into account in chapter 5. The governing equation of the vortensity, directly obtained through Navier-Stokes equations, takes the form:

$$\frac{D}{Dt} \left(\frac{\omega}{\Sigma} \right) = -\frac{\nabla p \times \nabla \Sigma}{\Sigma^3} \cdot \mathbf{e}_z + \nu \Delta \left(\frac{\omega}{\Sigma} \right). \quad (2.15)$$

For an inviscid, locally isothermal disc, the right-hand side of equation (2.15) is proportional to dT/dr . If in addition the temperature is uniform, $D(\omega/\Sigma)/Dt = 0$ and the vortensity is conserved along fluid element paths.

Saturation, desaturation of the corotation torque

The disc response at a corotation resonance corresponds to a set of m eye-shaped libration islands, which define the corotation region, and inside which fluid elements have librating trajectories. This is illustrated in the left-hand panel of figure 2.5, where we display the $m = 3$ component of the gas vortensity. The disc response was obtained with a hydrodynamic calculation assuming an isothermal, inviscid disc with $h = 0.01$. The streamlines overplotted on the panel illustrate the vortensity conservation along the trajectories of the fluid elements. The latter have circulating trajectories outside the corotation region, and librating trajectories inside

⁴The perturbed gas enthalpy is equal to the perturbed pressure divided by the unperturbed surface density.

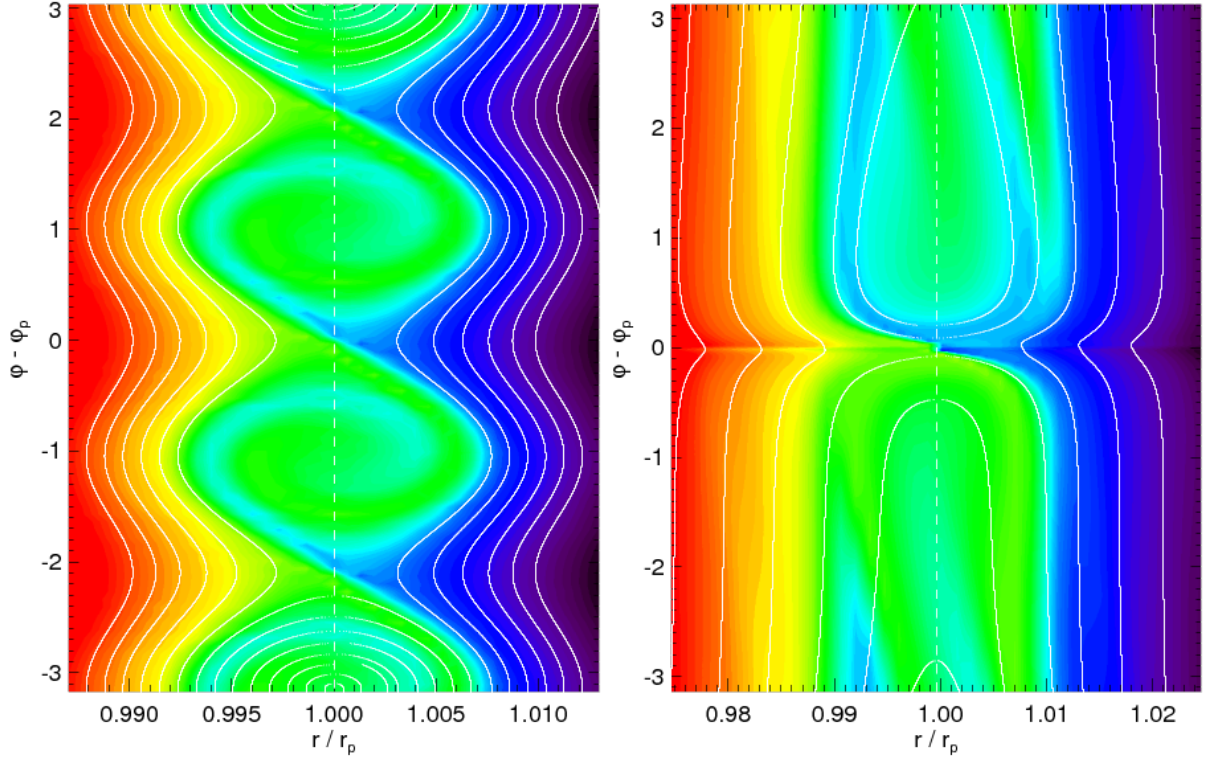


FIGURE 2.5: Left: disc response to an $m = 3$ -folded potential around the corotation region. The gas vortensity is displayed in polar coordinates. While the azimuthal range in y -axis spans the whole $[0-2\pi]$ interval, the radial range in x -axis is restricted to a narrow range around the corotation radius (dashed line). Streamlines (solid curves) show the trajectories of the fluid elements in the frame rotating with the perturbing potential. Right: result of a calculation with a $q = 5 \times 10^{-6}$ planet to primary mass ratio. The planet is located at $r = r_p$, $\varphi = \varphi_p$. The disc has a uniform temperature profile, no viscosity, and $h = 0.05$. Like in the left panel, we display the gas vortensity around the planet's corotation region, which has this time a rectangular shape.

it. The particular streamlines that separate circulating and librating elements are called *separatrices*. They delimit the borders of the corotation region. As fluid elements librate inside the corotation region, the vortensity is progressively stirred up. After a few libration timescales, the vortensity is uniform over the islands and the corotation torque, which scales with the vortensity gradient across the corotation region, cancels out. This process is called the *saturation* of the corotation torque. It relies on the finite value of the libration time. Thus, one should bear in mind that the saturation process cannot be explained by linear theory, for which the corotation region is a singularity (see e.g. chapter 5). In linear theory, the libration timescale, which scales as the inverse of the width of the corotation region, is infinite and saturation cannot occur.

The saturation can also be understood as follows. The perturber being on a fixed circular orbit and the disc being inviscid, the angular momentum of the perturber and of the corotation region remains constant. As fluid elements librate, they periodically borrow angular momentum from the perturber (for their semi-major axis to increase) and leave angular momentum to it (when their semi-major axis decreases). Along a given streamline, the exchange of angular momentum oscillates with time and averages out to zero over a timescale long compared to the libration timescale. This applies for each streamline, but note that the libration period, which scales with the inverse of $\Omega - \Omega(r_c)$, varies from one streamline to another. The angular momentum exchange between the perturber and the corotation region therefore amounts to the sum of periodic functions of zero mean and of different periods, sum which tends to zero as time

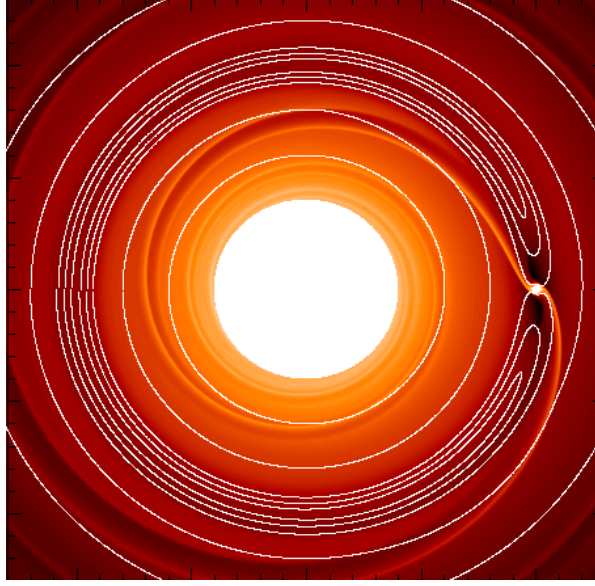


FIGURE 2.6: Surface density field obtained with a high-mass planet held on a fixed circular orbit in an inviscid disc. Streamlines are superimposed to emphasize the librating and circulating trajectories of the fluid elements, as seen from the planet location. All the librating elements form the planet's horseshoe region.

goes to infinity, due to phase mixing. After yet a few libration timescales, the corotation torque vanishes not only on average, but also in instantaneous value.

The saturation can be avoided if the corotation region exchanges angular momentum with a third party. Viscous stress at the separatrices provides an exchange of angular momentum with the rest of the disc. Interestingly, this process is linked with the behavior of the vortensity in the corotation region. Equation (2.15) indicates indeed that viscosity acts as a diffusive source term for the vortensity. The viscous diffusion across the separatrices tends to permanently impose the initial, large-scale vortensity gradient over the corotation region. It therefore acts as preventing the flattening out of the vortensity profile, provided that the timescale for viscous diffusion across the corotation region is smaller than the libration timescale.

The planet's horseshoe region

We now turn to the global response of the disc at the corotation resonances. Not surprisingly, the superposition of all the libration islands gives a region where, seen from the planet, fluid elements have librating trajectories. This region is called the planet's *horseshoe region*. It is very similar to the horseshoe region of the restricted three-body problem. An illustration of this is given in figure 2.6. The horseshoe region is characterized by:

- Its half-width x_s . For low-mass planets, [Masset et al. \(2006a\)](#) showed that x_s is well approximated by:

$$x_s \sim 1.2r_p\sqrt{q/h}. \quad (2.16)$$

Assuming a $q = 5 \times 10^{-6}$ planet to primary mass ratio, and a $h = 0.05$ disc aspect ratio, we have $x_s \sim 1.2 \times 10^{-2} r_p$. This underscores the need for high-resolution calculations to investigate corotation torque issues with low-mass planets (see section 6.1.1).

- The libration timescale τ_{lib} . As stated above, the latter depends on the separation from the corotation radius. The shortest libration time is obtained at the distance x_s from

corotation:

$$\tau_{\text{lib}} = 4\pi / (x_s |d\Omega/dr|) = \frac{8\pi r_p}{3\Omega_p x_s}, \quad (2.17)$$

which amounts to ~ 130 planet orbital periods for the above values of q and h .

- The torque exerted on the planet, called the *horseshoe drag*. Its expression is given by Ward (1991):

$$\Gamma_{\text{HS}} = \frac{3}{4} \Sigma \Omega_p^2 x_s^4 \left[\frac{d \log(\Sigma/B)}{d \log r} \right]_{r_c}. \quad (2.18)$$

Masset et al. (2006a) have shown that the horseshoe drag is in good agreement with the corotation torque, defined above as the sum over m of the torque components $\Gamma_{C,m}$.

Similarly as in the libration islands, the gas vortensity is advected inside the horseshoe region. This can be seen in the right-hand panel of figure 2.5. On this polar representation, fluid elements describe *horseshoe U-turns* with respect to the planet. Again, the vortensity is progressively stirred up until it is uniformly distributed. Saturation occurs in a similar way as in libration islands, and it can be avoided if some viscosity is included. The saturation level of the corotation torque only depends on the ratio of the libration timescale, τ_{lib} , given by equation (2.17), and of the viscous timescale across the horseshoe region, $\tau_{\text{visc}} \sim x_s^2/\nu$ (Masset 2001; 2002, Ogilvie & Lubow 2003). In this context, we mention the work of Masset (2001), who generalized the horseshoe drag expression above in a viscous disc.

The corotation torque

Again, Tanaka et al. (2002) provided the most accurate estimate for the corotation torque⁵ in an isothermal disc, in two- and three-dimensions. Summing the torque expression of equation (2.13), the authors give the following estimate:

$$\Gamma_{\text{CR}} = C_{\text{CR}} q^2 \Sigma_p \Omega_p^2 r_p^4 h_p^{-2}, \quad (2.19)$$

with:

$$C_{\text{CR}} = 0.976 - 0.640\sigma \text{ in 3D, } C_{\text{CR}} = 2.040 - 1.360\sigma \text{ in 2D.} \quad (2.20)$$

The corotation torque and the differential Lindblad torque display the same dependence with the disc and planet parameters. Comparing both torques thus amounts to comparing the constants C_{LR} and C_{CR} , which only depend on σ . In three-dimensions for instance, the ratio $C_{\text{CR}}/C_{\text{LR}}$ increases roughly linearly from ~ -0.4 to 0.3 for σ between 0 and 2.5 . The corotation torque in an isothermal disc is most probably a small fraction of the differential Lindblad torque, especially as it may saturate, depending on the amount of viscosity in the planet vicinity. This confirms what we anticipated in section 2.3.1 for the calculation of migration timescales.

We proceed with an example of calculation results. We consider here the case of a $M_p = 5 \times 10^{-6} M_\star$ planet embedded in a disc with a $h = 0.05$ aspect ratio at the planet location. The temperature is taken uniform, whereas the surface density profile decreases as $r^{-1/2}$. The half-width of the horseshoe region is covered with ~ 10 cells in the radial direction. In the left panel of figure 2.7, the time variation of the total torque is displayed. The oscillatory behavior of the torque stems from the saturation of the corotation torque. Note that the oscillation period is slightly larger than the libration timescale calculated by equation (2.17). The steady-state value of the total torque corresponds to the differential Lindblad torque, which we compare to the 3D analytic estimate given by equation (2.8). The $\sim 20\%$ relative difference between both is

⁵Since the corotation resonances satisfy $\Omega(r) = \Omega_p$, the corotation torque is called the co-orbital corotation torque. Corotation resonances can be non-coorbital if the planet has a non-vanishing eccentricity.

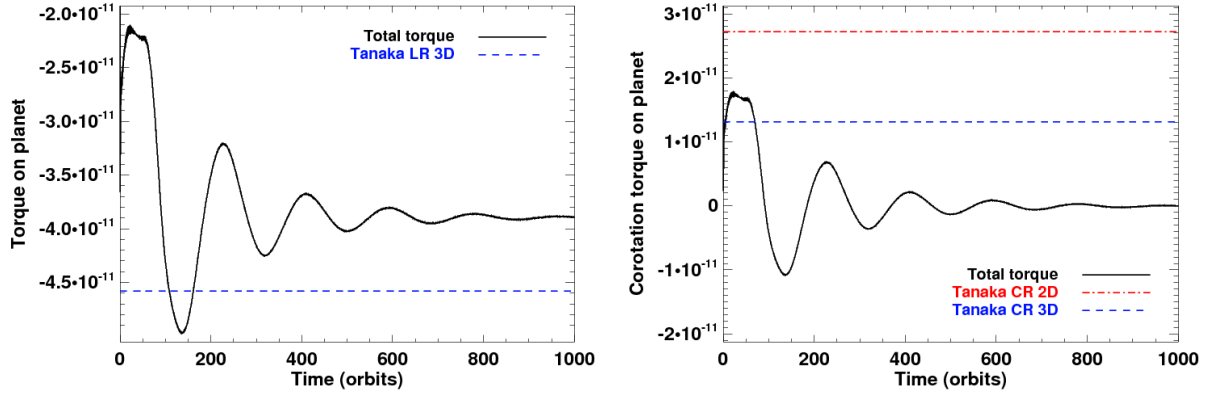


FIGURE 2.7: Calculation results with a $q = 5 \times 10^{-6}$ planet to primary mass ratio, a surface density decreasing as $r^{-1/2}$, and a uniform temperature profile. The left panel shows the total torque exerted on the planet as a function of time. The dashed line depicts the 3D differential Lindblad torque estimate of Tanaka et al. (2002). The right panel displays the corotation torque, calculated as the difference between the total torque, and the steady-state value of the total torque. The 2D (dot-dashed curve) and 3D (dashed curve) corotation torque estimates of Tanaka et al. (2002) are overplotted.

coherent with the one inferred from the results of figure 2.4, where the corotation torque cancels out. The difference between the total torque, and the steady-state value of the latter, gives the corotation torque. We display it in the right-hand panel of figure 2.7. As indicated above, we see that, after a few libration timescales, the corotation torque cancels out on average and on instantaneous value. In addition, we superimposed to this panel the 2D and 3D estimates of Tanaka et al. (2002), given by equations (2.19) and (2.20). These estimates are usually compared to the fully unsaturated value of the corotation torque, namely its maximum value before saturation starts (here at ~ 60 orbits). Accordingly, it corresponds to a somewhat long stationary stage preceding saturation, which is not captured by a linear analysis. Note that it is a positive quantity, since $\sigma < 3/2$. The agreement between our calculation results and the linear prediction is satisfactory. The value obtained with our calculations is smaller than the 2D estimate, and larger than the 3D estimate. This time, a somewhat smaller softening length would have given better agreement with the 3D estimate, in qualitative agreement with the findings of Masset (2002).

We end up this section with a comment on the dependence of the corotation torque with the temperature gradient. The torque expressions of Goldreich & Tremaine (1979), Ward (1991) and Tanaka et al. (2002) have all been derived assuming a uniform temperature profile. However, most of disc-planet studies take a non-uniform temperature profile. It is likely to alter the corotation torque, as the term $\nabla p \times \nabla \Sigma$ in the vortensity equation scales with the temperature gradient - see equation (2.15). To illustrate this, we performed a series of calculations with disc and planet parameters identical as in section 2.3.1 where we illustrated the time variation of the differential Lindblad torque (recall in particular that $\Sigma \propto r^{-3/2}$), except that we vary the temperature gradient. We denote by l the quantity $-d \log T / d \log r$. The results are shown in figure 2.8, where we display the torque variation with time for l varying from -1 to 1 . The amplitude of the differential Lindblad torque increases with l , in agreement with the results of Ward (1997). In addition, we clearly observe that the corotation torque depends on the temperature gradient. From the oscillatory behavior of the torques, we infer that the unsaturated corotation torque increases with l : here it is negative when l is negative (see e.g. uppermost curve), positive when l is positive (e.g. lowermost curve), and it cancels out when l does. These results show that in two-dimensional calculations, with a locally isothermal disc, the corotation

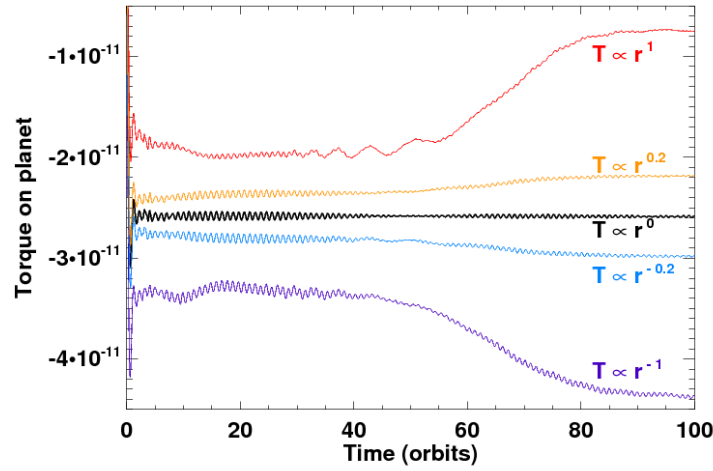


FIGURE 2.8: Calculation results obtained with a $q = 6 \times 10^{-6}$ planet to primary mass ratio and a surface density decreasing as $r^{-3/2}$. We vary in this series the quantity $l = -d \log T / d \log r$ from -1 (uppermost curve) to 1 (lowermost curve).

torque will strictly vanish only if *both* the vortensity gradient and the temperature gradient cancel out.

2.3.3 Any ideas to slow down type I migration ?

We have studied in the last two sections the properties of the differential Lindblad torque and of the corotation torque for a locally isothermal disc. The former is negative and rapidly stationary. The latter can be positive or negative, depending on the steepness of the surface density profile, and it is prone to saturation. We have seen however that the corotation torque can be unsaturated, depending on the disc viscosity. Even in the most favorable situation where the corotation torque is fully unsaturated and positive, the differential Lindblad torque dominates, and the migration of low-mass planets remains extremely rapid. Many recent studies on planetary migration have therefore challenged to propose mechanisms that may slow down migration, that may halt or even reverse it. We present hereafter some of these mechanisms.

Pressure buffer

The first of these mechanisms relies on the differential Lindblad torque. The latter is due to a small unbalance between the positive inner torque, and the negative outer one. As the torques scale with the surface density at the Lindblad resonances, increasing the steepness of the density profile could enhance the inner torque, and reduce the outer one. Nonetheless, a side-effect of this is to decrease the disc's angular velocity, which shifts all Lindblad resonance inwards (the reader is referred to figure 4.3, and asked to find the new locations of the resonances when the black curve is lowered). As inner resonances move away from the planet, the inner torque is reduced. Conversely, outer resonances get closer to the planet, so the outer torque increases! This side-effect is called the *pressure buffer* (Ward 1997). It roughly compensates the direct effect of increasing the steepness of the density profile... except if the density jump is very high. This has been recently revisited by Matsumura et al. (2007), for discs harboring a dead zone. The outer edge of the dead zone is associated with a huge increase of the disc viscosity when passing from inside to outside the dead zone. Thus, a very steep surface density profile occurs there. The authors showed that low-mass planets may be halted as they migrate inwards toward

the outer edge of the dead zone. This requires that a significant density jump occurs on a very small width, of typically $\sim H - 2H$.

Planetary trap

In the same vein, [Masset et al. \(2006b\)](#) have investigated the impact of a cavity edge on the migration of low-mass planets. They however considered the opposite case where a planet migrates toward a underdense region. This situation may model the inner edge of a dead zone, or the transition between a jet emitting disc and a standard accretion disc (see figure 2.1). The density jumps they assume have a smaller amplitude, and a larger width compared to those of [Matsumura et al. \(2007\)](#). They found that the sharp raise in surface density at the edge favors a strong, positive corotation torque, and allows for the existence of a stable fixed point where the total torque cancels out, thereby acting as a *planet trap*.

Stochastic migration

Among the sources of turbulence in discs seen in section 2.2, only the magneto-rotational instability has been intensively investigated in the context of planetary migration. [Nelson & Papaloizou \(2004\)](#) showed that type I migration reveals very different properties in discs invaded by the MRI, compared to laminar discs. As shown in the left-hand panel of figure 2.9, the torque exerted on a 10 Earth mass planet displays high temporal fluctuations, so migration is much like a random walk than a smooth, monotone decay. This behavior is called *stochastic migration*. It is not clear whether the torque of a turbulent disc amounts to the torque exerted by a laminar disc *plus* fluctuations arising from the turbulence. In particular, one would expect the turbulent torque, averaged out over a timescale much larger than the turbulence correlation time, to reduce to the laminar torque. This question is still unsolved, as (i) the duration of the calculations is strongly limited by the high computational cost of MRI calculations (typically ~ 100 orbits), and (ii) it is not even sure that the correlation time has a finite value ([Johnson et al. 2006](#), and references therein)

Radiative effects

The vast majority of disc-planet studies have assumed a barotropic or a locally isothermal disc. There has been some exceptions: [Morohoshi & Tanaka \(2003\)](#) considered the case of a planet interacting with an optically thin disc, in the shearing sheet approximation, and found that radiative effects can significantly alter the one-sided torque between the planet and the disc. More recently, [Paardekooper & Mellema \(2006\)](#) have performed global, high resolution 3D calculations with nested grids that include radiative transfer. They found that the torque on low-mass planets increases with the disc opacity. For sufficiently large values of the opacity (and in the limit case of an adiabatic flow, corresponding to an infinite opacity), the total torque on the planet is positive, meaning outward migration (see right panel of figure 2.9). The authors identified the existence of a hot, underdense part of the co-orbital region lagging the planet, which accounted for the torque excess that they measured. Considering a more restricted situation, namely a two-dimensional adiabatic disc, [Baruteau & Masset \(2008a\)](#) showed that the entropy advection inside the co-orbital region yields an additional contribution to the corotation torque, which is positive when the gas entropy is a decreasing function of radius. If the entropy gradient is sufficiently large, the fully unsaturated value of this *torque excess* renders the total torque positive. These results will be detailed in chapters 5 and 6.

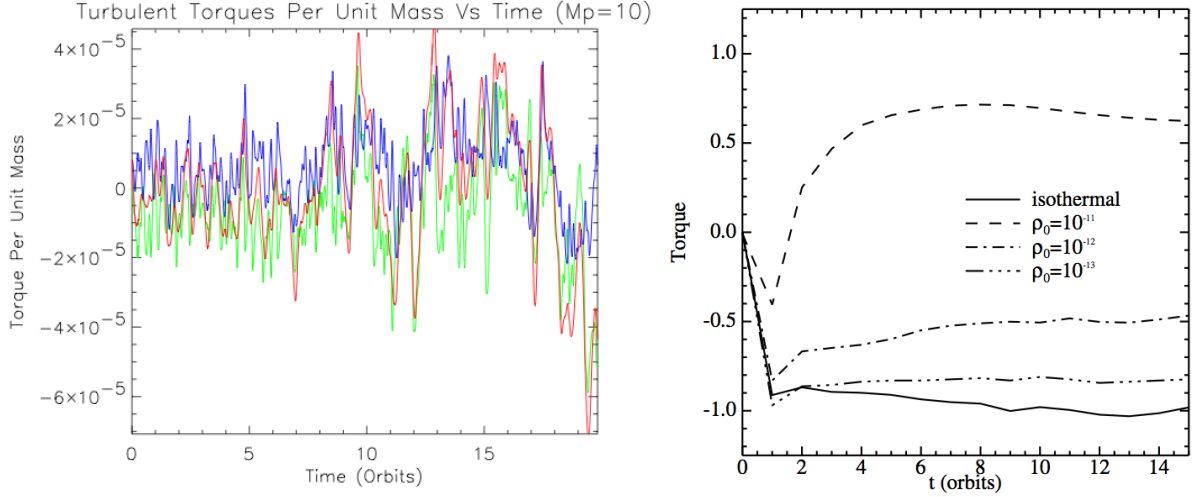


FIGURE 2.9: Left: calculation results obtained with a 10 Earth-mass planet embedded in a turbulent disc. The time variation of the inner Lindblad torque (blue curve), the outer one (green curve) and the differential Lindblad torque (red curve) is displayed. Figure taken from Nelson & Papaloizou (2004). Right: Impact of the disc opacity on the torque exerted on a 5 Earth-mass planet (the disc is laminar). This figure, taken from Paardekooper & Mellema (2006), shows that increasing the disc opacity, by increasing the surface density, renders the torque more and more positive. The torque values are normalized by the 3D analytic estimate of Tanaka et al. (2002), given by the sum of equations (2.8) and (2.19).

2.4 Transition to the non-linear regime

The disc response to a low-mass planet has been studied in section 2.3. We have assumed that the disc response is correctly described by a linear analysis, and we have checked that the torque expressions derived from linear theory are, to a large extent, in good agreement with the results of numerical simulations. However, we still have not mentioned for which planet masses the linear regime corresponds to. It is the object of this section, where we describe two processes that render the disc response significantly non-linear.

Shock formation

As the density waves excited by the planet propagate in the disc, their profile becomes steeper and steeper, in much the same way that an acoustic wave which travels in a homogeneous gas at rest. This ultimately leads to the formation of shocks. Thus, the disc response always turns to be non-linear at some distance from the planet, even for low-mass planets. However, as long as the disc response remains linear *in the planet vicinity*, where most of the angular momentum is exchanged, shocks formation does not impact on type I migration.

As the wake turns to a shock in the planet vicinity, it *gives* the angular momentum of the planet to the background disc elements. Fluid elements circulating in the inner disc thus lose angular momentum (recall that the inner Lindblad torque exerted *by* the planet *on* the disc is negative), so their semi-major axis decreases. Conversely, fluid elements circulating in the outer disc gain angular momentum and are pushed away from the orbit. The planet therefore tends to open a *gap*. The coorbital material is also affected. Fluid elements performing outward horseshoe U-turns gain angular momentum not only from the planet, but also indirectly through the wake. They are therefore more deflected than without shock. A similar conclusion applies for inward U-turns. Librating fluid elements are more and more repelled from the orbit at each U-turn, until they reach the inner or outer parts of the disc. A few libration timescales are typically required to significantly deplete the horseshoe region. This is illustrated in figure 2.10,

where we display the disc response to a Jupiter-mass planet ($q = 10^{-3}$), with an aspect ratio $h = 0.05$. The horseshoe region is almost completely depleted after ~ 250 orbits, which is about ~ 15 libration timescales. Notice that the gas opening will also depend on the gas viscosity, which tends to flatten out the surface density profile, and thus to close the gap.

We now examine the conditions for gap opening. Basically speaking, the planet mass must be large enough to induce shocks in the region where the wake is excited, and the viscosity must be small enough so as not to prevent gap opening. Goodman & Rafikov (2001) have calculated the distance d_s from the planet beyond which a shock forms. This distance reads approximately:

$$d_s \approx \left(\frac{3q}{2h^3} \right)^{-2/5} H(r_p). \quad (2.21)$$

A linear description of the differential Lindblad torque will fail when $d_s \lesssim \pm 4H(r_p)/3$, which corresponds to the location from the orbit where the wake excitation is the most important (that is where the amplitude of the Fourier components of the differential Lindblad torque is maximal). This can be recast as:

$$q \gtrsim 0.7h^3. \quad (2.22)$$

This condition, known as the *thermal criterion* for gap opening, is generally written as $R_H \geq H$ (Lin & Papaloizou 1993), where $R_H = r_p(q/3)^{1/3}$ is the planet's Hill radius, defined in section 1.3.2. Remember this only gives an order of magnitude estimate. Assuming a $h = 0.05$ disc aspect ratio, planet masses somewhat larger than $M_p \gtrsim 10^{-4} M_\star$ may therefore open a gap. As stated above, the viscosity may however prevent this process. A *viscous criterion* is expressed as (Lin & Papaloizou 1979, Bryden et al. 1999):

$$q \gtrsim \frac{40}{\mathcal{R}}, \quad (2.23)$$

where $\mathcal{R} = a_p^2 \Omega_p / \nu$ is the Reynolds number. Assuming an α -prescription for the viscosity, this criterion can be recast as $\alpha \lesssim q/(40h_p^2)$. For $q = 10^{-4}$ and $h = 0.05$, this yields $\alpha \lesssim 10^{-3}$, which is slightly smaller than the standard value $\alpha \sim 4 \times 10^{-3}$ used in numerical simulations. Notice that the above two conditions for gap opening have recently been revisited by Crida et al. (2006). The authors provide a unified criterion that takes the form:

$$\frac{3}{4} \frac{H}{R_H} + \frac{50}{q\mathcal{R}} < 1, \quad (2.24)$$

and which appears as a combination of the thermal and viscous criteria.

Width of the horseshoe region

Another source of non-linearities has been suggested by D'Angelo et al. (2003b). The authors performed three-dimensional, high-resolution calculations with a large range of planet to primary mass ratios, from $q = 3 \times 10^{-6}$ to $q = 3 \times 10^{-3}$. Their results are displayed in figure 2.11. The inverse of the migration timescale is depicted as a function of the planet mass. Up to $q \sim 3 \times 10^{-5}$, the numerical results are in very good agreement with the three-dimensional analytic estimate of Tanaka et al. (2002) (solid curve). From $q \sim 2 \times 10^{-4}$, the migration timescale is roughly independent of the planet mass, which is expected for planets opening a gap (type II migration, see section 2.5). In between both trends, the migration timescale is significantly smaller than analytically predicted, indicating a strong departure from linearity. This is an important result as hitherto the onset on non-linearities was associated to the formation of a gap. Interestingly, this non-linear process slows down migration, and its impact is maximum for planets of ~ 10

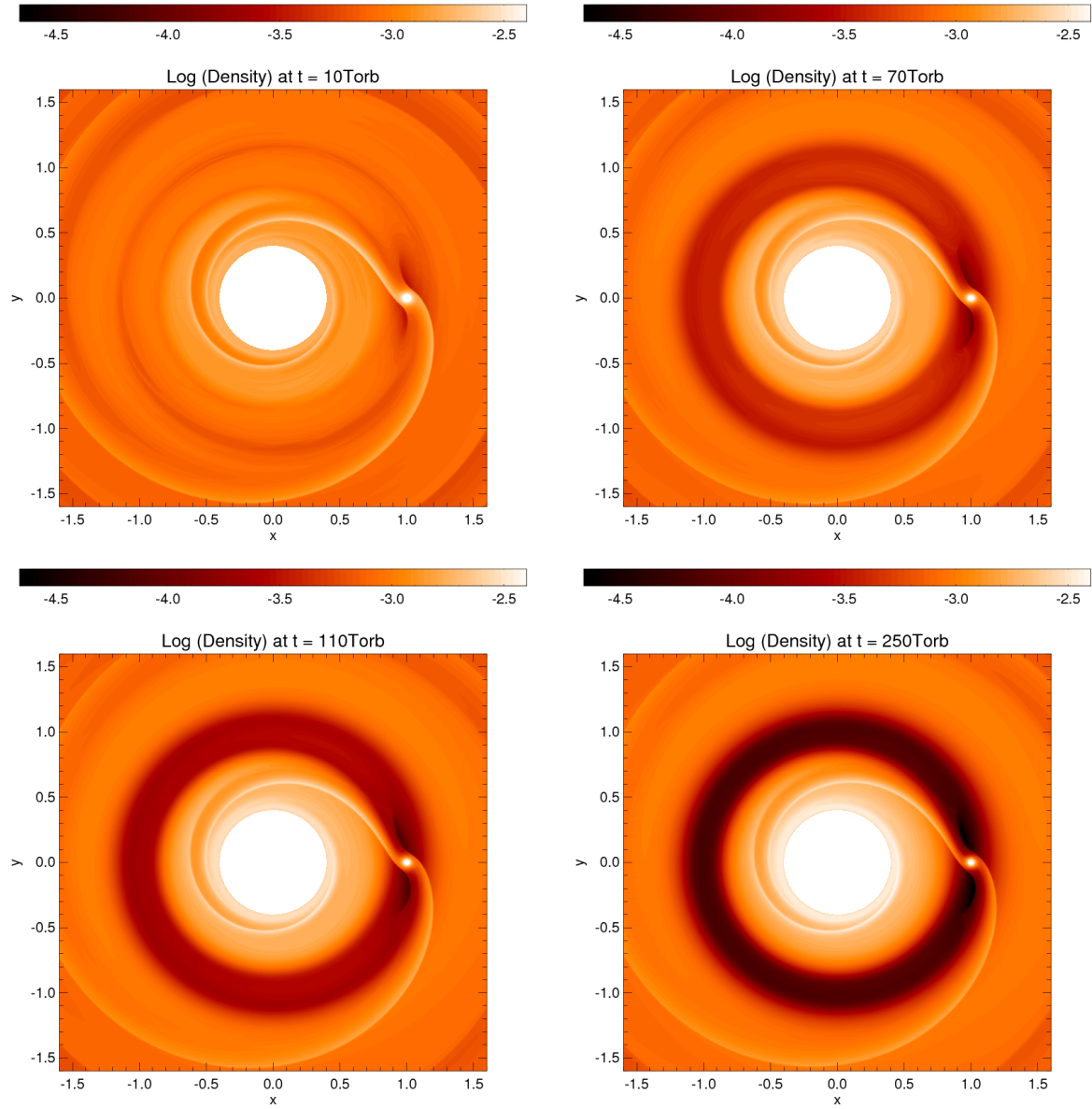


FIGURE 2.10: Gap opening around a Jupiter-mass planet, on a fixed circular orbit at $r = 1$. From top-left to bottom-right, the disc surface density is displayed at $t = 10, 70, 110$ and 250 orbits.

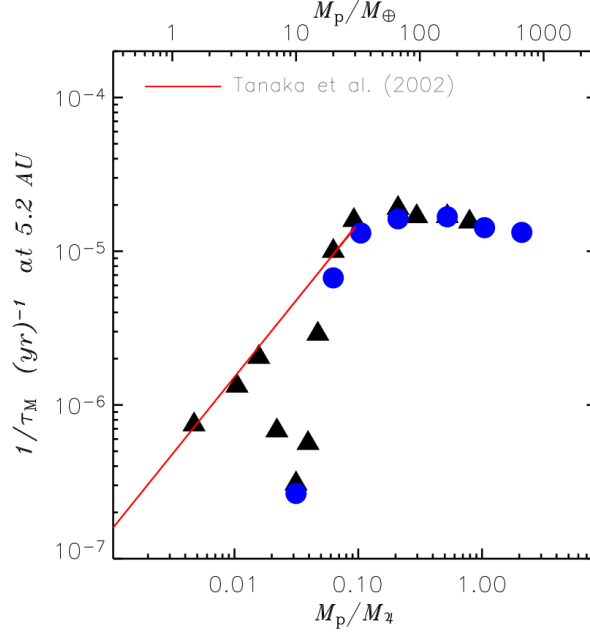


FIGURE 2.11: Inverse of the migration timescale as a function of the planet mass, for a disc aspect ratio $h = 0.05$. The symbols depict results of three-dimensional hydrodynamic calculations performed by D’Angelo et al. (2003b). Triangles and circles refer to different prescriptions for the softening length of the planet potential. The solid curve shows the three-dimensional analytic estimate of Tanaka et al. (2002).

Earth-masses, which is approximately the critical core mass for runaway gas accretion in the core-accretion model, described in section 1.3.2.

Masset et al. (2006a) explained the onset of non-linearities by a significant growth of the horseshoe region, linked to the flow transition near the planet from a low-mass situation, where fluid elements only perform horseshoe U-turns, to a high-mass situation, where fluid elements can be trapped in the circumplanetary disc around the planet. The increase of the horseshoe half-width x_s turns to a significant increase of the corotation torque, since the latter scales as x_s^4 , see equation (2.18). For shallow surface density profiles, as in D’Angelo et al. (2003b), the (unsaturated value of the) corotation torque becomes much more positive, and migration is dramatically slowed down. Masset et al. (2006a) found that this effect is maximum for $q \sim 0.6h^3$, that is for $M_p \sim 20$ Earth masses for $h = 0.05$. These results underscore the corotation torque potential to slow down migration of rather low-mass planets.

We end up this section by clarifying at last what has been called “low-mass planets” from the beginning of this chapter. The clarification work has been done by Masset et al. (2006a), who showed that, in the two-dimensional framework, the flow in the planet vicinity remains linear as long as:

$$r_B \ll \varepsilon, \quad (2.25)$$

where $r_B = GM_p/c_s^2(r_p)$ is the planet’s Bondi radius, and ε is the softening length of the planet’s potential. When this *linearity criterion* is satisfied, the torque exerted on the planet scales with q^2 . We will apply it in chapters 4 and 6 to justify that the planet masses used in our calculations do belong to the linear migration regime (that is type I migration). Equation (2.25) translates into $q \ll q_{\text{lin}}$, with:

$$q_{\text{lin}} = h^3 \times \varepsilon/H(r_p). \quad (2.26)$$

As mentioned in section 2.3.1, the softening length used in numerical simulations is typically $\sim 0.6H(r_p)$, even though the numerical factor may differ, depending on the context. For a

$h = 5\%$ disc aspect ratio, we find $q_{\text{lin}} \approx 7.5 \times 10^{-5}$, while for $h = 3\%$, $q_{\text{lin}} \approx 2 \times 10^{-5}$.

2.5 Migration in a gap: type II migration

The migration of planets that have opened a gap is called type II migration. In this section, we thus assume that the condition for gap opening, described in the last section, is satisfied. We also assume that the gap is well depleted, the residual surface density at the gap location being a small fraction of the initial one. The planet is supposed to isolate the inner and outer discs from each other, which independently follow their viscous drift. According to type II migration theory, the planet is locked into the viscous evolution of the disc. This can be understood as follows. Suppose that the planet drifts inward slightly faster than the background disc. The planet getting closer to the gap's inner edge, the (positive) torque exerted on it by the inner disc increases, and the planet is repelled outward. Similarly, did the planet get closer to the gap's outer edge, it would be pushed inward by the increase of the outer torque. The planet therefore remains at the gap center, and it follows the viscous disc evolution. Differently stated, the migration rate \dot{a} for type II migration is the disc radial velocity v_r . Its amplitude *and its sign* are radius- and time-dependent (Lynden-Bell & Pringle 1974). In the particular case where the background surface density is uniform, $v_r = -3\nu/2r$, and the type II migration timescale reads:

$$\tau_{\text{II}}[\text{yrs}] \sim 25 \left(\frac{\alpha}{4 \times 10^{-3}} \right)^{-1} \left(\frac{H}{r} \right)^{-2} \left(\frac{r}{1 \text{AU}} \right)^{3/2}, \quad (2.27)$$

where we have assumed that the central star has a solar mass. Contrary to the type I migration timescale, given by equation (2.12), τ_{II} displays no dependence on the planet mass nor in the disc surface density. Assuming again a disc with $h = 0.05$ and $\alpha = 4 \times 10^{-3}$, we find $\tau_{\text{II}} \sim 1.2 \times 10^5$ yrs at $r = 5$ AU, and $\tau_{\text{II}} \sim 1.0 \times 10^4$ yrs at $r = 1$ AU.

2.6 Runaway migration: type III migration

In section 2.3.2, we have reviewed the properties of the corotation torque for a planet held on a fixed orbit. The corotation torque ultimately saturates, unless angular momentum is exchanged with the disc outside the corotation region, through viscous stress. In this section, we consider a migrating planet. We neglect the disc viscous drift, whose timescale is much larger than the migration timescale. This supposes a planet mass smaller than a few Saturn masses. The planet and all the coorbital material (the horseshoe region and the circumplanetary disc, if any) migrate at the same drift rate, \dot{a} , which we assume to be *stationary*. Assume first that migration is directed inward. As the planet migrates, fluid elements circulating in the inner disc very close to the horseshoe separatrix are caught in libration. They execute an outward horseshoe U-turn when they are at conjunction with the planet. At the next conjunction however, the fluid elements have left the horseshoe region as the planet has kept migrating. They cannot perform an inward U-turn, and they are left circulating in the outer disc. During this crossing episode, a negative torque is exerted on the planet, whose migration is thus accelerated. Similarly, if the planet migrates outward, fluid elements belonging to the outer disc may cross the horseshoe region after performing an inward horseshoe U-turn. A positive torque is then applied on the planet, whose migration is again accelerated. This contribution to the corotation torque reads:

$$\Gamma_{\text{cross}} = 2\pi a_p \dot{a}_p \Sigma_s \times 4Ba_p x_s, \quad (2.28)$$

where Σ_s denotes the surface density at the inner (outer) horseshoe separatrix for a planet migrating inwards (outwards). The first term in the right-hand side of equation (2.28) is the

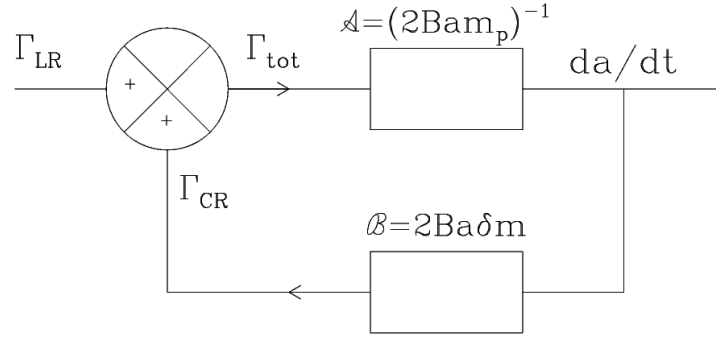


FIGURE 2.12: Type III planetary migration seen as a feedback loop. The latter remains stable while the open-loop transfer function $\mathcal{A} \times \mathcal{B} < 1$, that is while $\delta m < M_p$ (see text). From [Masset \(2008\)](#).

mass flux crossing the horseshoe region. The second term is the specific angular momentum exchanged by the planet and the fluid elements performing a horseshoe U-turn.

The rate of angular momentum of the system made of the planet and the coorbital region is the sum of (i) the contribution Γ_{cross} of the crossing elements to the corotation torque and (ii) of the differential Lindblad torque $\Delta\Gamma_{\text{LR}}$. This reads:

$$2Ba_p\dot{a}_p(M_p + M_{\text{cpd}} + M_{\text{hs}}) = 2\pi a_p\dot{a}_p\Sigma_s \times 4Ba_px_s + \Delta\Gamma_{\text{LR}}, \quad (2.29)$$

where M_{cpd} and M_{hs} denote the mass of the circumplanetary disc and of the horseshoe region, respectively. This can be transformed into:

$$2Ba_p\dot{a}_p\tilde{M}_p = 2Ba_p\dot{a}_p\delta m + \Delta\Gamma_{\text{LR}}, \quad (2.30)$$

where $\tilde{M}_p = M_p + M_{\text{cpd}}$ is the *effective* planet mass, and where $\delta m = 4\pi a_px_s\Sigma_s - M_{\text{hs}}$ is called the *coorbital mass deficit* ([Masset & Papaloizou 2003](#)). It represents the difference between (i) the mass the horseshoe region would have if its surface density was uniform and equal to Σ_s , and (ii) the actual horseshoe region mass. For the sake of simplicity, we denote by M_p the effective planet mass, which we simply call the "planet mass". We note in passing that the above expression of Γ_{cross} assumes that all crossing fluid elements perform horseshoe U-turns, none of them can be captured in the circumplanetary disc. We will discuss this point below.

Equation (2.30) can be interpreted as the angular momentum conservation of the planet where, contrary to the differential Lindblad torque, the corotation torque scales with the migration rate. Planetary migration can therefore be described as a feedback loop ([Masset 2008](#)). This is illustrated in figure 2.12. Note that this representation is valid as long as the system is steady-state (\dot{a} is stationary). The loop input is the differential Lindblad torque (denoted Γ_{LR} here), its output is the migration rate da/dt . The feedback loop is stable when its open-loop transfer function $\mathcal{A} \times \mathcal{B}$ is smaller than unity. This schematic representation argues that migration turns out to be unstable when $\delta m > M_p$. This unstable regime has been identified by [Masset & Papaloizou \(2003\)](#). It is called *runaway migration*, or type III migration (because it was discovered after types I and II - see sections 2.3 and 2.5 respectively). It relies on the planet ability to build up a coorbital mass deficit, hence to open a gap. It does not apply to low-mass planets, which do not alter the surface density profile of the disc. It does not apply to high-mass planets neither, where the gap can be wide enough to enclose the horseshoe separatrices, resulting in a very low coorbital mass deficit. It therefore concerns intermediate mass planets, typically of the mass of Saturn ($q \sim 10^{-4}$), in sufficiently massive discs. This is illustrated in figure 2.13, where the occurrence of the three migration types is displayed as a function of the planet and the disc masses.

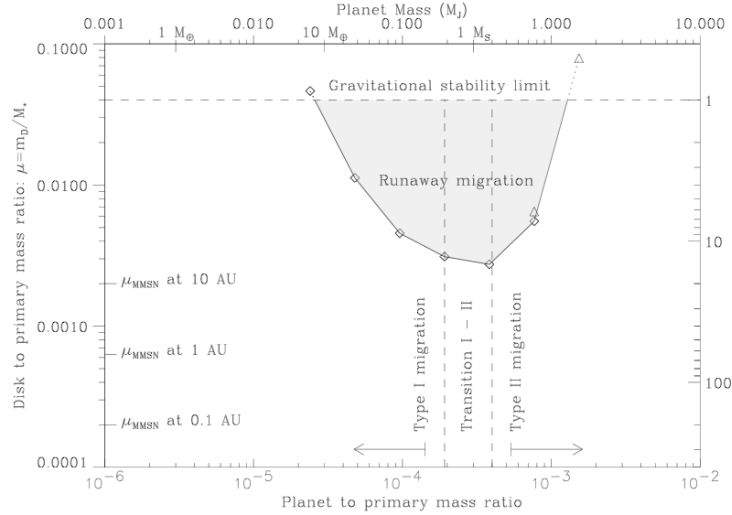


FIGURE 2.13: Occurrence of the three migration types, as a function of the planet to primary mass ratio (bottom x -axis), and the disc to primary mass ratio at the planet location (left y -axis). The disc aspect ratio is $h = 0.03$. The right y -axis shows the Toomre parameter Q at the planet location. The upper part of the plot is thus limited by the gravitational instability limit (dashed line). From [Masset & Papaloizou \(2003\)](#).

As stated above, the sign of Γ_{cross} is dictated by the initial drift of the planet. Runaway migration can therefore be directed inwards, or outwards, depending on the sign of \dot{a}_p before runaway starts. This sign is very sensitive to the asymmetry of the mass distribution inside the horseshoe region and the circumplanetary disc ([Pepliński et al. 2008b;c](#)). It turns out to have a complex dependence on the initial surface density profile, on the viscosity, and on the planet mass. Predicting the direction of runaway migration is therefore an intricate task, so we are led to rely on numerical simulations. However, their results show great dependence on the mass flow inside the circumplanetary disc and the horseshoe region, which is very sensitive to numerical parameters, in particular the resolution ([D’Angelo et al. 2005](#), [Pepliński et al. 2008a](#)) or the inclusion of the gas thermodynamics. We furthermore recall that the mass M_p that appears in the runaway criterion $\delta m > M_p$ includes the mass of the planet and of the circumplanetary. Any physical process increasing the *effective planet mass*, such as the accretion onto the planet ([D’Angelo & Lubow 2008](#)) or the inclusion of the gas self-gravity ([Zhang et al. 2008](#)) may cause a departure from the runaway regime to type II migration regime.

2.7 Concluding remarks

We have detailed in this chapter the interaction between a planet and a protoplanetary gaseous disc. The planet’s migration is dictated by the total torque exerted on it by the disc. We have studied in the linear context the properties of the differential Lindblad torque and of the coorbital corotation torque. While the former is negative and rapidly stationary, the latter oscillates about zero with a time-decreasing amplitude. This saturation of the corotation torque may however be prevented by viscous diffusion across the planet’s coorbital region. For sufficiently shallow surface density profiles, the unsaturated corotation torque is positive. This underscores the potential importance of the corotation torque to slow down type I migration, even though for a locally isothermal disc the differential Lindblad torque still prevails, and type I migration remains very fast. We will see in chapter 5 that an additional contribution to the corotation torque arises when the gas thermodynamics is taken into account. This *torque excess*, as we

will call it, is positive for realistic profiles of the surface density and temperature. By means of hydrodynamic calculations, we will show in chapter 6 that the torque excess may be positive enough so that migration be significantly slowed down (by typically an order of magnitude) with respect to the locally isothermal case. In some cases, we will see that the migration may even be directed outwards.

Although we made restrictive assumptions on the disc model, we tried as far as possible to present results with extended physics, for instance the impact of the disc's magnetic structure. Notice that the effect of the gas self-gravity will be largely discussed in chapter 4. Some additional discussions and perspectives will also be addressed in section 7. The reader eager to learn more results on planetary migration (e.g. the impact on the planet's eccentricity, or the case of multiple systems) is referred to the reading of [Papaloizou & Terquem \(2006\)](#) and [Masset \(2008\)](#).

I would like to end up this chapter by recalling that gas-planet interactions occur only during the disc lifetime. Once the gas is dissipated, planetary systems harbor a host star, one or several formed planets, and residual planetesimals not accreted by the planets. As mentioned in section 2.1, planet-planet and planet-planetesimals interactions may be very efficient at altering the planet's orbital elements. The planet migration due to the interaction with the gaseous disc is likely to *leave no traces*.

Chapter 3

Disc-planet interactions: numerical calculations

WE PRESENT in this chapter the hydrodynamic code we use to investigate disc-planet interactions. We give in section 3.1 a detailed presentation of the code features. The major modifications we made in the code, namely the implementation of the gas self-gravity and the inclusion of an energy equation, are respectively described in sections 3.2 and 3.3. After some general background on these topics, we detail their implementations in the code and we present test problems.

Contents of this chapter

3.1	The FARGO code	42
3.1.1	Initialization	43
3.1.2	Courant limit evaluation	44
3.1.3	Planet update	47
3.1.4	Gas update	47
3.1.5	Output step	50
3.1.6	Code units	50
3.2	Implementation of the self-gravity	50
3.2.1	Introduction	50
3.2.2	Implementation in the FARGO code	55
3.2.3	Test problems	57
3.2.4	Domain decomposition	59
3.3	Implementation of an energy equation	61
3.3.1	Thermodynamic background	61
3.3.2	Heat transport equation	62
3.3.3	Contact discontinuities	63
3.3.4	Implementation in the FARGO code	64
3.3.5	Test problems	65
3.4	Appendix: wave propagation properties	69

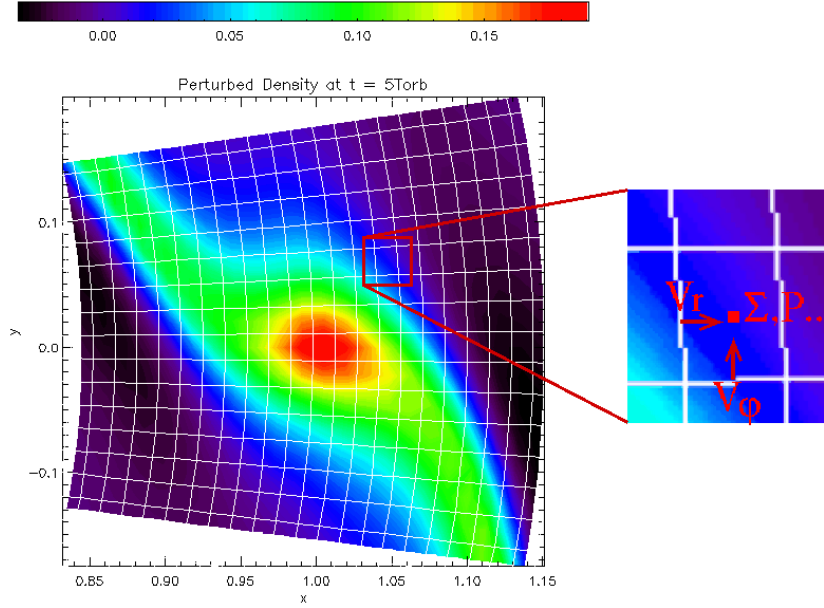


FIGURE 3.1: An illustrative example of an output produced by the FARGO code. We show the surface density perturbation by a low-mass planet, in the vicinity of the planet (the latter is fixed at $x = 1$, $y = 0$). The grid used for this calculation is superimposed with white lines. The close-up in the right panel shows the location of the scalar and vector fields for a given cell (see text). Note that the radial velocity v_r is located at the radial interface between two cells and is half-centered in azimuth, whereas the azimuthal velocity v_ϕ is located at the azimuthal interface between two cells, and it is half-centered in radius.

3.1 The FARGO code

FARGO is a two-dimensional hydrodynamic code dedicated to planet-disc interactions. It solves the Navier-Stokes and continuity equations for a gaseous, viscous disc subject to the gravity of the central object and that of embedded planets. It calculates the time evolution of the radial and azimuthal velocities (v_r and v_ϕ), and of the surface density Σ on a polar mesh. The gas pressure p is related to the disc surface density and temperature T by an ideal equation of state, $p = \mathcal{R}\Sigma T$, with \mathcal{R} a constant. This turns to $p = \Sigma c_s^2$, where c_s is the isothermal sound speed. In its public version, the code does not include the time evolution of the gas temperature, but it uses a stationary, arbitrary temperature (or sound speed) radial profile. The connection between p , Σ and T is usually referred to as a *locally isothermal equation of state*.

Akin to the famous ZEUS code¹, FARGO is a *staggered-mesh* code. As illustrated in figure 3.1, this means that all scalar quantities, like the surface density, the pressure or the temperature are defined at the cell centers, while vector quantities are defined at the interfaces between cells. It renders the calculations of fluxes between the cells more convenient, since the velocity field is naturally stored at the interfaces. Only the surface density needs to be interpolated at the interfaces. Other classes of codes set out all quantities at the center of cells, be they scalar or vector fields. The fluxes calculation, which can be based on a Godunov method, is then more complex.

The code is parallelized with the Message Passing Interface procedure, or MPI for short. A given calculation can be run on several CPUs, each process dealing with a fraction of the total mesh, or sub-mesh. The split of the mesh on several sub-meshes is called the *domain decomposition*. A two-dimensional polar mesh is usually split both in the radial and in the azimuthal

¹see <http://www.astro.princeton.edu/~jstone/zeus.html>

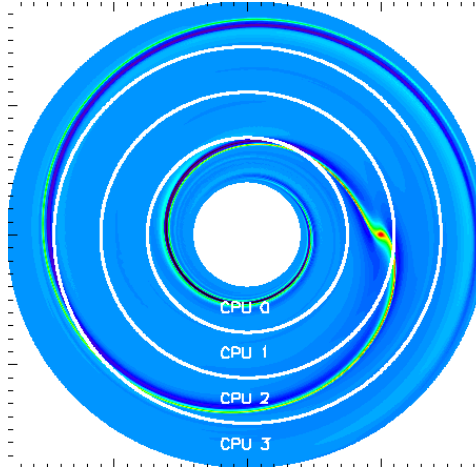
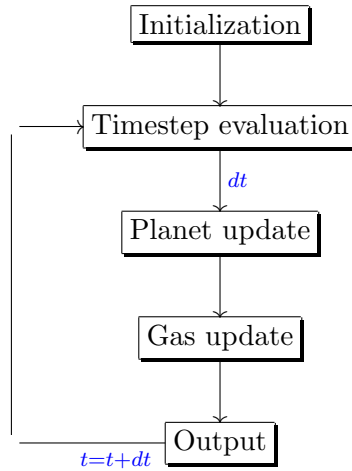


FIGURE 3.2: Illustration of the domain decomposition used with FARGO. The mesh is exclusively split radially (see text), here between four CPUs. The background picture shows the gas surface density perturbation by a low-mass planet.

directions. Such a decomposition is not possible with the FARGO code as it implies azimuthal displacement of material of several zones over one timestep (Masset 2000a;b). The level of communications in the azimuthal direction at each timestep would otherwise be prohibitive. Instead, the mesh is only split in the radial direction, each CPU dealing with a given number of rings in the mesh, as depicted in figure 3.2.

The diagram structure of the code is displayed below, and we now detail its different steps.



3.1.1 Initialization

In addition to the definition of the grid properties (e.g. the mesh domain decomposition), this step deals with the initialization of the planet and the disc. The planet's initial velocity is strictly Keplerian, its angular frequency Ω_p reads:

$$\Omega_p = \Omega_K(r_p) = \sqrt{\frac{\mathcal{G}M_\star}{r_p^3}}, \quad (3.1)$$

where Ω_K denotes the Keplerian angular velocity, and we recall that \mathcal{G} is the gravitational constant, M_\star the mass of the central object, and r_p the planet's orbital radius. As customarily

assumed, the disc is initially axisymmetric, its surface density and temperature (or, equivalently, the square of the sound speed) being power laws of the radius r :

$$\Sigma(r) = \Sigma(r_p) \left(\frac{r}{r_p} \right)^{-\sigma} \quad \text{and} \quad T(r) = T(r_p) \left(\frac{r}{r_p} \right)^{-1+2f}, \quad (3.2)$$

where $\Sigma(r_p)$ and $T(r_p)$ are respectively the surface density and temperature at the planet initial location. The quantity f is usually called the disc's flaring index. Writing the condition for vertical hydrostatic equilibrium defines a putative disc scale height as $H(r) = c_s(r)/\Omega_K(r)$. Using the ideal gas law, the isothermal sound speed profile is given by $c_s(r) = \sqrt{\mathcal{R}T(r)}$ (see section 3.3.1), so that:

$$H(r) = H(r_p) \left(\frac{r}{r_p} \right)^{1+f}, \quad \text{with} \quad H(r_p) = \sqrt{\frac{r_p^3 \mathcal{R} T(r_p)}{\mathcal{G} M_\star}}. \quad (3.3)$$

We will largely make use of the disc aspect ratio, which reads $h(r) = H(r)/r = h(r_p)(r/r_p)^f$. In the particular case where f cancels out, h is uniform and $H(r)$ scales with r . Furthermore, the disc's initial azimuthal velocity $v_\varphi = r\Omega$ is calculated so that we impose a strict balance between the gravitational force due to the central star, the pressure force, and the centrifugal force:

$$v_\varphi(r) = r\Omega_K(r) [1 - (1 + \sigma - 2f) h^2(r)]^{1/2}. \quad (3.4)$$

The initial radial velocity is that of a viscous drift with a kinematic viscosity profile $\nu(r)$. It is evaluated from the conservation equations of the mass and of the angular momentum (Lynden-Bell & Pringle 1974):

$$v_r(r) = -\frac{3}{\Sigma(r)r^{1/2}} \partial_r \left\{ \nu(r) \Sigma(r) r^{1/2} \right\}. \quad (3.5)$$

Note that the above profiles are those of the unperturbed disc, so they can be significantly altered by the introduction of a massive, gap-opening planet (see e.g. figure 2.10). We will essentially deal with a uniform kinematic viscosity, so equation (3.5) turns to

$$v_r(r) = -\frac{3}{2} \frac{\nu}{r} (1 - 2\sigma). \quad (3.6)$$

Equation (3.6) shows that the disc accretes onto the central object (v_r is negative) *only if* Σ decreases less sharply than $r^{-1/2}$; otherwise the disc drifts outwards. Another prescription for the viscosity is the so-called α -model of Shakura & Sunyaev (1973), which we presented in section 2.2. When an α -viscosity is included, equation (3.5) leads to

$$v_r(r) = -\frac{3\nu(r_p)}{r_p} \{1 + 2f - \sigma\} \left(\frac{r}{r_p} \right)^{-1/2+2f}. \quad (3.7)$$

The sign of v_r now depends both on f and on σ . For a vanishing flaring index, the disc will accrete onto the central object provided that the background surface density decreases less sharply than r^{-1} .

3.1.2 Courant limit evaluation

We enter the hydrodynamic loop with the timestep evaluation. The timestep limitation in hydrocodes arises from a condition known as the Courant-Friedrichs-Levy condition, or CFL condition. It essentially imposes that the information cannot sweep a distance larger than the size of a cell over each timestep. This induces four constraints, each one defining a timestep

limit. On the one hand, the wavefront of any wave should not propagate over a whole cell, which gives the timestep limit

$$\delta t_1 = \min(\delta r, r\delta\varphi)/c_s, \quad (3.8)$$

where δr and $r\delta\varphi$ are the mesh sizes respectively in the radial and azimuthal directions. On the other hand, a test particle in a given cell should not travel a distance greater than δr in the radial direction, nor greater than $r\delta\varphi$ in the azimuthal one. This provides the timestep limits

$$\delta t_2 = \delta r/v_r \quad \text{and} \quad \delta t_3 = r\delta\varphi/v_\varphi. \quad (3.9)$$

A fourth constraint stems from the viscosity, and implies the timestep limit

$$\delta t_4 = \min\left(\frac{\delta r}{4C_{\text{vnr}}^2\delta v_r}, \frac{r\delta\varphi}{4C_{\text{vnr}}^2\delta v_\varphi}\right), \quad (3.10)$$

with $\delta v_r = \partial_r v_r \delta r$, $\delta v_\varphi = \partial_\varphi v_\varphi \delta\varphi$, and C_{vnr} is von Neumann-Richtmyer's constant (Stone & Norman 1992, Masset 2000a). It measures the number of zones over which the artificial viscosity spreads shocks, and is typically between 1 and 2.

Among the above timestep limitations, the one arising from the sweep in the azimuthal direction, δt_3 , is by far the most constraining, in particular at the inner boundary of the mesh, where the motion is fast and the cells are narrow. We note in passing that $\delta t_3 = \delta\varphi/\Omega_K(r) \propto r^{3/2}$. Since we are primarily concerned by the gas dynamics in the planet vicinity, and not by the flow near the inner edge of the grid, this limitation is a *waste* of computational time. Interestingly, as we shall see in section 3.1.4, FARGO uses a slightly different scheme for the transport step: the material is transported in the azimuthal direction owing to the residual azimuthal velocity $v_\varphi - \tilde{v}_\varphi$, where \tilde{v}_φ stands for the mean average azimuthal velocity with respect to φ (Masset 2000a). The material will be further shifted azimuthally by $r\tilde{v}_\varphi dt$. This trick reduces the δt_3 limit into $\delta t_3 = r\delta\varphi/(v_\varphi - \tilde{v}_\varphi)$. An additional timestep constraint is thus defined to ensure that two cells having same azimuth, but belonging to two neighboring rings, are not disconnected after a timestep. This fifth (and last) limitation, which is specific to the FARGO code, involves the timestep limit

$$\delta t_5 = \delta\varphi \times |\Omega(r) - \Omega(r + \delta r)|^{-1}. \quad (3.11)$$

The hydrodynamic timestep is eventually given, for the FARGO code, by:

$$dt = C_0 \times \min\left(\left[\delta t_1^{-2} + \delta t_2^{-2} + \delta t_3^{-2} + \delta t_4^{-2}\right]^{-1/2}, \delta t_5\right), \quad (3.12)$$

where C_0 is a numerical factor between 0 and 1, called CFL number. We show in figure 3.3 the inverse of the five timestep limits δt_i^{-1} above, without and with the FARGO algorithm, and the resulting hydrodynamic timestep dt calculated with equation (3.12). This is done for a low-mass and a high-mass planet. In both cases, the timestep without the FARGO algorithm is limited by the distance swept in the azimuthal direction, as expected for a standard advection scheme. When the FARGO algorithm is used, the limitation for a low-mass planet clearly comes from the sound speed at the inner edge (δt_1^{-1} panel). The minimum timestep in this case amounts to $dt \sim 1.5 \times 10^{-2} \Omega_p^{-1}$ with the FARGO algorithm, while its value is as small as $dt \sim 5.2 \times 10^{-4} \Omega_p^{-1}$ for the same run without the FARGO algorithm. Here, the FARGO calculation is thus ~ 28 times faster than the standard one. Since we use a uniform disc aspect ratio $H/r = 0.03$, this speedup is compatible with the maximum ratio $v_\varphi/c_s = r/H \approx 33$ reachable (Masset 2000b). In the high-mass planet regime, the timestep is limited not only by the sound speed at the inner edge, but also by the numerical viscosity as well as the shear in the planet vicinity, as a circumplanetary disc builds up around the planet. The minimum timestep with the FARGO run is nevertheless ~ 14 times larger than the one of the standard run.

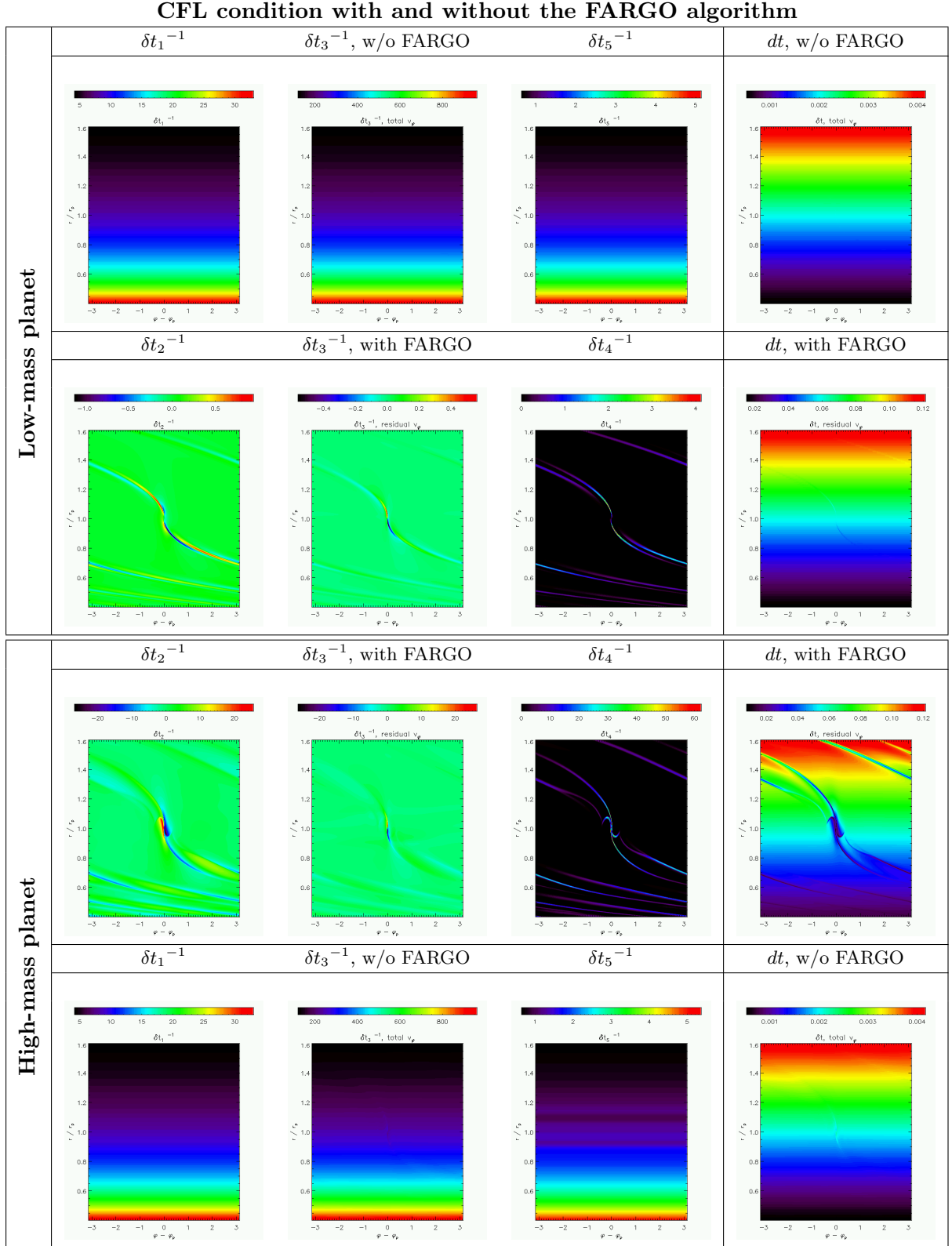


FIGURE 3.3: We display here the inverse of the five timestep limitations δt_1^{-1} to δt_5^{-1} , and the resulting hydrodynamic timestep dt . The results are obtained with a low-mass planet in the two first rows, and with a high-mass planet in the two last ones. In both cases, the limitation arising from the azimuthal velocity δt_3^{-1} , and the corresponding timestep dt , are displayed with and without (w/o) the FARGO algorithm.

3.1.3 Planet update

We follow the structure diagram of figure 3.2, and we now come to the planet update. This update is two-fold. First, the planets velocities are updated with the disc gravity. Then, the planets positions and velocities are updated with the gravity of the star and of the other planets, assuming they behave like an N-body system. This step is done with a fifth-order Runge-Kutta integrator.

3.1.4 Gas update

In this section, we detail the gas update for the release version of FARGO. The modifications related to the disc self-gravity and to the energy equation are deferred to sections 3.2 and 3.3. The Navier-Stokes and continuity equations solved by the code write

$$\frac{\partial v_r}{\partial t} + v_r \frac{\partial v_r}{\partial r} + v_\varphi \frac{1}{r} \frac{\partial v_r}{\partial \varphi} = \frac{v_\varphi^2}{r} - \frac{1}{\Sigma} \frac{\partial P}{\partial r} - \frac{\partial \Phi}{\partial r} + a_r^{\text{visc}} - \frac{1}{\Sigma} \frac{\partial q_r}{\partial r}, \quad (3.13)$$

$$\frac{\partial v_\varphi}{\partial t} + v_r \frac{\partial v_\varphi}{\partial r} + v_\varphi \frac{1}{r} \frac{\partial v_\varphi}{\partial \varphi} + \frac{v_r v_\varphi}{r} = -\frac{1}{\Sigma} \frac{1}{r} \frac{\partial P}{\partial \varphi} - \frac{1}{r} \frac{\partial \Phi}{\partial \varphi} + a_\varphi^{\text{visc}} - \frac{1}{\Sigma} \frac{1}{r} \frac{\partial q_\varphi}{\partial \varphi}, \quad (3.14)$$

$$\frac{\partial \Sigma}{\partial t} + \frac{1}{r} \frac{\partial}{\partial r} (r \Sigma v_r) + \frac{1}{r} \frac{\partial}{\partial \varphi} (\Sigma v_\varphi) = 0, \quad (3.15)$$

where we denote by a_r^{visc} and a_φ^{visc} the radial and azimuthal accelerations due to the disc viscosity, given by (see e.g. [Masset 2002](#), [D'Angelo et al. 2002](#))

$$a_r^{\text{visc}} = \frac{1}{r \Sigma} \left[\frac{\partial}{\partial r} (r \tau_{r,r}) + \frac{\partial \tau_{r,\varphi}}{\partial \varphi} - \tau_{\varphi,\varphi} \right] \quad \text{and} \quad a_\varphi^{\text{visc}} = \frac{1}{r \Sigma} \left[\frac{\partial}{\partial r} (r \tau_{r,\varphi}) + \frac{\partial \tau_{\varphi,\varphi}}{\partial \varphi} + \tau_{r,\varphi} \right], \quad (3.16)$$

with the components of the viscous stress tensor reading

$$\tau_{r,r} = 2\nu \Sigma \left[\frac{\partial v_r}{\partial r} - \frac{1}{3} \text{div}(\mathbf{v}) \right], \quad \tau_{\varphi,\varphi} = 2\nu \Sigma \left[\frac{1}{r} \frac{\partial v_\varphi}{\partial \varphi} + \frac{v_r}{r} - \frac{1}{3} \text{div}(\mathbf{v}) \right], \quad (3.17)$$

$$\tau_{r,\varphi} = \nu \Sigma \left[r \frac{\partial}{\partial r} \left(\frac{v_\varphi}{r} \right) + \frac{1}{r} \frac{\partial v_r}{\partial \varphi} \right], \quad \text{and} \quad \text{div}(\mathbf{v}) = \frac{1}{r} \frac{\partial}{\partial r} (r v_r) + \frac{1}{r} \frac{\partial v_\varphi}{\partial \varphi}. \quad (3.18)$$

In equations (3.13) and (3.14), Φ stands for the gravitational potential of the star and of the planets. In our calculations, we will use either the frame centered on the primary, or the frame corotating with the planet (or with one of them if there are several planets). In both cases, the frame is *not inertial*, so we must include the indirect part of the potential due to the star and to the planets. As will be explained in the transport step, we do not add a Coriolis acceleration source term in equation (3.14). We also point out the recent work of [Crida et al. \(2007\)](#), who use a frame centered on the center of mass of the primary and of the planets. Such precaution allows to suppress the indirect terms, and it leads to a significant enhancement of the angular momentum conservation of the whole system. Eventually, the quantities q_r and q_φ are the components of an artificial viscous pressure, required to smooth shocks with a staggered-mesh code. Their expression is given by [Stone & Norman \(1992\)](#):

$$q_r = \begin{cases} C_{\text{vnr}}^2 \Sigma \delta v_r^2 & \text{if } \delta v_r < 0 \\ 0 & \text{otherwise} \end{cases} \quad \text{and} \quad q_\varphi = \begin{cases} C_{\text{vnr}}^2 \Sigma \delta v_\varphi^2 & \text{if } \delta v_\varphi < 0 \\ 0 & \text{otherwise,} \end{cases} \quad (3.19)$$

where the quantities C_{vnr} , δv_r and δv_φ have been defined in equation (3.10). As pointed out by the authors, the expressions in equation (3.19) are not covariant, since they depend on the mesh

geometry. For instance, the amount of artificial viscosity used for a given problem can be very different whether a cartesian or a polar mesh is used. However, this should not be an issue with our calculations since the problems we investigate are rather smooth (the shocks that propagate in the disc are not that strong, even when a high-mass planet is assumed) and the flow is largely dominated by the Keplerian shear.

The gas update is made of the following substeps:

- **Source terms:** first, the velocities are updated with the source terms of the Navier-Stokes equations (green terms in equations (3.13) and (3.14)), with a first-order integrator:

$$\{v_r, v_\varphi\}(t + dt) = \{v_r, v_\varphi\}(t) + \text{source terms} \times dt. \quad (3.20)$$

The source terms include the potential and pressure gradients, the physical and artificial viscous accelerations, and the centrifugal acceleration. Of course, the surface density is not concerned by this substep since there is no source terms in the continuity equation.

- **Boundary conditions:** we then apply the boundary conditions at the mesh edges. We impose the azimuthal velocity to match the initial equilibrium profile given by equation (3.4). Regarding the surface density and the radial velocity, we apply a *non-reflecting* wave boundary condition. To do so, we evaluate the wake's pitch angle at each boundary using a WKB approximation. The content of the border ring is then copied into the ghost ring, properly azimuthally shifted by the amount dictated by the pitch angle. This technique is very efficient at removing any reflected wave, as shown in figure 3.4. In this figure, we compare the disc response to an embedded Saturn-mass planet at the same date, the disc being described either with a *rigid* boundary condition (left panel, we impose the radial velocity to be zero at the borders, so that no material can flow from or to the mesh) or with a non-reflecting boundary condition (right panel). Note that, even if there are several planets, this technique evaluates only one pitch angle, that of the closest planet from the inner edge. Only the reflected wave of the latter will be removed efficiently. One should bear in mind that this boundary condition does not strictly conserve the disc mass and angular momentum, since the transmitted wave carries away some angular momentum from the mesh.
- **Transport step:** we now update the components of the velocity and the surface density with the advective (red) terms of equations (3.13) to (3.15). In absence of source terms, these equations can be recast as:

$$\partial_t \Sigma + \text{div}(\Sigma \mathbf{v}) = 0, \quad \partial_t(\Sigma v_r) + \text{div}(\Sigma v_r \mathbf{v}) = 0 \quad \text{and} \quad \partial_t(r \Sigma v_\varphi) + \text{div}(r \Sigma v_\varphi \mathbf{v}) = 0, \quad (3.21)$$

which reads respectively as the conservation of the mass, the radial momentum and the angular momenta. Using Green-Ostrogradsky theorem, these three conservation equations take the form

$$\partial_t W = - \oint \mathbf{F} \cdot d\mathbf{S}, \quad (3.22)$$

where $W = \iiint w dV$, $w = {}^T(\Sigma, \Sigma v_r, r \Sigma v_\varphi)$, and $\mathbf{F} = w \mathbf{v} = {}^T(\Sigma \mathbf{v}, \Sigma v_r \mathbf{v}, r \Sigma v_\varphi \mathbf{v})$ is the flux associated to w . Thus, all quantities in w can be updated by taking into account their fluxes at each cell interface. The difficulty comes from the flux evaluation at the interfaces, where the surface density needs to be interpolated. We define five *momenta*: the surface density Σ , the radial (or linear) momentum Σv_r at each radial interface of a cell (they are usually called the left and right radial momenta), and the angular momentum $\Sigma r(v_\varphi + r \Omega_{\text{frame}})$ at each azimuthal interface (left and right angular momenta). In the angular momentum

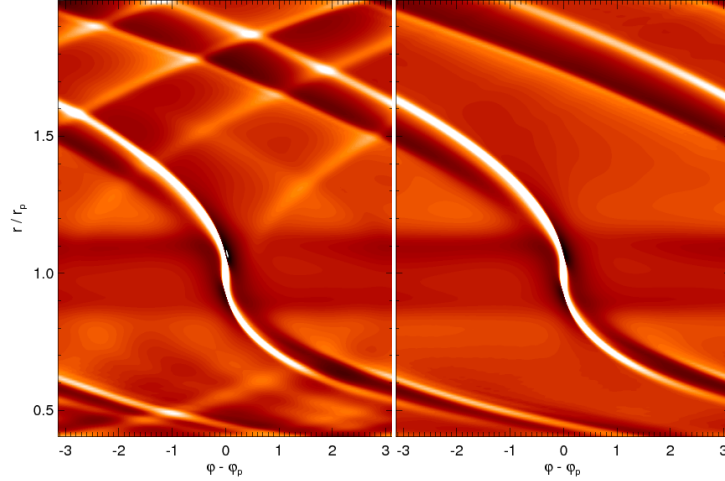


FIGURE 3.4: Disc response to an embedded Saturn-mass planet after 20 orbits, for two calculations having same disc parameters, but different boundary conditions (rigid boundary in the left panel, non-reflecting boundary in the right panel). The disc response with a rigid boundary displays stationary waves between the corotation region and the edges of the mesh.

expression, Ω_{frame} denotes the frame's angular velocity. The customary practice in disc-planet calculations is indeed to assume a frame rotating with the planet ($\Omega_{\text{frame}} = \Omega_p$), so that the planet remains fixed azimuthally on the mesh, which results in less numerical diffusion than if the planet was drifting along the azimuthal direction. As already stated in section 3.1.4, working in this non-inertial frame should lead to an additional Coriolis acceleration in the azimuthal Navier-Stokes equation (3.14). Kley (1998) showed that including this Coriolis source term breaks the angular momentum conservation. Instead of resorting to an explicit source term, the Coriolis acceleration is taken into account with the term $r\Omega_{\text{frame}}$ in the above expression of the angular momentum. This approach enforces the global conservation of the angular momentum. Note however that the local conservation of the momenta can be seriously affected by the numerical diffusion inherent in the finite-difference equations and interpolation algorithm (Stone & Norman 1992). To minimize numerical diffusion, the *constrained transport* method is used. This technique is based on updating the five momenta with the fluxes of the *specific momenta* (momenta divided by the surface density). This process is done in each direction (directional splitting). The update of any momentum X therefore reads:

$$X_{i,j}^a = X_{i,j} + \frac{dt}{S} \left[r_i \Delta\varphi \Sigma_{i,j}^* v_{r,i,j} \left(\frac{X}{\Sigma} \right)_{i,j}^* - r_{i+1} \Delta\varphi \Sigma_{i+1,j}^* v_{r,i+1,j} \left(\frac{X}{\Sigma} \right)_{i+1,j}^* \right], \quad (3.23)$$

in the radial direction, and then:

$$X_{i,j}^b = X_{i,j}^a + \frac{dt}{S} \left[\Delta r \Sigma_{i,j}^* v_{\varphi,i,j} \left(\frac{X^a}{\Sigma} \right)_{i,j}^* - \Delta r \Sigma_{i,j+1}^* v_{\varphi,i,j+1} \left(\frac{X^a}{\Sigma} \right)_{i,j+1}^* \right] \quad (3.24)$$

in the azimuthal direction. In equations (3.23) and (3.24), X^a and X^b denote the quantity X updated respectively with the radial and the azimuthal transport. The quantities denoted by a star superscript are calculated at the corresponding interfaces, with a second-order upwind interpolation (piecewise linear function, see van Leer (1977), Stone & Norman (1992)). FARGO uses the standard radial transport given by equation (3.23), but uses a slightly different method for the azimuthal transport. Masset (2000a) decomposes the

azimuthal velocity into

$$v_\varphi(i, j) = \underbrace{v_\varphi(i, j) - \bar{v}_\varphi(i)}_{v_\varphi^{\text{nu, res}}(i, j)} + \underbrace{\bar{v}_\varphi(i) - N_i \frac{r_i \delta \varphi}{dt}}_{v_\varphi^{\text{u, res}}(i)} + N_i \frac{r_i \delta \varphi}{dt}, \quad (3.25)$$

where \bar{v}_φ is the axisymmetric azimuthal velocity, $N_i = E[\bar{v}_\varphi dt / r_i \delta \varphi]$ is called the shift number, and where $E[X]$ denotes the nearest integer to the real X . There are therefore two azimuthal transport steps, one with the *non-uniform residual velocity* $v_\varphi^{\text{nu, res}}$, the other one with the *uniform residual velocity* $v_\varphi^{\text{u, res}}$. The last step is an azimuthal shift of N_i zones of the five momenta. Once the momenta update by the transport substep is over, we update the components of the velocity, and we apply again the boundary conditions. The transport substep with the FARGO code is finally summed up with the following diagram:

$$X_{i,j} \xrightarrow[\textcolor{blue}{v_r}]{(3.23)} X_{i,j}^a \xrightarrow[\textcolor{blue}{v_\varphi \equiv v_\varphi^{\text{nu, res}}}]{(3.24)} X_{i,j}^b \xrightarrow[\textcolor{blue}{v_\varphi \equiv v_\varphi^{\text{u, res}}}]{(3.24)} X_{i,j}^c \longrightarrow X_{i,j}^d = X_{i,j-N_i}^c$$

3.1.5 Output step

Once the planet and the gas updates are performed, outputs are produced by the code. The main gas fields (surface density, temperature, components of the velocity) are produced. Furthermore, we monitor the quantities related to the planets migration, namely their semi-major axis a and eccentricity e , the torque Γ and the power Π of the force exerted by the disc on them. Note that Γ and Π are connected to the growth rate of a and e , defined respectively as \dot{a}/a and \dot{e}/e . Assuming that each planet behaves like a two-body problem with the central object, their mechanical energy is $E = -\mathcal{G}(M_\star + M_p)M_p/2a$, and their angular momentum reads $H = M_p[\mathcal{G}(M_\star + M_p)a(1 - e^2)]^{1/2}$. We thus have:

$$\frac{\dot{a}}{a} = -\frac{\dot{E}}{E} \quad \text{and} \quad \frac{\dot{e}}{e} = \frac{e^2 - 1}{2e^2} \left(\frac{\dot{E}}{E} + 2\frac{\dot{H}}{H} \right), \quad (3.26)$$

with $\dot{E} = \Pi$ and $\dot{H} = \Gamma$.

3.1.6 Code units

As usual in numerical simulations of planet-disc interactions, we adopt the initial orbital radius r_p of the planet as the length unit, the mass of the central object M_\star as the mass unit and $(\mathcal{G}M_\star/r_p^3)^{-1/2}$ as the time unit. Notice that \mathcal{G} is therefore equal to one in our unit system. Similarly, we take $[\mathcal{G}M_\star/(\mathcal{R}r_p^3)]^{1/2}$ as the temperature unit, so $\mathcal{R} = 1$ in our units.

3.2 Implementation of the self-gravity

We describe in this section how we worked out the implementation of the disc self-gravity on the FARGO code. Some of the information supplied here has been made public on the website of the [FARGO code](http://fargo.in2p3.fr) (<http://fargo.in2p3.fr>).

3.2.1 Introduction

In two-dimensions, we write the disc potential as

$$V(\mathbf{r}) = -\mathcal{G} \iint \frac{\sigma(\mathbf{r}') d\mathbf{r}'}{\|(\mathbf{r} - \mathbf{r}')^2 + \varepsilon^2\|^{1/2}}, \quad (3.27)$$

where σ denotes the surface density field, and where ε is a softening length over which the distance $\|\mathbf{r} - \mathbf{r}'\|$ is smoothed, to avoid any singularity when $\mathbf{r}' = \mathbf{r}$. Assuming the mass to be distributed in a squared mesh of dimension $N \times N$, the potential calculation by direct summation requires $N(N-1)/2 \equiv \mathcal{O}(N^2)$ operations, which rapidly comes to be prohibitive when N reaches a few thousands. Nevertheless, we can benefit from the fact that the potential reads as a *convolution product* to calculate it in Fourier space. We denote by M the mass field, and we refer to $K = \|\mathbf{r}^2 + \varepsilon^2\|^{-1/2}$ as the Green kernel. From equation (3.27), the potential can be recast as

$$V = -\mathcal{G} \mathcal{F}^{-1}[\mathcal{F}(M) \times \mathcal{F}(K)], \quad (3.28)$$

where \mathcal{F} and \mathcal{F}^{-1} denote respectively the direct and inverse Fourier transform operators. The strong point of this method is to reduce the number of operations to $\mathcal{O}(N \log N)$. This greatly motivated us to compute the self-gravitating potential with Fast Fourier Transforms (hereafter FFTs). Their calculation is done using the 2.1.5 MPI-parallelized version of the FFTW library (see <http://www.fftw.org>).

Let us detail the potential calculation with Fourier transforms. We assume for simplicity a one-dimensional mesh with uniform step Δ . Let a be an array of dimension N , whose real elements are denoted by a_k . The j^{th} elements of the direct and inverse Fourier transforms of a are respectively defined² as

$$\mathcal{F}[a]_j = \sum_k a_k \exp\left(-2i\pi k \frac{j}{N}\right) \quad \text{and} \quad \mathcal{F}^{-1}[a]_j = \sum_k a_k \exp\left(2i\pi k \frac{j}{N}\right), \quad (3.29)$$

where $i^2 = -1$. We now denote by M_j the j^{th} element of the mass field M , and by K_j that of the Green kernel K . From equation (3.28), the elements V_m of the potential read

$$\begin{aligned} V_m &= -\mathcal{G} \sum_j \mathcal{F}[M]_j \mathcal{F}[K]_j \exp\left(2i\pi m \frac{j}{N}\right) \\ &= -\mathcal{G} \sum_j \sum_k \sum_l M_k K_l \exp\left(2i\pi \{m - k - l\} \frac{j}{N}\right) \\ &= -\mathcal{G} \sum_k \sum_l M_k K_l \underbrace{\sum_{j=0}^{N-1} \exp\left(-2i\pi \{k + l - m\} \frac{j}{N}\right)}_{S_{klm}}. \end{aligned} \quad (3.30)$$

Now have a look at the last sum S_{klm} . To calculate it, we distinguish between the two cases:

- if $k + l - m = 0$ or N , then $S_{klm} = N$,
- otherwise, $k + l - m \in \mathbb{N}$ so that $\exp(-2i\pi \{k + l - m\}/N)$ is N^{th} root of unity, which we denote by z . In this case, we are therefore left with $S_{klm} = \sum_{j=0}^{N-1} z^j = \frac{1 - z^N}{1 - z} = 0$ since $z^N = 1$.

We see that S_{klm} has a non-vanishing contribution in only two cases: $l = m - k$ if $k \leq m$, and $l = N + m - k$ otherwise. Equation (3.30) can be finally written as:

$$V_m = -N\mathcal{G} \left[\sum_{k=0}^m M_k K_{m-k} + \sum_{k=m+1}^{N-1} M_k K_{N+m-k} \right]. \quad (3.31)$$

²This definition is the one used by the FFTW library.

The expression obtained in equation (3.31) leads to a few comments. First, the presence of the N factor simply stems from the fact that the Fourier transforms calculated with equation (3.29) are not normalized (we have $\mathcal{F}^{-1} \circ \mathcal{F} = N \text{Id}$ instead of Id , with Id the identity operator). The expression in equation (3.31) therefore needs to be divided by N . In this one-dimensional example, the potential is more conveniently expressed with the linear density $\lambda = M/\Delta$. Equation (3.28) eventually translates into

$$V = -\mathcal{G}(\Delta/N) \mathcal{F}^{-1}[\mathcal{F}(\lambda) \times \mathcal{F}(K)]. \quad (3.32)$$

This example raises another issue, which is illustrated in figure 3.5. We show the particular case where the linear density is singular, for which we expect the potential to decrease as the inverse of the distance from the singularity. The linear density λ (left panel) cancels out for all x except for $x = 0.1$ where it is equal to unity. The Green kernel K (middle panel) is N -periodic and corresponds to a Plummer function with softening parameter $\varepsilon = 0.01$:

$$K_i = \begin{cases} (x_i^2 + \varepsilon^2)^{-1/2} & \text{if } i < N/2, \\ (x_{N-i}^2 + \varepsilon^2)^{-1/2} & \text{otherwise.} \end{cases}$$

The numerical potential V_N , given by equation (3.32), is calculated by the FFTW library. The analytical potential V_A for this problem is a Plummer function centered on the singularity location and smoothed over ε . Both potentials are depicted in the right panel of figure 3.5, together with (the absolute value of) their relative difference in the close-up. We see that V_A and V_N are equal to within the machine precision as far as the distance from the singularity is smaller than $N\Delta/2$ (that is, half the grid extent). Above this distance, V_N increases with x , which is a side effect of the periodicity of the Green function. We point out that such a periodicity is required to obtain the correct shape of the potential on both sides of the singularity.

This issue, which is inherent to the FFT method, is usually known as the *alias issue*. All occurs as if the linear density field interacted with all its periodic aliases in Fourier space. This feature is customarily avoided by calculating the FFTs on a grid with *twice* as many cells as in the hydrodynamic mesh, the *additional cells being left empty of mass*. Thus, the mass distribution of the hydrodynamic mesh (that of physical interest) can not tidally interact with its adjacent aliases in Fourier space (Sellwood 1987), and it remains isolated. The doubling of the cells number has to be done in each space direction, except when the problem has a natural periodicity. With a two-dimensional polar mesh for instance, the doubling is not required in the azimuthal direction. In the FARGO code, we will therefore calculate the FFTs on a grid whose radial zone number is twice that of the hydrodynamic mesh. We will now refer to this extended grid as the *fft grid*. A sketch of the alias issue in this situation is displayed and commented in figure 3.6.

Now that we have highlighted the main issues regarding the potential calculation with FFTs, let us go back to the expression of the disc potential V given by equation (3.27). We now denote by ε_{sg} the softening length of the disc potential, since ε is generally used to denote that of the planet potential. Using the polar coordinates (r, φ) , equation (3.27) reads

$$V(r, \varphi) = -\mathcal{G} \int_{r_{\min}}^{r_{\max}} \int_0^{2\pi} \frac{\sigma(r', \varphi') r' dr' d\varphi'}{\sqrt{r^2 + r'^2 - 2rr' \cos(\varphi - \varphi') + \varepsilon_{\text{sg}}^2}}, \quad (3.33)$$

where r_{\min} and r_{\max} are respectively the radii of the inner and outer edge of the fft mesh. Binney & Tremaine (1987) showed that equation (3.33) reads as a convolution product with the variables $\{u = \log(r/r_{\min}), \varphi\}$. The potential can therefore be calculated at low-computational

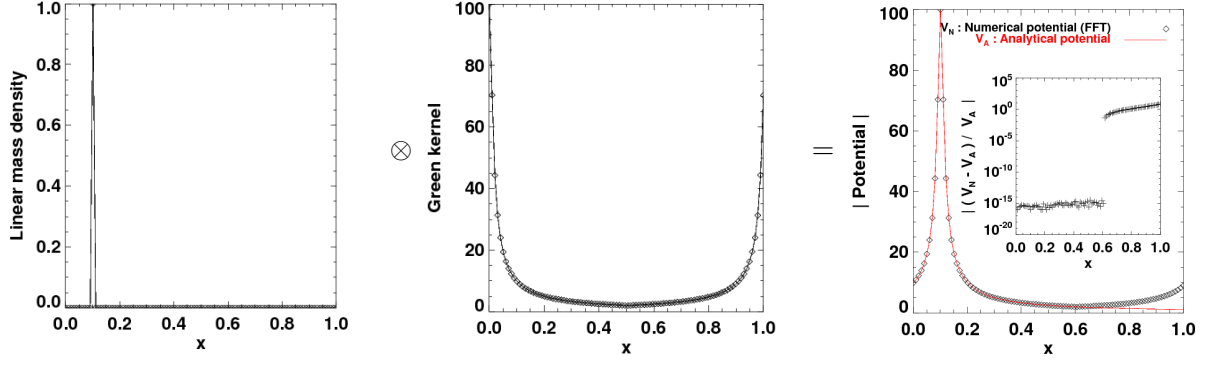


FIGURE 3.5: One-dimensional illustration of the alias issue. We assume a singular linear density (left panel). The middle panel displays the periodic Green kernel. The right panel shows the numerical potential V_N obtained with the FFTW library (diamonds) and the expected potential V_A (solid curve), both in absolute value. The close-up in the right panel shows the relative difference between V_N and V_A .

cost using FFTs, provided that a grid with a logarithmic radial spacing is used. We also point out that ε_{sg} must scale with r so that the expression of V , smoothed over the softening length ε_{sg} , writes indeed as a convolution product. We find:

$$V(u, \varphi) = -\mathcal{G} r_{\min} e^{-u/2} \int_0^{u_{\max}} \int_0^{2\pi} S(u', \varphi') K(u - u', \varphi - \varphi') du' d\varphi', \quad (3.34)$$

where S and K are defined as

$$S(u, \varphi) = \sigma(u, \varphi) e^{3u/2} \quad \text{and} \quad K(u, \varphi) = [(1 + B^2)e^u + e^{-u} - 2\cos(\varphi)]^{-1/2}. \quad (3.35)$$

In equations (3.34) and (3.35), $u_{\max} = \log(r_{\max}/r_{\min})$, and $B = \varepsilon_{\text{sg}}/r$ is uniform over the grid. Now let σ have a singular distribution (a Dirac delta function) centered on $\{u = u_d, \varphi = \varphi_d\}$. Equation (3.34) yields:

$$\begin{aligned} V(u, \varphi) &= -\mathcal{G} r_{\min} e^{-u/2} S(u_d, \varphi_d) K(0, 0) \\ &= -\mathcal{G} r_{\min} \frac{\sigma(u_d, \varphi_d)}{B} e^{(3u_d - u)/2} \propto e^{-u/2}. \end{aligned} \quad (3.36)$$

Since equation (3.36) does not depend on φ , there is no azimuthal self-acceleration at the singularity $\{u = u_d, \varphi = \varphi_d\}$, which could be anticipated from symmetry reasons. However, since the potential scales as $e^{-u/2}$, $V(u_d + \delta u, \varphi_d) \neq V(u_d - \delta u, \varphi_d)$: there is a radial self-acceleration at the singularity location, in *contradiction* with Newton's first law. This is a bad point for this technique. And there is no simple way to cancel out the self-acceleration by adding a corrective term to equation (3.34).

We therefore propose an alternative technique based on the direct calculation of the self-gravitating accelerations g_r and g_φ . Akin to the potential, these accelerations read as convolution products (provided that $\varepsilon_{\text{sg}} \propto r$) and can be calculated with Fourier transforms. After some algebra, we find that

$$\begin{aligned} g_r(u, \varphi) &= -\mathcal{G} e^{-u/2} \int_0^{u_{\max}} \int_0^{2\pi} S_r(u', \varphi') K_r(u - u', \varphi - \varphi') du' d\varphi' \\ &\quad + \mathcal{G} \sigma(u, \varphi) \Delta u \Delta \varphi / B, \end{aligned} \quad (3.37)$$

where Δu and $\Delta \varphi$ are the mesh sizes, and S_r and K_r are given by

$$S_r(u, \varphi) = \sigma(u, \varphi) e^{u/2} \quad \text{and} \quad K_r(u, \varphi) = \frac{1 + B^2 - e^{-u} \cos(\varphi)}{\{2(\cosh(u) - \cos(\varphi)) + B^2 e^u\}^{3/2}}. \quad (3.38)$$

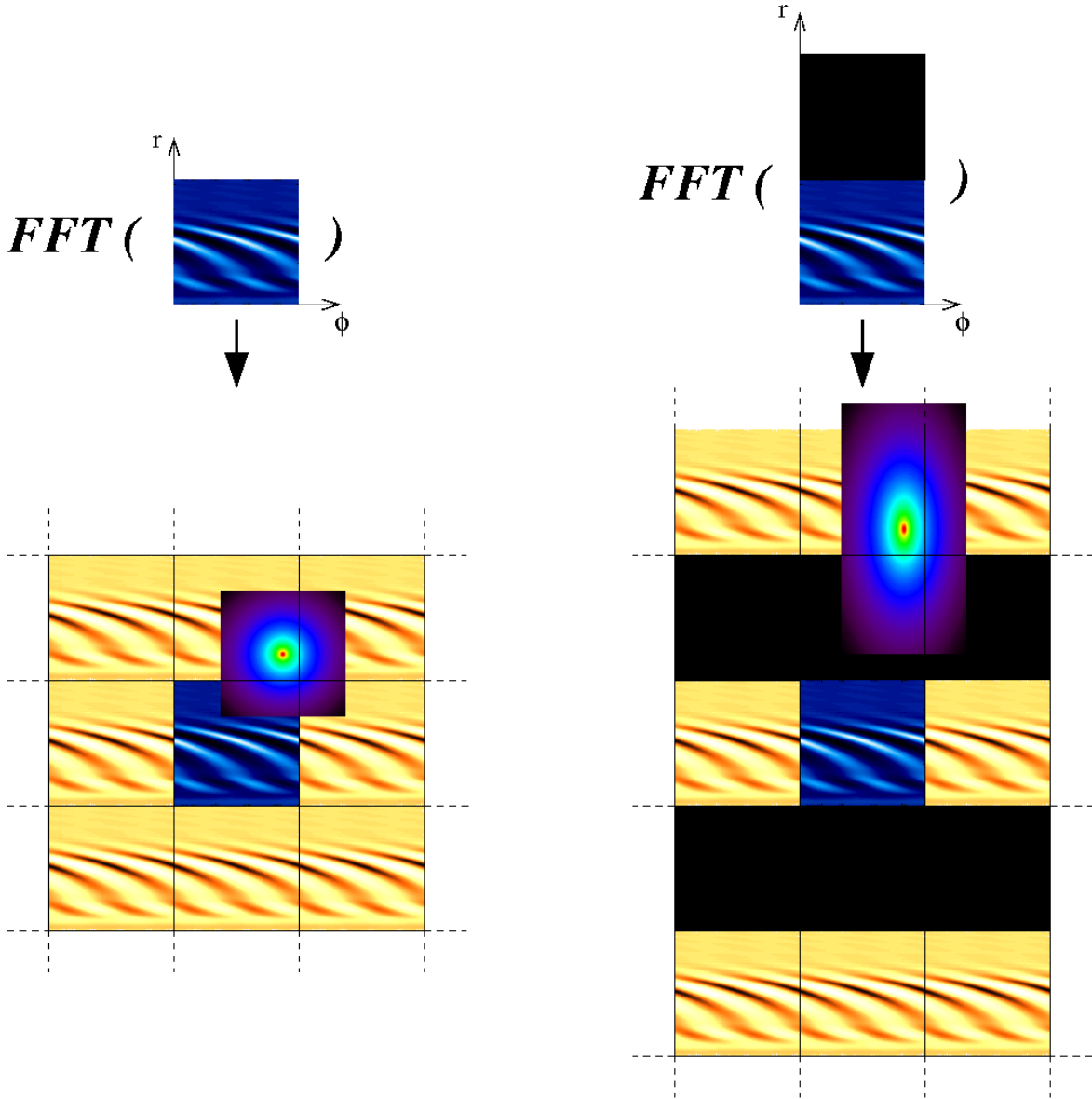


FIGURE 3.6: Sketch of the alias issue with a two-dimensional polar mesh. Suppose first that we calculate the Fourier transform of the surface density field without mesh doubling (top-left side of the panel). In the bottom-left side are depicted the density field and the closest of its periodic aliases in Fourier space. Any mass in these aliases may interact with the original density field, provided that its zone of gravitational influence (the extent of the Green kernel centered on the mass location) intersects the original field. We show here the case of a zone belonging to an alias in the radial direction and interacting with the original field. To remove the spurious interaction of the density field with its aliases in the radial direction (that in the azimuthal direction is expected because of the 2π -periodicity), the FFT calculation is done on the *fft* grid, which has a radial zone number twice that of the hydrodynamic grid, the additional cells being left empty of mass (top-right side). As shown in the bottom-right side, the aliases in the radial direction can only intersect the part of the density field where the mass cancels out. The potential calculation here will therefore be erroneous, but this has no impact on the original density field since this zone is massless. Since the aliases in the radial direction do not intersect anymore the original density field, the potential calculation here will not suffer from the alias issue.

The second term on the right-hand side of equation (3.37) is a corrective term required to remove radial self-forces, as $K_r(0, 0) = 1/B \neq 0$. Similarly, $g_\varphi(u, \varphi)$ reads

$$g_\varphi(u, \varphi) = -\mathcal{G} e^{-3u/2} \int_0^{u_{\max}} \int_0^{2\pi} S_\varphi(u', \varphi') K_\varphi(u - u', \varphi - \varphi') du' d\varphi', \quad (3.39)$$

with S_φ and K_φ given by

$$S_\varphi(u, \varphi) = \sigma(u, \varphi) e^{3u/2} \quad \text{and} \quad K_\varphi(u, \varphi) = \frac{\sin(\varphi)}{\{2(\cosh(u) - \cos(\varphi)) + B^2 e^u\}^{3/2}}. \quad (3.40)$$

Note that $K_\varphi(0, 0) = 0$ so that there is no azimuthal self-acceleration. Thus, due to the simple corrective term added in g_r expression, our self-gravitating accelerations eventually satisfy Newton's first law. This makes our method interesting, notwithstanding the need to perform twice as many FFTs calculations as if we calculated the potential.

We end up this section with a particular case. In chapter 4, we will often refer to the case where only the axisymmetric component of the disc self-gravity is accounted for, thereby involving the axisymmetric component of the disc surface density $\bar{\Sigma}(u) = (2\pi)^{-1} \int_0^{2\pi} \Sigma(u, \varphi) d\varphi$. In this case, g_φ cancels out and

$$g_r(u) = -\mathcal{G} e^{-u/2} \int_0^{u_{\max}} \bar{S}_r(u') \widetilde{K}_r(u - u') du' + \mathcal{G} \bar{\Sigma}(u) \Delta u \widetilde{K}_r(0), \quad (3.41)$$

where $\bar{S}_r(u) = (2\pi)^{-1} \int_0^{2\pi} S_r(u, \varphi) d\varphi$ and $\widetilde{K}_r(u) = \int_0^{2\pi} K_r(u, \varphi) d\varphi$.

3.2.2 Implementation in the FARGO code

In previous section, we described in details how to solve Poisson equation with FFTs on a two-dimensional polar mesh. We primarily dealt with the difficulties stemming from the FFTs calculation (normalization factors, alias issue, correction for the self-forces). We now focus on how our self-gravity module impacts the FARGO code. Among the different steps of the code's diagram structure (section 3.1), the self-gravity affects the initialization and the gas update processes.

- (a) **Initialization:** if the disc is self-gravitating, the radial self-gravitating acceleration g_r must be included in the initial centrifugal balance with the gravity of the central and the pressure force. This changes equation (3.4) into:

$$v_\varphi(r) = r \left(\Omega_K^2(r) [1 - (1 + \sigma - 2f) h^2(r)] - \frac{g_r(r)}{r} \right)^{1/2}. \quad (3.42)$$

- (b) **Gas update:** the gas self-gravity acts as an acceleration source term in the gas update process. To compute the self-gravitating accelerations g_r and g_φ , the following steps are performed:

- Calculation of K_r and K_φ on the FFT grid, whose dimension is $2N_r \times N_\varphi$. The only difficulty is to pay attention to the radial periodicity of these kernels. Their discretized expression is given by equations (3.38)b and (3.40)b, with $u_{i \in [0, N_r-1]} = \log(r_i/r_0)$ and $u_{i \in [N_r, 2N_r-1]} = -\log(r_{2N_r-i}/r_0)$. The typical shape of K_r and K_φ on the FFT grid is displayed in figure 3.7. Once both kernels are calculated, we evaluate their FFTs. Since the kernels do not evolve with time, this step is done once at the beginning of the simulation.

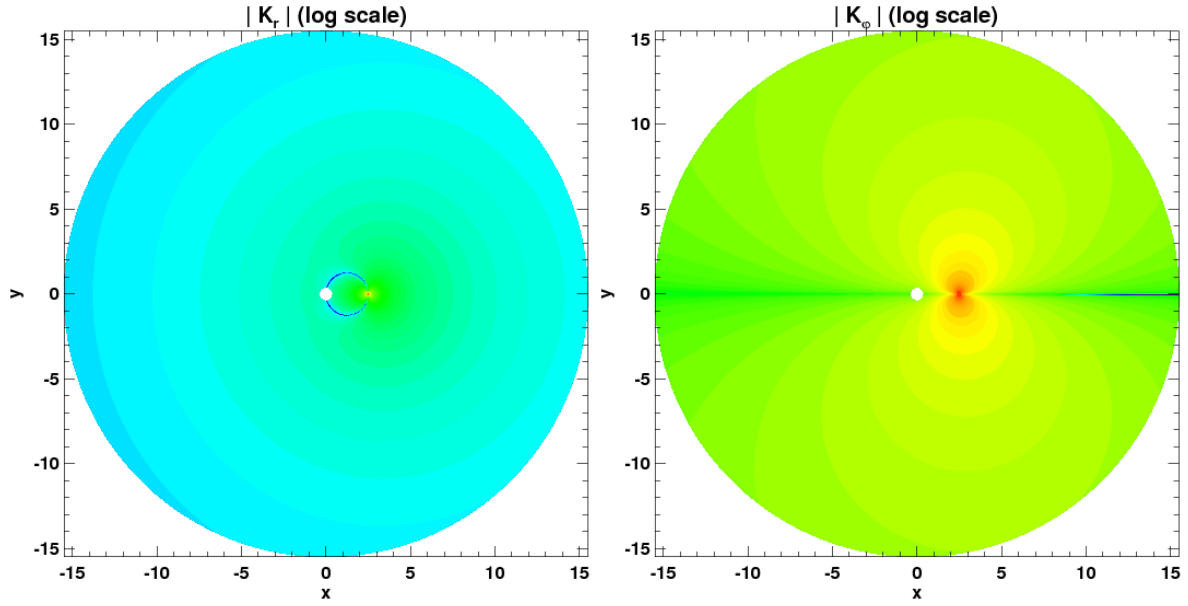


FIGURE 3.7: We display the typical shape of the radial and azimuthal kernels K_r and K_φ (their absolute value actually, with a logarithmic scale), in the cartesian framework. To improve legibility, both kernels have been shifted in the radial and azimuthal directions so that their maximum be located at $(i = N_r, j = N_\varphi/2)$. Note the axial [anti-]symmetry with respect to the $y = 0$ axis, as can be inferred from equations (3.38)b [(3.40)b]. In the left panel, the dark blue curve shows the locations where K_r vanishes. It corresponds to the points M where the radial acceleration g_r would cancel out if a point-like mass was applied. It is therefore a circle whose diameter is the distance between the frame origin O and the maximum K of $|K_r|$ (K is located at $x = 2.5, y = 0$). The points M belonging to this circle are indeed the only ones such that the triangle OMK is rectangular in M .

- Calculation of S_r and S_φ on the FFT grid. Their discretized expression is given by equations (3.38)a and (3.40)a for $i \in [0, N_r - 1]$, while they are filled with zeros beyond. Because the surface density field evolves at each timestep, we calculate S_r , S_φ and their FFTs at each timestep.
- Calculation of g_r and g_φ on the FFT grid:

$$g_r(u, \varphi) = -\mathcal{G} e^{-u/2} \frac{\Delta u \Delta \varphi}{2N_r N_\varphi} \mathcal{F}^{-1} [\mathcal{F}[S_r] \times \mathcal{F}[K_r]](u, \varphi) + \mathcal{G} \sigma(u, \varphi) \Delta u \Delta \varphi / B, \quad (3.43)$$

and

$$g_\varphi(u, \varphi) = -\mathcal{G} e^{-3u/2} \frac{\Delta u \Delta \varphi}{2N_r N_\varphi} \mathcal{F}^{-1} [\mathcal{F}[S_\varphi] \times \mathcal{F}[K_\varphi]](u, \varphi). \quad (3.44)$$

There remains a last step before updating the velocities. The quantities g_r and g_φ are centered-in-cells. We therefore need to calculate them at the cells interfaces to update the gas velocities. This is done with a bilinear interpolation. The gas self-gravity has eventually a second and last impact on the gas update process: the set of boundary conditions. As explained in section 3.1.4, the gas azimuthal velocity at the mesh edges matches the initial equilibrium profile. The profile to consider is now given by equation (3.42) instead of equation (3.4).

3.2.3 Test problems

We present hereafter some of the test problems we performed to validate the self-gravity solver.

(a) *Newton laws:*

We first tested our self-gravity solver against Newton laws. Assuming the mass distribution reduces to a unique, isolated particle, Newton's first law says that no force acts on this particle. To check this, we took a surface density distribution vanishing everywhere except at a given cell. We verified that the expressions of g_r and g_φ , given by equations (3.43) and (3.44), cancel out, to within the machine precision, at the center of this cell. Note that this test is valid only at the initial stage of the disc, otherwise the density distribution changes under the disc hydrodynamic evolution. In addition, Newton's third law, also known as the law of reciprocal actions, means that the accelerations felt by two isolated particles have same amplitude, but opposite signs. We checked that our algorithm does not satisfy Newton's third law, as the self-gravitating softening length ε_{sg} varies from one ring to another. We will discuss in details the consequences on this in section 4.2. We now provide two test problems that allow a direct comparison of our calculations with analytics.

(b) *Case of a uniform surface density field:*

The radial self-gravitating acceleration of a disc of uniform surface density Σ reads

$$g_r(r) = 4\mathcal{G} \Sigma \left[\frac{E(v_{\text{max}}) - K(v_{\text{max}})}{v_{\text{max}}} + K(u_{\text{min}}) - E(u_{\text{min}}) \right], \quad (3.45)$$

where K and E denote the complete elliptic integrals of the first and second kinds, respectively, where $u_{\text{min}} = r_{\text{min}}/r$ and $v_{\text{max}} = r/r_{\text{max}}$, r_{min} (r_{max}) denoting the disc inner (outer) radius (Pierens & Huré 2005). We performed a self-gravitating calculation with $\Sigma = 2 \times 10^{-3}$, $r_{\text{min}} = 0.4$ and $r_{\text{max}} = 2.5$. The radial zone number is $N_r = 512$, and we took a very small softening length ($\varepsilon_{\text{sg}}(r = 1)$ is 100 times smaller than the grid radial spacing at the same location). The left-hand panel of figure 3.8 shows the excellent agreement between the result

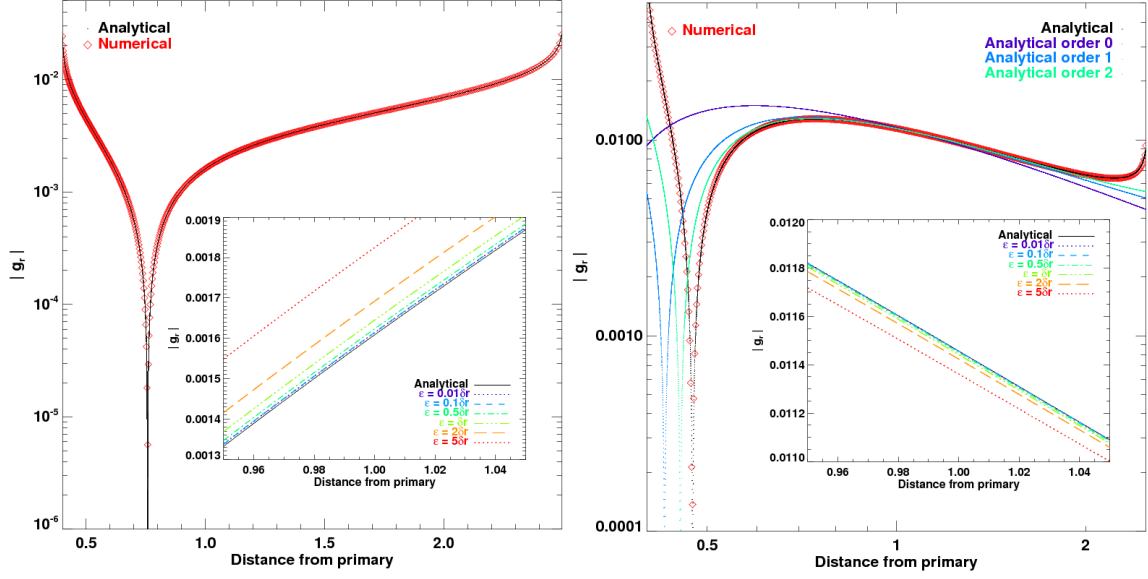


FIGURE 3.8: Left: radial self-gravitating acceleration $g_r(r)$, in absolute value, for a uniform surface density field. The analytical expression of g_r , given by equation (3.45), is compared with the result of a self-gravitating calculation with a small softening length (see text). We point out that $g_r(r)$ is positive at the inner edge, then it becomes negative (here from $r \gtrsim 0.75$). The close-up reveals the influence of the softening length on the agreement between the numerical calculation and the analytical expectation. Right: same study as in the left panel, except the surface density profile decreases as $r^{-3/2}$. We compare the result of a numerical calculation with the analytic series expansion of equation (3.46), for different truncature orders: $N = 0, 1, 2$ and 100. The reference analytical result is that obtained with $N = 100$.

of our calculation and the analytical expression of equation (3.45). The close-up displays g_r around $r = 1$, for different softening length to mesh resolution ratios, $\epsilon/\delta r$, at $r = 1$. This shows the good convergence of our numerical calculation toward the analytical expectation when the softening length tends to zero.

(c) *Case of an axisymmetric surface density field decreasing as $r^{-3/2}$:*

This test is also of interest as we will mainly use this surface density profile in chapter 4. Nonetheless, this problem has no exact tractable solution, except an integral form whose integrand is logarithmically singular everywhere inside the disc (Huré et al. 2008). These authors derived an exact expression for the disc potential of any flat disc having a power-law surface density profile $\Sigma(r) \propto r^s$. This expression reads as an infinite series that converges very rapidly. From their potential expression, the self-gravitating acceleration writes $g_r(r) = \lim_{N \rightarrow \infty} g_r^{(N)}(r)$, with:

$$g_r^{(N)}(r) = -\frac{\Psi_x}{r_{\max}} \left[A_s (1+s) \varpi^s + \sum_{k=0}^N \left(2k a_k \varpi^{2k-1} - (2k+1) b_k \varpi^{-2(k+1)} \right) \right], \quad (3.46)$$

where the series a_n and b_n are defined as

$$a_n = \frac{\gamma_n}{2n-s-1} \quad \text{and} \quad b_n = \frac{\gamma_n}{2n+s+2} \left(\frac{r_{\min}}{r_{\max}} \right)^{2n+s+2}, \quad \text{with} \quad \gamma_n = \begin{cases} 1 & \text{if } n = 0 \\ \gamma_{n-1} \left(\frac{2n-1}{2n} \right)^2 & \text{if } n \geq 1 \end{cases}.$$

In equation (3.46), $\Psi_x = 2\pi\mathcal{G}\Sigma(r_{\max})r_{\max}$, $\varpi = r/r_{\max}$, and A_s is a numerical coefficient calculated by Huré et al. (2008). We performed the same calculation as for previous test problem, this time with a surface density profile decreasing as $r^{-3/2}$. We compare in the right panel of

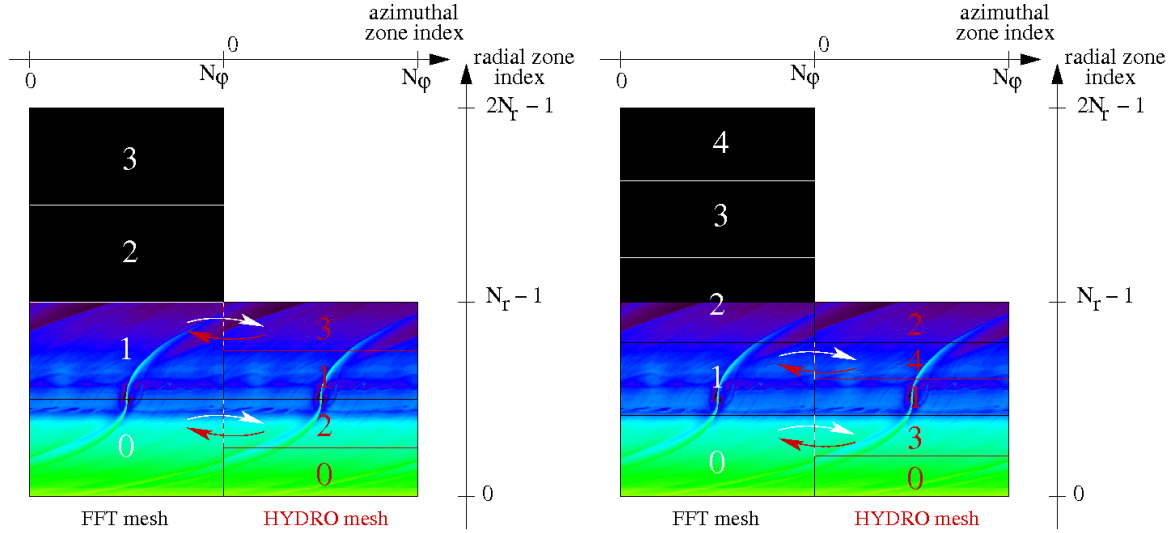


FIGURE 3.9: Domain decompositions of the *fft* and hydrodynamic meshes, for an even and an odd number of CPUs (left and right panels respectively). The domain decomposition of the hydrodynamic mesh is adjusted from that of the *fft* grid so as to minimize the amount of communications between both grids (red and white arrows). Note that the CPU numbers are ordered within the *fft* mesh. We display in the background the surface density field on the *fft* grid (hence the massless black cells for radial indexes greater than N_r , to avoid the interaction with aliases in Fourier space, as explained in section 3.2.1).

figure 3.8 the result of a numerical calculation with the analytical expansion given by equation (3.46) with $s = -3/2$ (for which $A_s \approx -4.38$), for $N = 0, 1, 2$ and 100 (which we will refer to as *the* analytical solution). Similarly as for $s = 0$, our numerical calculation is in excellent agreement with the analytical solution. The close-up displays again our numerical results for different softening length to mesh resolution ratios around $r = 1$ (which would correspond to the planet's location if any), indicating a convincing convergence toward the analytical expression. We end up by stressing that the series expansion of equation (3.46) is a rapidly convergent series, far from the disc edges. Even the second order of the expansion yields a reliable approximation for g_r in the major part of the disc. This is a strong point for this method, apart from the simplicity of its implementation.

3.2.4 Domain decomposition

As explained in sections 3.2.1 and 3.2.2, FFTs are calculated on the *fft* grid, which has twice as many cells in the radial direction as the hydrodynamic mesh, where the surface density field is defined. The FFTs calculation is parallelized with MPI. The 2.1.5 MPI-compatible version of the FFTW library gives the possibility to parallelize the FFTs calculation in one direction. We thus chose to parallelize along the radial direction, similarly as the FARGO code parallelizes the hydrodynamic equations (see figure 3.2). However, since the *fft* and the hydrodynamic meshes do not have the same radial zone number, a domain decomposition must be defined for each grid. Unfortunately, the domain decomposition can not be imposed to the *fft* mesh. It is automatically adjusted during the initialization of the FFTs calculation. Given the domain decomposition of the *fft* grid, we had to alter the standard domain decomposition of the hydrodynamic mesh so as to minimize the amount of communications between both grids. An illustration of this is given in figure 3.9. These communications are two-fold:

- Before the FFTs calculations, the CPUs exchange their local information of the surface density field in order to calculate S_r and S_ϕ on the *fft* grid (red arrows in figure 3.9). In

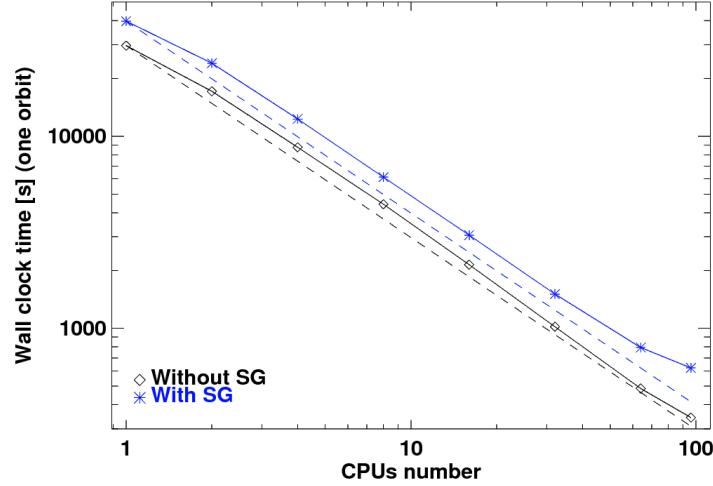


FIGURE 3.10: *Benchmark tests: we display the Wall clock time (in seconds) to perform one planet orbit for a simulation including the disc self-gravity (stars) or not (diamonds), as a function of the CPUs number. If the running time scaled with the inverse of the processors numbers, our results would match the long-dashed lines. The departure from the scaling behavior beyond ~ 96 processors with self-gravity suggests the running time be limited by the communications needed for the FFTs calculation.*

the example shown in the left panel of figure 3.9, CPU 3 communicates its surface density to CPU 1, and CPU 2 to CPU 0. In the fft mesh, only CPUs 0 and 1 eventually represent the surface density of the hydrodynamic mesh; the buffered surface densities of CPUs 2 and 3 are filled with zeros to avoid the alias issue (hence the black boxes in the figure).

- Once the calculations of the accelerations g_r and g_φ are performed on the fft mesh, they need to be transported back to the hydrodynamic mesh (white arrows: here, CPU 1 communicates back its accelerations to CPU 3, and CPU 0 to CPU2), where the components of the gas velocity will then be updated.

All these communications, in addition to those required for the FFTs calculation itself, may significantly slow down self-gravitating hydrodynamic calculations. To investigate this, we performed numerical simulations without and with self-gravity, varying the number of CPUs from 1 to 96. These calculations include a low-mass planet (the planet to primary mass ratio is $q = 5 \times 10^{-6}$) and the disc parameters that will be described in section 4.3. For these tests only, the grid has 2048 cells both in the radial and in the azimuthal directions. Calculations were performed on a cluster of quadriprocessor nodes having a frequency of 2.6 GHz, and with an Infiniband network. We display in figure 3.10 the Wall clock time (in seconds) required to perform one planet orbit, the disc being either self-gravitating (stars) or not (diamonds). In each case, the long-dashed curves represent the calculation time over one processor, divided by the number of processors. Without or with self-gravity, the FARGO code has a *good scaling*, which means that the calculation time approximately scales with the inverse of the number of CPUs. Only from 96 processors do the self-gravitating runs show a significant departure from the scaling behavior. With a smaller number of processors, the computational cost of a hydrodynamic simulation is increased typically by a 40 % factor when the disc self-gravity is taken into account. We mention that the (good) scaling behavior with self-gravity is very sensitive to the network performances. Preliminary tests involving a similar cluster but having a Gigabit network revealed a significant departure from the scaling behavior from only 8 processors!

3.3 Implementation of an energy equation

3.3.1 Thermodynamic background

Before coming to the energy equation implemented in the code, we mention all the thermodynamic quantities we shall use in the following. Recall that we have five variables in the code: the two components v_r and v_φ of the velocity field, the surface density Σ , the pressure p and the temperature T . The Navier-Stokes and continuity equations provide three equations. As customarily assumed, we use an ideal gas law to connect p with Σ and T ,

$$p = \mathcal{R}\Sigma T, \quad (3.47)$$

where \mathcal{R} is a constant, equal to the universal gas constant divided by the mean molecular mass ($\mathcal{R} = 1$ is the code units). And hitherto, the temperature profile is taken stationary to simply close the hydrodynamic set of equations. We now wish to get rid of this last assumption, and rather consider the temporal evolution of the temperature through an energy equation. We will however proceed with all other assumptions, including the ideal gas law.

For an ideal gas, the specific thermal energy u (thermal energy per unit mass) is a function of temperature alone, $u = u(T)$. To good approximation, u scales with the temperature,

$$u = c_v T, \quad (3.48)$$

so the specific heat at constant volume, $c_v = (\partial U / \partial T)_V$, is constant. In the same vein, the specific enthalpy $h = u + p/\Sigma$ is approximately proportional to T , with the specific heat at constant pressure, c_p , as the constant scaling factor. Ideal gases for which u and h scale with T , and for which c_v and c_p are therefore constant, are called *polytropic* gases. For polytropic gases, the equation of state depends only on the ratio γ of the specific heats, $\gamma = c_p/c_v$. This ratio is also called the adiabatic index. Since protoplanetary discs are primarily composed of H_2 molecules, we will take $\gamma = 7/5 = 1.4$ (principle of equipartition of energy). In addition, from equation (3.47), c_v and c_p are connected with the so-called Mayer formula, $c_p - c_v = \mathcal{R}$. This yields $c_v = \mathcal{R}/(\gamma - 1)$, and equation (3.48) reads $\Sigma u = p/(\gamma - 1)$. From now on, we will work with the *thermal energy per unit area*, $e = u\Sigma$ ($[e] = M.T^{-2}$), which is thus connected to the gas pressure by

$$p = (\gamma - 1)e. \quad (3.49)$$

The adiabatic index γ appears as a measure of how a change in the thermal energy affects the gas pressure, and, given the surface density, the gas temperature.

Another key quantity we will largely refer to is the gas *specific entropy* s (entropy per unit mass). It is defined up to an additive constant s_0 as:

$$s = s_0 + c_v \log(p/\Sigma^\gamma), \quad (3.50)$$

which can be inverted to give

$$p = e^{(s-s_0)/c_v} \Sigma^\gamma. \quad (3.51)$$

For an *adiabatic* evolution, and in absence of any irreversible processes in the gas, such as thermal diffusivity, viscosity or shocks, the specific entropy remains constant along particle paths: $Ds/Dt = 0$. Assuming a polytropic gas, equation (3.51) becomes $p = \kappa(s)\Sigma^\gamma$, where $\kappa(s)$ varies from one element path to another. Setting the hydrodynamic variables as Σ, \mathbf{v} and s provides a configuration of interest where the equation of state gives p as a function of Σ and s alone. In this form, the partial derivative of p with Σ , holding s constant, defines the square of the local sound speed in the gas. For a polytropic gas, we find

$$c_s^2 = \left(\frac{\partial p}{\partial \Sigma} \right)_s = \frac{\gamma p}{\Sigma},$$

and

$$c_s = \sqrt{\gamma \mathcal{R} T}. \quad (3.52)$$

A particular case of interest is that of a polytropic gas for which s is constant everywhere. This can be achieved if the gas undergoes an adiabatic evolution with a uniform initial entropy. Thus, $p = \kappa \Sigma^\gamma$, with κ constant everywhere. As p is a function of Σ alone, the energy equation becomes redundant and the set of hydrodynamic equations reduces to the conservations of mass and momentum. This situation corresponds to what is logically called an *isentropic* flow. Note that an isentropic flow is a particular case of *barotropic* flows, for which the pressure is a function of the density alone. In the literature, an isentropic flow is also referred to as a *homotropic* flow. In the limit $\gamma \rightarrow 1$, an isentropic flow corresponds to an *isothermal* flow.

3.3.2 Heat transport equation

The general equation for heat transport can be derived from the conservations of mass, momentum and total energy. See for instance [Landau & Lifchitz \(1999\)](#) (paragraph 49) for a complete description. The equation formally reads

$$\Sigma T \frac{Ds}{Dt} = \text{div}(\chi \mathbf{grad}(T)) + \sigma_{i,k} \frac{\partial v_i}{\partial x_k}, \quad (3.53)$$

where χ is the thermal conductivity, and $\sigma_{i,k}$ are the components of the viscous stress tensor. In the left-hand side of equation (3.53), $\Sigma T Ds/Dt$ corresponds to the heat quantity received by the gas per unit of area and time. This *heat flux* has two contributions: the heat brought by thermal diffusion (first term on the right-hand side), and the heat dissipated by the viscosity (second term). Interestingly, combining equations (3.49), (3.50) and the continuity equation, we find

$$\Sigma T \frac{Ds}{Dt} = \frac{\partial e}{\partial t} + \text{div}(e\mathbf{v}) + (\gamma - 1)e \text{div}(\mathbf{v}).$$

The heat transport equation naturally provides an equation for e , which takes the form

$$\frac{\partial e}{\partial t} + \text{div}(e\mathbf{v}) = -(\gamma - 1)e \text{div}(\mathbf{v}) + \text{div}(\chi \mathbf{grad}(T)) + Q_+, \quad (3.54)$$

where $Q_+ = \sigma_{i,k} \partial v_i / \partial x_k$ denotes the viscous heat flux. With a two-dimensional polar mesh, and neglecting the contribution of the bulk viscosity, Q_+ is given by (see e.g. [D'Angelo et al. \(2003a\)](#) and references therein):

$$Q_+ = \frac{1}{2\nu\Sigma} [\tau_{r,r}^2 + \tau_{r,\varphi}^2 + \tau_{\varphi,\varphi}^2] + \frac{2\nu\Sigma}{9} \text{div}^2(\mathbf{v}), \quad (3.55)$$

where $\tau_{r,r}$, $\tau_{r,\varphi}$, $\tau_{\varphi,\varphi}$ and $\text{div}(\mathbf{v})$ are given by equations (3.17) and (3.18). In the particular case of a Keplerian disc ($v_r = 0$, $v_\varphi = r\Omega_K$), the viscous heat flux reduces to $Q_+ = \tau_{r,\varphi}^2 / 2\nu\Sigma = 9/8 \nu\Sigma\Omega_K^2$.

Equation (3.54) leads to a few remarks. This equation reads as a conservative equation with source terms on the right-hand side, as does for instance the equation of momentum conservation. The first source term represents the variation of thermal energy due to the work of pressure forces. The second term is the thermal diffusion flux. When we include thermal diffusion, we will assume a constant *conductivity* χ , proportional to the surface density, so $\text{div}(\chi \mathbf{grad}(T))$ writes $\lambda\Sigma \Delta(e/\Sigma)$, with λ the thermal *diffusivity* (note that $[\lambda] = \text{L}^2 \cdot \text{T}^{-1}$). An important point is that, like the viscous heating flux Q_+ , the thermal diffusion flux conspires to *increase the entropy of the whole disc* ([Landau & Lifchitz 1999](#)). A calculation including either viscosity or

thermal diffusion alone will therefore increase the entropy and the temperature profiles of the disc, without achieving a stationary state. This is why we will add an extra cooling source term, Q_- , in the right-hand side of equation (3.54) (this term is assumed to be positive). We will discuss later on the expression of Q_- . The energy equation we implemented in the FARGO code eventually takes the form

$$\boxed{\frac{\partial e}{\partial t} + \text{div}(e\mathbf{v}) = -(\gamma - 1)e \text{div}(\mathbf{v}) + \lambda \Sigma \Delta \left(\frac{e}{\Sigma} \right) + Q_+ - Q_-}. \quad (3.56)$$

3.3.3 Contact discontinuities

The aim of this section is to provide some insight on the numerical implementation of the energy equation. At this stage, the reader may wonder indeed why we implement an equation for the thermal energy e , and not for the temperature T or for the specific entropy s . The answer to this question involves the numerical handling of the so-called *contact discontinuities*, which are non-linear waves across which the density is discontinuous, whereas the pressure and the velocity remain continuous. We introduce them in the appendix section 3.4, where we describe the wave propagation properties in an adiabatic one-dimensional gas. As we shall see in next chapters, contact discontinuities will play a key role on the migration of low-mass planets in adiabatic discs.

Let us have an eye on the numerical handling of contact discontinuities. As in section 3.4, we consider an adiabatic, isolated one-dimensional gas. We assume uniform velocity and pressure fields, along with a discontinuous density (imagine for instance that the gas density has a step profile). The continuity equation then writes $\partial_t \rho + u \partial_x \rho = 0$. Using a first-order upwind scheme for the spatial derivative, this equation is discretized as³ $\rho_i^{n+1} = \rho_i^n (1 - C_0) + C_0 \rho_{i-1}^n$, where $C_0 = u_i^n / (dx/dt)$, dt is the timestep and dx is the cell size, taken uniform. The quantity C_0 is the CFL number we introduced in equation (3.12). It can be regarded as the ratio of two speeds, namely the local flow velocity u , and the grid speed dx/dt defined by the mesh discretization. Now assume our energy equation takes the form $Ds/Dt = 0$ (this is equation (3.53) with previous assumptions, namely the gas adiabaticity and the absence of shocks). Its discretization similarly leads to $s_i^{n+1} = s_i^n (1 - C_0) + C_0 s_{i-1}^n$. A first-order expansion thus yields

$$p_i^{n+1} \approx p_i^n \left(1 + C_0 \frac{s_{i-1}^n - s_i^n}{s_i^n} \right) \left(1 + \gamma C_0 \frac{\rho_{i-1}^n - \rho_i^n}{\rho_i^n} \right) \neq p_i^n.$$

The discretization of the entropy conservation equation inevitably leads to a small jump in the pressure field at the location of the contact discontinuity. This pressure jump entails a velocity jump from the momentum equation, which gives in turn a jump of the density from the continuity equation, and so on. This scheme might become unstable. This is precisely the reason why our energy equation does not take the form of an entropy equation. Similarly, it can be shown that an equation on the temperature is not appropriate to correctly handle contact discontinuities. The natural outcome is to consider an equation for the thermal energy e . In our example, since e and u are initially uniform, this equation restricts to $\partial_t e = 0$, which ensures that the pressure remains continuous at the location of the contact discontinuity. To our knowledge, only one non-conservative code works out an entropy equation, the **PENCIL code** (<http://www.nordita.org/software/pencil-code>). The particularity of this code is the use of very high-order finite differences (6 in space, 3 in time). Presumably this suffices to prevent from any instabilities when handling an entropy equation.

³The quantities ρ_i^n and ρ_i^{n+1} respectively denote the density in the i^{th} cell at time t and $t + dt$.

3.3.4 Implementation in the FARGO code

We now review the major modifications impacted in the code by our energy equation. The steps of the code's diagram structure (section 3.1) altered by the energy equation are the initialization and the gas update processes. Since boundary conditions caused us particular trouble, we dedicate a special paragraph on this topic.

- (a) **Initialization:** We initialize the profile $e(r)$ of the thermal energy⁴ such that the initial profiles of the surface density and of the temperature be identical with or without energy equation (they are given by equation (3.2)). Note that the initial azimuthal velocity is therefore the same in both cases. Using equations (3.47) and (3.49), we have

$$e(r) = e(r_p) \left(\frac{r}{r_p} \right)^{-1-\sigma+2f} \quad \text{with} \quad e(r_p) = \frac{\mathcal{R}}{\gamma-1} \Sigma(r_p) T(r_p). \quad (3.57)$$

- (b) **Gas update:** Like the Navier-Stokes equations, our energy equation is solved in two steps. First, e is updated with the source terms of equation (3.56). We comment that an additional source term has to be taken into account, namely the heat flux arising from the artificial viscosity. This heat flux Q_{art} reads (Stone & Norman 1992)

$$Q_{\text{art}} = -q_r \frac{\partial v_r}{\partial r} - q_\varphi \frac{1}{r} \frac{\partial v_\varphi}{\partial \varphi},$$

with q_r and q_φ given by equation (3.19). Then, e is updated with the transport step. The constrained transport technique is used again, e being updated with the flux of e/Σ through equations (3.23) and (3.24).

- (c) **Boundary conditions:** Oddly enough, boundary conditions caused us lingering trouble. We first used the non-reflective boundary condition described in section 3.1.4. Concerning the thermal energy, we used the same prescription as for the surface density. We show in figure 3.11 the result of a calculation with our energy equation in the adiabatic limit (equation (3.56) with $Q_- = Q_+ = \lambda = 0$). The relative perturbation of the gas pressure due to a low-mass planet is depicted. The left panel displays our results with the non-reflective boundary condition. The color scale has been adjusted to saturate the planet wake and thus to underline the additional pressure perturbations propagating in the disc. They correspond to the wake excited by a vortex growing up at the disc inner edge (the vortex is located at $r \sim 0.4r_p$, $\varphi - \varphi_p \sim 0.4$ on the left panel). In the frame corotating with the planet, the vortex moves along the inner edge, towards increasing azimuths. This is why periodic replications of the vortex wake can be seen. We observed that vortices grew up exponentially only at the disc inner edge, and only when the unperturbed entropy profile has a *negative gradient*. In the latter case, we observe that this process disappears if the compression/dilatation source term $-(\gamma-1)e \operatorname{div}(\mathbf{v})$ is removed from the energy equation. However unphysical this removal might be, it indicates that a positive retroaction between the velocity divergence and the internal energy may be at work at the inner edge, which is somewhat analogous to the instability cycle described by Klahr (2004) in the context of the global baroclinic instability.

These observations might suggest a physical instability. However, we checked that the production of vortices always occurred at the disc inner edge, even when we varied the location of the latter. This is a strong evidence that the effect reported above is in fact a numerical artefact. To avoid this, calculations including the energy equation will therefore

⁴We shall now call e the thermal energy and skip the implicit mention “per unit area”.

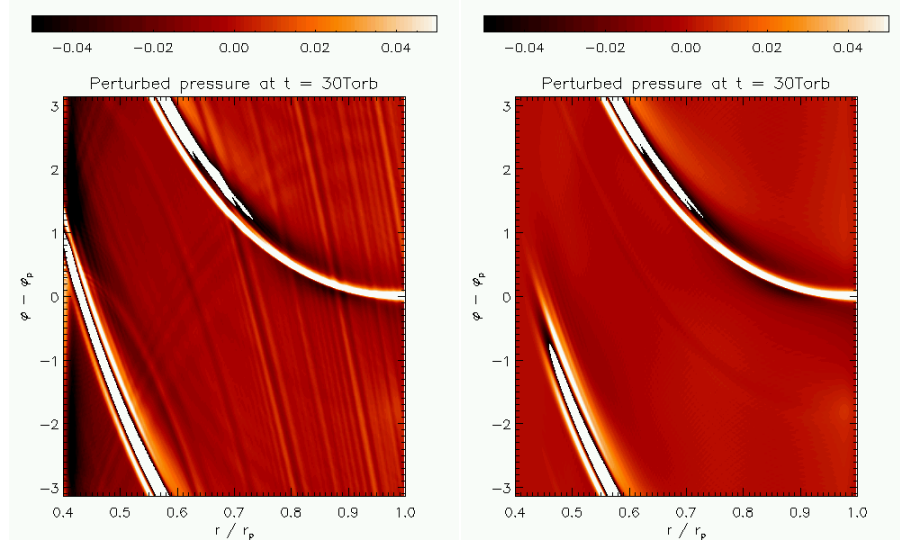


FIGURE 3.11: Disc response to an embedded low-mass planet (the latter is located at $r = r_p, \varphi = \varphi_p$). We display the relative perturbation of the gas pressure obtained with the energy equation in the adiabatic limit, with two different boundary conditions. With a non-reflective boundary (left panel), one or several vortices may grow up exponentially at the inner edge, provided that the unperturbed entropy profile decreases with r . The vortex, located here at $r \sim 0.4r_p, \varphi - \varphi_p \sim 0.4$, induces a wake that propagates in the disc. To remove vortices, which perturb the disc response to the protoplanet, we implemented a wake-killing zone (right panel). The color scale has been adjusted in both panel so as to highlight the propagation of the vortex wake in the left panel.

use another boundary condition, based on wave-killing zones at the disc edges (de Val-Borro et al. 2006). As shown in the right-hand panel of figure 3.11, this boundary condition is particularly efficient at removing any non-axisymmetric perturbations (including the planet wake).

3.3.5 Test problems

We present in this section several test problems. The first one, the shock-tube test, checks the advective transport step. Next tests are dedicated to the source terms part of the energy equation.

(a) The shock-tube problem:

Let us consider two *stationary* gases that are separated by a membrane. The shock-tube problem studies the time evolution of the whole system after the membrane is removed at $t = 0$. It is a particular class of *Riemann problems*, for which the initial gas speeds are allowed to be non-zero. On each side of the membrane, the gas is described with a set of initial variables. They are generally called the left and right states, and denoted by a L and a R subscript. We consider here a one-dimensional adiabatic gas. The membrane is located at $x = 0.5$, and the initial configuration is:

- * Left state ($0 < x < 0.5$): $\rho_L = 1.0, e_L = 2.5, p_L = (\gamma - 1)e_L = 1.0$ and $u_L = 0$.
- * Right state ($0.5 < x < 1$): $\rho_R = 0.125, e_R = 0.25, p_R = (\gamma - 1)e_R = 0.1$ and $u_R = 0$.

The membrane corresponds to an initial discontinuity for all the gas quantities, except the velocity. The analytical solution for this problem is quite complex. One has to assume what

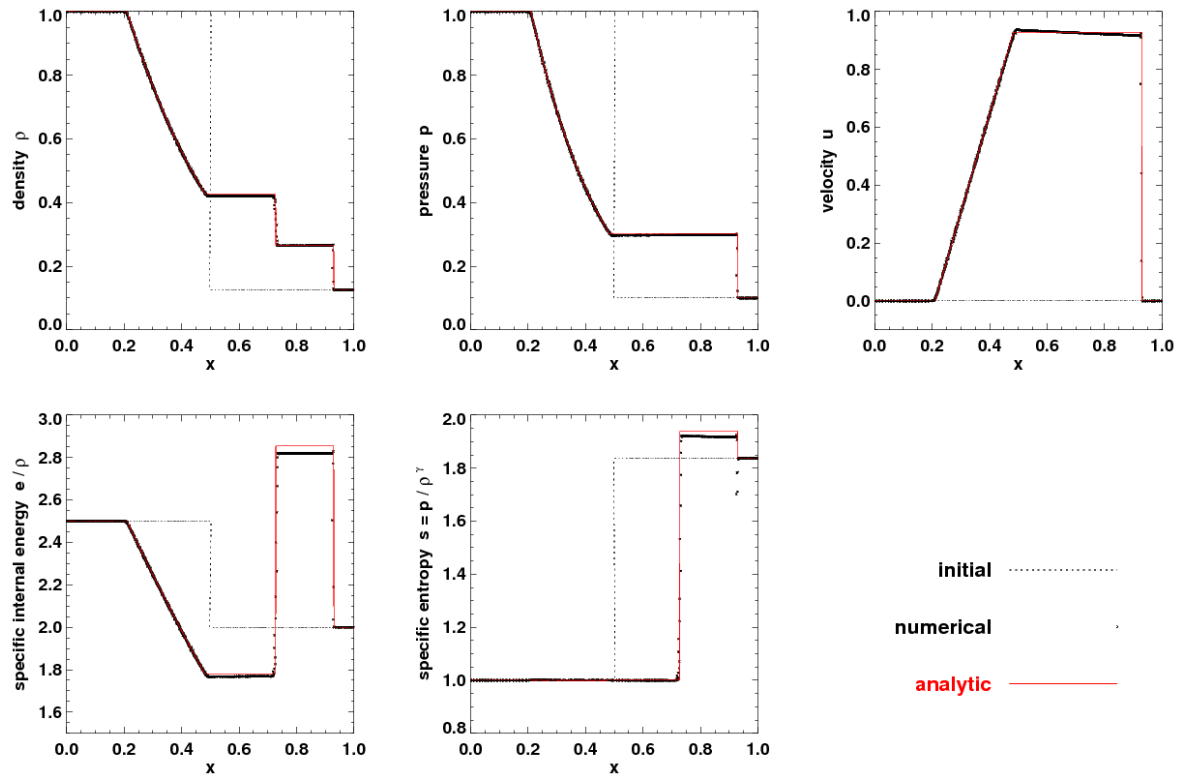


FIGURE 3.12: Shock-tube test problem: comparison of our calculation results (black dots) with the analytical solution (red curve). From top-left to bottom-right, we display the density, pressure, velocity, specific internal energy and specific entropy at $t = 0.245$. In each panel, the initial configuration is indicated with the dotted curve (the membrane is located at $x = 0.5$).

Parameter	Value (code units)	Value (physical units)
Surface density Σ	10^{-3}	$8.9 \times 10^4 \text{ kg.m}^{-2}$
Temperature T	2.5×10^{-3}	645 K
Viscosity ν	10^{-5}	$4.5 \times 10^{10} \text{ m}^2.\text{s}^{-1}$
Opacity κ	2.2×10^4	$2.5 \times 10^{-4} \text{ m}^2.\text{kg}^{-1}$

TABLE 3.1: Parameters used for the stationary test problem, expressed in the code units and converted into physical units. Our value of Σ corresponds to a disc to primary mass ratio $\sim 10^{-2}$.

kind of waves can propagate in the gas. A complete description of the analytical solution will be found in LeVeque (1998) or in Toro (1999). We performed a numerical calculation with FARGO with the above initial configuration, using 1024 cells in the radial direction. The gas fields obtained with our calculation are displayed in figure 3.12 with their analytical expectation. The propagation of three waves may be inferred:

- A *shock wave*, located at $x \sim 0.92$, across which all fields jump discontinuously.
- A *contact discontinuity*, located at $x \sim 0.72$, across which the density is discontinuous, whereas the pressure and the velocity remain continuous.
- A smooth wave having a fan-type shape, and corresponding to an isentropic evolution between the so-called head of the wave (at $x \sim 0.48$) and its tail (at $x \sim 0.2$). This kind of wave is called a *rarefaction wave*.

The agreement between the numerical and analytical results is fairly good. The position of the jumps, as well as their steepness, are sensitive to the resolution and to the artificial bulk viscosity used to spread shocks. In particular, increasing the artificial viscosity (by the coefficient C_{vnr} defined in section 3.1) significantly improves the agreement in the plateau between the contact discontinuity and the shock wave. But note that there is no unique value for the coefficient C_{vnr} that enables a good comparison between numerical and analytical results. Its optimal value is problem dependent.

(b) Stationary state of an axisymmetric disc, with uniform kinematic viscosity :

This test problem is intended to check whether the stationary state obtained with our calculations is consistent with analytical expectations. This test is inspired from D’Angelo et al. (2003a). We assume an unperturbed gaseous disc, without any planet inside. The disc has a uniform kinematic viscosity ν , and we neglect thermal diffusion. The cooling source term Q_- accounts for the energy flux radiated exclusively in the vertical direction. This assumption is valid provided that the disc vertical extent be much smaller than the disc characteristic size in the other directions. Furthermore assuming the disc to be optically thick, we find (D’Angelo et al. 2003a, Pelat & Huré 2002)

$$Q_- = \frac{16}{3} \frac{\sigma_R}{\kappa \Sigma} T^4, \quad (3.58)$$

where σ_R is the Stefan-Boltzmann constant, κ is a frequency-integrated opacity coefficient ($\kappa \Sigma \gg 1$ so that the disc be considered as optically thick), and T is the disc mid-plane temperature, assumed to be much larger than the temperature at $z = \pm H(r)$, where the radiation is liberated

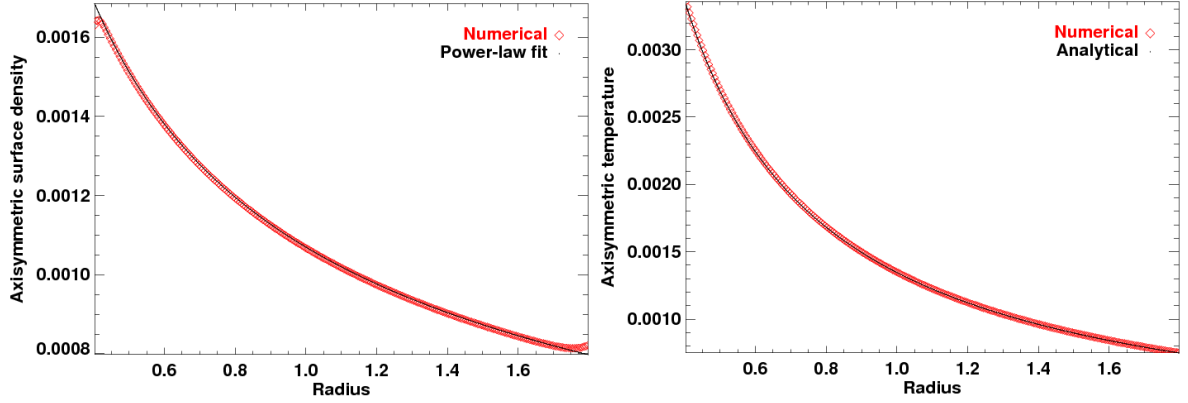


FIGURE 3.13: *Stationary state test problem.* The left panel shows the stationary surface density profile $\Sigma(r)$ reached by an unperturbed disc with uniform kinematic viscosity. Our numerical profile (diamonds) is in good agreement with the expected $r^{-1/2}$ profile (solid curve, see equation (3.61)). The right panel displays the stationary temperature profile obtained with our calculation, along with the analytical expression of equation (3.60), using the $r^{-1/2}$ fit done on the left panel.

(see D’Angelo et al. 2003a, and references therein). The advective and compressional terms of equation (3.56) are negligibly small compared with the heating and cooling source terms. Thus, when the disc reaches a stationary state, the energy equation simplifies as $Q_+ - Q_- = 0$. Furthermore, the heating source term can be approximated as

$$Q_+ = \frac{9}{8} \nu \Sigma \Omega_K^2. \quad (3.59)$$

From equations (3.58) and (3.59), the temperature profile reached by the disc in its stationary state is

$$T(r) = \left(\frac{27}{128} \frac{\nu \kappa}{\sigma_R} \right)^{1/4} \Sigma^{1/2}(r) \Omega_K^{1/2}(r), \quad (3.60)$$

where $\Sigma(r)$ denotes the stationary profile of the disc surface density. Combining the equations of mass and angular momentum conservations, one finds (Pelat & Huré 2002)

$$\frac{\partial \Sigma}{\partial t} = \frac{3}{r} \frac{\partial}{\partial r} \left[r^{1/2} \frac{\partial}{\partial r} \left(\nu \Sigma r^{1/2} \right) \right], \quad (3.61)$$

which shows that, for a uniform kinematic viscosity, the stationary surface density profile may be either decreasing as $r^{-1/2}$, or uniform. From equation (3.6), the radial velocity tends to zero in the former case, while it converges toward a negative value in the latter case. The final state reached by the disc depends on the set of boundary conditions. Assuming open boundaries, allowing for mass outflow at the mesh inner edge, the radial velocity will tend to a non-vanishing, accretion-like profile, so the density will be uniform. On the contrary, the use of rigid boundaries imposes the radial velocity to cancel out, and therefore the disc profile to scale as $r^{-1/2}$. For our calculation, we took rigid boundaries. From equation (3.60), the stationary temperature profile should therefore scale as r^{-1} . We assumed initial surface density and temperature profiles that are uniform. Like the kinematic viscosity, the disc opacity κ is taken uniform. We display in table 3.1 the parameters we considered, in code units and in physical units. We point out that $\kappa \Sigma \gg 1$, in agreement with the assumption of a large optical thickness.

The left-hand panel of figure 3.13 shows the surface density profile the disc reaches in its stationary state (red diamonds) along with a $r^{-1/2}$ fit (black dots). The agreement between the numerical and expected profiles is convincing, except at the very vicinity of the disc edges,

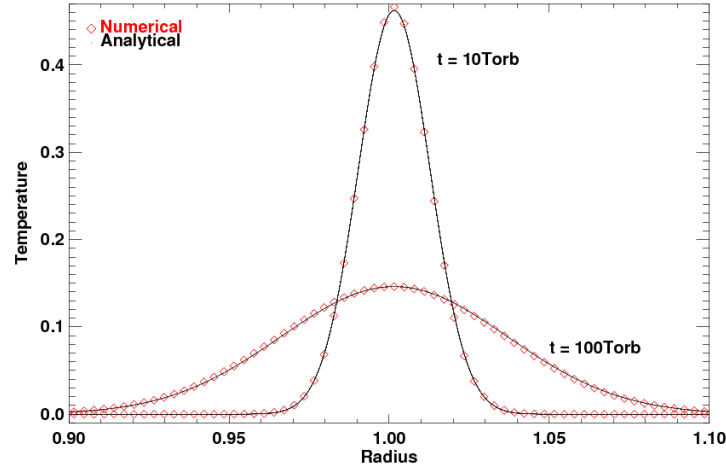


FIGURE 3.14: Temperature profile obtained in the thermal diffusion test-problem. The initial temperature profile is singular. The solution of the heat diffusion equation, given by equation (3.62), is displayed along with our calculation result at 10 and 100 orbital periods at the singularity location.

presumably due to our set of boundary conditions (which prevents any mass loss at the disc edges when the disc is not stationary yet). The right panel of the figure displays the stationary temperature profile and its analytical expression, given by equation (3.60) with the $r^{-1/2}$ fit done on the surface density profile. The agreement is excellent, even at the disc edges. Although not reported here, we checked that the stationary state of the disc does not depend on the set of initial profiles.

(c) *A thermal diffusion test-problem:*

The last test-problem we report here focuses on the thermal diffusion part of the energy equation. The disc we simulated is axisymmetric, inviscid and no cooling source term is included. The initial temperature cancels out everywhere but in the ring $r = r_D$, where its value is denoted by T_D . This mimics a one-dimensional singular distribution for the temperature. The surface density initial profile is chosen so that the initial pressure be uniform. Since the disc is inviscid, the initial radial velocity vanishes. The disc evolves only with the source terms of the hydrodynamic equations, the advection transport is inhibited by resetting to zero the velocities at each timestep. This suffices to avoid the propagation of pressure-supported waves. With these assumptions, the radial velocity and the surface density remain stationary, and our energy equation simply takes the form $\partial_t T = \lambda \Delta T$. Given our initial temperature profile, the solution of this equation is

$$T(r, t) = T_D \delta r \frac{e^{-(r-r_D)^2/4\lambda t}}{\sqrt{4\pi\lambda t}}, \quad (3.62)$$

where δr is the (uniform) mesh radial step. Our calculation was performed with $\lambda = 10^{-6}$, $\delta r \sim 3.1 \times 10^{-3}$, $r_D \sim 1$ and $T_D \sim 4.16$. Figure 3.14 compares the result of our calculation and the analytic solution, given by equation (3.62), after 10 and 100 orbital periods at $r = r_D$. The agreement is excellent.

3.4 Appendix: wave propagation properties

In this appendix section, we describe the wave propagation properties in a one-dimensional gas. The gas is assumed to be either isentropic or adiabatic. We consider the gas as an isolated

system, so the only forces acting on it arise from the pressure p . We denote by ρ and u the (linear) density and velocity.

Isentropic case

For an isentropic gas, the pressure is an explicit expression of the density alone, $p = \kappa \rho^\gamma$, and the energy equation is redundant with the continuity and momentum equations (see section 3.3.1). Using the primitive variables $W = {}^T(\rho, u)$, Euler equations write

$$\partial_t \rho + \partial_x(\rho u) = 0 \quad \text{and} \quad \partial_t u + u \partial_x u + \rho^{-1} \partial_x(\kappa \rho^\gamma) = 0.$$

Suppose that a small perturbation is applied to our system. We denote with a zero (one) subscript the unperturbed (perturbed) quantities; for instance, the gas density reads $\rho = \rho_0 + \rho_1$, with $\rho_1 \ll \rho_0$. The perturbed quantities $W_1 = {}^T(\rho_1, u_1)$ satisfy the linearized equations

$$\partial_t \rho_1 + u_0 \partial_x \rho_1 + \rho_0 \partial_x u_1 = 0 \quad \text{and} \quad \partial_t u_1 + \frac{c_s^2}{\rho_0} \partial_x \rho_1 + u_0 \partial_x u_1 = 0,$$

which can be recast as

$$\partial_t W_1 + A \partial_x W_1 = 0 \quad \text{with} \quad A = \begin{pmatrix} u_0 & \rho_0 \\ \frac{c_s^2}{\rho_0} & u_0 \end{pmatrix}. \quad (3.63)$$

The eigenvalues of A are simply $\lambda^\pm = u_0 \pm c_s$. The left eigenvectors L , defined by $LA = \lambda L$, read $L^\pm = \alpha^\pm(1, \pm \rho_0/c_s)$, where α^- and α^+ are two arbitrary constants. The solution of equation (3.63) is a linear combination of the states ${}^T L^-$ and ${}^T L^+$,

$$W_1 = \omega_1^- {}^T L^- + \omega_1^+ {}^T L^+, \quad \text{with} \quad \omega_1^\pm = L^\pm W_1 = \alpha^\pm \left(\rho_1 \pm \rho_0 \frac{u_1}{c_s} \right). \quad (3.64)$$

Any linear perturbation in an isentropic gas thus gives rise either to:

- a *sound wave* related to the state ${}^T L^-$, which travels with velocity $u_0 - c_s$. Such wave has $\omega_1^+ = 0$, that is $\rho_1/\rho_0 = -u_1/c_s$,
- or a *sound wave*, corresponding to the state ${}^T L^+$, and propagating with velocity $u_0 + c_s$. This wave has $\omega_1^- = 0$, hence $\rho_1/\rho_0 = u_1/c_s$.

This simple study shows that only *sound waves* can propagate in a one-dimensional isentropic gas. As we shall see now, the adiabatic case shows more diversity.

Adiabatic case

For an adiabatic gas, the energy equation has to be accounted for. It is given by equation (3.56), with $Q_- = Q_+ = \lambda = 0$. The primitive variables are this time $W = {}^T(\rho, u, p)$, and Euler equations read

$$\partial_t \rho + \partial_x(\rho u) = 0, \quad \partial_t u + u \partial_x u + \rho^{-1} \partial_x p = 0 \quad \text{and} \quad \partial_t p + \gamma p \partial_x u + u \partial_x p = 0.$$

Similarly as in the isentropic case, we linearize Euler equations, and find that the perturbed quantities $W_1 = {}^T(\rho_1, u_1, p_1)$ satisfy

$$\partial_t W_1 + A \partial_x W_1 = 0 \quad \text{with} \quad A = \begin{pmatrix} u_0 & \rho_0 & 0 \\ 0 & u_0 & \rho_0^{-1} \\ 0 & \rho_0 c_s^2 & u_0 \end{pmatrix}. \quad (3.65)$$

This time, A has three eigenvalues, $\lambda^- = u_0 - c_s$, $\lambda^0 = u_0$, and $\lambda^+ = u_0 + c_s$. The corresponding left eigenvectors read respectively $L^- = \alpha^-(0, 1, -1/\rho_0 c_s)$, $L^0 = \alpha^0(1, 0, -1/c_s^2)$, and $L^+ = \alpha^+(0, 1, 1/\rho_0 c_s)$, with α^\pm and α^0 three arbitrary constants. The solution of equation (3.65) is given by

$$W_1 = \omega_1^- {}^T L^- + \omega_1^0 {}^T L^0 + \omega_1^+ {}^T L^+, \quad (3.66)$$

where

$$\omega_1^\pm = \alpha^\pm \left(u_1 \pm \frac{p_1}{\rho_0 c_s} \right) \quad \text{and} \quad \omega_1^0 = \alpha^0 \left(\rho_1 - \frac{p_1}{c_s^2} \right). \quad (3.67)$$

The linear perturbation of a one-dimensional adiabatic gas induces two kinds of waves:

- two *sound waves*, related to the states ${}^T L^\pm$. As in an isentropic gas, these waves travel with the velocity $u_0 \pm c_s$, and the perturbed fields satisfy $\rho_1/\rho_0 = \pm u_1/c_s$ and $p_1 = \rho_1 c_s^2$.
- an additional wave, associated with the state ${}^T L^0$, which propagates at the velocity of the flow u_0 . This wave is known as an *entropy wave*. Canceling out the coefficients ω_1^\pm leads to $p_1 = 0$ and $u_1 = 0$. Contrary to sound waves, entropy waves are associated to a density perturbation, while the pressure and the velocity remain unchanged.

Quite remarkably, these results hold even when non-linearities arise in the gas, simply because W and W_1 satisfy the same differential equation. This is true whether the gas is isentropic or adiabatic. In the non-linear context however, depending on the initial conditions, perturbations may be discontinuities, such as *shock waves* (across which all hydrodynamic quantities are discontinuous) and *contact waves* (across which the density is discontinuous, while the pressure and the velocity remain continuous). Note that, contrary to shock waves, there is no particle transport across contact waves. Perturbations may also be smooth transition waves, like the *rarefaction waves* (see section 3.3.5).

Chapter 4

Type I planetary migration in a self-gravitating disc

WE INVESTIGATE in this chapter the impact of the gas self-gravity on type I migration, by means of two-dimensional hydrodynamic simulations. We show in section 4.4 that considering a planet freely migrating in a disc without self-gravity leads to a significant overestimate of the migration rate, which stems from a spurious shift of Lindblad resonances. Unbiased drift rates may be obtained only by considering a planet and a disc orbiting within the same gravitational potential. In section 4.5, we confirm that the disc gravity slightly enhances the differential Lindblad torque compared to the situation where neither the planet nor the disc feels the disc gravity. This enhancement can be entirely accounted for by a shift of Lindblad resonances, and we show in section 4.6 that it can be reproduced by the use of an anisotropic pressure tensor. We eventually investigate in section 4.7 the impact of the disc gravity on the corotation torque.

Contents of this chapter

4.1	Introduction	74
4.2	Numerical method	74
4.3	Physical model	75
4.4	Unexpected results without self-gravity	77
4.4.1	Inward shift of Lindblad resonances	77
4.4.2	Torque discrepancy	79
4.5	Inclusion of the disc self-gravity	82
4.5.1	Axisymmetric self-gravitating calculations	82
4.5.2	Fully self-gravitating calculations	83
4.5.3	Comparison with analytical results	86
4.6	The anisotropy model	89
4.6.1	Motivation	89
4.6.2	Validity	91
4.7	Corotation torque issues	92
4.8	Conclusions	94

4.1 Introduction

After the numerical interlude in chapter 3, we come back to our investigation of planetary migration. We have stressed in chapters 1 and 2 the key challenge to yield precise estimates of the migration timescale, and the important role played by hydrodynamic calculations in this way. Nevertheless, a very common simplification of numerical algorithms consists in discarding the disc self-gravity. Apart from a considerable gain in computational cost, this is justified by the fact that protoplanetary discs have large Toomre parameters, so that the disc self-gravity should be unimportant. Even in discs that are not subject to the gravitational instability, neglecting the self-gravity may have important consequences on planetary migration, as we shall see.

Thus far, a very limited number of works has taken the disc self-gravity into account in numerical simulations of planet-disc interactions. [Boss \(2005\)](#) performed a large number of disc simulations in which the self-gravity induces giant planet formation by gravitational instability. His calculations are therefore short, running for a few dynamical times, and involve only very massive objects. The planets formed in these simulations excite a strongly non-linear response of the disc, and any migration effects are probably marginal or negligible. Furthermore, [Nelson & Benz \(2003a,b\)](#) included the disc self-gravity in their two-dimensional simulations of planet-disc interactions. The authors find that the migration rate of a planet that does not open a gap is slowed down by at least a factor of two in a self-gravitating disc. Nonetheless, [Pierens & Huré \(2005\)](#) (hereafter PH05) reported an analytical expression for the shifts of Lindblad resonances due to the disc gravity, and find that the disc gravity accelerates type I planetary migration. The apparent contradiction between these findings motivated our investigation.

4.2 Numerical method

We study the impact of the disc self-gravity on planetary migration by performing a large number of two-dimensional hydrodynamic calculations. Notwithstanding the need for a gravitational softening length, the two-dimensional restriction provides a direct comparison of our calculation results with the analytical findings of PH05, and enables us to achieve a wide exploration of the parameter space, mainly in terms of disc surface density, disc thickness and planet mass. Our calculations are performed with the FARGO code, whose self-gravity solver has been detailed in section 3.2. The implementation of the disc self-gravity addresses two important issues regarding the study of planet-disc interactions, which we describe hereafter.

The first issue concerns the convergence properties of our results. We present here the results of preliminary runs aimed at checking the *torque convergence*, without and with self-gravity. As in all the simulations of this chapter, the computational domain is covered with N_r zones radially between $r_{\min} = 0.4r_p$ and $r_{\max} = 2.5r_p$, and N_φ zones azimuthally between $\varphi = 0$ and $\varphi = 2\pi$. For a comparative purpose, a logarithmic radial spacing is also used for the runs without self-gravity, so that the mesh resolution is the same in all our calculations. We adopt disc parameters and a planet mass that are representative of the study led in this chapter, namely a $Q = 8$ Toomre parameter at the planet location, and a $M_p = 5 \times 10^{-6} M_*$ planet mass (the description of the physical model is deferred to section 4.3). We evaluate the torque obtained without self-gravity (Γ_{nog}) and with self-gravity (Γ_{fsg}) for several pairs (N_r, N_φ) . The relative difference of these torques is displayed in figure 4.1a. We see in particular that the torque convergence is already achieved for $N_r = 512$ and $N_\varphi = 1536$, values that we adopt for the continuation of this chapter. We indicate that, without self-gravity, the *torque evaluation* takes all the disc into account, it does not exclude¹ the content of the planet's Hill sphere.

¹Although it is still a matter of debate, it is generally thought that, without self-gravity, the torque evaluation

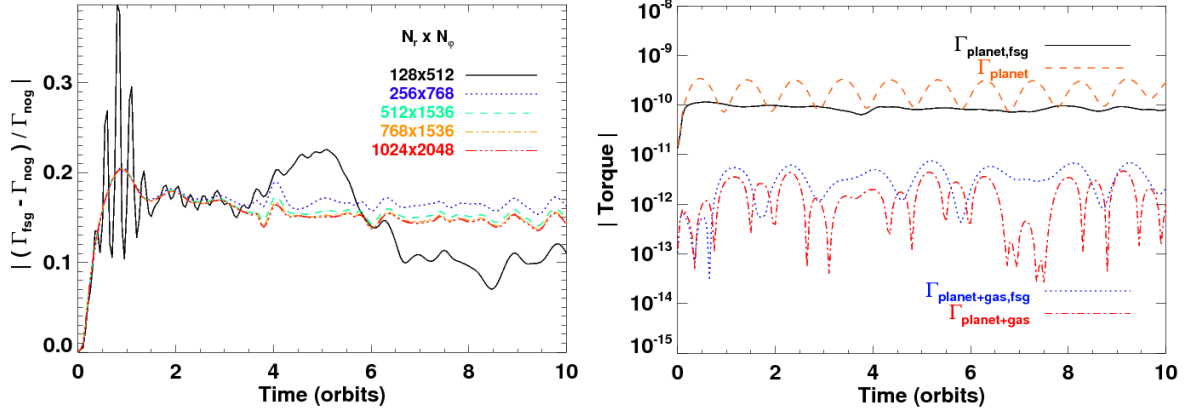


FIGURE 4.1: Left: relative difference of the torques obtained with and without self-gravity (Γ_{fsg} and Γ_{nog}), for different mesh resolutions $N_r \times N_\phi$. Right: torque exerted on a $M_p = 5 \times 10^{-6}$ planet mass, and on the system $\{\text{gas}+\text{planet}\}$, for a calculation without self-gravity (long-dashed and dash-dotted curves), and with self-gravity (solid and dotted curves).

We checked that excluding it or not makes however no difference in the torque measurement. This is consistent with the fact that, for the planet mass considered here, we do not find any material trapped in libration around the planet, be it inside a circumplanetary disc (a fraction of the planet's Hill radius) or inside a Bondi sphere (see section 4.3).

The second issue is connected with the softening length ε_{sg} used to avoid numerical divergences. As explained in section 3.2.1, ε_{sg} scales with r . Since it varies from one ring to another, our self-gravity solver does not ensure an exact action-reaction reciprocity (Newton's third law). Thus, the disc self-gravity may worsen the *conservation of the total angular momentum* (that of the system $\{\text{gas}+\text{planet}\}$). To investigate this issue, we performed calculations with a planet migrating in a disc without and with self-gravity. For these calculations only, the disc is inviscid, and reflecting boundaries are adopted. As for the above convergence study, we adopted a $M_p = 5 \times 10^{-6} M_*$ planet mass, and a Toomre parameter $Q = 8$ at the planet location. The value of $\varepsilon_{sg}(r_p)$ is the one used regularly throughout the calculations of this chapter. We display in figure 4.1b the torques on the planet (Γ_{planet}) and on the whole system ($\Gamma_{planet+gas}$), for both calculations. If the code were perfectly conservative, the ratio $\Gamma_{planet+gas}/\Gamma_{planet}$ would cancel out, to within the machine (double) precision. This ratio is typically $\sim 0.5\%$ without self-gravity, and $\sim 3\%$ with self-gravity. Although, as expected, the conservation of the total angular momentum is worse with self-gravity, it remains satisfactory.

4.3 Physical model

We now come to the physical model used in the following study. The disc surface density Σ is initially axisymmetric with a power-law profile, $\Sigma(r) = \Sigma_p (r/r_p)^{-\sigma}$, where Σ_p is the surface

should exclude the contribution of the fluid elements trapped in libration around the planet, and migrating with the planet. This can be understood as follows. With self-gravity, the wake applies both on the planet and on the librating material around it, and it contributes to make them migrate at the same drift rate. Without self-gravity however, the wake can only interact with the planet, and the librating material remains a passive spectator of the migration. The planet thus has to produce an additional effort to compensate for the passiveness of the librating fluid. Differently stated, this material slows down artificially the migration rate in absence of self-gravity. To alleviate the planet drift, a customary practice is to neglect the torque exerted on the planet by the librating material. Of course, such an approach would be meaningless with self-gravity. We will come back later on this issue in chapter 7.

density at the planet location. The default value for σ is $3/2$, so we expect the corotation torque to cancel out for a non self-gravitating disc, see section 2.3.2. The vertically integrated pressure p and Σ are connected by an isothermal equation of state, $p = \Sigma c_s^2$, where c_s is the local isothermal sound speed. The disc aspect ratio is $h(r) = H(r)/r = c_s(r)/r\Omega_K(r)$, where $H(r)$ is the disc scale height at radius r , and Ω_K denotes the Keplerian angular velocity. We take h uniform, ranging from $h = 0.03$ to $h = 0.05$, depending on the calculations. We use a uniform kinematic viscosity ν , which is 10^{-5} in our unit system. The gravitational forces exerted on the disc include:

- the gravity of the central star,
- that of an embedded planet, modeled with a Plummer potential with a softening parameter $\varepsilon = 0.3H(r_p)$,
- the disc self-gravity, whenever mentioned. The self-gravity softening length ε_{sg} is chosen to scale with r , and to be equal to ε at the planet's orbital radius, which yields $\varepsilon_{\text{sg}}(r) = \varepsilon r/r_p$. Since h is taken uniform, $H(r)$ scales with r , and we are left with $\varepsilon_{\text{sg}}(r) = 0.3H(r)$. We comment that $\varepsilon_{\text{sg}}(r_p)$ is very close to the recent prescription of [Huré & Pierens \(2006\)](#) for the softening length of a flat, axisymmetric self-gravitating disc. From now on, whenever we mention the softening length, we will refer to ε .

The disc's initial rotation profile $\Omega(r)$ is slightly sub-Keplerian, the pressure gradient being accounted for in the centrifugal balance. When the disc self-gravity is taken into account, it reads

$$\Omega(r) = \left(\Omega_K^2(r) [1 - (1 + \sigma)h^2] - \frac{g_r(r)}{r} \right)^{1/2}. \quad (4.1)$$

We point out that equation (3.42) reduces to equation (4.1) with a uniform disc aspect ratio ($f = 0$). We also comment that $g_r(r)$ is not necessarily a *negative* quantity. When it is so, the disc rotates slightly faster with self-gravity than without. In a two-dimensional truncated disc, g_r is positive at the inner edge and becomes negative at a distance from the inner edge that depends on σ . We checked that, whatever the values of σ used hereafter, g_r is always negative in a radial range around the planet's orbital radius that is large enough to embrace all Lindblad resonances (except the inner Lindblad resonance of $m = 2$ for $\sigma = 0$, as can be inferred from figure 3.8a).

Since our study deals with the linear perturbation regime, we consider a $q = 5 \times 10^{-6}$ planet to primary mass ratio. This value satisfies indeed the linearity criterion proposed by [Masset et al. \(2006a\)](#) and given by equation (2.26). Recall that this criterion reads $q \ll q_{\text{lin}}$, where $q_{\text{lin}} = 0.3h^3$ given our softening length value. For a $h = 5\%$ disc aspect ratio, $q_{\text{lin}} \approx 4 \times 10^{-5}$, while for $h = 3\%$, $q_{\text{lin}} \approx 8 \times 10^{-6}$. The *linearity criterion* is satisfied with both aspect ratios, although in an approximate way for $h = 3\%$. We also recall that the departure from the linear criterion is not equivalent to the gap clearance criterion. The latter criterion, recently revisited by [Crida et al. \(2006\)](#), reads in our unit system (equation (2.24)):

$$\frac{3}{4} h \left(\frac{q}{3} \right)^{-1/3} + 50 \frac{\nu}{q} \leq 1. \quad (4.2)$$

The left-hand side of equation (4.2) being ~ 100 , there will not be any gap opening in our calculations. In this case, and in absence of self-gravity, the torque Γ scales with Σ_p . We therefore expect to check this scaling with our calculations without self-gravity.

Parameter	Fixed Case	Free Case
$\Omega_p(r_p)$	$\Omega_K(r_p)$	$\left[\Omega_K^2(r_p) - \frac{g_r(r_p)}{r_p} \right]^{1/2}$
$\Omega(r)$	$\Omega_K(r) [1 - (1 + \sigma)h^2]^{1/2}$	$\Omega_K(r) [1 - (1 + \sigma)h^2]^{1/2}$

TABLE 4.1: Planet’s angular velocity $\Omega_p(r_p)$ and disc’s rotation profile $\Omega(r)$ for a non self-gravitating disc. In both cases, the initial planet’s angular velocity is strictly Keplerian. For all the runs presented here, $g_r(r_p) < 0$ so that $\Omega_p(r_p)$ is slightly greater in the free case than in the fixed case.

4.4 Unexpected results without self-gravity

4.4.1 Inward shift of Lindblad resonances

We present in this section the results of our calculations without self-gravity. These calculations follow the physical model detailed in section 4.3. The runs lasted for 20 orbits, which was long enough to get stationary values of the torque. We aim at measuring the specific torque $\gamma = \Gamma/q$ on the planet for six different values of Σ_p , ranging from $\Sigma_p = 2 \times 10^{-4}$ to $\Sigma_p = 2 \times 10^{-3}$. This corresponds to varying the initial surface density at the planet location from one to ten times that of the minimum mass solar nebula. Two situations are considered (see also table 4.1):

- *The planet does not feel the disc gravity.* It is held on a fixed circular orbit, with a strictly Keplerian orbital velocity. In this case, referred to as the *fixed case*, both the planet and the disc feel the star gravity but do not feel the disc gravity. The disc non-Keplerianity is exclusively accounted for by the radial pressure gradient. This is the configuration that has been contemplated in analytical torque estimates (see e.g. [Tanaka et al. 2002](#)).
- *The planet feels the disc gravity.* In other words, we let the planet evolve freely in the disc, so its angular velocity, which reads

$$\Omega_p(r_p) = [\Omega_K^2(r_p) - g_r(r_p)/r_p]^{1/2}, \quad (4.3)$$

is slightly greater than Keplerian. In this case, which we call the *free case*, the planet feels the gravity of the star and of the disc while, as previously stated, the disc does not feel its own gravity. Contrary to the fixed case, the free case is not a self-consistent configuration since the planet and the disc do not orbit under the same gravitational potential. Nevertheless, this situation is of interest as it corresponds to the standard scheme of all simulations dealing with disc-planet interactions.

We show in figure 4.2 the specific torques obtained with the fixed and free cases, for a $h = 0.05$ disc aspect ratio. In the fixed situation, there is an excellent agreement with the expectation $\gamma \propto \Sigma_p$, and, due to our choice for ε , the torques are bounded by the two- and three-dimensional analytical estimates of [Tanaka et al. \(2002\)](#). Nonetheless, the free case reveals two *unexpected* results. For a given surface density, the absolute value of the torque is larger than expected from the fixed case. Moreover, it increases faster than linearly with the disc surface density.

The two latter results can be explained with the relative positions of the Lindblad Resonances (hereafter LR) in the fixed and free cases. We display in figure 4.3a the locations r_{ILR} (r_{OLR}) of an Inner (Outer) LR, when the planet is on a fixed orbit. They are given by $r_{\text{ILR}} = \Omega^{-1}(\Omega_{\text{ILR}})$ and $r_{\text{OLR}} = \Omega^{-1}(\Omega_{\text{OLR}})$, with $\Omega(r)$ the disc’s rotation profile (solid curve), and Ω_{ILR} (Ω_{OLR}) the frequency of the ILR (OLR), simply deduced from the planet frequency Ω_p . When the planet

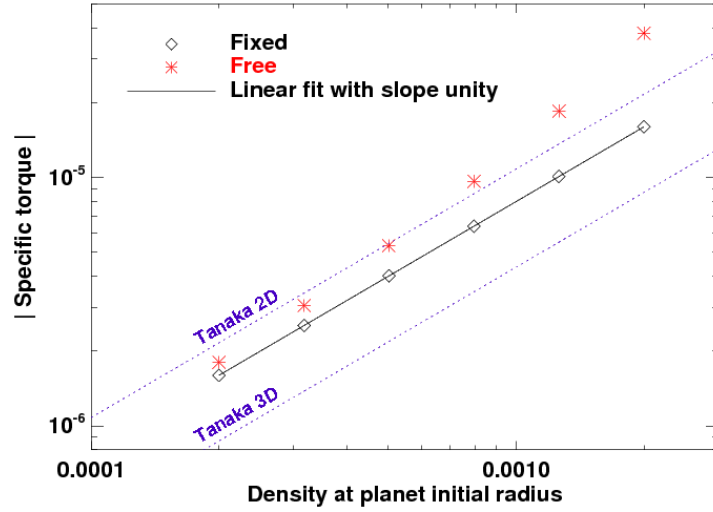


FIGURE 4.2: specific torque γ exerted on a $M_p = 5 \times 10^{-6} M_*$ planet mass by a non self-gravitating disc, with a $h = 5\%$ aspect ratio. Diamonds refer to the fixed case (the planet is held on a fixed circular orbit, with a strictly Keplerian angular velocity) while asterisks refer to the free case (the planet freely evolves in the disc, the planet's angular velocity is greater than Keplerian). The solid line, which corresponds to a proportional fit of the fixed case data, shows the excellent agreement between our calculation results and the expectation $\gamma \propto \Sigma_p$ in the fixed case. The two dotted lines depict the two- and three-dimensional analytical estimates of Tanaka et al. (2002).

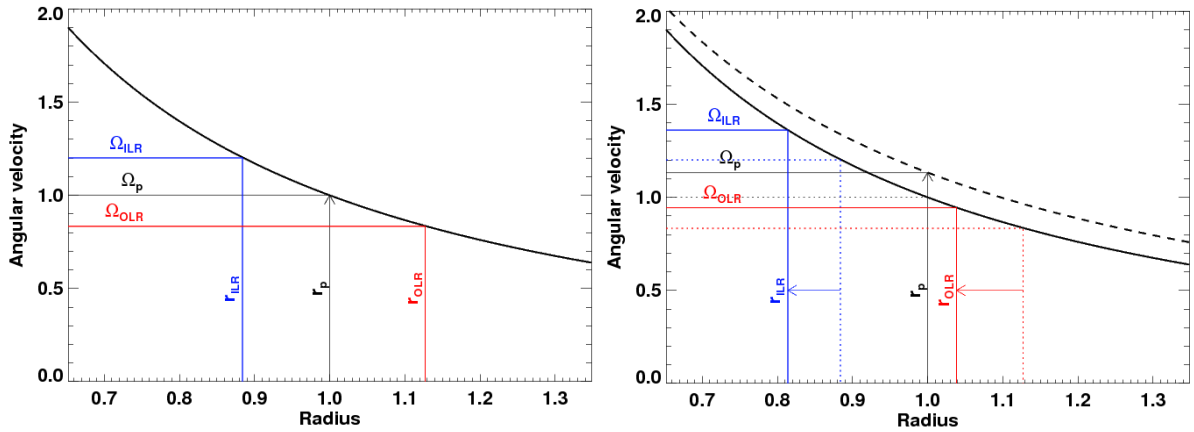


FIGURE 4.3: Location of two Lindblad resonances in the fixed case (left panel) and in the free case (right panel): the ILR of $m = 6$ ($\Omega_{\text{ILR}} = 6/5 \Omega_p$), and the OLR of $m = 5$ ($\Omega_{\text{OLR}} = 5/6 \Omega_p$). The disc's rotation profile $\Omega(r)$ is depicted without self-gravity (solid curve) and with self-gravity (dashed curve, right panel). In the latter case, $g_r(r)$ is given by a calculation with $\Sigma_p = 5 \times 10^{-2}$, a value exaggerated to improve legibility. Note also that the pressure buffer has been discarded in both profiles, for the sake of simplicity. The vertical arrow at $r = 1$ indicates the planet location, it reaches the upper curve in the free case (right panel) since the planet feels the disc gravity. The ILR and OLR are located, respectively, at $r_{\text{ILR}} = \Omega^{-1}(\Omega_{\text{ILR}})$ and $r_{\text{OLR}} = \Omega^{-1}(\Omega_{\text{OLR}})$. The nominal position of the resonances (that of the fixed case) is indicated by dash-dotted lines on the right panel to appreciate their shift, highlighted by a horizontal arrow.

is on a free orbit (figure 4.3b), its frequency is slightly larger than in the fixed case. Thus, the frequencies of the LR are also larger in the free case, which induces a spurious *inward shift* of all the resonances. OLR get closer to the orbit, which increases the (negative) outer Lindblad torque. ILR are shifted away from the orbit, which reduces the (positive) inner Lindblad torque. The (negative) differential Lindblad torque is therefore artificially larger in the free case.

We write δR the inward shift of the LR. A simple estimate can be obtained as follows. We denote by R_* the nominal position of the resonances without disc gravity. We assume that the disc's rotation profile is strictly Keplerian. The shift δR being induced by the increase of the planet frequency, we have $\delta R/R_* = -2\delta\Omega_p(r_p)/3\Omega_K(r_p)$, where $\delta\Omega_p(r_p)$ is the difference of the planet frequencies between the free and fixed cases. Using equation (4.3) and a first-order expansion, we find

$$\frac{\delta R}{R_*} = \frac{g_r(r_p)}{3r_p\Omega_K^2(r_p)}. \quad (4.4)$$

A more accurate expression for $\delta R/R_*$ is given by PH05 (see their equation [7c]). Equation (4.4) shows that the shift of the LR scales with $g_r(r_p)$, hence with Σ_p . This explains why the torque in the free case increases faster than linearly with the disc surface density. The relative shift of the resonances $\delta R/R_*$ typically amounts from -3×10^{-4} to -3×10^{-3} for our range value of surface densities, corresponding however to a torque relative discrepancy between $\sim 12\%$ and $\sim 120\%$ (see figure 4.2).

4.4.2 Torque discrepancy

We are primarily interested in a quantitative estimate of the torque discrepancy between the fixed and free cases. It scales with $g_r(r_p)$, like the LR shift [see equation (4.4)]. It therefore depends on the *mass distribution on the whole disc*, hence on the precise values of Σ_p , σ , r_{\min} and r_{\max} , as inferred from equation (3.37). In particular, if the planet is close enough to the disc's inner edge, $g_r(r_p)$ is positive (see e.g. figure 3.8). In this case, all LR are this time shifted outward (instead of inward), which reduces the differential Lindblad torque (instead of increasing it). We have checked this prediction with an appropriate calculation (not presented here). In our calculations however, only Σ_p is a free parameter. The index σ of the unperturbed surface density profile is fixed to $3/2$ to avoid any contribution of the corotation torque to the torque evaluation (see section 4.3). And the values of r_{\min} and r_{\max} are those customarily used in numerical simulations of planet-disc interactions (see e.g. [de Val-Borro et al. 2006](#)). Thus, a useful quantitative comparison of the torques between the free and fixed cases can be provided just by varying Σ_p . This section is organized as follows. We first derive a simple analytical model to show that the relative difference of the torques between the free and fixed situations scales with $(Qh)^{-1}$, where Q is the Toomre parameter at the planet's orbital radius (Q is defined below). This scaling is then checked against our calculation results.

Analytical expectation

We present in this section a simple model to evaluate the torque relative difference between the fixed and free cases. We will often make use of this model in what follows. We assume that the shift induced by the free case has same order of magnitude at inner and outer LR (PH05). We therefore focus on the one-sided Lindblad torque and use a local *shearing sheet* approximation. We set up local Cartesian coordinates (x, y) with origin at the planet position, the x and y -axis pointing toward the radial and azimuthal directions. Our x -coordinate is taken normalized as

$$x = \frac{r - r_p}{H(r_p)} = \frac{r - r_p}{hr_p}. \quad (4.5)$$

As is usually done in the shearing sheet framework, we discard the radial dependence of the disc surface density and scale height (Narayan et al. 1987). In the fixed situation, the LR associated with wavenumber m are therefore located at

$$x_{\text{fixed}} = \frac{2}{3}\epsilon \frac{\sqrt{1+\xi^2}}{\xi}, \quad (4.6)$$

where $\xi = mh$, $\epsilon = +1$ for outer resonances, $\epsilon = -1$ for inner resonances.

In the linear regime, the one-sided Lindblad torque Γ amounts to a summation over m of the Fourier components Γ_m . In the shearing sheet approximation, since all quantities depend on m through ξ , the summation over m is approximated as an integral over ξ ,

$$\Gamma = \frac{1}{h} \int_0^\infty T(x = x_L, \xi) d\xi, \quad (4.7)$$

where x_L denotes the positions of the LR, T is the m^{th} Fourier component of the one-sided Lindblad torque (see e.g. Ward 1997),

$$T(x, \xi) = K \frac{\xi^2 \Psi^2(x, \xi)}{\sqrt{1+\xi^2}(1+4\xi^2)}, \quad (4.8)$$

with K a constant, proportional to $\Sigma_p h^{-2}$. The forcing function Ψ in equation (4.8) is approximated in a standard way as a function of the Bessel K_0 and K_1 functions,

$$\Psi(x, \xi) = K_1(|x|\xi) + 2\sqrt{1+\xi^2}K_0(|x|\xi). \quad (4.9)$$

We furthermore approximate $\Psi(x, \xi)$ as $(|x|\xi)^{-1}$, to within a numerical factor of the order of unity (Abramowitz & Stegun 1972). This approximation is valid when $\xi \lesssim 1$, hence for low m -values. The difference $\delta\Gamma$ of the one-sided Lindblad torques between the free and fixed cases is then given by

$$\delta\Gamma \approx \frac{1}{h} \int_0^\infty \left(\frac{\partial T}{\partial x} \right)_{x=x_{\text{fixed}}, \xi} \delta x d\xi \equiv \frac{1}{h} \int_0^\infty \left(\frac{\partial_x T}{T} \right)_{x=x_{\text{fixed}}} \times T \delta x d\xi, \quad (4.10)$$

where δx is the shift of the Lindblad resonances induced by the free case. Since $\Psi \propto |x|^{-1}$, we have $T \propto x^{-2}$ and $\partial_x T/T \propto x^{-1}$. At the location of Lindblad resonances, given by equation (4.6), this yields $\partial_x T/T \propto \epsilon$. Moreover, $T \propto \epsilon \Sigma_p h^{-2}$. From equations (4.4) and (4.5), the shift δx , which has same sign at inner and outer Lindblad resonances, scales with $\Sigma_p h^{-1}$. The difference of the differential Lindblad torques is eventually obtained by summing equation (4.10) at inner and outer Lindblad resonances:

$$\delta\Gamma_{\text{ILR}} + \delta\Gamma_{\text{OLR}} \propto \Sigma_p h^{-2} \int (T_{\text{OLR}} - T_{\text{ILR}}) d\xi \propto \Sigma_p h^{-2} \times \Sigma_p h^{-2} \propto \Sigma_p^2 h^{-4}. \quad (4.11)$$

Since the differential Lindblad torque scales with $\Sigma_p h^{-2}$, the relative difference of the differential Lindblad torques between the free and fixed cases scales with $\Sigma_p h^{-2}$. We furthermore introduce the Toomre parameter at the planet's orbital radius:

$$Q = \left[\frac{c_s \kappa}{\pi G \Sigma} \right]_{r_p} \equiv h/m_D, \quad (4.12)$$

with κ the horizontal epicyclic frequency, defined as $\kappa = [2\Omega r^{-1} d(r^2 \Omega)/dr]^{1/2}$, and $m_D = \pi r_p^2 \Sigma_p / M_*$. The mass m_D corresponds to the normalized mass interior to the protoplanet for a uniform surface density. Equation (4.12) reads $Q = h/\pi \Sigma_p$ in our units, hence $(Qh)^{-1} \propto \Sigma_p h^{-2}$. The relative difference of the differential Lindblad torques between the free and fixed cases therefore scales with $(Qh)^{-1}$.

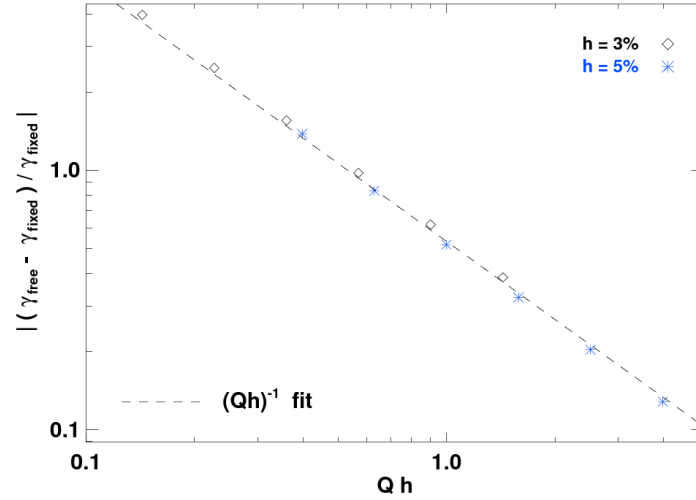


FIGURE 4.4: Relative difference of the torques between the free and fixed situations, as a function of Qh [see text and equation (4.12)]. The dashed curve corresponds to a $(Qh)^{-1}$ fit of the results.

Numerical results

One may think that the torque discrepancy displayed in figure 4.2 is significant only for high values of Σ_p . Nevertheless, as shown above, the discrepancy depends both on Σ_p and on the disc aspect ratio h . To study the impact of h on our results, we performed another set of calculations with $h = 0.03$. Figure 4.4 confirms that the relative difference of the torques does scale with the inverse of Qh . It yields an estimate of the error done on the torque evaluation when involving the strongly biased free situation rather than the self-consistent fixed situation. For instance, with a $h = 3\%$ disc aspect ratio, the free situation overestimates the torque by as much as a factor of two in a disc having only ~ 3 times the disc surface density of the MMSN. Moreover, the torque relative difference is less than 20 % as long as $Qh \gtrsim 2.5$, hence as long as the Toomre parameter at the planet location is approximately greater than 50 if $h = 0.05$, or 80 if $h = 0.03$. Remember that these estimates depend on the precise value of $g_r(r_p)$, hence on the mass distribution of the whole disc. They are provided with fixed, but customarily used values of σ , r_{\min} and r_{\max} .

To avoid the torque discrepancy, one must ensure that the planet and the disc feel the same gravitational potential. The workaround depends on whether the disc is self-gravitating or not, and whether the planet freely migrates in the disc or not:

- *The disc is not self-gravitating.* The planet's angular velocity should therefore be strictly Keplerian:
 - The planet evolves *freely* in the disc. Thus, its angular velocity, given by equation (4.3), is slightly greater than Keplerian. A workaround could be to subtract the axisymmetric component of the disc surface density to the surface density before calculating the force exerted on the planet by the disc. This would cancel out $g_r(r_p)$, and the planet's angular velocity would remain strictly Keplerian.
 - The planet is held on a *fixed* circular orbit, with necessarily a Keplerian angular velocity. This is a self-consistent situation.
- *The disc is self-gravitating.* The planet's angular velocity should therefore be given by equation (4.3):

Parameter	Without disc gravity	With disc gravity
$\Omega_p(r_p) \dots\dots\dots$	$\Omega_K(r_p)$	$\left\{ \Omega_K^2(r_p) - \frac{g_r(r_p)}{r_p} \right\}^{1/2}$
$\Omega(r) \dots\dots\dots$	$\Omega_K(r) [1 - (1 + \sigma)h^2]^{1/2}$	$\left\{ \Omega_K^2(r) [1 - (1 + \sigma)h^2] - \frac{g_r(r)}{r} \right\}^{1/2}$

TABLE 4.2: Planet's angular velocity $\Omega_p(r_p)$ and disc's rotation profile $\Omega(r)$, without and with disc gravity.

- The planet evolves *freely* in the disc. This is a self-consistent situation.
- The planet is held on a *fixed* circular orbit. This situation is self-consistent only if the planet's *fixed* angular velocity is given by equation (4.3).

From now on, whenever calculations without disc gravity are mentioned, they will refer to the fixed situation. We mention them as *nog* calculations.

4.5 Inclusion of the disc self-gravity

We study hereafter how the results of section 4.4 differ when the disc gravity is felt both by the planet and the disc. The planet is still held on a fixed circular orbit at $r = r_p$, its angular velocity is given by equation (4.3). As in the situation without disc gravity, the planet's initial velocity is that of a fluid element that would not be subject to the radial pressure gradient (see table 4.2). Taking the disc self-gravity into account induces two shifts of Lindblad resonances (PH05): (i) a shift arising from the axisymmetric component of the disc self-gravity, and (ii) a shift stemming from the non-axisymmetric component of the disc self-gravity. We therefore performed two series of calculations:

1. Calculations that involve only the axisymmetric part of the disc self-gravity. They are mentioned as axisymmetric self-gravitating calculations (*asg* calculations). Their computational cost is the same as that of a calculation without disc gravity since only one-dimensional FFTs are performed. The results of these calculations are presented in section 4.5.1.
2. Fully self-gravitating calculations (*fsg* calculations), which are more computationally expensive as they involve two-dimensional FFTs. Their results are presented in section 4.5.2.

4.5.1 Axisymmetric self-gravitating calculations

We display in figure 4.5 the torques obtained with the *nog*, *asg* and *fsg* calculations, when varying Σ_p . We will comment the results of the *fsg* calculations in section 4.5.2. The torques obtained in the *asg* situation, which we denote by γ_{asg} , are hardly distinguishable from the torques without disc gravity, mentioned as γ_{nog} . A straightforward consequence is that γ_{asg} scales with Σ_p with a good level of accuracy. We point out however that the torque difference $|\gamma_{\text{asg}}| - |\gamma_{\text{nog}}|$ is slightly negative and decreases with Σ_p (not displayed here). The relative difference $||\gamma_{\text{asg}}| - |\gamma_{\text{nog}}|| / |\gamma_{\text{nog}}|$ varies from ~ 0.2 % for $\Sigma_p = 2 \times 10^{-4}$, to ~ 2 % for $\Sigma_p = 2 \times 10^{-3}$.

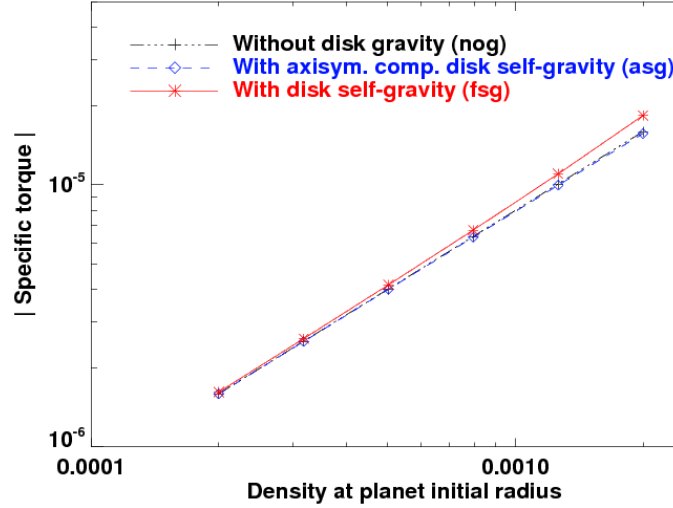


FIGURE 4.5: Specific torque on a $M_p = 5 \times 10^{-6} M_*$ planet mass, obtained with axisymmetric and fully self-gravitating calculations, with a $h = 5\%$ disc aspect ratio. Torques achieved without disc gravity (see section 4.4) are also displayed, for comparison.

The interpretation of these results is as follows. In the asg situation, the positions of the LR related to the Fourier component with wavenumber m are the roots of equation (see PH05 and references therein)

$$D_{\text{asg}}(r) = \kappa^2(r) - m^2[\Omega(r) - \Omega_p]^2 + m^2 c_s^2(r)/r^2 = 0, \quad (4.13)$$

where, contrary to the nog situation, $\Omega(r)$ and Ω_p depend on g_r (see table 4.2). As in section 4.4, the increase of the planet frequency implies an inward shift of the LR, which increases the differential Lindblad torque (see figure 4.3b). Furthermore, as pointed out in figure 4.6a, the increase of the disc frequency causes an outward shift of all LR, which reduces the differential Lindblad torque. Accounting for the axisymmetric component of the disc gravity therefore leads to two shifts of the resonances, acting in opposite ways. Figure 4.6b shows that both shifts do not compensate exactly: the LR are slightly² moved away from corotation with respect to their nominal position without disc gravity. This is in qualitative agreement with PH05, who found a resulting shift which is negative for inward resonances, and positive for outward resonances (see their $\delta R_1 + \delta R_3$ expression). The sign of the shift results from the fact that the disc's rotation profile decreases more slowly with self-gravity than without³, and explains why $|\gamma_{\text{asg}}| - |\gamma_{\text{nog}}|$ is negative. The absolute value of this shift increases with Σ_p , which entails that $||\gamma_{\text{asg}}| - |\gamma_{\text{nog}}||$ increases with Σ_p .

4.5.2 Fully self-gravitating calculations

We now come to the results of the fsg calculations depicted in figure 4.5. The torques obtained with the fsg calculations, denoted by γ_{fsg} , are larger than γ_{asg} and γ_{nog} . Moreover, $|\gamma_{\text{fsg}}|$ grows faster than linearly with the disc surface density, a result already mentioned by Tanigawa & Lin (2005). These results can be understood again in terms of shifts of the LR. Besides the shift due to the slight increase of the planet and of the disc frequency, the fsg situation triggers another

²To improve the legibility of figures 4.3 and 4.6, the disc's rotation profile with self-gravity is depicted with a value of Σ_p that is 25 times greater than the maximal value of our set of calculations.

³We comment that this statement is not straightforward since it involves both the sign and the variations of function g_r ; here again we checked that this statement is valid in a radial range around the orbit that is large enough to concern all LR.

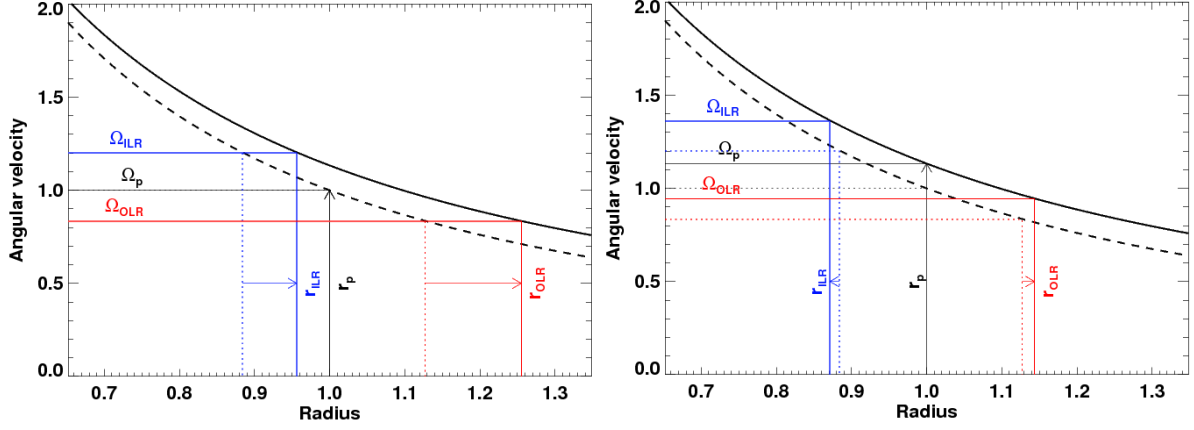


FIGURE 4.6: Same as figure 4.3, except that we examine the shift of the LR when the disc is self-gravitating (its rotation profile is now the solid, upper curve). In the left panel, the planet does not feel the disc gravity: the frequency of the planet, and therefore that of the LR, are the same as in figure 4.3a. In the right panel, both the planet and the disc feel the disc gravity: the frequencies of the planet and of the LR are those of figure 4.3b.

shift stemming from the additional non-axisymmetric term $-2\pi G\Sigma m/r$ in the dispersion relation of density waves (in the WKB approximation, see PH05). The positions of the LR associated with wavenumber m are this time the roots of equation

$$D_{\text{fsg}}(r) = D_{\text{asg}}(r) - 2\pi G\Sigma(r)m/r = 0, \quad (4.14)$$

where D_{asg} is given by equation (4.13). PH05 showed that:

- This non-axisymmetric contribution moves inner and outer LR toward the orbit, with respect to their location in the asg situation. This explains why $|\gamma_{\text{fsg}}| > |\gamma_{\text{asg}}|$, and implies that the torque variations at inner and outer resonances have opposite signs.
- The shift induced by the non-axisymmetric part of the disc self-gravity dominates that of its axisymmetric component. Therefore, it approximately accounts for the total shift due to the disc gravity, and explains why $|\gamma_{\text{fsg}}| > |\gamma_{\text{nog}}| \approx |\gamma_{\text{asg}}|$.
- This shift increases with Σ_p , so that $|\gamma_{\text{fsg}}|$ increases faster than linearly with Σ_p .

Our results of calculations are in qualitative agreement with the analytical work of PH05. Before coming to a quantitative comparison in section 4.5.3, we focus on the relative difference of the torques between the fsg and nog situations. From previous results, we assume that the only shift of the LR is due to the non-axisymmetric part of the disc gravity. Interestingly, this shift does not feature g_r , so it does not depend on the mass distribution of the whole disc. It only depends on the surface density at the planet location. Since the torque variations at inner and outer resonances are of opposite sign, we expect the relative difference of the torques to scale with Q^{-1} , for high to moderate values of Q . It differs from the $(Qh)^{-1}$ scaling obtained in figure 4.4, where the torque variations at inner and outer resonances were of identical sign. Like in section 4.4.2, we proceed this section by first arguing the $(Qh)^{-1}$ scaling mentioned above, which we then check against our calculation results.

Analytical expectation

The difference $\delta\Gamma$ of the one-sided Lindblad torques between the fully self-gravitating and non-gravitating situations is given again by equation (4.10), where δx is this time the shift induced

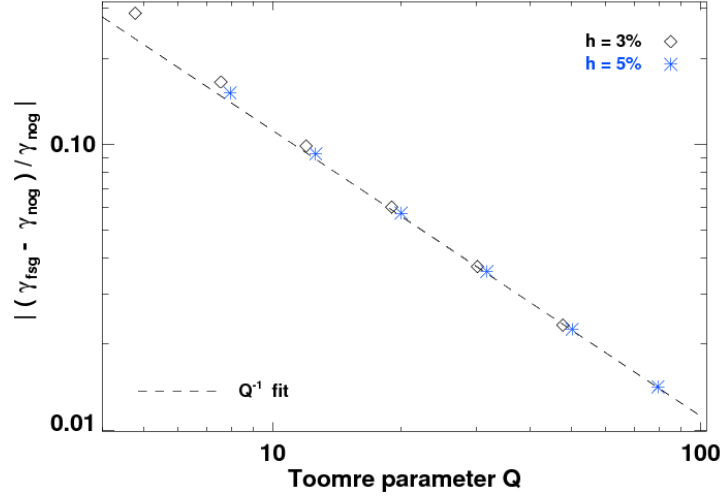


FIGURE 4.7: Relative difference of the torques obtained with the fully self-gravitating calculations (γ_{fsg}) and the calculations without disc gravity (γ_{nog}), as a function of the Toomre parameter Q at the planet location. The dashed curve depicts as Q^{-1} power-law fit of the results.

by the fsg situation. We assume that the only shift of the LR in the fsg situation arises from its non-axisymmetric contribution. This comes to approximating the nog and asg situations, which is a reasonable assumption from figure 4.5. The shift δx is evaluated with $D_{\text{fsg}}(x_{\text{fixed}} + \delta x) = 0$. Using equations (4.13), (4.14) and (4.6), a first-order expansion yields

$$\delta x = -\frac{2}{3\epsilon Q} \frac{1}{\sqrt{1 + \xi^2}}. \quad (4.15)$$

We point out that equation (7b) of PH05 reduces to our equation (4.15) for a surface density profile decreasing as $r^{-3/2}$. Note also that this shift has an opposite sign at inner and outer Lindblad resonances: $\delta x \propto \epsilon \Sigma_p h^{-1}$. Furthermore, assuming that the expression of T given by equation (4.8) can be applied again for a self-gravitating disc (Goldreich & Tremaine 1979), we still have $\partial_x T / T \propto \epsilon$. Since the differential Lindblad torque scales with $\Sigma_p h^{-2}$, we find

$$\delta \Gamma_{\text{ILR}} + \delta \Gamma_{\text{OLR}} \propto \Sigma_p h^{-2} \underbrace{\int (T_{\text{OLR}} + T_{\text{ILR}}) d\xi}_{\propto \Sigma_p h^{-1}} \propto \Sigma_p h^{-2} \times \Sigma_p h^{-1} \propto \Sigma_p^2 h^{-3}. \quad (4.16)$$

The relative difference of the differential Lindblad torques between the fsg and nog cases therefore scales with $\Sigma_p h^{-1}$, hence with Q^{-1} .

Numerical results

We display in figure 4.7 this relative difference as a function of Q for previous results and for another series of runs performed with a $h = 0.03$ disc aspect ratio. Our calculation results confirm the Q^{-1} scaling derived above, the departure from this expected scaling occurring for $Q \lesssim 6$. The behavior at low Q will be tackled in section 4.5.3. Figure 4.7 yields a useful estimate of the torque increase due to the disc gravity, or, differently stated, of the torque underestimate if one discards the disc gravity. This estimate only depends on the Toomre parameter at the planet location, whatever the global mass distribution of the disc. The torques relative difference

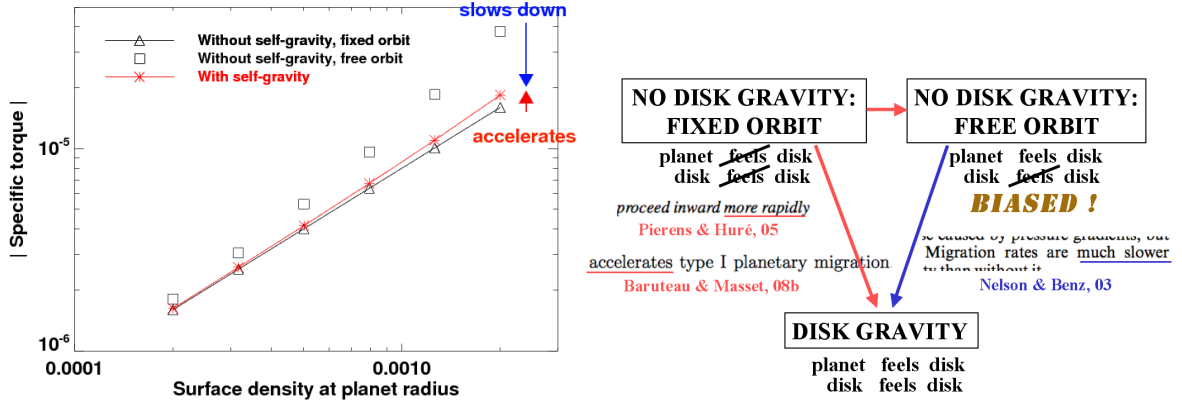


FIGURE 4.8: The left panel sums up figures 4.2 and 4.5. Depending on whether we assume the fixed or the free cases without self-gravity, we may conclude that the disc self-gravity either accelerates or slows down type I migration. This paradox is illustrated on the right panel.

is typically one order of magnitude⁴ smaller than in the situation of a planet freely migrating in a non self-gravitating disc (figure 4.4). It amounts typically to 10 % for $Q \approx 10$. For $Q \gtrsim 50$, accounting for the disc gravity or not has no significant impact on the torque measurement.

Our results confirm that the disc *gravity* accelerates type I migration. This might sound contradictory with the results of Nelson & Benz (2003a;b), who found that the disc *self-gravity* slows down migration for a planet that does not open a gap. The authors compared however the results of their self-gravitating calculations (where both the planet and the disc feel the disc gravity) to those obtained with the misleading situation of a planet freely migrating in a disc without self-gravity. As shown by figure 4.8, comparing both situations would lead us to the same conclusion. There is therefore no contradiction between their findings and ours. From now on, we do not distinguish the *gravity* and *self-gravity* designations, since the planet and the disc orbit within the same potential in our calculations. Whenever calculations with disc gravity are mentioned, they refer to the fsg situation.

4.5.3 Comparison with analytical results

In this section, we apply again the analytical model used in sections 4.4.2 and 4.5.2 in order to provide a simple estimate of the torque relative difference between the fsg and nog situations. This is motivated again by the fact that the shift induced by the fsg situation has same order of magnitude at ILR and OLR (PH05). The difference of the one-sided Lindblad torques between the fsg and nog situations is analogous to equation (4.10):

$$\Gamma_{\text{fsg}} - \Gamma_{\text{nog}} \approx \frac{1}{h} \int_0^\infty \left(\frac{\partial T}{\partial x} \right)_{x=x_{\text{fixed}}, \xi} \delta x d\xi, \quad (4.17)$$

except that δx is this time given by equation (4.15). Combining equations (4.5) to (4.9), and (4.17), we are left with

$$\left| \frac{\Gamma_{\text{fsg}} - \Gamma_{\text{nog}}}{\Gamma_{\text{nog}}} \right| = \frac{2I}{3Q}, \quad (4.18)$$

⁴The torque relative difference scales with Q^{-1} in the fsg situation, while it scales with $(Qh)^{-1}$ with in free biased case. The relative difference in the former case is thus reduced by a factor of $\sim h$ compared to the latter case, that is by an order of magnitude.

where

$$I = 3 \times \frac{\int_0^\infty \frac{\xi^3}{(1+\xi^2)^{5/2}(1+4\xi^2)} d\xi}{\int_0^\infty \frac{\xi^2}{(1+\xi^2)^{3/2}(1+4\xi^2)} d\xi} = \frac{2\sqrt{3} - \log(7+4\sqrt{3})}{\sqrt{3} - \pi/3} \approx 1.21. \quad (4.19)$$

Not surprisingly, the relative difference of the one-sided Lindblad torques scales with the inverse of Q , assuming high to moderate values of Q . This is of course the same scaling as for the relative difference of the differential Lindblad torques (see section 4.5.2 and figure 4.7).

We come to a quantitative comparison of our results of calculations with our analytical estimate, given by equation (4.18), and the analytical results of PH05, who estimated the dependence of the differential Lindblad torque on the disc mass, for a fully self-gravitating disc (see their figure 4b). Another series of fsg calculations was performed with disc parameters similar to those of PH05, namely a $h = 5\%$ disc aspect ratio, a planet mass corresponding to the linear regime (its value is precised below). We vary the disc surface density at the planet's orbital radius from $\Sigma_p = 4 \times 10^{-4}$ to $\Sigma_p = 10^{-2}$. This corresponds to varying Q from 40 to 1.6. The runs lasted for 10 planet's orbital periods, which was long enough to get stationary torques for the largest values of Q , but short enough to avoid a significant growth of non-axisymmetric perturbations for the lowest values of Q , probably due to SWING amplification (Toomre 1964). As we aim at comparing the results of two-dimensional calculations with analytical expectations (for which there is no softening parameter), we investigated how much our results of calculations depend on the softening length. For this purpose, the calculations were performed with three values of ε : $0.1H(r_p)$, $0.3H(r_p)$ and $0.6H(r_p)$. The planet mass is $M_p = 4.4 \times 10^{-6}M_*$ for $\varepsilon = 0.3H(r_p)$ and $\varepsilon = 0.6H(r_p)$, whereas $M_p = 10^{-6}M_*$ for $\varepsilon = 0.1H(r_p)$. This choice ensures that the Bondi radius to softening length ratio does not exceed $\sim 10\%$ for each value of ε .

Each calculation was performed with and without disc gravity, so as to compute the relative difference of the torques between both situations. The reason why we compute this relative difference is that it does not depend on the details of the torque normalization, be it for the numerical or the analytical results. Nonetheless, PH05 only calculated the normalized torque in the fsg situation as a function of the disc mass. We then evaluated their normalized torque without disc gravity by extrapolating their torque with disc gravity in the limit where the disc mass tends to zero. Figure 4.9 displays the relative difference of the torques between the fsg situation (γ_{fsg}) and the nog situation (γ_{nog}), obtained with our calculations, the analytical expectation of PH05 and our analytical estimate. This relative difference grows faster than linearly with Σ_p , although a linear approximation is valid at low surface density, as already stated in section 4.5.2. Our linear estimate is in agreement with the results of calculations with $\varepsilon = 0.6H(r_p)$ up to $Q \sim 3$, where it leads to a torque enhancement that is typically half the one estimated by PH05. Furthermore, our results of calculations depend much on ε , more especially at high Σ_p . For a given value of Σ_p , the relative difference of the torques decreases as ε increases. Differently stated, increasing the softening length reduces γ_{fsg} more significantly than γ_{nog} .

We comment that our calculation results with $\varepsilon = 0.1H(r_p)$, which matches the mesh resolution in the planet vicinity, are in quite good agreement with the analytical prediction of PH05. The relative difference between our results and theirs is $\sim 15\%$ for $Q \sim 8$, and does not exceed $\sim 30\%$ for $Q \leq 2$. This confirms that the impact of the disc gravity on the differential Lindblad torque may be exclusively accounted for by a shift of Lindblad resonances.

We would like to stress however that our calculations display a relative difference that is always stronger than the one obtained with PH05 estimate, which does not involve a softening

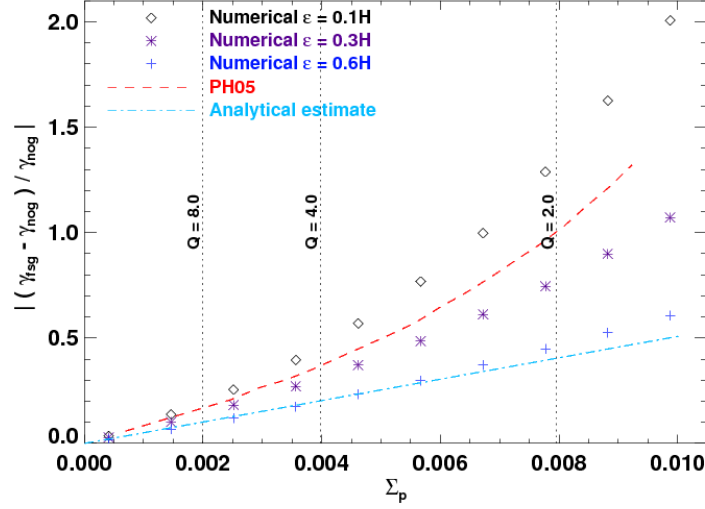


FIGURE 4.9: Relative difference of the torques between with the fsg situation (γ_{fsg}) and the nog situation (γ_{nog}) as a function of the disc surface density Σ_p . We compare the results of our calculations (each symbol refers to a different value of the softening length ϵ) with the analytical results of PH05 (dashed curve), and our analytical estimate (dash-dotted curve, see text and equation (4.18)). The vertical dotted lines display different values of the Toomre parameter at the planet location.

parameter. We give hereafter more insight into this result. We propose to evaluate for each azimuthal wavenumber m the shift of the Lindblad resonances induced by our fsg calculations, and compare it with its theoretical expression given by equation (4.15). This theoretical expression predicts that the shifts at inner and outer resonances are of opposite sign, their absolute value, which we denote by $\delta x_{th,m}$, being identical. We furthermore denote by $\delta x_{num,m}$ the shift (in absolute value) inferred from our calculations, and by $\Gamma_{fsg,m}^i$ ($\Gamma_{fsg,m}^o$) the m^{th} Fourier component of the inner (outer) Lindblad torque of a fsg calculation. We use similar notations for a nog calculation, and we drop hereafter the m subscripts for the sake of legibility. A first-order expansion yields

$$\Gamma_{fsg}^i = \Gamma_{nog}^i + \partial_x \Gamma_{nog}^i \delta x_{num} \quad \text{and} \quad \Gamma_{fsg}^o = \Gamma_{nog}^o - \partial_x \Gamma_{nog}^o \delta x_{num}. \quad (4.20)$$

To estimate the quantities $\partial_x \Gamma_{nog}^i$ and $\partial_x \Gamma_{nog}^o$, we performed an additional nog calculation, mentioned as *nogo* calculation, for which we imposed a slight, known shift of the resonances. This was done by fixing the planet's angular velocity at $\Omega_p - \delta\Omega_p$, with $\delta\Omega_p = 10^{-5}\Omega_p$. This slight decrease of the planet's angular velocity, with respect to the nog situation, implies an outward shift of inner and outer Lindblad resonances that reads $\delta x_o = (2\delta\Omega_p)/(3h\Omega_p)$, expression that is independent of m . With similar notations as before for the *nogo* calculation, and using again a first-order expansion, we have

$$\Gamma_{nogo}^i = \Gamma_{nog}^i + \partial_x \Gamma_{nog}^i \delta x_o \quad \text{and} \quad \Gamma_{nogo}^o = \Gamma_{nog}^o + \partial_x \Gamma_{nog}^o \delta x_o. \quad (4.21)$$

Combining equations (4.20) and (4.21), we are finally left with

$$\delta x_{num} = \frac{(\Gamma_{fsg}^i - \Gamma_{fsg}^o) - (\Gamma_{nog}^i - \Gamma_{nog}^o)}{(\Gamma_{nogo}^i + \Gamma_{nogo}^o) - (\Gamma_{nog}^i + \Gamma_{nog}^o)} \times \delta x_o. \quad (4.22)$$

We plot in figure 4.10 the ratio $\delta x_{num}/\delta x_{th}$ as a function of the azimuthal wavenumber m , for $\Sigma_p = 2 \times 10^{-3}$ ($Q \sim 8$). We first comment that the ratio is negative for $m \leq 6$, positive beyond, with a divergent behavior at the transition. We checked that this behavior is caused by

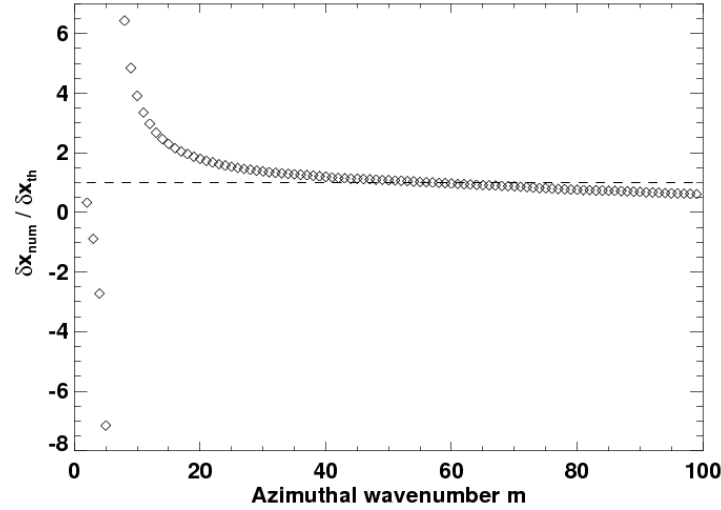


FIGURE 4.10: Ratio of δx_{num} , the shift of Lindblad resonances obtained with our fsg calculations (see equation (4.22)), and of δx_{th} , its analytically expected value (see equation (4.15)).

a change of sign of the denominator⁵ of equation (4.22), which is negative for $m \leq 6$ and positive beyond. Furthermore, the ratio $\delta x_{\text{num}}/\delta x_{\text{th}}$ is significantly greater than unity for m ranging from ~ 7 to ~ 20 , that is for the dominant Lindblad resonances. Differently stated, the dominant Lindblad resonances are more shifted by our calculations than analytically expected by PH05, which explains why the torque enhancement is more important with our calculations. Beyond, the ratio is close to unity for a rather large range of high m -values. This confirms that for high values of m the WKB approximation yields analytical estimates that are in good agreement with the results of numerical simulations. However, since our calculations involve a softening parameter, the ratio does not converge when increasing m , and slowly tends to zero. We checked that the value of m for which the ratio becomes lower than unity increases when decreasing the softening length. This explains why the torque enhancement is increasingly important at smaller softening length, as inferred from figure 4.9.

4.6 The anisotropy model

4.6.1 Motivation

In section 4.5, we have investigated the impact of the disc gravity on the differential Lindblad torque for low-mass planets. The torque of an asg calculation (where only the axisymmetric component of the disc self-gravity is taken into account) is close to that of a nog calculation (without disc gravity). However, a fsg calculation (which furthermore involves the non-axisymmetric contribution of the self-gravity) displays a significant increase of the torque, which can be exclusively accounted for by a shift of the LR.

We propose in this section to model this torque enhancement for low-mass planets. Our model aims at calculating only the axisymmetric part of the disc self-gravity, and applying an additional shift of the LR that mimics the one of its non-axisymmetric part. Altering the location of the LR comes to modifying the dispersion relation of the density waves. The dispersion relations of the asg and fsg cases differ only from the $-2\pi G\Sigma m/r$ term [in the WKB approximation, see equations (4.13) and (4.14)]. There is however no straightforward way to add an extra term

⁵This denominator corresponds to the difference of the differential Lindblad torques between the nog and nogo situations, expected to be positive for all m .

proportional to m in the dispersion relation D_{asg} of the asg situation. We propose to multiply the $m^2 c_s^2 / r^2$ term of D_{asg} by a constant, positive factor $1 - \alpha$, with $\alpha > 0$ to ensure that LR are shifted toward the orbit. This can be achieved by multiplying the azimuthal pressure gradient $\partial_\varphi P$ by $1 - \alpha$ in the Navier-Stokes equation or, differently stated, by assuming an *anisotropic pressure tensor*, for which the pressure in the azimuthal direction reads $P_\varphi = (1 - \alpha)P_r$, where P_r , the pressure in the radial direction, is given by $P_r = \Sigma c_s^2$. We call α the anisotropy coefficient. When an asg calculation includes the anisotropic pressure model, it is mentioned as an *asg+ap* calculation. An important point is that the anisotropy model does not alter the radial pressure gradient. Thus, it does not alter the rotational equilibrium of the disc, nor does it introduce a shift of the corotation resonance (the latter point is especially important when the disc is described with an adiabatic energy equation, case for which the corotation torque depends dramatically on the location of the corotation resonance. This will be detailed in chapter 5).

We now explain how to take the adequate value for the anisotropy coefficient. As previously, we assume an initial surface density profile scaling with $r^{-3/2}$, inducing a negligible⁶ vortensity gradient, hence a negligible corotation torque. Thus, the torques obtained with our calculations only include the differential Lindblad torque. We denote by Γ_{fsg} , Γ_{asg} and $\Gamma_{\text{asg+ap}}$ the differential Lindblad torques obtained with the fsg, asg and asg+ap calculations. Our model aims at imposing that

$$\Gamma_{\text{asg+ap}} - \Gamma_{\text{asg}} = \Gamma_{\text{fsg}} - \Gamma_{\text{asg}}. \quad (4.23)$$

A first-order expansion of the left-hand side of equation (4.23) with α , and of its right-hand side with Q^{-1} leads to

$$\alpha = \beta Q^{-1}, \quad (4.24)$$

where

$$\beta = \frac{(\partial \Gamma_{\text{fsg}} / \partial Q^{-1})_{Q^{-1}=0}}{(\partial \Gamma_{\text{asg+ap}} / \partial \alpha)_{\alpha=0}}. \quad (4.25)$$

The parameter β depends only on the softening length to disc scale height ratio $\eta = \varepsilon/H$. We calculated it for $\eta = 0.1, 0.3$ and 0.6 for small, fixed values of α and Q^{-1} , which we denote with a zero subscript. For each value of η , we performed an asg, an asg+ap and a fsg calculation with $q = 10^{-6}$ and $h = 5\%$, corresponding to a Bondi radius to softening length ratio of $\sim 2.7\%$. Furthermore, we adopted $\Sigma_p = 5 \times 10^{-4}$, yielding $Q_0^{-1} \sim 0.03$. The asg+ap calculation had $\alpha_0 = 0.01$. Using equation (4.25), the parameter β was therefore calculated by

$$\beta = \alpha_0 Q_0 \frac{\Gamma_{\text{fsg}} - \Gamma_{\text{asg}}}{\Gamma_{\text{asg+ap}} - \Gamma_{\text{asg}}}. \quad (4.26)$$

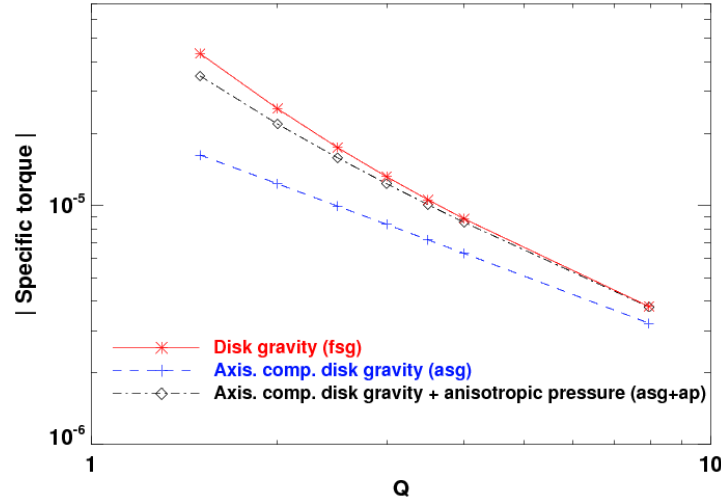
We display in table 4.3 the values of β for $\eta = 0.1, 0.3$ and 0.6 . We note that our anisotropic pressure model should be applied only when $Q > \beta$ to satisfy the constrain $1 - \alpha > 0$. This is not a stringent constrain since $\beta < 1$ for these values of η .

We comment that the value of m for which the resonance shifts induced by the self gravity and by the anisotropic pressure are equal is beyond the torque cut-off. Several reasons may conspire for that:

- For a given shift, the relative torque variation is larger for resonances that lie closer to the orbit, which gives more weight to high- m component.

⁶With a uniform disc aspect ratio, the vortensity gradient vanishes for a non self-gravitating disc while it is negligible, but does not cancel out, for a self-gravitating disc.

$\eta = \varepsilon/H$	β
0.1	0.32(4)
0.3	0.61(4)
0.6	0.94(1)

TABLE 4.3: Calculation of the anisotropy coefficient: values of β for different values of η .FIGURE 4.11: Specific torque exerted on a $M_p = 10^{-6}M_*$ planet mass, as a function of the Toomre parameter Q at the planet location. We display the torques obtained with asg calculations (plus signs), fsg calculations (asterisks) and asg+ap calculations (diamonds).

- The shifts estimated by a WKB analysis may dramatically differ from the real shifts (see section 4.5.3), especially at low $-m$, where significant torque is exerted.
- The torque expression for an anisotropic pressure has not been worked out in the literature, and may differ from the standard expression (Ward 1997), with the consequence that equal shifts will not yield equal torque variations.

4.6.2 Validity

We first test the validity of our model by performing a series of calculations with Q ranging from 1.5 to 8. From equation (4.12), Q can be set by varying either h or Σ_p . Varying h however alters the ratio r_B/ε , which controls the flow linearity in the planet vicinity. We therefore fixed $h = 0.05$ and varied Σ_p . The planet to primary mass ratio is $q = 10^{-6}$, the softening length is $\varepsilon = 0.3H(r_p)$. For each value of Q , we performed a fsg, an asg, and an asg+ap calculation, for which the anisotropy coefficient is $\alpha = \beta/Q$, with $\beta = 0.614$ (see table 4.3). The results are displayed in figure 4.11. As expected from the first-order expansion in Q^{-1} used to derive equation (4.24), the difference between the torques of the fsg and asg+ap calculations increases when decreasing Q . The relative difference is $\sim 0.4\%$ for $Q = 8$, $\sim 10\%$ for $Q = 2.5$, and reaches $\sim 25\%$ for $Q = 1.5$. The anisotropic pressure model therefore reproduces the torque of a fsg calculation with a good level of accuracy up to $Q \sim 4$.

The robustness of our model is furthermore tested against the onset of non-linearities, by varying the planet to primary mass ratio q . The Toomre parameter at the planet location is

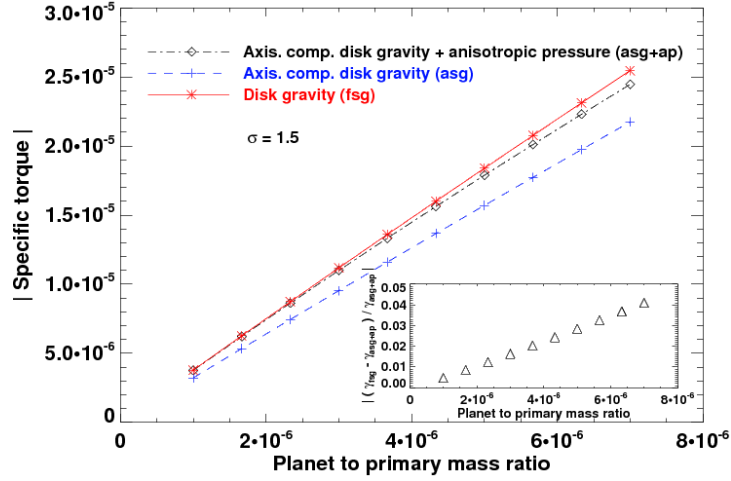


FIGURE 4.12: *Specific torque as a function of the planet to primary mass ratio. Calculations obtained with the anisotropic pressure model (asg+ap) are compared with axisymmetric self-gravitating calculations (asg) and fully self-gravitating calculations (fsg). The close-up displays the relative difference of the torques between the fsg and asg+ap situations. For all these calculations, $Q = 8$ at the planet location (the disc mass is $\sim 0.024M_*$).*

fixed at $Q = 8$. A series of asg, asg+ap and fsg calculations was performed with q ranging from 10^{-6} to 7×10^{-6} , hence with r_B/ε ranging from $\sim 2.7\%$ to $\sim 18.7\%$. Figure 4.12 displays the specific torque as a function of q for each calculation. The torques obtained with the fsg and asg+ap agree with a good level of accuracy. Their relative difference, shown in the close-up, increases almost linearly from $\sim 0.4\%$ to $\sim 4\%$, due to the onset of non-linearities.

These results indicate that the anisotropic pressure model succeeds in reproducing the *total torque* obtained with a fully self-gravitating disc, as far as a low-mass planet, a high to moderate Toomre parameter, and a surface density profile scaling with $r^{-3/2}$ are considered. With these limitations, these results present another confirmation that the impact of the disc gravity on the differential Lindblad torque can be entirely accounted for by a shift of the LR. We suggest that in the restricted cases mentioned above, the anisotropic pressure model could be used as a low-computational cost method to model the contribution of the disc gravity. We finally comment that, not surprisingly, these results do not differ if the planet freely migrates in the disc, which we checked with long-term fsg and asg+ap calculations (not presented here).

4.7 Corotation torque issues

Hitherto, we have considered an initial surface density profile scaling with $r^{-3/2}$, inducing a negligible vortensity gradient, hence a negligible corotation torque. This assumption ensured that the torques derived from our calculations accounted only for the differential Lindblad torque. It enabled a direct comparison with analytical expectations focusing on the differential Lindblad torque. We release this assumption and evaluate the impact of the disc self-gravity on the corotation torque Γ_C , in the linear regime. For a disc without self-gravity, [Masset et al. \(2006a\)](#) showed that the corotation torque is well approximated by the horseshoe drag expression, which reads (see section 2.3.2):

$$\Gamma_C = \frac{3}{4} x_s^4 \Omega^2(r_c) \Sigma(r_c) \left[\frac{d \ln(\Sigma/B)}{d \ln r} \right]_{r=r_c}, \quad (4.27)$$

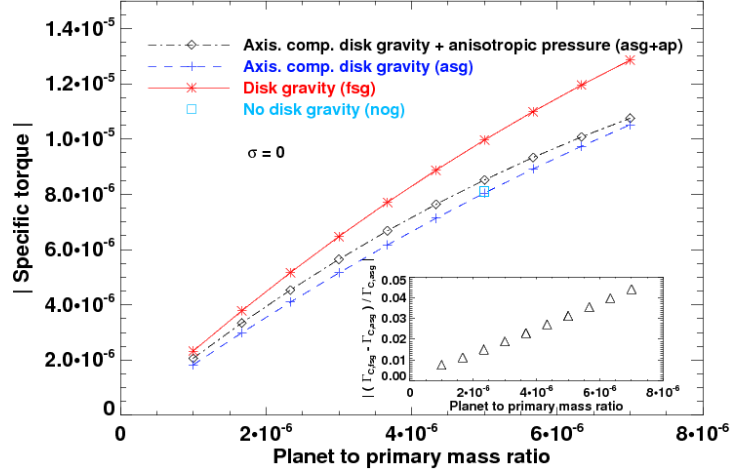


FIGURE 4.13: Same as figure 4.12, but for a flat initial surface density profile. The square corresponds to an additional nog calculation performed with $q = 5 \times 10^{-6}$. The close-up displays the relative difference of the corotation torques between the asg and fsg situations (see text and equation (4.30)).

where x_s is the half-width of the horseshoe region, r_c denotes the corotation radius, and $B = (2r)^{-1}d(r^2\Omega)/dr$ is half the vertical component of the flow vorticity. We denote by $\Gamma_{C,asg}$, $\Gamma_{C,asg+ap}$, and $\Gamma_{C,fsg}$ the corotation torques in the asg, asg+ap, and fsg situations. The same quantities without the C subscript refer to the total torque in the corresponding situation.

We performed the same set of asg, asg+ap and fsg calculations as in section 4.6.2, but with a flat initial surface density profile (we vary the planet to primary mass ratio q , for $Q = 8$). An additional nog calculation was also performed for $q = 5 \times 10^{-6}$. The results of these calculations are displayed in figure 4.13. The torques of the nog and asg calculations are hardly distinguishable, their relative difference being $\sim 2\%$, similarly as in section 4.5.1, where $\sigma = 1.5$. This difference should therefore be attributed to the differential Lindblad torque rather than to the corotation torque. It confirms that the corotation torque is not altered by the axisymmetric component of the disc gravity.

Furthermore, the torques of the fsg runs are significantly larger than those of the asg+ap runs. Their relative difference varies from $\sim 11\%$ to $\sim 17\%$. We do not expect this difference to arise from the differential Lindblad torque, despite the change of σ . The differential Lindblad torques should therefore differ from $\sim 0.4\%$ to $\sim 4\%$, as for $\sigma = 1.5$ (close-up of figure 4.12). This reveals that the fsg situation, or the asg+ap situation, or both, boosts the (positive) corotation torque.

We expect in fact the asg+ap situation to enhance the corotation torque. [Masset et al. \(2006a\)](#) have estimated x_s for a disc without self-gravity, in the linear regime. Their estimate reads $x_s \approx 1.16r_p\sqrt{q/h}$. In the limit where the planet mass vanishes, a fluid element on a horseshoe separatrix has a circular trajectory and is only sensitive to the azimuthal gradient of the disc pressure. The above estimate of x_s therefore holds for an asg+ap calculation if one substitutes h with $\sqrt{1-\alpha}h$, which we checked by a streamline analysis. Thus, we expect the anisotropic pressure model to slightly increase the half-width of the horseshoe zone, thereby increasing the corotation torque as

$$\Gamma_{C,asg+ap} = \frac{\Gamma_{C,asg}}{1-\alpha}, \quad (4.28)$$

with $\Gamma_{C,asg}$ given by equation (4.27), and $\alpha = \beta/Q$.

To investigate whether the fsg situation also increases the corotation torque, we evaluate the

quantity $(\Gamma_{C,\text{fsg}} - \Gamma_{C,\text{asg}})/\Gamma_{C,\text{asg}}$, which can be recast as

$$\frac{\Gamma_{C,\text{fsg}} - \Gamma_{C,\text{asg}}}{\Gamma_{C,\text{asg}}} = \frac{\Gamma_{C,\text{fsg}} - \Gamma_{C,\text{asg+ap}}}{\Gamma_{C,\text{asg}}} + \frac{\Gamma_{C,\text{asg+ap}} - \Gamma_{C,\text{asg}}}{\Gamma_{C,\text{asg}}}. \quad (4.29)$$

Using equation (4.28), the second right-hand side of equation (4.29) reads $\alpha/(1 - \alpha)$, and is $\sim 8.4\%$. Moreover, for the sake of simplicity, we neglect the relative change of the differential Lindblad torques. This assumption applies to the smallest planet masses that we consider, for which, as stated above, this change does not exceed $\sim 1\%$. The first right-hand side of equation (4.29) therefore reads $(\Gamma_{\text{fsg}} - \Gamma_{\text{asg+ap}})/\Gamma_{C,\text{asg}}$. The quantity $\Gamma_{C,\text{asg}}$ can be connected with Γ_{asg} , using the estimate of [Tanaka et al. \(2002\)](#) for a flat surface density profile. This connection is motivated by the fact that both the differential Lindblad torque, and the corotation torque are almost identical in the nog and asg situations. This leads to $\Gamma_{C,\text{asg}} \approx -1.56\Gamma_{\text{asg}}$. Equation (4.29) finally reads

$$\frac{\Gamma_{C,\text{fsg}} - \Gamma_{C,\text{asg}}}{\Gamma_{C,\text{asg}}} = -\frac{\Gamma_{\text{fsg}} - \Gamma_{\text{asg+ap}}}{1.56\Gamma_{\text{asg}}} + \frac{\alpha}{1 - \alpha}. \quad (4.30)$$

This ratio is displayed in the close-up of figure 4.13. It shows that the fsg situation slightly enhances the corotation torque, but this enhancement does not exceed $\sim 4.5\%$ for the highest planet mass that we consider. For the smallest planet masses, it is negligible with respect to the increase of the corotation torque triggered by the asg+ap situation. Thus, the large difference between the torques of the asg+ap and fsg calculations can be exclusively accounted for by the boost of the corotation torque in the asg+ap situation. The slight increase of the corotation torque in the fsg calculations should be compared to that of the differential Lindblad torque, which typically amounts to $\sim 17\%$ (for $\sigma = 1.5$, see figure 4.12). This comparison indicates that the disc self-gravity does hardly change, if at all, the corotation torque.

4.8 Conclusions

We have investigated in this chapter the impact of the disc self-gravity on type I migration. The assumption customarily used in planet-disc calculations, namely a planet freely migrating in a disc without self-gravity, can lead to a strong overestimate of the migration rate. We provide a simple evaluation of this overestimate through figure 4.4. The drift rate can be overestimated by as much as a factor of two for a disc having three times the surface density of the minimum mass solar nebula. Such a factor is inappropriate for the accurate calculation of migration rates, which is one of the main objectives of disc-planet investigations. We emphasize that the planet and the disc must orbit within the same potential to provide unbiased estimates of the migration timescale.

The inclusion of the self-gravity in our calculations confirms that the disc gravity slightly accelerates type I migration. We have solved the apparent contradiction between the statements of [Nelson & Benz \(2003a;b\)](#) and [Pierens & H  r   \(2005\)](#) regarding the impact of the disc self-gravity on the migration rate. The increase of the differential Lindblad torque due to the disc gravity is typically one order of magnitude smaller than the spurious one induced by a planet freely migrating in a non self-gravitating disc. We provide again a simple evaluation of this torque increase with figure 4.7. It is found to depend only on the Toomre parameter at the planet location, whatever the mass distribution of the whole disc. In addition, we have shown that the torque increase can be entirely accounted for by a shift of the Lindblad resonances, and be modeled with an anisotropic pressure tensor. This model succeeds in reproducing the differential Lindblad torque of a self-gravitating calculation, but increases the corotation torque. This model enables us to conclude that there is no significant impact of the disc self-gravity

on the corotation torque, in the linear regime. Perspectives of this work will be addressed in chapter 7.

Chapter 5

On the corotation torque in adiabatic discs

WE EVALUATE THE COROTATION TORQUE between a two-dimensional gaseous disc and a uniformly rotating external potential, assuming that the disc flow is adiabatic. We derive in section 5.2 the linearized hydrodynamic equations at an isolated resonance. In section 5.3, we give a generalized expression of the corotation torque that involves the pressure perturbation, and which reduces to the usual dependence on the vortensity gradient in the limit of a cold disc. In the general case, we find an additional dependence on the entropy gradient. We check in section 5.3 our torque expression through customized two-dimensional hydrodynamical simulations.

Contents of this chapter

5.1	Introduction	98
5.2	Linear analysis at an isolated resonance	98
5.3	Corotation torque	100
5.3.1	Limit of a cold disc	102
5.3.2	General case	104
5.4	Numerical study of an isolated corotation resonance	106
5.4.1	Numerical method	106
5.4.2	Results	107
5.4.3	Dynamics of the corotation region	110
5.5	Conclusions	113

5.1 Introduction

As emphasized in chapter 1, planetary migration plays a key role in the formation and evolution of young planetary systems. One major issue in the current paradigm of planet migration is that the migration of low-mass planets (type I migration) should occur on timescales much smaller than the disc lifetime, see chapter 2. While it may explain the existence of the Hot Jupiters, it renders difficult the formation of giant planets at large distances from their central star (e.g. at several astronomical units, as in the Solar System). We described in section 2.3.3 several mechanisms that may slow down or even halt migration, and we underscored the potential importance of the corotation torque to act in this way. In particular, we mentioned the recent work of [Paardekooper & Mellema \(2006\)](#), who showed that type I migration could be reversed in adiabatic discs. They found the presence of underdense gas lagging the planet in the corotation region, which indicates that the corotation torque should be responsible for the migration reversal.

In order to further investigate these results, we consider the simplified situation of an inviscid, adiabatic two-dimensional disc. The unperturbed axisymmetric state of the disc is described in section 3.1.1. The only change of notations compared to previous chapters consists in denoting by u and v respectively the radial and azimuthal velocities. In addition, we will write with a “0” subscript the unperturbed quantities, and with a “1” subscript the perturbed ones. For instance, the gas pressure reads $p(r, \varphi) = p_0(r) + p_1(r, \varphi)$. We will make use of the two Oort’s constants:

$$A = \frac{1}{2r} \frac{d\Omega}{dr}, \quad (5.1)$$

which scales with the local shear in the flow, and:

$$B = \frac{1}{2r} \frac{d(r^2\Omega)}{dr} = \Omega + A, \quad (5.2)$$

which is half the vertical component of the flow vorticity, and which is also $(2r)^{-1}$ times the radial derivative of the specific angular momentum. We recall that the horizontal epicyclic frequency reads $\kappa = (4\Omega B)^{1/2}$.

5.2 Linear analysis at an isolated resonance

We study the linear response of the disc to a perturbing non-axisymmetric potential $\Phi(r, \varphi) = \Phi_m(r) \cos[m(\varphi - \Omega_p t)]$. The perturbing potential rotates at constant angular velocity Ω_p . In the inertial frame, the linearized Euler equations of the disc are:

$$\frac{\partial u_1}{\partial t} + \Omega \frac{\partial u_1}{\partial \varphi} - 2\Omega v_1 = -\frac{\partial \Phi}{\partial r} - \frac{1}{\Sigma_0} \frac{\partial p_1}{\partial r} + \frac{\Sigma_1}{\Sigma_0^2} \frac{\partial p_0}{\partial r} \quad (5.3)$$

and

$$\frac{\partial v_1}{\partial t} + \Omega \frac{\partial v_1}{\partial \varphi} + \frac{\kappa^2}{2\Omega} u_1 = -\frac{1}{r} \frac{\partial}{\partial \varphi} \left(\Phi + \frac{p_1}{\Sigma_0} \right). \quad (5.4)$$

The linearized continuity equation is:

$$\frac{\partial \Sigma_1}{\partial t} + \Omega \frac{\partial \Sigma_1}{\partial \varphi} + \frac{1}{r} \frac{\partial}{\partial r} (r \Sigma_0 u_1) + \frac{1}{r} \frac{\partial}{\partial \varphi} (\Sigma_0 v_1) = 0. \quad (5.5)$$

For the sake of simplicity, we will refer to the quantity $S = p\Sigma^{-\gamma}$ as the gas (specific) entropy, where γ is the adiabatic index (see equation (3.50) for a more rigorous expression). The disc

being inviscid and adiabatic, the energy equation reduces to the Lagrangian conservation of the entropy (see section 3.3.2). The linearized conservation of the entropy along element paths reads

$$\frac{\partial S_1}{\partial t} + \Omega \frac{\partial S_1}{\partial \varphi} + u_1 \frac{\partial S_0}{\partial r} = 0, \quad (5.6)$$

where $S_1 = S_0(p_1/p_0 - \gamma \Sigma_1/\Sigma_0)$. We furthermore assume that the gas is described by an ideal equation of state so that p_0 and Σ_0 are connected by $p_0 = \Sigma_0 c_s^2/\gamma$, c_s being the adiabatic sound speed (see equation (3.52)).

We assume a perturbation of the form $x_{1,m}(r) \exp(im\{\varphi - \Omega_p t\})$ where x_1 stands for any perturbed quantity of the flow¹. We note $\Delta\omega = m(\Omega_p - \Omega)$ and we use the prime notation to denote $\partial/\partial r$. Equation (5.6) can be recast as:

$$\Sigma_1 = \frac{p_1}{c_s^2} + \frac{i\mathcal{S}\Sigma_0 u_1}{r\Delta\omega}. \quad (5.7)$$

Combining equations (5.3), (5.4) and (5.7) we are led to:

$$\Sigma_0 u_1 = i\mathcal{F} \left[\frac{\Delta\omega}{\Omega} \left\{ (\Phi + \Psi)' - \frac{\mathcal{S}}{r} \Psi \right\} - \frac{2m}{r} (\Phi + \Psi) \right] \quad (5.8)$$

and

$$\Sigma_0 v_1 = \mathcal{F} \left[\frac{\kappa^2}{2\Omega^2} \left\{ (\Phi + \Psi)' - \frac{\mathcal{S}}{r} \Psi \right\} - \frac{m}{r} \left\{ \frac{\Delta\omega}{\Omega} + \mathcal{S}\mathcal{P} \frac{c_s^2/r^2}{\Delta\omega\Omega} \right\} (\Phi + \Psi) \right], \quad (5.9)$$

where \mathcal{S} and \mathcal{P} are given by

$$\mathcal{S} = \frac{1}{\gamma} \frac{d \ln S_0}{d \ln r} \quad (5.10)$$

and

$$\mathcal{P} = \frac{1}{\gamma} \frac{d \ln p_0}{d \ln r}, \quad (5.11)$$

where Ψ is defined as

$$\Psi = p_1/\Sigma_0 \quad (5.12)$$

and where \mathcal{F} is defined by

$$\mathcal{F} = \frac{\Sigma_0 \Omega}{D}, \quad (5.13)$$

with $D = \kappa^2 - \Delta\omega^2 - \mathcal{S}\mathcal{P}c_s^2/r^2$. We point out that, in an isothermal disc, Ψ corresponds to the perturbed flow enthalpy. Substituting equations (5.7), (5.8) and (5.9) into equation (5.5) gives the second-order differential equation for the perturbed quantity Ψ ,

$$\boxed{r^2(\Phi + \Psi)'' + r(\mathcal{B} + \mathcal{S})(\Phi + \Psi)' - r\mathcal{S}\Psi' + \mathcal{C}\Psi + \mathcal{D}\Phi = 0}, \quad (5.14)$$

where:

$$\mathcal{B} = 1 + \mathcal{V} - \frac{d \ln \Omega}{d \ln r}, \quad (5.15)$$

$$\begin{aligned} \mathcal{C} = & -\frac{D}{c_s^2/r^2} - 2m \frac{\Omega}{\Delta\omega} (\mathcal{V} + 2\mathcal{S}) - \mathcal{B}\mathcal{S} \\ & + \mathcal{S}^2 \left[(r/\mathcal{S})' - 1 \right] - m^2 \left(1 + \mathcal{S}\mathcal{P} \frac{c_s^2/r^2}{\Delta\omega^2} \right), \end{aligned} \quad (5.16)$$

¹We drop the subscript m in $x_{1,m}(r)$ to improve legibility.

$$\mathcal{D} = -2m \frac{\Omega}{\Delta\omega} (\mathcal{V} + \mathcal{S}) - m^2 \left(1 + \mathcal{S} \mathcal{P} \frac{c_s^2/r^2}{\Delta\omega^2} \right), \quad (5.17)$$

and

$$\mathcal{V} = \frac{d \ln \mathcal{F}}{d \ln r}. \quad (5.18)$$

Equation (5.14) reduces to the equation (15) of [Li et al. \(2000b\)](#) if one considers the propagation of free waves ($\Phi = 0$), while it reduces to the equation (13) of [Goldreich & Tremaine \(1979\)](#) (hereafter GT79) for an isentropic flow. There are two apparent singularities in equation (5.14). The first one is a real singularity that arises when $\Delta\omega = 0$, and which defines the corotation resonance. The angular momentum exchanged between the disc and the perturber at this location is calculated in section 5.3. The second one is regular and stems from $D(r) = 0$, whose roots define generalized locations for the Lindblad resonances in adiabatic discs. The last term in $D(r)$ is very small compared to the $m^2 c_s^2 / r^2$ term in the dispersion relation of density waves (see section 2.3), so its impact on the resonances location should be of negligible importance. Note however that, as the adiabatic sound speed is larger than the isothermal one, Lindblad resonances are located further from the orbit in the adiabatic case, with direct consequences on the torque. We expect indeed the differential Lindblad torque, which scales as c_s^{-2} , to be reduced by a factor of γ in the adiabatic case. This will be checked by hydrodynamic calculations in chapter 6, which confirms that the last term in the expression of $D(r)$ hardly alters the resonances location.

5.3 Corotation torque

We now estimate the rate of angular momentum exchanged between the perturber and the adiabatic disc described in last section. This rate therefore corresponds to the disc torque, which we denote by Γ , and which we define as the torque exerted by the disc on the perturber (unless otherwise stated). It reads:

$$\Gamma = \int_{\text{disc}} (\mathbf{r} \times d\mathbf{F}_{\text{disc} \rightarrow \text{perturber}}) \cdot \mathbf{e}_z = \int_{\text{disc}} \Sigma_1(r, \varphi) \frac{\partial \Phi}{\partial \varphi} r dr d\varphi. \quad (5.19)$$

We limit ourselves to the torque exerted by the disc material lying in the vicinity of corotation, hence to the corotation torque, which we denote by Γ_c . In equation (5.19), the real quantities Φ and Σ_1 can be written as the half-sum of their complex and complex conjugate, $\Sigma_1 = (\overline{\Sigma_1} + \Sigma_1^*)/2$ and $\Phi = (\overline{\Phi} + \Phi^*)/2$ (the star superscript denotes the complex conjugate). These complex quantities can be expressed as a series of contributions at each azimuthal wavenumber m ,

$$\overline{X}(r, \varphi) = \sum_{m>0} x_m(r) e^{im(\varphi - \Omega_p t)},$$

where $x_m(r) = \{\Sigma_{1,m}(r), \Phi_m(r)\}$. In the potential expansion, $\Phi_m(r)$ are real quantities. Keeping only the non-vanishing contributions to the integral, equation (5.19) is recast as:

$$\begin{aligned} \Gamma &= \frac{1}{4} \int r dr \int_0^{2\pi} d\varphi \left(\overline{\Sigma_1} \frac{\partial \Phi^*}{\partial \varphi} + \Sigma_1^* \frac{\partial \Phi}{\partial \varphi} \right) \\ &= \frac{1}{4} \int r dr \times 2i\pi \sum_{m>0} m \Phi_m(r) \underbrace{\{\Sigma_{1,m}^*(r) - \Sigma_{1,m}(r)\}}_{-2i \text{Im}(\Sigma_{1,m}(r))}, \end{aligned} \quad (5.20)$$

where Im denotes the imaginary part. Contrary to GT79, we do not neglect the radial variation of r and of $\Phi(r)$ compared to that of $\text{Im} \Sigma_{1,m}(r)$ across corotation. Using variable $x = (r - r_c)/r_c$,

where r_c denotes the corotation radius, the corotation torque takes the form $\Gamma_c = \sum_m \Gamma_{c,m}$, with

$$\Gamma_{c,m} = m\pi r_c^2 \int_{-\infty}^{\infty} dx \operatorname{Im}[\Sigma_{1,m}(x)] \Phi_m(x) (1+x). \quad (5.21)$$

We will now drop again m subscripts to improve legibility. As in GT79, we assume that the disc responds to a slowly increasing perturbation and take $\Delta\omega$ to have a small, positive imaginary part α :

$$\Delta\omega = m(\Omega_p - \Omega) + i\alpha \approx -mr_c\Omega'(r_c)(x + i\epsilon), \quad (5.22)$$

where $\epsilon = -\alpha/[mr_c\Omega'(r_c)] > 0$. In equation (5.22), the time α^{-1} may be interpreted as a characteristic timescale above which the linear analysis will fail (Paardekooper & Papaloizou 2008). We then substitute $\Sigma_0 u_1$ in equation (5.7) by the expression given by equation (5.8). Using equation (5.22), we find:

$$\Sigma_1(x) = \Psi(x) \left[\frac{\Sigma_0}{c_s^2} + \frac{\mathcal{FS}^2}{r^2\Omega} \right]_{r_c} - \frac{(\Phi + \Psi)(x)}{x + i\epsilon} \left[\frac{2\mathcal{FS}}{r^3\Omega'} \right]_{r_c} + \frac{d(\Phi + \Psi)(x)}{dx} \left[\frac{3\mathcal{FS}}{2r^3\Omega'} \right]_{r_c}. \quad (5.23)$$

Note that in the first term on the right-hand side of equation (5.23), the second term in the bracket is much smaller compared with the first one, by a factor $\sim h^2$, with h the disc aspect ratio at the corotation resonance. We are primarily interested in the imaginary part of Σ_1 to evaluate the corotation torque. We stress that the torques between the disc and the perturber converge as ϵ tends to zero. In the limit $\epsilon \rightarrow 0$, we are left with:

$$\begin{aligned} \operatorname{Im}[\Sigma_1(x)] &= \operatorname{Im}[\Psi(x)] \left[\frac{\Sigma_0}{c_s^2} \right]_{r_c} + \pi\delta(x)[\Phi + \operatorname{Re}(\Psi)](x) \left[\frac{2\mathcal{FS}}{r^3\Omega'} \right]_{r_c} \\ &\quad - \frac{\operatorname{Im}[\Psi(x)]}{x} \left[\frac{2\mathcal{FS}}{r^3\Omega'} \right]_{r_c} + \frac{d\operatorname{Im}\Psi(x)}{dx} \left[\frac{3\mathcal{FS}}{2r^3\Omega'} \right]_{r_c}, \end{aligned} \quad (5.24)$$

where Re stands for the real part, and $\delta(x)$ is Dirac's delta function. Each term on the right-hand side of equation (5.24) yields a contribution to the corotation torque. We now provide an order of magnitude estimate of these contributions, that we denote respectively by $\gamma_{c,m,1}$ to $\gamma_{c,m,4}$. They write

$$\gamma_{c,m,1} = \frac{1}{h^2} \int_{-\infty}^{\infty} \Phi(x) \operatorname{Im}\Psi(x) (1+x) dx \quad , \quad \gamma_{c,m,2} = \Phi(r_c) \{ \Phi(r_c) + \operatorname{Re}\Psi(r_c) \} \quad (5.25)$$

and

$$\gamma_{c,m,3} = - \int_{-\infty}^{\infty} \Phi(x) \frac{\operatorname{Im}\Psi(x)}{x} (1+x) dx \quad , \quad \gamma_{c,m,4} = \int_{-\infty}^{\infty} \Phi(x) \frac{d\operatorname{Im}\Psi(x)}{dx} (1+x) dx. \quad (5.26)$$

We evaluate the latter quantities for two calculations of section 5.4.2. The numerical setup used for these runs will be presented in section 5.4.1. In short, we use the FARGO code to solve the hydrodynamic equations with the Fourier component of $m = 3$ of an external, rotating potential. The contributions to the corotation torques $\gamma_{c,m,1}$ to $\gamma_{c,m,4}$ are calculated with equations (5.25) and (5.26), with $\Psi = p_1/\Sigma_0$ evaluated numerically. The results are displayed in table 5.1 for the run with a flat potential profile, and the one having a peaked potential profile with $\mathcal{S} \approx 0.43$ (see section 5.4.2). The first and second contributions are of same order of magnitude, and are much larger than the third and fourth contributions. The high value of $\gamma_{c,m,1}$, compared to $\gamma_{c,m,3}$ and $\gamma_{c,m,4}$, stems from the h^{-2} factor preceding the integral. We can therefore safely neglect the torque contributions arising from the last two terms on the

Potential	$\gamma_{c,m,1}$	$\gamma_{c,m,2}$	$\gamma_{c,m,3}$	$\gamma_{c,m,4}$
Flat	-2×10^{-11}	5×10^{-12}	6×10^{-15}	-4×10^{-15}
Peaked	4×10^{-12}	4×10^{-12}	5×10^{-15}	-4×10^{-15}

TABLE 5.1: Order of magnitude estimate of the four contributions to the corotation torque $\gamma_{c,m,1}$ to $\gamma_{c,m,4}$, given by equations (5.25) and (5.26). These contributions are calculated with two numerical simulations of section 5.4.2, for which the radial profile of the external potential is either flat (first line) or peaked around the corotation radius (second line, see text). In both cases, the first and second contributions have same order of magnitude and are much larger compared to the third and fourth one.

right-hand side of equation (5.24). Furthermore, we checked that neglecting the radial variation of the term $(1+x)\Phi(x)$ in equation (5.21) induces a relative error on the torque evaluation that does not exceed $\sim 5\%$. It confirms the assumption made by GT79, who treat all quantities in equation (5.21), except $\text{Im}\Psi(x)$, the most rapidly varying, as uniform. We will now use the same approximation. This will greatly simplify the calculation of $\gamma_{c,m,1}$ in the limit of a cold disc, as we shall see in section 5.3.1).

We are at the end left with two contributions to the corotation torque, arising from the first two terms of the right-hand side of equation (5.24), that read respectively:

$$\Gamma_{c,m,1} = \left[\frac{m\pi\Sigma_0 r^2 \Phi}{c_s^2} \right]_{r_c} \int_{-\infty}^{\infty} dx \text{Im}[\Psi(x)] \quad (5.27)$$

$$\Gamma_{c,m,2} = \left[\frac{2m\pi^2 \mathcal{F} \mathcal{S} \Phi (\Phi + \text{Re}(\Psi))}{r\Omega'} \right]_{r_c}. \quad (5.28)$$

The term $\Gamma_{c,m,1}$ is the contribution of the function Ψ , such as in the isentropic case. The second term, $\Gamma_{c,m,2}$, corresponds to a singularity at corotation, associated to a non-vanishing entropy gradient. It corresponds to the torque arising from the advection of entropy in the corotation region, which results in a surface density perturbation if the entropy is not uniform. The perturbation is *singular* for the surface density and the entropy, but not for the pressure (we will come back on this statement in the next paragraph). Some further insight into the dynamics of this perturbation will be given in section 5.4.3. It remains confined to corotation, where it yields a *finite* contribution to the torque. Our contribution estimate above points out that $\Gamma_{c,m,2}$ has same order of magnitude than $\Gamma_{c,m,1}$. We provide in the next section an expression for the corotation torque in the limit of a cold disc, then we turn to the general case.

5.3.1 Limit of a cold disc

We contemplate here the case for which $|\Psi| \ll |\Phi|$, which we refer to as a cold case. This condition depends on the strength of the perturbing potential, its radial scale, and on the disc temperature. In particular, in the planetary context, some corotation resonances may correspond to a cold situation, while others have $|\Psi| \sim |\Phi|$. Nevertheless, a given resonance eventually satisfies the cold case condition as the disc temperature tends to zero.

The evaluation of equation (5.27) requires an explicit expression for Ψ , obtained by solving the differential equation (5.14) in the vicinity of corotation. This has been done by GT79 for a cold isentropic disc. An explicit solution can also be obtained for a cold adiabatic disc within the same level of approximation. Note however that some additional difficulties arise, in particular

the existence of a *double pole* (term proportional to $\Delta\omega^{-2}$) in the coefficients \mathcal{C} and \mathcal{D} , defined respectively by equations (5.16) and (5.17). We discard the double pole for the following reasons:

- Unlike the simple pole, it scales with c_s^2 , which indicates that when the disc aspect ratio tends to zero, it becomes negligible; differently stated, there should be a critical disc thickness under which it is safe to neglect this term.
- This term is the only one that depends both on the entropy and on the pressure gradients. As we shall see at the next chapter, our results of calculations for a planet embedded in a disc with aspect ratio $h = 0.05$ show that the torque excess with respect to an isothermal situation essentially depends on the entropy gradient, which indicates that already for $h = 0.05$ the double pole term is negligible.
- The double pole is regularized with a very small amount of dissipation. Even the molecular viscosity suffices to render it negligible in the discs that we consider (S.-J. Paardekooper, 2007, private communication).

Discarding the double pole, and within the same level of approximation as GT79, equation (5.14) can be recast, in the vicinity of the corotation, as

$$\frac{d^2\Psi}{dx^2} - q^2\Psi = -\frac{P_1\Phi(r_c)}{x + i\epsilon}, \quad (5.29)$$

where

$$P_1 = \left[\frac{2\Omega}{r\Omega'} (\mathcal{V} + \mathcal{S}) \right]_{r_c} \quad \text{and} \quad q = (Dr/c_s)_{r_c} \approx (\kappa r/c_s)_{r_c}.$$

Solving the corresponding homogeneous equation, then using the variation of parameters technique, the general solution of equation (5.29) reads

$$\Psi(x) = \frac{P_1}{2q}\Phi(r_c) \left[e^{qx} \int_x^\infty \frac{dt}{t + i\epsilon} e^{-qt} + e^{-qx} \int_{-\infty}^x \frac{dt}{t + i\epsilon} e^{qt} \right], \quad (5.30)$$

which reduces to the equation (53) of GT79 when $\mathcal{S} = 0$. Combining equations (5.27) and (5.30) yields the contribution $\Gamma_{c,m,1}$ to the corotation torque:

$$\Gamma_{c,m,1} = \Gamma_0 [(\mathcal{V} + \mathcal{S})\Phi^2]_{r_c}, \quad (5.31)$$

where $\Gamma_0 = -(m\pi^2\Sigma_0)/(2Br\Omega')$ is to be evaluated at the corotation radius. It can be approximated as $(4m\pi^2\Sigma_0/3\Omega^2)_{r_c}$ in a Keplerian disc. It is thus a positive quantity.

The second contribution to the corotation torque, given by equation (5.28), is specific to the adiabatic case and involves the singularity arising from the entropy advection. Using equation (5.28) and noting that $|\text{Re}(\Psi)| \ll |\Phi|$, this contribution to the corotation torque reads

$$\Gamma_{c,m,2} = -\Gamma_0 [\mathcal{S}\Phi^2]_{r_c}. \quad (5.32)$$

From equations (5.31) and (5.32), we infer the corotation torque for a cold, adiabatic disc, which reads:

$$\boxed{\Gamma_{c,m} = \Gamma_0 [\mathcal{V}\Phi^2]_{r_c}}. \quad (5.33)$$

This expression does not depend on \mathcal{S} . We note from equations (5.13) and (5.18) that \mathcal{V} can be approximated as

$$\mathcal{V} = \frac{d \ln \Sigma_0 / B}{d \ln r}, \quad (5.34)$$

since the disc aspect ratio at corotation $h(r_c) = c_s(r_c)/[r_c\Omega(r_c)]$ satisfies $h(r_c) \ll 1$. Equation (5.33) therefore corresponds to the corotation torque expression² of GT79. This argues that the corotation torque for a cold case does not depend on whether the disc can radiate energy efficiently (assuming a locally isothermal equation of state) or not (assuming an adiabatic energy equation). This can be expected on general grounds: in the cold disc limit, the internal energy of the fluid is negligible with respect to its mechanical energy, hence the power (and the torque) of the tidal force correspond to the case of non-interacting test particles, for which the expression of GT79 prevails.

5.3.2 General case

We consider in this section the general case where we cannot neglect Ψ with respect to Φ in equations (5.27) and (5.28), as we have done in the previous section. Instead of resorting to a solution of equation (5.14), we shall use a method similar to the method used by Tanaka et al. (2002), based on the jump of angular momentum flux at corotation. In the case of Tanaka et al. (2002), this eventually yields a torque expression similar to the expression of GT79, except that Φ has to be substituted by $\Phi + \Psi$ (as stated in section 5.2, Ψ corresponds to the enthalpy perturbation in the isothermal case, where it is usually denoted by η). The drawback of this method is that it provides a torque expression that features the *unknown* solution $\Psi = p_1/\Sigma_0$ of the differential equation for the perturbations. Nevertheless, it gives some insight into the dynamics of the corotation region, and allows to draw the general trends of the corotation torque in the adiabatic limit. We note that in the isothermal case, Zhang & Lai (2006) have provided an explicit solution for the perturbed enthalpy at corotation, leading to a corotation torque expression that only depends on the forcing potential.

The angular momentum flux F_A is given (Goldreich & Tremaine 1979):

$$F_A = \Sigma_0 r^2 \int_0^{2\pi} \text{Re}(u)\text{Re}(v)d\varphi = \pi\Sigma_0 r^2 \text{Re}(uv^*). \quad (5.35)$$

Equation (5.35) can thus be written as $F_A = \sum_m F_{A,m}$ with:

$$F_{A,m} = \pi\Sigma_0 r^2 [\text{Re}(u_1)\text{Re}(v_1) + \text{Im}(u_1)\text{Im}(v_1)]. \quad (5.36)$$

Combining equations (5.8), (5.9) and (5.36), we obtain

$$\begin{aligned} F_{A,m} &= \frac{m\pi\Sigma_0 r}{D} \left[\text{Im}(\Phi + \Psi) \frac{d\text{Re}(\Phi + \Psi)}{dr} - \text{Re}(\Phi + \Psi) \frac{d\text{Im}(\Phi + \Psi)}{dr} \right. \\ &\quad \left. + \frac{\mathcal{S}}{r} \{ \text{Re}(\Phi)\text{Im}(\Psi) - \text{Im}(\Phi)\text{Re}(\Psi) \} \right]. \end{aligned} \quad (5.37)$$

In the isentropic ($\mathcal{S} = 0$) case, equation (5.37) reduces to the expression used by Tanaka et al. (2002) in two-dimensions. The jump in the angular momentum flux is then given by $\sum_m \Delta F_{A,m}$, with

$$\Delta F_{A,m} = \lim_{r_c^+, r_c^- \rightarrow r_c} [F_{A,m}(r_c^+) - F_{A,m}(r_c^-)], \quad (5.38)$$

where $r_c^+ > r_c$ and $r_c^- < r_c$ denote the locations respectively beyond and before corotation.

Tanaka et al. (2002) showed that $\Phi + \Psi$ is continuous at corotation in the isothermal case, with no assumption on Φ and Ψ . Here, since equation (5.14) cannot be recast as an ordinary differential equation involving only $\Phi + \Psi$, we have to consider more stringent albeit reasonable

²They have a negative sign because they consider the torque exerted by the perturber on the disc.

assumptions, namely that both Φ and Ψ are *continuous* at corotation. The fact that Φ is continuous at corotation can be realized with an arbitrarily small softening length of the potential, in the case of an embedded point-like mass (for which the potential components would diverge logarithmically at corotation, in the absence of any softening). Assuming that Φ is continuous at corotation, equation (5.14) imposes that Ψ is also continuous at corotation; we would otherwise have a null linear combination of $\delta(x)$ and $\delta'(x)$ functions with non-vanishing coefficients, which is impossible. This implies that the disc pressure remains continuous at the corotation resonance, despite the singular behavior of the surface density and of the entropy.

We then integrate equation (5.14) over an infinitesimal interval containing $r = r_c$. All finite terms in this equation yield a vanishing contribution. In particular, our continuity assumption for Φ and Ψ , and thus for the sum $\Phi + \Psi$, implies that the term proportional to \mathcal{S} in the right-hand side of equation (5.37) does not contribute to the torque, so the jump in the advected flux will only come from the jump in $d(\Phi + \Psi)/dr$, as in the isothermal case. This reads:

$$\frac{d(\Phi + \Psi)}{dr}(r_c^+) - \frac{d(\Phi + \Psi)}{dr}(r_c^-) = \frac{i\pi}{r_c} [P_2(\Phi + \Psi)(r_c) - Q\Phi(r_c)], \quad (5.39)$$

where

$$P_2 = \left[\frac{2\Omega}{r\Omega'} (\mathcal{V} + 2\mathcal{S}) \right]_{r_c} \quad \text{and} \quad Q = \left[\frac{2\Omega}{r\Omega'} \mathcal{S} \right]_{r_c}.$$

Using equations (5.37), (5.38), (5.39) and $2B = \kappa^2/2\Omega$, we find that

$$\Delta F_{A,m} = \Gamma_0 [\{\mathcal{V} + 2\mathcal{S}\} |\Phi + \Psi|^2 - \mathcal{S} \Phi \text{Re}(\Phi + \Psi)]_{r_c}. \quad (5.40)$$

We stress that in the limit of a cold disc, the above expression of $\Delta F_{A,m}$ does not reduce to the corotation torque expression given by equation (5.33), but it reduces to the expression of $\Gamma_{c,m,1}$. This indicates that the jump of angular momentum flux at corotation *misses* the singular contribution of the entropy perturbation at corotation, and as such leads only to an evaluation of $\Gamma_{c,m,1}$. There is at least one case in which this important though non-trivial point can be easily understood, that of a uniform unperturbed pressure profile ($\mathcal{P} = 0$). The general solution of the set of hydrodynamic equations is divided into the solution of the homogeneous equations and a particular solution accounting for the forcing potential. In the adiabatic case, a solution of the homogeneous equations is associated to a singular perturbation of the surface density, of the form $\Sigma_1(x) \equiv \delta(x) \exp\{im(\varphi - \Omega_p t)\}$, and to vanishing perturbations of the pressure and of the velocity. Note from the radial Euler equation that this solution exists only if $\mathcal{P} = 0$. Note also that such solution does not exist in the barotropic situation, because the perturbations of the surface density and of the pressure cannot be separated. The above *particular solution*, for which the perturbed surface density cancels out everywhere but at the corotation radius, is not related to any advection of angular momentum ($F_{A,m}(r_c^+) = 0 = F_{A,m}(r_c^-)$), so it cannot be accounted for by the jump flux method. The torque contribution of this solution has to be calculated separately, as in the cold disc limit. This contribution is given by equation (5.28):

$$\Gamma_{c,m,2} = -\Gamma_0 [\mathcal{S} \Phi \text{Re}(\Phi + \Psi)]_{r_c}, \quad (5.41)$$

which reduces to equation (5.32) in the cold disc limit. The general expression for the corotation torque is therefore obtained by accounting for the contributions given by equation (5.40) and (5.41):

$$\Gamma_{c,m} = \Gamma_0 [\{\mathcal{V} + 2\mathcal{S}\} |\Phi + \Psi|^2 - 2\mathcal{S} \Phi \text{Re}(\Phi + \Psi)]_{r_c}. \quad (5.42)$$

Equation (5.42) reduces to the expression of Tanaka et al. (2002) when $\mathcal{S} = 0$, while it now reduces to that of GT79 for a cold disc.

A case of interest is that of a disc perturbed by a peaked potential (that of an embedded protoplanet for instance), for which $|\Phi + \text{Re}(\Psi)| \ll |\Phi|$, and $|\Phi + \text{Re}(\Psi)| \ll |\text{Re}(\Psi)|$ at corotation. For such case, $|\Phi \text{Re}(\Phi + \Psi)|_{r_c} \gg |\Phi + \Psi|_{r_c}^2$, hence the corotation torque may be approximated as $\Gamma_{c,m} \approx -2\Gamma_0[\mathcal{S} \Phi \text{Re}(\Phi + \Psi)]_{r_c}$. The corotation torque may therefore be much larger in the non-isentropic case ($\mathcal{S} \neq 0$) than in the isentropic case ($\mathcal{S} = 0$). Furthermore, its sign is given by that of \mathcal{S} rather than that of \mathcal{V} . This enhancement of the corotation torque in an adiabatic flow may have a dramatic impact on the type I migration of an embedded protoplanet, as was noted by [Paardekooper & Mellema \(2006\)](#).

5.4 Numerical study of an isolated corotation resonance

We check in this section the analytical predictions of section 5.3 by means of numerical simulations involving an isolated corotation resonance.

5.4.1 Numerical method

Our setup offers a number of similarities with the one of [Masset & Ogilvie \(2004\)](#) for the case of an isothermal disc. We solve with the FARGO code the hydrodynamic equations along with an energy equation, in the limit of an adiabatic disc. A complete description of the code properties, in particular the implementation of the energy equation, is addressed in section 3.3. As in [Masset & Ogilvie \(2004\)](#), we deal with the $m = 3$ corotation resonance. The disc is thus torqued by an $m = 3$ external potential Φ that reads

$$\Phi(r, \varphi, t) = T(t/\tau) \phi(r) \cos[3(\varphi - \Omega_p t)], \quad (5.43)$$

where $\phi(r)$ denotes the radial profile of the potential, Ω_p its pattern speed (note that we work in the frame corotating with the corotation resonance), t is the time and where

$$T(x) = \begin{cases} \sin^2(\pi x/2) & \text{if } x < 1 \\ 1 & \text{otherwise} \end{cases}$$

is a temporal tapering that turns on the potential on the timescale τ .

The total torque Γ_c exerted by the disc on the perturber, given by equation (5.19), is evaluated by

$$\Gamma_c = \sum_{i=0}^{N_r-1} \sum_{j=0}^{N_s-1} \frac{\Phi_{i,j+1} - \Phi_{i,j-1}}{2\Delta\varphi} \Sigma_{i,j} S_{i,j}, \quad (5.44)$$

where N_r (N_s) is the radial (azimuthal) number of zones of the mesh, $S_{i,j}$ is the surface area of zone $\{i, j\}$, $\Phi_{i,j}$ and $\Sigma_{i,j}$ are the external potential and surface density at the center of this zone, and $\Delta\varphi = 2\pi/N_s$ is the azimuthal resolution. Furthermore, the contribution $\Gamma_{c,1}$ of function Ψ to the torque is obtained by substituting Σ_1 by p_1/c_s^2 in equation (5.19). It is therefore evaluated by

$$\Gamma_{c,1} = \sum_{i=0}^{N_r-1} \sum_{j=0}^{N_s-1} \frac{\Phi_{i,j+1} - \Phi_{i,j-1}}{2\Delta\varphi} \frac{p_{i,j}}{c_{si,j}^2} S_{i,j}, \quad (5.45)$$

where $p_{i,j}$ and $c_{si,j}$ are the pressure and sound speed at the center of zone $\{i, j\}$. The contribution $\Gamma_{c,2}$ of the entropy perturbation to the torque is eventually estimated by

$$\Gamma_{c,2} = \Gamma_c - \Gamma_{c,1}. \quad (5.46)$$

The radial computational domain is narrow enough to avoid the location of the $m = 3$ inner and outer Lindblad resonances (see [Masset & Ogilvie 2004](#)). Despite this precaution, wave killing

zones next to the boundaries were implemented to minimize unphysical wave reflections (see [de Val-Borro et al. \(2006\)](#) and section 3.3.4). Furthermore, the torque evaluation is performed by summing only on a grid domain that does not contain the wave killing zones, and the summation includes a spatial tapering on the edges of that domain.

As usual, the disc surface density and temperature are initially axisymmetric with power-law profiles:

$$\Sigma(r) = \Sigma_c (r/r_c)^{-\sigma} \quad \text{and} \quad T(r) = T_c (r/r_c)^{-1+2f}, \quad (5.47)$$

where Σ_c and T_c are the surface density and temperature at the corotation radius r_c , and where f is the disc flaring index. Recall that the disc aspect ratio is given by $h(r) = H(r)/r = h(r_c)(r/r_c)^f$, where $H(r)$ is the disc scale height at radius r . A vanishing value of the flaring index f therefore corresponds to a uniform disc aspect ratio. The functions \mathcal{V} and \mathcal{S} are constant and read:

$$\mathcal{V} = 3/2 - \sigma \quad (5.48)$$

$$\mathcal{S} = \sigma - (\sigma + 1 - 2f)/\gamma. \quad (5.49)$$

The main numerical parameters are those taken by [Masset & Ogilvie \(2004\)](#), namely a $h(r_c) = 0.01$ disc aspect ratio at corotation, and $\Sigma_c = 1$. Our disc is inviscid. The libration islands are resolved by 30 zones azimuthally. As the potential increases, the radial width of the islands also increases. Their maximal radial width W spans approximately 20 zones.

The results presented in next section have the following units: the mass of the central object M_* is the mass unit, the corotation radius r_c of our $m = 3$ corotation resonance is the distance unit and the Keplerian orbital period T_{orb} at $r = r_c$ is 2π times the time unit.

5.4.2 Results

We consider three cases, corresponding respectively to figures 5.1, 5.2 and 5.3:

1. An external potential with flat profile $\phi(r) = -10^{-5}$, as in [Masset & Ogilvie \(2004\)](#). This case, that we call the “flat potential case”, has $\sigma = 2$ and $f = -0.3$ so that, from equations (5.48) and (5.49), $\mathcal{V} = -0.5$ and $\mathcal{S} \approx -0.57$,
2. A potential profile that corresponds to the $m = 3$ Fourier component of the smoothed potential of a $M = 3.1 \times 10^{-6} M_*$ point-like object. The softening length is $\varepsilon = H(r_c)$, which is approximately equal to W . The object rotates at speed Ω_p , with orbital radius r_c . This neglects the pressure gradient effects, as we do not resolve the distance from orbit to corotation, but this distance is much smaller than the potential softening length, thus this is not an issue in the present case. By contrast to the previous case, we call this situation the “peaked potential case”. The value of M is chosen so that $\phi(r_c) = -10^{-5}$, as in the flat potential case. For this calculation we have $\sigma = 1.5$ and $f = 0.5$, hence $\mathcal{V} = 0$ and $\mathcal{S} \approx 0.43$. This situation is of interest since there is no vortensity gradient, so the corotation torque would cancel out if the disc was isothermal.
3. A calculation similar to the previous one, except that $\sigma = 0.5$ and $f = -0.1$, so that $\mathcal{V} = 1$ and $\mathcal{S} \approx -0.71$.

For the three pairs $(\mathcal{V}, \mathcal{S})$ quoted above, the tapering timescale value is $\tau = 150 T_{\text{orb}}$, which corresponds to the duration of the calculations. This is about three times larger than the final libration time, estimated as ([Masset & Ogilvie 2004](#))

$$T_{\text{lib}} \sim \frac{1}{m} \left(\frac{3|\phi(r_c)|}{32} \right)^{-1/2} \approx 55 T_{\text{orb}}. \quad (5.50)$$

In each case we evaluate:

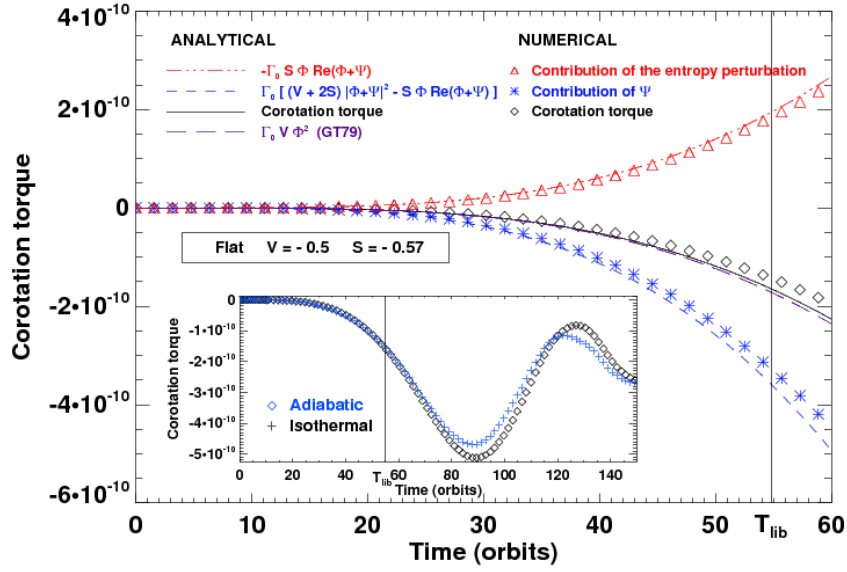


FIGURE 5.1: Corotation torque exerted by the disc on the perturber, as a function of time, assuming a flat radial profile of the potential. The results shown are obtained with an adiabatic calculation, except in the close-up, where we compare the isothermal and adiabatic torques over the whole duration of the calculations. Numerical results are displayed with symbols while the theoretical expectations are displayed with curves. We plot as a function of time the adiabatic corotation torque (diamonds and solid curve), the contribution of function Ψ to the torque (stars and dashed curve), and the contribution of the entropy perturbation (triangles and dot-dashed curve). The long-dashed curve, which is nearly superimposed to the solid curve, displays the corotation torque expression of GT79. The vertical solid line gives an estimate of the final libration time (see text).

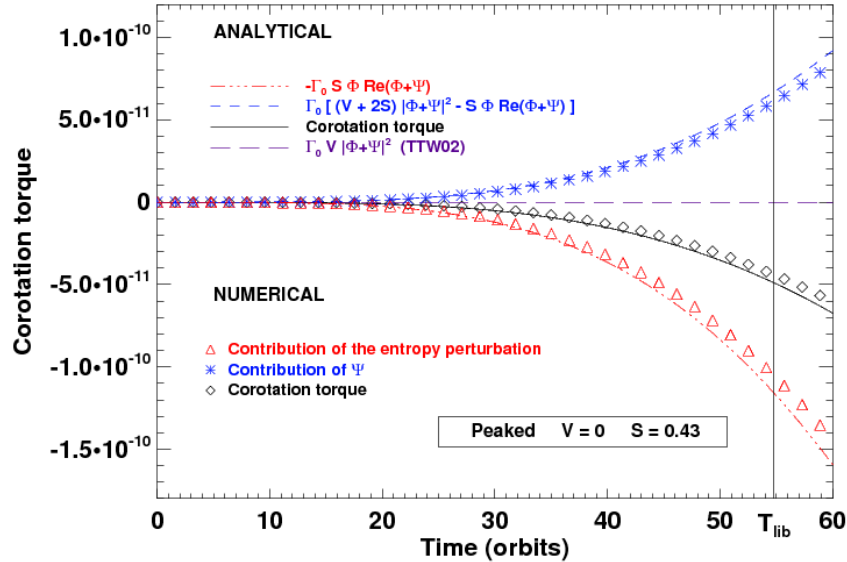


FIGURE 5.2: Same as figure 5.1, except that the results are obtained with a peaked potential, with $V = 0$ and $S \approx 0.43$. The long-dashed curve shows the expectation from the corotation torque expression of Tanaka et al. (2002), denoted by TTW02. The latter expression vanishes since there is no unperturbed vortensity gradient.

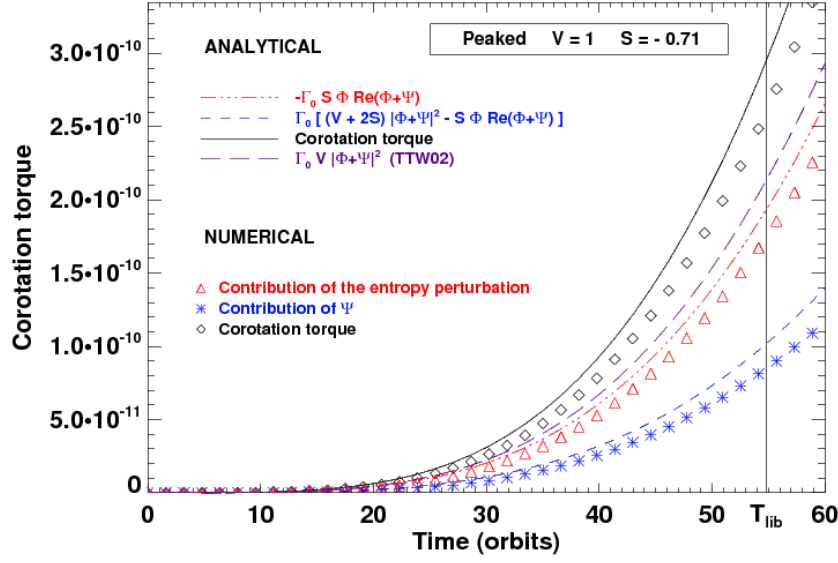


FIGURE 5.3: Same as figure 5.2 (peaked potential case), except that the calculation has $V = 1$ and $S \approx -0.71$.

- the total corotation torque (diamonds) with equation (5.44), to be compared to the analytical expression (solid curve) given by equation (5.42). In our units, $\Gamma_0 \approx 39.5$,
- the contribution of function Ψ to the corotation torque (stars) obtained with equation (5.45), the expected expression of which (dashed curve) is calculated using equation (5.40),
- the contribution of the entropy perturbation to the torque (triangles) using equation (5.46), which is to compare to the prediction of equation (5.41), represented by the dot-dashed curve.

The torque amplitudes first increase with time since the potential is progressively turned on until it reaches its final value at the end of the calculation. After some time they start to oscillate, as can be seen in the close-up of figure 5.1 for the total corotation torque. This oscillation corresponds to the *saturation* of the corotation resonance, as the ratio t/T_{lib} tends to unity (Ogilvie & Lubow 2003). A global inspection at figures 5.1 to 5.3 show that our numerical simulations succeed in reproducing the results of our analytical study as long as $t \lesssim T_{\text{lib}}$, that is when a linear analysis can be applied (which requires that the time of the calculation be much smaller than the libration time). A closer examination of our results leads to the following comments:

- In the flat potential case, depicted in figure 5.1, we find that $\text{Re}[\psi(r_c)] \approx -0.02\phi(r_c)$ throughout the calculation, with $\psi(r)$ the radial profile of Ψ . This situation thus corresponds to the cold disc limit detailed in section 5.3.1. As expected from equation (5.33), the analytical corotation torque and the expression of GT79 almost coincide. The close-up shows the torque evolution over the whole extent of the calculation, up to $t = \tau$. The torque obtained with a locally isothermal equation of state, having same parameters as the adiabatic run, is also depicted. Although there is an entropy gradient in this isothermal calculation, it *does not* contribute to the corotation torque as it would in an adiabatic disc. The appearance of the singular contribution at corotation in the adiabatic case is linked indeed (i) to the advection of entropy and (ii) to the appearance of a singularity

in the perturbed density and temperature fields. In the isothermal situation, *neither* the entropy is conserved along fluid element paths, *nor* is a temperature singularity allowed to appear. The comparison of both calculations shows that, as expected in the cold disc limit, the adiabatic and isothermal corotation torques coincide, as long as the linear regime is concerned. We note that both torques do not oscillate about 0 since the potential reaches a stationary value only at the end of the calculation.

- For the runs with a peaked potential, depicted in figures 5.2 and 5.3, we find that $\text{Re}[\psi(r_c)] \approx -0.2\phi(r_c)$. This time, the term $|\Phi + \text{Re}(\Psi)|$ slightly dominates the term $|\Phi + \Psi|^2$ in equation (5.42), and the sign of the corotation torque (diamonds and solid curve) is that of the entropy contribution to the torque (triangles and dash-dotted curve). In the particular case where $\mathcal{V} = 0$ (figure 5.2), the isothermal corotation torque, whose expression is given by Tanaka et al. (2002), cancels out while we find here a net, negative torque for the adiabatic situation, in correct agreement with our analytical expression. Concerning the case where $\mathcal{V} = 1$ and $\mathcal{S} \approx -0.71$, we mention that the comparison with the formula of Tanaka et al. (2002) is a bit biased since it applies only for a uniform temperature profile, whereas here the background temperature decreases as $r^{-0.8}$. Our extended torque formula has no such restriction.

5.4.3 Dynamics of the corotation region

We discuss in this section the dynamics of the corotation resonance for an adiabatic disc, and we give some comments about the corotation torque expression of equation (5.42). In the isothermal case, the corotation torque expression involves the product of the gradient of vortensity and the square of the effective potential $(\Phi + \Psi)$, see e.g. Tanaka et al. (2002). The torque is then given by the angular momentum budget between material flowing outwards and material flowing inwards at corotation, regardless of the sign of $\Phi + \Psi$. Equation (5.42) displays a term that has a similar behavior, except that it does not feature the vortensity gradient only, but rather $\mathcal{V} + 2\mathcal{S}$. This factor scales with the (logarithmic) gradient of $(\Sigma_0/B)S^{2/\gamma}$, which is a key quantity considered by Li et al. (2000b) and by Lovelace et al. (1999b), who pointed out that vortensity is not conserved in a two-dimensional adiabatic flow.

In addition to this term, equation (5.42) contains a term that scales with $\Phi[\Phi + \text{Re}(\Psi)]$. The sign of this term therefore depends on the relative signs of Φ and $\Phi + \text{Re}(\Psi)$. In order to get some insight into the physical meaning of this term, we show at figure 5.4 the response of the disc in the corotation region, for the entropy and the surface density. These fields correspond to the calculation with the flat potential profile considered at the previous section, for which we recall that $\mathcal{V} = -0.5$ and $\mathcal{S} \approx -0.57$. Since the disc has a negative radial entropy gradient, libration brings the (larger) inner entropy to the outer part of the libration islands, yielding a positive perturbed entropy (brighter areas). Similarly, libration brings the (smaller) outer entropy to the inner part of the libration islands, yielding a negative perturbed entropy (darker areas). An opposite behavior is observed for the perturbed density, since the relative pressure perturbation (not represented here) is much smaller. These results are very similar to those obtained with the vortensity advection in the isothermal case, see the left-hand panel of figure 2.5.

The *sign* of this torque component can be understood as follows. Figure 5.5 depicts the two following possibilities: Φ and $\Phi + \text{Re}(\Psi)$ have same sign (left), and Φ and $\Phi + \text{Re}(\Psi)$ have opposite signs (right). Depending on the azimuthal wavenumber, we may obtain the former or the latter case. We checked this result with global disc-planet calculations (not presented here), and we noticed that only the lowest azimuthal wavenumbers have Φ and $\Phi + \text{Re}(\Psi)$ in phase. In the left panel of figure 5.5, the negative perturbed surface density on the outside of corotation is located in the region where $\partial\varphi\Phi < 0$, hence from equation (5.19) the perturbation yields a

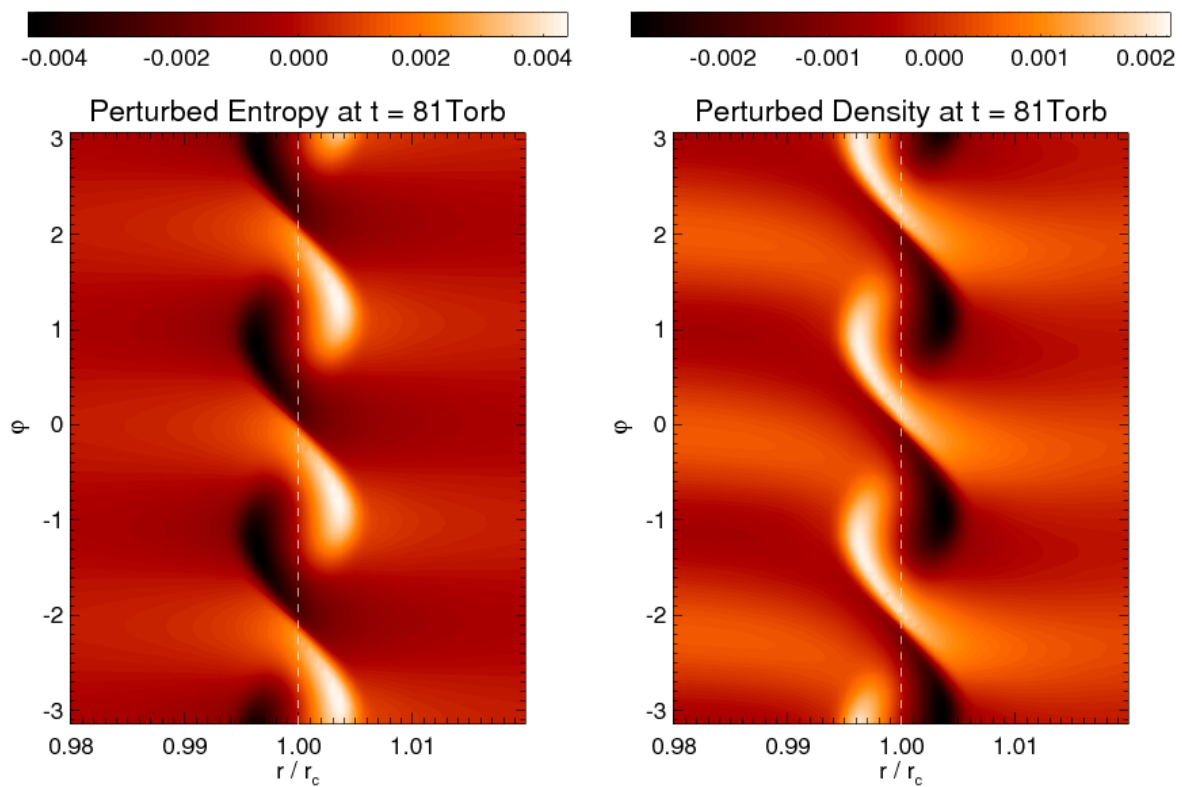


FIGURE 5.4: Relative perturbation of entropy (left) and surface density (right) for an isolated resonance, at $t \approx 1.5 T_{\text{lib}}$. These results are obtained with the run having a flat potential profile, $\mathcal{V} = -0.5$ and $\mathcal{S} \approx -0.57$. Libration is clockwise.

5.5 Conclusions

We have evaluated in this chapter the corotation torque between an adiabatic two-dimensional disc and a uniformly rotating external potential. We have found a generalized expression for the corotation torque at an isolated resonance, which reduces to the usual dependence on the vortensity gradient in the limit of a cold disc. Our torque expression displays an additional contribution arising from the entropy advection within the libration islands, which scales with the entropy gradient. We have successfully checked the results of our linear analysis with two-dimensional hydrodynamical calculations of an isolated corotation resonance. In the next chapter, we will check our analytical findings in the disc-planet context.

Chapter 6

Type I planetary migration in a radiative disc

WE CONTINUE IN THIS CHAPTER our investigation of type I migration in two-dimensional radiative discs. The external rotating potential is now that of a low-mass planet held on a fixed circular orbit, for which all co-orbital corotation resonances and all Lindblad resonances are simultaneously active. As a bridge with the linear analysis presented in chapter 5, we consider in section 6.1 the case of an adiabatic disc. Our calculation results confirm that a significant excess of corotation torque arises from the entropy advection within the planet's horseshoe region. We show in particular that the fully unsaturated value of this torque excess scales with the opposite of the unperturbed entropy gradient. Similarly as the corotation torque in a locally isothermal disc, this torque excess ultimately saturates unless source terms in the energy equation (viscous heating, radiative cooling or thermal diffusion) are taken into account. We demonstrate in section 6.2 that the torque excess can be maintained to an unsaturated value on the long term.

Contents of this chapter

6.1	Excess of corotation torque in an adiabatic disc	116
6.1.1	An illustrative example	116
6.1.2	Connection with analytics	122
6.1.3	Beyond linear analysis: the horseshoe model	125
6.1.4	Dependence on the entropy gradient	127
6.1.5	Impact of the softening length	129
6.1.6	Impact of the adiabatic index	130
6.1.7	Vortensity - entropy coupling	132
6.2	Desaturation of the corotation torque in a radiative disc	133
6.2.1	Saturation issues	133
6.2.2	A simple temperature prescription	137
6.2.3	Heat diffusion in the disc mid-plane	139
6.3	Concluding remarks	140
6.4	Appendix: estimate of the horseshoe U-turn time . . .	140

Parameter	Notation	Reference value
Aspect ratio at $r = r_p$	$h(r_p)$	0.05
Surface density at $r = r_p$	Σ_p	2×10^{-3}
Temperature at $r = r_p$	$T_p \equiv h^2(r_p)$	2.5×10^{-3}
Adiabatic index	γ	1.4
Planet to primary mass ratio	q	5×10^{-6}
Softening length	ε	0.03
Mesh inner radius	r_{\min}	0.4
Mesh outer radius	r_{\max}	1.8
Radial zones number	N_r	1024
Azimuthal zones number	N_s	2048

TABLE 6.1: Reference parameters for the illustrative calculation of section 6.1.1. The disc is inviscid.

6.1 Excess of corotation torque in an adiabatic disc

The disc that we consider in this section is inviscid and radiatively inefficient (adiabatic), the energy equation is thus equivalent to the Lagrangian conservation of the gas specific entropy s ($Ds/Dt = 0$, see equation (3.53)). In the following, calculations including an adiabatic energy equation will be called adiabatic calculations. Calculations that do not include an energy equation will be referred to as locally isothermal runs, or just isothermal runs for short. In all cases, an adiabatic run and its equivalent isothermal run will have the same initial surface density and temperature profiles.

6.1.1 An illustrative example

We start with an overview of the disc response to the introduction of a low-mass planet, with and without energy equation. The disc and planet parameters are summed up in table 6.1, where they are expressed in the code units (see section 3.1.6). The planet to primary mass ratio is $q = 5 \times 10^{-6}$. The Bondi radius to softening length ratio, which we introduced in section 4.3 as a parameter that controls the flow linearity in a two-dimensional disc, is thus ~ 6.5 %. We recall that the horseshoe libration time is

$$\tau_{\text{lib}} = \frac{8\pi r_p}{3\Omega_p x_s}, \quad (6.1)$$

where Ω_p is the planet's angular velocity, and x_s denotes the half-width of the horseshoe region. We have seen in chapter 2 that x_s can be approximated as $x_s \approx 1.2r_p\sqrt{q/h(r_p)}$ for an isothermal disc. A streamline analysis was performed and confirmed that this estimate holds for an adiabatic disc if one substitutes $h(r_p)$ with $\sqrt{\gamma}h(r_p)$. This yields $\tau_{\text{lib}} \approx 105 T_{\text{orb}}$. We comment that numerical diffusion eventually alters the conservation of advected quantities, such as the entropy in the adiabatic case. Nevertheless, for the planet to primary mass ratio quoted above, the horseshoe region spans 20 zones radially, which is sufficient to follow the horseshoe dynamics over several libration times. For now, we are concerned with only a fraction of the libration time, so the entropy should be conserved with a good level of accuracy over the duration of our runs, and be regarded as a *Lagrangian tracer* of the flow.

As an illustrative example, we present the results of an adiabatic and an isothermal calculations for which the initial surface density and temperature profiles decrease respectively as $r^{-0.5}$ and $r^{-0.6}$. The unperturbed entropy profile then decreases as $r^{-0.4}$. For these calculations, the planet is held on a fixed circular orbit at $r = r_p$. The results are depicted in figure 6.1,

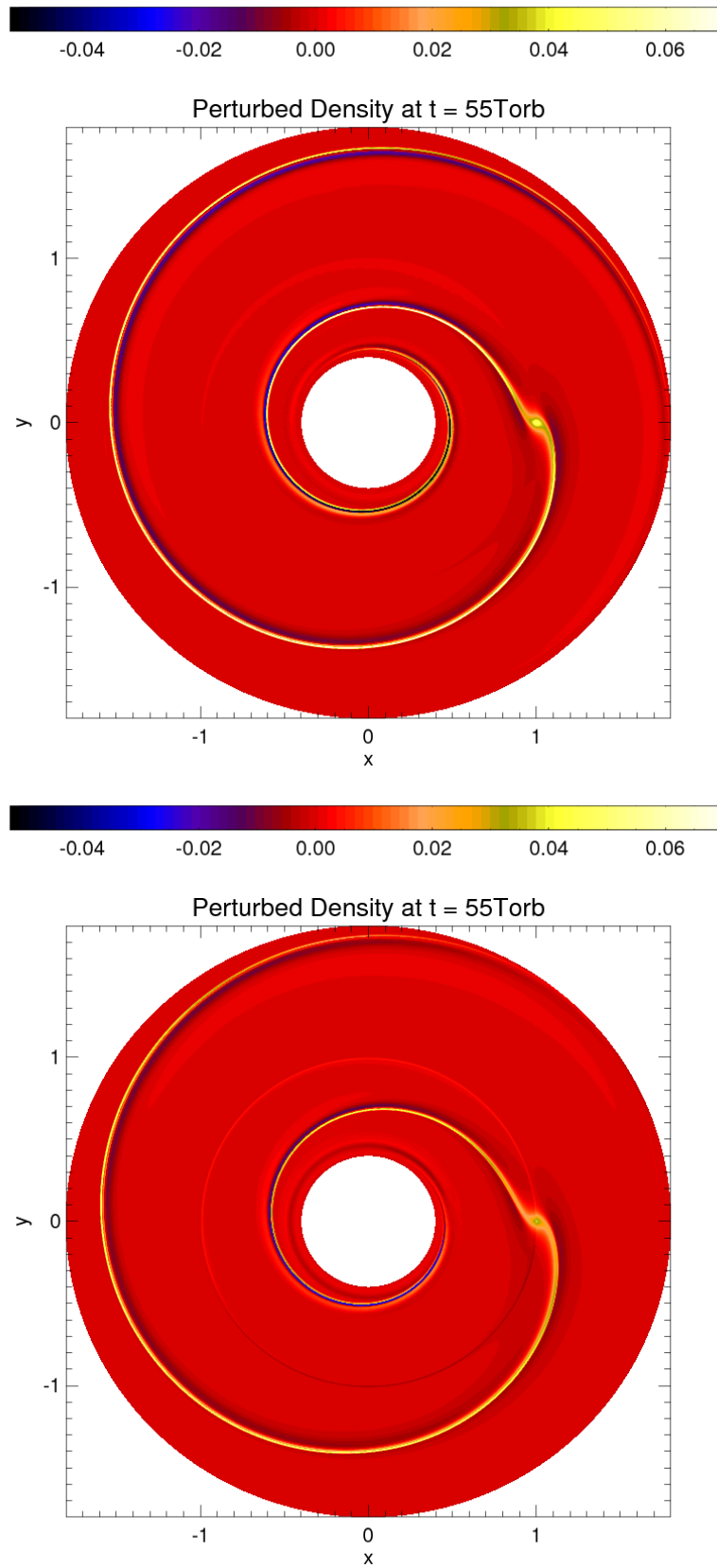


FIGURE 6.1: Disc response to a $M_p = 5 \times 10^{-6} M_\star$ planet mass. The relative perturbation of the surface density is displayed with a locally isothermal calculation (top panel), and with an adiabatic calculation (bottom panel). The color scale is identical in both panels.

where the panels have the same color scale to appreciate their differences. The clearest difference arises from the planet wake. The latter is *less tightly wound* in the adiabatic case (bottom panel), as the adiabatic sound speed is larger than the isothermal one (by a factor of $\sqrt{\gamma}$, see equation (3.52)). In addition, the density perturbations corresponding to the wake have *smaller* amplitude in the adiabatic run. This results from the fact that acoustic waves are isentropic, so that the perturbed pressure p_1 and the perturbed surface density Σ_1 always satisfy $p_1 = \Sigma_1 c_s^2$. The pressure perturbations along the wake depend on the perturbing potential, which is the same in both situations. The density perturbations are therefore reduced in the adiabatic case, by a factor of $\sim \gamma$. Furthermore, the adiabatic panel shows additional density perturbations, that propagate inside the planet horseshoe region. However faint these perturbations might seem, their contribution to the torque may be strong enough to slow down type I migration significantly. They may even reverse it, as we will see.

Additional surface density perturbations in the planet's coorbital region

To understand the presence of additional density perturbations in the adiabatic calculation, we display in figure 6.2 the gas entropy, and the relative perturbations of the gas entropy, of the pressure and of the surface density inside the planet's horseshoe region. While the azimuthal range spans the whole $[0, 2\pi]$ interval, the radial range depicted is restricted to a band of width $2.5x_s$ around the corotation radius r_c . The above quantities are shown at $t = 55 T_{\text{orb}}$, that is about half the libration time. The streamlines overplotted on the top-left panel illustrate the *entropy conservation* of the fluid elements as they perform a horseshoe U-turn in the planet co-orbital region. Since the unperturbed entropy profile decreases with r , the horseshoe dynamics brings a negative entropy perturbation to the inner side of the coorbital region ($r < r_c$), as can be seen on the top-right panel. Similarly, the horseshoe dynamics gives a positive entropy perturbation on the outer side ($r > r_c$). More generally, when there is initially an entropy gradient at corotation, the co-orbital dynamics yields an entropy perturbation that has a sign opposite of that of the entropy gradient on the outwards U-turns, and the sign of the entropy gradient on the inwards U-turns. In the bottom-left panel, the perturbed pressure does not exhibit similar perturbations, so it essentially accounts for the planet wake (the horizontal, saturated structure at $\varphi = \varphi_p$). Since the *pressure* field is only *weakly* perturbed, entropy perturbations are related to density perturbations of opposite sign and, in relative value, of same order of magnitude (bottom-right panel). This is reminiscent of the behavior commented in the case of an isolated resonance at section 5.4.3. This is also reminiscent of the behavior of the contact discontinuities (or contact waves) mentioned in section 3.4. Recall that a contact discontinuity is characterized by a discontinuity in the density and temperature fields, while the pressure and the velocity remain continuous, and that a contact discontinuity is simply *advected* by the flow. The above entropy perturbations will thus be referred to as a *contact discontinuity*.

A simple advection model

We give hereafter a simple estimate of the surface density perturbation due to the advection of entropy. We consider a fluid element that performs a horseshoe U-turn from the inner part of the horseshoe region (where we assume that there is no entropy perturbation, which is true as long as $t < \tau_{\text{lib}}/2$) to the outer part. All physical quantities at the inner (outer) leg of the horseshoe streamline are denoted by a minus (plus) subscript. A first-order expansion yields, assuming no pressure perturbation:

$$p_{\pm} = p_0(r_c)(1 \mp \{\sigma + 1 - 2f\} x/r_c), \quad (6.2)$$

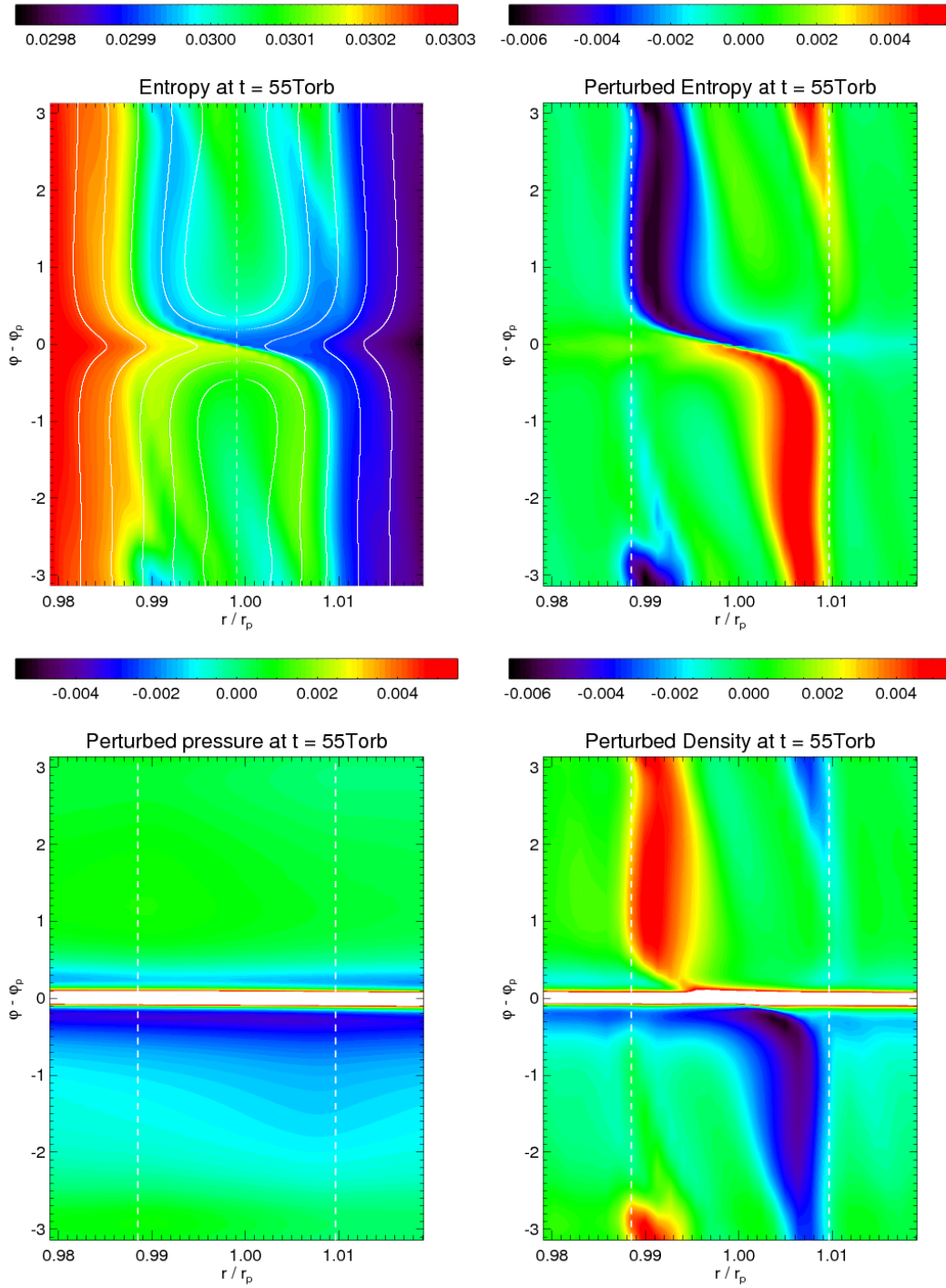


FIGURE 6.2: Results of the illustrative adiabatic calculation of section 6.1.1, at $t = 55 T_{\text{orb}} \lesssim \tau_{\text{lib}}/2$. The top-left panel shows the gas entropy in the planet's horseshoe region. Streamlines are overplotted to underline the entropy advection inside the horseshoe region. The protoplanet is located at $r = r_p$, $\varphi = \varphi_p$, and the corotation radius r_c is indicated here with a vertical dashed line. From top-right to bottom-right, we display the relative perturbations of the gas entropy, pressure and surface density. For instance, the bottom-right panel displays $[\Sigma(r, \varphi) - \Sigma_0(r)]/\Sigma_0(r)$. The bold dashed lines represent the approximative location of the separatrices of the horseshoe region. The color scale has been adjusted in the pressure and density panels to highlight the perturbations moving along the separatrices. In the bottom row panels, the nearly horizontal structure at $\varphi = \varphi_p$ is the planet wake.

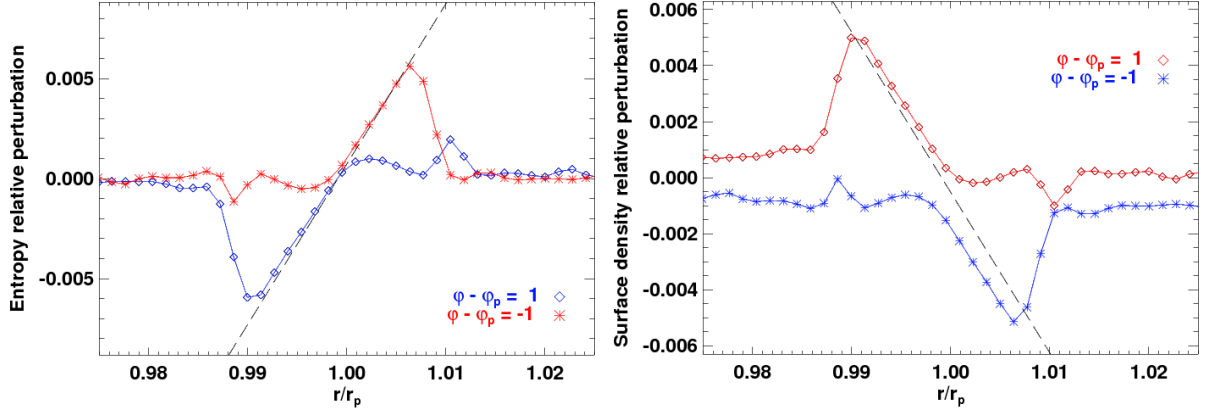


FIGURE 6.3: Slices of the perturbed entropy (left panel) and of the perturbed density (right panel), obtained with the calculation results depicted in figure 6.2. The slices correspond to $\varphi - \varphi_p = 1$ (diamonds) and to $\varphi - \varphi_p = -1$ (stars). In the left panel, the dashed line shows the quantity $-2\gamma\mathcal{S}(r-r_c)/r_c$, which represents the relative perturbation of the entropy, assuming the entropy is conserved along elements paths. In the right panel, the dashed line displays this time the quantity $2\mathcal{S}(r-r_c)/r_c$, which corresponds to the relative perturbation of the surface density due to the entropy advection (see equation (6.6)).

where $0 < x < x_s$ is the distance of the streamline to corotation, and:

$$\Sigma_- = \Sigma_0(r_c)(1 + \sigma x/r_c). \quad (6.3)$$

On the outer horseshoe leg, the disc surface density is perturbed according to the entropy perturbation and reads:

$$\Sigma_+ = \Sigma_0(r_c)(1 + R - \sigma x/r_c), \quad (6.4)$$

where R is the relative perturbation of surface density at $r = r_c + x$ (we assume a symmetric horseshoe U-turn), due to the entropy advection. Entropy conservation along the fluid element path ($S_- = S_+$) leads to:

$$R = 2 \frac{x}{r_c} \left(\sigma - \frac{\sigma + 1 - 2f}{\gamma} \right) = 2\mathcal{S}x/r_c. \quad (6.5)$$

Recall that $\gamma\mathcal{S}$ is the power-law index of the unperturbed entropy profile (namely the quantity $d \log S_0 / d \log r$, with S_0 the unperturbed entropy). The horseshoe U-turn that we have considered lags the planet ($\varphi < \varphi_p$). A similar conclusion holds for a horseshoe U-turn that switches from the outer leg to the inner one (at $\varphi > \varphi_p$), hence we finally have:

$$R(x) = 2\mathcal{S}x/r_c, \quad \forall x \in [-x_s, +x_s]. \quad (6.6)$$

We show in figure 6.3 two slices of the perturbed entropy and surface density fields displayed in figure 6.2, at $\varphi - \varphi_p = 1$ (diamonds) and $\varphi - \varphi_p = -1$ (stars). In the entropy panel (left one), the dashed curve depicts the quantity $-2\gamma\mathcal{S}(r-r_c)/r_c$. It represents the entropy relative perturbation, assuming the entropy is conserved along horseshoe U-turns. The agreement with our calculation results is excellent. Similarly, the dashed curve in the right panel depicts the quantity $R(x)$, given by equation (6.6), which corresponds to the density relative perturbation due to the entropy advection. It is in fairly good agreement with our calculation results, the difference arising from the pressure perturbations that we neglected in our model. This shows that the density perturbations inside the horseshoe region may be exclusively accounted for by the entropy advection. In particular, we checked that there are no such perturbations in the isentropic ($\mathcal{S} = 0$) case.

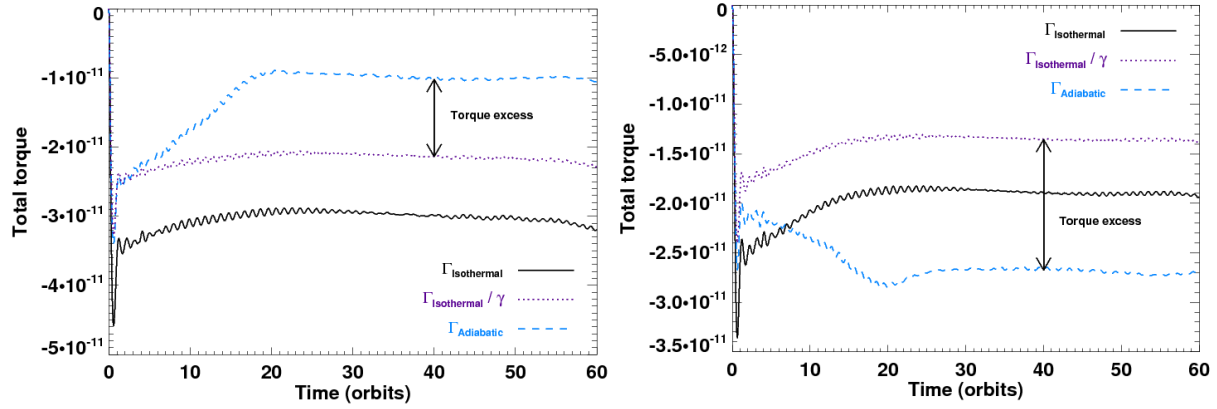


FIGURE 6.4: Left: torque variation with time of the illustrative adiabatic calculation (dashed curve). The torque obtained with a similar (locally) isothermal calculation is depicted for comparison (solid curve). The dotted curve depicts the isothermal torque divided by the adiabatic index γ . The difference between the adiabatic torque, and the isothermal torque divided by γ , defines the torque excess. Right: calculations results with same parameters as in the left panel, except the initial temperature increases as $r^{0.2}$, hence the unperturbed entropy profile increases as $r^{0.4}$. The entropy gradients are thus opposite in both panels, and so are the torque excesses in the plateau starting at ~ 20 orbits.

Impact on the corotation torque

To investigate the torque contribution from the above density perturbations, we compare the torques obtained with our adiabatic and locally isothermal runs. Their time variation is displayed in figure 6.4a. The adiabatic torque is more positive than the isothermal one, hence type I migration is slowed down in the adiabatic case. During the very first orbits, the adiabatic torque closely matches the isothermal torque divided by the adiabatic index γ (dotted curve). Then, the adiabatic torque rises faster than the isothermal one, until both reach a plateau at ~ 20 orbits. These results can be understood as follows. As in the locally isothermal case, the adiabatic torque includes:

- The differential Lindblad torque. The latter scales as c_s^{-2} , it is thus reduced by a factor of γ in the adiabatic case.
- The contribution of the vortensity gradient to the corotation torque. It scales with x_s^4 , that is with c_s^{-2} . Again, it is reduced by a factor of γ in the adiabatic case. In absence of any additional torque contributions, we would expect the adiabatic torque to be equal to the locally isothermal torque divided by γ .

The adiabatic calculation displays here an additional torque contribution that comes from the density perturbations due to the entropy advection in the coorbital region. It represents the difference between the adiabatic torque, and the locally isothermal torque divided by γ . This additional contribution will be called *excess of corotation torque* or *torque excess* for future reference. Its sign depends on that of the density perturbations in the coorbital region. In our example, the positive torque exerted by the fluid elements performing an inward U-turn is enhanced, since the surface density is larger in the inner side of the coorbital region. Similarly, the negative torque exerted by the fluid elements doing an outward U-turn is decreased, as the surface density is smaller in the outer side. We thus have a positive torque excess, as shown in figure 6.4a. The torque excess increases with time until reaching a maximum value or plateau (here at ~ 20 orbits), much like the corotation torque in the locally isothermal case. The torque excess begins to saturate at about half the libration time (~ 60 orbits here), as the entropy perturbations start to mix up. The study of the saturation process is deferred to section 6.2.1.

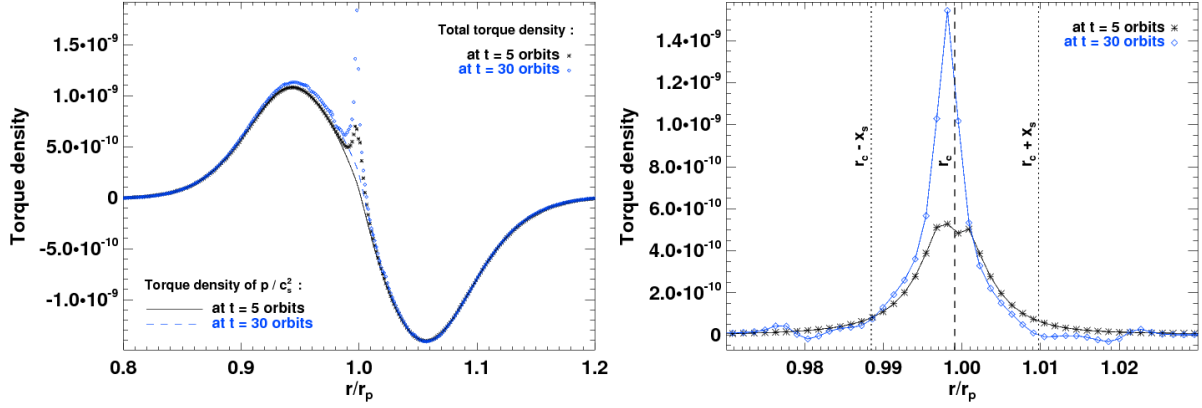


FIGURE 6.5: Left: total torque density (symbols) and torque density of p/c_s^2 (lines), at $t = 5 T_{\text{orb}}$ and $t = 30 T_{\text{orb}}$. Right: torque density of $\Sigma - p/c_s^2$ at the same instants. The vertical dashed line shows the corotation radius, while the two vertical dotted lines show the extent of the horseshoe region. The torque density inside the coorbital region is positive as (i) the unperturbed entropy gradient is negative, and (ii) saturation has not begun.

For the calculation results displayed in figure 6.4b, the disc and planet parameters are identical as those of our illustrative example, but the initial temperature profile increases as $r^{0.2}$. This choice may be surprising, as one would not expect the temperature to increase with radius. Our motivation was to get an initial entropy profile increasing as $r^{0.4}$, so the entropy gradients be exactly opposite between figures 6.4a and 6.4b. The entropy perturbations in the coorbital region thus have same amplitude but opposite signs, and so are the density perturbations. Subsequently, the torque excesses between both cases are opposite. These two examples illustrate that the torque excess *scales with the unperturbed entropy gradient*, in agreement with the scaling of the density perturbations with \mathcal{S} derived in equation (6.6). This will be further investigated in section 6.1.4.

Also of interest are the torque densities associated to p/c_s^2 and $\Sigma - p/c_s^2$. The sum of these two torque densities is the total torque density. They are depicted in figure 6.5 for our illustrative run at $t = 5 T_{\text{orb}}$ and $t = 30 T_{\text{orb}}$. In the left panel, the total torque density displays a smooth profile and a narrow peak at corotation. This is reminiscent of the torque density found by [Paardekooper & Mellema \(2006\)](#) (their figure 2) or by [Morohoshi & Tanaka \(2003\)](#) (their figure 3). The decomposition above splits this total torque density in a smooth component arising from p/c_s^2 , which reminds of the torque density in a locally isothermal disc, and a sharp, localized torque density arising from $\Sigma - p/c_s^2$. The latter corresponds to the torque density stemming from the contact discontinuity contribution. It is displayed in the right panel of figure 6.5. Its time evolution corresponds to¹ that of the torque excess depicted in figure 6.4a. It is thus a positive quantity, which reaches its maximum value on the plateau, at ~ 20 orbits. We stress that this torque density, which is localized at the corotation radius in the linear case for an isolated resonance, is here bounded by the extent of the horseshoe region.

6.1.2 Connection with analytics

In chapter 5, we derived an expression for the corotation torque between an adiabatic disc and an external rotating potential. This expression is successfully reproduced by local numerical simulations of an isolated corotation resonance, in the linear regime. We now apply our linear analysis to a low-mass planet. This case is more complex to analyze as all Lindblad resonances

¹We point out that the torque excess and the torque due to the contact discontinuity are not necessarily identical, as will be justified in section 6.1.2.

and all co-orbital corotation resonances are simultaneously active. In the torque evaluation for instance, it is not straightforward to separate the contribution of the differential Lindblad torque from that of the corotation torque. The analysis of [Tanaka et al. \(2002\)](#) may be used however to estimate both contributions separately, as we did in section 4.7 in the self-gravitating context. Interestingly, as pointed out at the end of last section, the contribution of the contact discontinuity to the corotation torque, denoted by Γ_{cd} , may be directly calculated as

$$\Gamma_{\text{cd}} = \int_{\text{disc}} \left(\Sigma - \frac{p}{c_s^2} \right) \frac{\partial \Phi}{\partial \varphi} r dr d\varphi, \quad (6.7)$$

expression that features the surface density perturbations that do not have a pressure counterpart. This expression is to be compared with the sum over m of the torque $\Gamma_{c,m,2}$:

$$\Gamma_{\infty} = \lim_{k \rightarrow +\infty} \Gamma'_k, \quad (6.8)$$

where

$$\Gamma'_k = -\frac{4\pi^2}{3} \frac{\mathcal{S}\Sigma_0}{\Omega^2} \sum_{m=1}^{m \leq k} m \Phi_m [\Phi_m + \text{Re}(\Psi_m)] \quad (6.9)$$

is the partial sum of $\Gamma_{c,m,2}$, to calculate at $r = r_c$ (see equation (5.41)). In equation (6.9), the quantities Φ_m and $\text{Re}(\Psi_m)$ are evaluated from the calculation outputs. Before coming to the comparison between numerical and analytical results, we introduce two timescales we will largely refer to in the following. The first of them, which we denote by $\tau_{\text{u-turn}}$, gives an estimate of the time required to perform a horseshoe U-turn in the horseshoe region. We demonstrate in the appendix (section 6.4) that $\tau_{\text{u-turn}} \sim h(r_p) \tau_{\text{lib}}$, with τ_{lib} the libration timescale, given by equation (6.1). The second timescale is deduced from the linear study of [Paardekooper & Papaloizou \(2008\)](#). The authors derive a criterion for the departure from linearity, that depends on the planet to primary mass ratio q , on the softening length ε , and on a parameter similar to the parameter α in equation (5.22). Their inequality can be recast to give an estimate of the time above which the linear analysis will ultimately fail. We denote by τ_{pp08} this timescale. In our code units, we find:

$$\tau_{\text{u-turn}} \approx 1.25 q^{-1/2} h^{3/2}(r_p) T_{\text{orb}} \quad (6.10)$$

and

$$\tau_{\text{pp08}} \approx 4.9 \times 10^{-2} q^{-1/2} \varepsilon^{1/8} T_{\text{orb}}, \quad (6.11)$$

with ε the softening length.

In the left panel of figure 6.6, we display the time evolution of Γ_{cd} for the illustrative run of section 6.1.1. The numerical and analytical evaluations of Γ_{cd} are respectively given by equations (6.7) and (6.8). For comparison, we also depict the torque excess between the adiabatic and the locally isothermal calculations. We make the following comments:

- The results of our calculations are in *excellent agreement* with those of the linear analysis as long as t remains somewhat smaller than a time in between $\tau_{\text{u-turn}}$ and τ'_{pp08} . This is highlighted at figure 6.6b, where we show that the cumulative torque Γ'_m , given by equation (6.9), converges at high m toward the direct numerical estimate. The results are those obtained at $t = 5 T_{\text{orb}}$.
- Beyond this date, the numerical results show a boost that corresponds to the grasp of the plateau, and which is not reproduced by the linear analysis. We note in passing that the temporal evolution of our analytic expression is that of the quantity $\text{Re}[\Psi(r_c)]$, hence that of the perturbed pressure p_1 at the corotation radius. Since the latter quantity is hardly

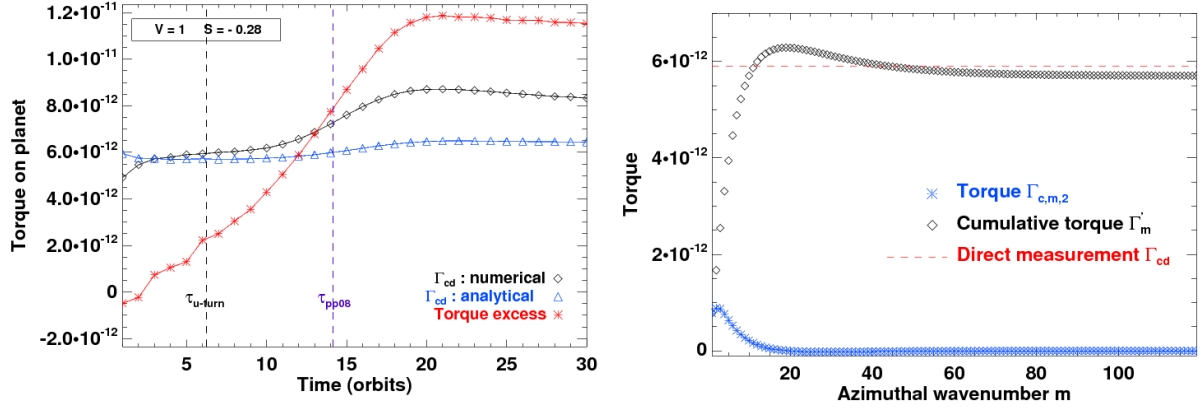


FIGURE 6.6: Left: contribution of the contact discontinuity to the corotation torque, Γ_{cd} , as a function of time. We compare the numerical results of our illustrative calculation, given by equation (6.7), with our analytical estimate of equation (6.8). The time evolution of the torque excess is also displayed for comparison. The vertical dashed lines represent the two characteristic timescales given by equations (6.10) and (6.11) (see text). Right: comparison of the numerical and analytical evaluations of Γ_{cd} for our illustrative run at $t = 5$ orbits. We show the partial sums of the torque series given by equation (6.9) (diamonds), and the direct estimate of the contact discontinuity contribution, given by equation (6.7) (dashed line). The asymptotic value of the partial sum almost coincides with the direct estimate (i.e. the diamonds almost lie on the dashed line at large m), hence with a very good accuracy we have $\Gamma_{\infty} = \Gamma_{cd}$.

perturbed, this is not surprising that our analytic estimate does not change significantly with time. We performed many additional calculations that differ only from the gradients of the unperturbed vortensity and entropy profiles. For all of them, we observed that the numerical evaluation of Γ_{cd} in the plateau is larger than the analytic estimate, by typically a factor of 20% to 50%. This indicates that the linear analysis always underestimates the unsaturated value of Γ_{cd} obtained with numerical simulations. It illustrates that the entropy advection along horseshoe U-turns is a *non-linear* process. It might also suggest that already in the locally isothermal case, the unsaturated value of the corotation torque can not be caught up with a linear analysis, contrary to what is usually thought, and to what we exposed in chapter 2 (Paardekooper, 2008, priv. comm.).

- Furthermore, the torque stemming from the contact discontinuity and the torque excess show totally different behaviors. Contrary to Γ_{cd} , the torque excess increases monotonically with time until reaching the plateau at ~ 20 orbits. Let us denote by E the torque excess. It may be intuitive to think that Γ_{cd} and E represent the same quantity, namely the contribution of the entropy perturbations to the torque. Nevertheless, the linear analysis suggests that E should be the sum of $\Gamma_{0,m} [2\mathcal{S}|\Phi_m + \Psi_m|^2 - 2\mathcal{S}\Phi_m(\Phi_m + \text{Re}(\Psi_m))]$, which, in the limit where $|\Phi_m + \text{Re}(\Psi_m)| \ll |\text{Re}(\Psi_m)|$ and $|\Phi_m + \text{Re}(\Psi_m)| \ll |\Phi_m|$, should reduce to $-2\Gamma_{0,m} \mathcal{S}\Phi_m(\Phi_m + \text{Re}(\Psi_m))$, that is twice Γ_{cd} (see equations (5.40) and (5.41)). For the calculations presented here, we checked that $2 \sum_m m|\Phi_m + \Psi_m|^2$ is almost exactly compensated by $\sum_m m\Phi_m(\Phi_m + \text{Re}(\Psi_m))$ on the plateau. This explains why the torque excess essentially amounts to the contact discontinuity contribution on the plateau. Presumably this coincidence is fortuitous and linked to the relatively large softening length we use. At smaller softening length, the term in $\Phi_m(\Phi_m + \text{Re}(\Psi_m))$ should largely dominate, yielding a ratio of 2 between the torque excess and the contribution of the contact discontinuity. This will be checked in section 6.1.5. We note that Paardekooper & Mellema (2006) also quote that the torque estimate given by their equation (1) accounts for the total torque within 25 % (this equation can also be seen as an estimate of the contact

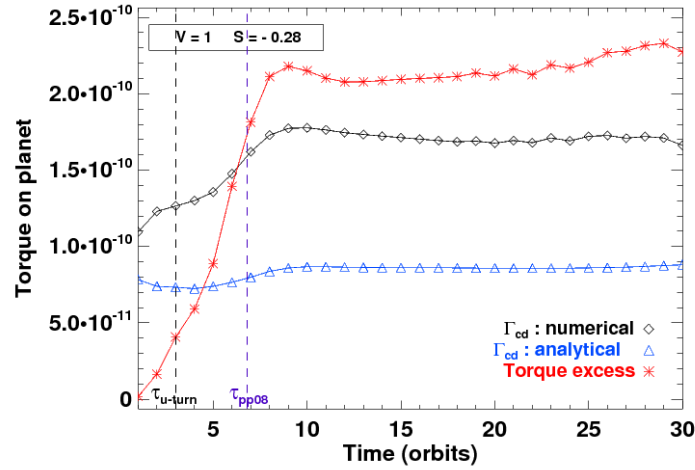


FIGURE 6.7: Same as figure 6.6a, except the planet to primary mass ratio is increased to $q = 2.2 \times 10^{-5}$. There is no match between the numerical and analytical evaluations of Γ_{cd} .

discontinuity contribution). This seems to suggest that the softening length of $0.6H(r_p)$ that we adopted is a correct choice to reproduce the magnitude of the corotational effects in adiabatic three-dimensional discs.

We end up this section with an additional result regarding the comparison of the numerical and analytical estimates of Γ_{cd} . In figure 6.7, we display again the time variations of Γ_{cd} and of E , but for a planet to primary mass ratio increased to $q = 2.2 \times 10^{-5}$. All disc parameters are identical to those of the calculation presented in figure 6.6a. This time, the numerical and analytical estimates of Γ_{cd} are not in agreement, even at the very early stages of the disc evolution. This discrepancy is presumably due to the onset of non-linearities in the flow at early stages, as the Bondi Radius to softening length ratio is $\sim 30\%$ in this case (Masset et al. 2006a). This shows once more the high sensitivity of the corotation torque to non-linear features. We note that the relative difference of Γ_{cd} and of E on the plateau is the same as that obtained with $q = 5 \times 10^{-6}$.

6.1.3 Beyond linear analysis: the horseshoe model

Since our linear analysis does not reproduce the unsaturated value of the contact discontinuity contribution to the torque, we propose in this section an alternative model that inspires from the standard horseshoe drag expression described in section 2.3.2, but that applies to the advection of the entropy perturbations in the horseshoe region. We use the simple model derived in section 6.1.1 to estimate the perturbations $R(x)\Sigma_0(r_c)$ of the surface density in the horseshoe region, due to the entropy advection. We first consider the outwards horseshoe U-turns occurring at $\varphi < \varphi_p$. Assuming, in this order of magnitude estimate, that the rotation profile of the disc is unperturbed, we evaluate the variation of the angular momentum flux of the horseshoe disc material after the U-turn attributable to the change of the disc's surface density:

$$\Delta\Gamma_{HS-} = \int_0^{x_s} (-2Ax)\Sigma_0(r_c)R(x)(j_c + 2Br_cx)dx, \quad (6.12)$$

where j_c is the specific angular momentum of the material at corotation. The first factor of the integrand of equation (6.12) represents the material velocity in the corotating frame, due to the shear. The last factor is the material specific angular momentum obtained from a first order

expansion at corotation. Similarly, we obtain the change of angular momentum flux due to the perturbation of surface density on inwards horseshoe U-turns:

$$\Delta\Gamma_{\text{HS}^+} = \int_0^{x_s} (-2Ax)\Sigma_0(r_c)R(-x)(j_c - 2Br_c x)dx. \quad (6.13)$$

Adding equations (6.12) and (6.13), we are left with:

$$\Delta\Gamma_{\text{HS}} = 2 \int_0^{x_s} (-2Ax) \cdot \Sigma_0(r_c)R(x) \cdot 2Br_c x dx = -4AB\Sigma_0(r_c)\mathcal{S}x_s^4, \quad (6.14)$$

and the horseshoe drag exerted *on the planet* is $-\Delta\Gamma_{\text{HS}}$. Whenever the horseshoe drag² is mentioned, it will implicitly refer to as the horseshoe drag on the planet. It represents the torque exerted by the density perturbations within the horseshoe region. Once again, this quantity naturally compares to Γ_{cd} . Assuming a Keplerian flow, the horseshoe drag expression simplifies into:

$$-\Delta\Gamma_{\text{HS}} = -3/4 \Sigma_0(r_c)\Omega_K^2(r_c)\mathcal{S}x_s^4. \quad (6.15)$$

This expression shows that our horseshoe drag scales with the opposite of the unperturbed entropy gradient, as was already apparent at the end of section 6.1.1. We will check this scaling with appropriate numerical calculations in the next section. In addition, the horseshoe drag scales with x_s^4 , hence with $(q/h)^2$ in the low-mass regime. We point out that the scaling of the horseshoe half-width x_s with $(q/h)^{1/2}$ comes from the identification done by [Masset et al. \(2006a\)](#) of (i) the horseshoe drag expression calculated by [Ward \(1991\)](#) for the vortensity perturbations inside the coorbital region and (ii) of the *linear* estimate of the coorbital corotation torque of [Tanaka et al. \(2002\)](#). None of these studies considered a softening length for the planet potential, so there is likely to be an additional dependence of the horseshoe drag (and certainly also of Γ_{cd}) on the softening length ε . This dependence will be investigated in section 6.1.5.

In figure 6.8, we look at the variation with q of the unsaturated value of Γ_{cd} (stars). All calculations have same disc parameters as those of the illustrative example of section 6.1.1. The values displayed in the figure are not obtained at the same time, as the time required to reach the unsaturated value decreases as the planet mass increases, namely it scales as $q^{-1/2}$, like the horseshoe U-turn time. The dashed line displays the horseshoe drag expression given by equation (6.15), with $x_s \sim 1.2r_p \sqrt{q/h(r_p)}\gamma^{-1/4}$. Recall that this expression is valid only for low-mass planets. For high-mass planets, [Masset et al. \(2006a\)](#) showed that x_s is somewhat smaller than expected from the restricted three-body theory, although it has the right scaling with q (the authors found $x_s \sim 1.7r_p q^{1/3}$). The examination of figure 6.8 leads to the following remarks. For the smallest planet to primary mass ratios reported, that is up to $q \sim 5 \times 10^{-5}$, our horseshoe drag expression underestimates by typically a factor of 50% the results of numerical simulations. We stress in particular that, for this range of q , Γ_{cd} scales with q^2 . This scaling is quite confusing, as it may be associated to a linear process. However, as we saw in the last section, already for $q \sim 5 \times 10^{-6}$ the unsaturated value of Γ_{cd} is not reproduced by linear analysis. In addition, we also display the *opposite* of the total adiabatic torque (red circles). This is meant to show that, even in the adiabatic case, the total torque shows a boost of the corotation torque for intermediate planet masses. Here the boost is a positive one as \mathcal{V} is positive and \mathcal{S} is negative. As in the locally isothermal situation ([Masset et al. 2006a](#)), we find that the torque boost effect is maximal for $q \approx q_{\text{offset}} \sim 0.6h^3(r_p)$ (dotted line). Surprisingly, there seems to be no connection between this maximum boost and the contribution of the entropy perturbations to the torque, since the latter continues to rise slightly faster than in q^2 .

²Recall that we only consider the horseshoe drag attributable to the entropy advection within the horseshoe region. A generalized expression will also account for the horseshoe drag arising from the vortensity advection.

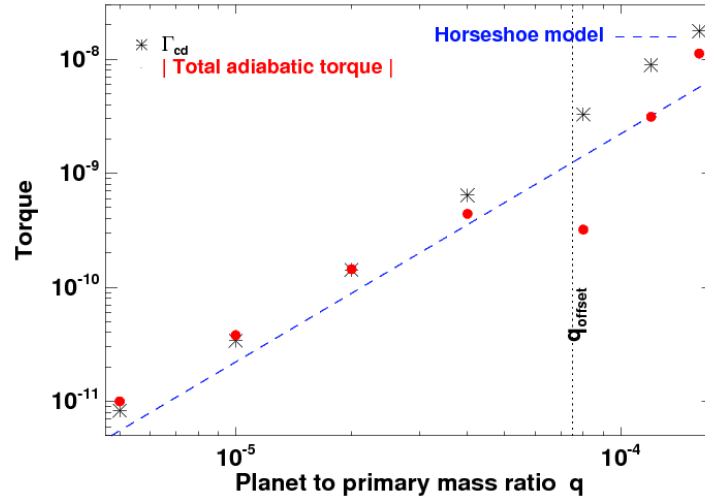


FIGURE 6.8: Unsaturated value of the torque excess (that obtained in the plateau) as a function of q . The dashed line depicts the estimate given by the horseshoe model (see equation (6.14)). The vertical dotted line shows the location of $q_{\text{offset}} = 0.6h^3$, where a boost of the corotation torque is normally expected in the locally isothermal case. In our case, the total adiabatic torque does display a boost near the location of q_{offset} , but it does not seem to be related with a boost of the torque due to the contact discontinuity.

6.1.4 Dependence on the entropy gradient

The torque expression of equation (5.42) and the horseshoe drag expression of equation (6.14) suggest that E and Γ_{cd} scale with \mathcal{S} , that is with the unperturbed entropy gradient. To check this prediction, we have undertaken a number of calculations with different values of \mathcal{S} , through different power-law indexes of the initial surface density and temperature profiles. As the unperturbed entropy S_0 , surface density Σ_0 and temperature T_0 are connected with $S_0 \equiv T_0 \Sigma_0^{1-\gamma}$, we varied, for a given entropy gradient, the temperature and surface density gradients. All other disc and planet parameters are again those of the illustrative run of section 6.1.1, summarized in table 6.1. At the top row of figure 6.9, we display the unsaturated value of E (left panel) and of Γ_{cd} (right panel) as a function of the unperturbed entropy gradient $d \ln S_0 / d \ln r$. Near each calculation result, represented with a filled circle, we indicate the corresponding unperturbed surface density and temperature profiles. The main trend coming out of these panels is that both E and Γ_{cd} essentially *scale with the unperturbed entropy gradient*. For a positive entropy gradient, E is negative, hence type I migration is accelerated compared to the locally isothermal configuration. For a negative entropy gradient, E is positive and type I migration is slowed down. If the entropy gradient is sufficiently negative, the excess of corotation torque may be positive enough so that the total torque on the planet become positive. In this case, the planet will migrate *outwards*. This is what we obtained for instance with $\Sigma_0 \propto r^{-0.5}$ and $T_0 \propto r^{-1}$, in agreement with the findings of [Paardekooper & Mellema \(2008\)](#). Note that interestingly, these profiles are those of the thermodynamic equilibrium of a disc with a uniform kinematic viscosity and a uniform opacity (see e.g. section 3.3.5). Of course, the above conclusion that type I migration may be significantly slowed down or even be reversed with an adiabatic energy equation holds *as long as* saturation is not active or of negligible impact. The study in section 6.2 of the desaturation properties will thus be of overriding importance so that migration be really slowed down on the long term, and not only for a few tens of orbits.

Furthermore, for a given entropy gradient, the results show a relatively small dependence with the surface density and temperature gradients, hence with the pressure gradient. This justifies

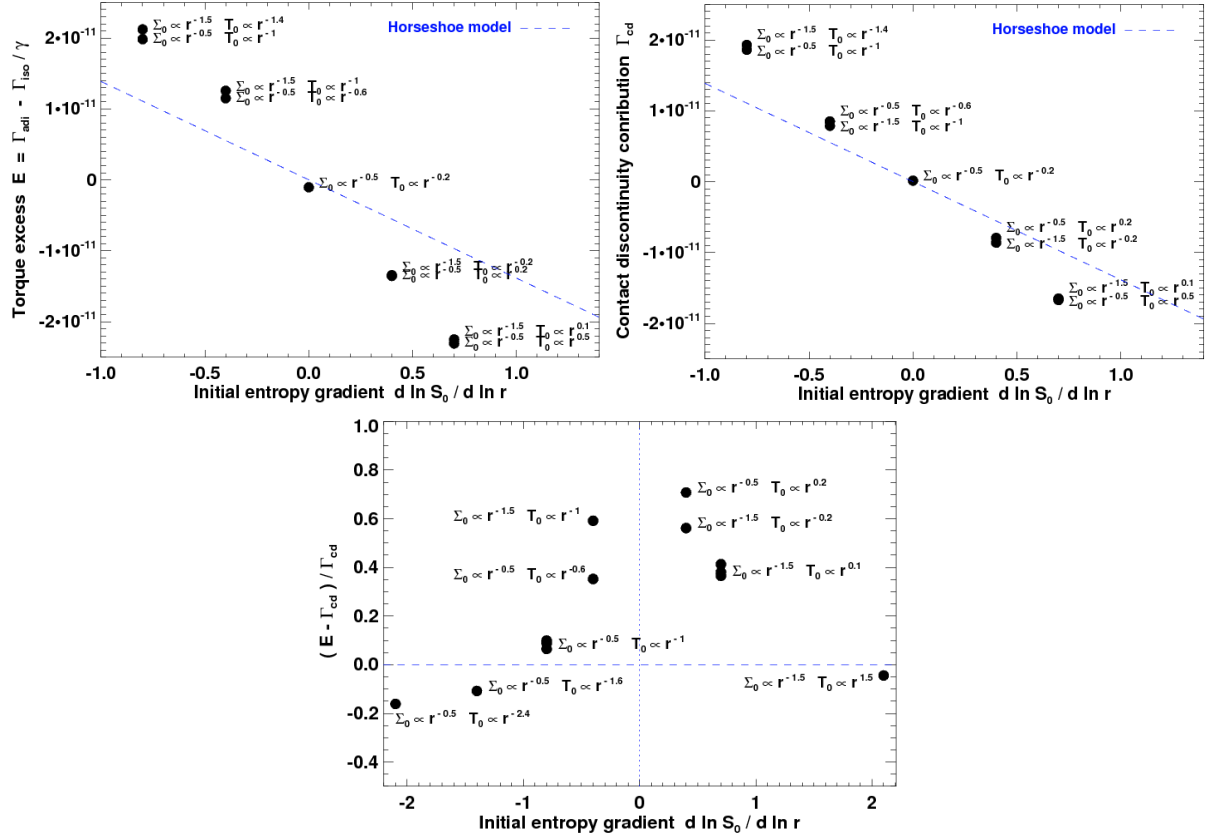


FIGURE 6.9: Torque excess E (top-left panel) and contact discontinuity contribution to the torque Γ_{cd} (top-right panel) as a function of the unperturbed entropy gradient. Although the calculations display little scatter for a given value of the entropy gradient, the different points can be considered as aligned within a good level of approximation. The slope of the dependence is negative. The bottom panel shows that the relative difference of E and of Γ_{cd} depends on the unperturbed entropy gradient.

a posteriori the fact we neglected the double pole term in our linear analysis (this strongly divergent term precisely scales with the unperturbed pressure gradient, see section 5.3.1). This small dependence with the pressure gradient, and the global scaling with the entropy gradient, are a nice confirmation of the results of our linear analysis. In addition, we superimposed to these panels the torque expression of our horseshoe drag model. The latter underestimates Γ_{cd} by typically a factor of $\sim 50\%$, whatever the unperturbed entropy gradient. For the entropy gradients reported in these panels, we note that E is always larger than Γ_{cd} , as already been discussed in section 6.1.2. The relative difference between them seems however to vary with the entropy gradient. To check this quantitatively, we display in the bottom panel of figure 6.9 the relative difference of E and of Γ_{cd} versus the unperturbed entropy gradient. We performed three additional calculations with larger entropy gradients ($|d \log S_0 / d \log r| > 1$). Surprisingly, this relative difference depends much on the entropy gradient, whereas from our linear analysis we expect it to be ~ 1 , whatever \mathcal{S} . Note that the smaller the amplitude of the entropy gradient, the closer the relative difference to unity. For large values of $|\mathcal{S}|$, Γ_{cd} even becomes larger than E . This suggests that at some point the torque excess does not account only for the entropy perturbations in the coorbital region. As will be presented in section 6.1.7, additional vortensity perturbations may also be at work.

6.1.5 Impact of the softening length

In this section, we follow up our investigation of the parameter space with the impact of the softening length on the excess of corotation torque. In an isothermal disc, the corotation torque scales with $|\Phi + \Psi|^2$ (Tanaka et al. 2002), where we recall that Φ is the planet potential, and $\Psi = p_1 / \Sigma_0$ (Ψ is the gas enthalpy for an isothermal disc). Even if Φ diverges at corotation, $\Phi + \Psi$ remains finite, which makes the isothermal corotation torque a quantity relatively insensitive to the softening length. The situation is quite different for the effects linked to the entropy advection: they involve the product $\Phi(\Phi + \Psi)$, which diverges when Φ does. Adiabatic effects on the corotation torque should acquire a very large magnitude at small softening length. In particular, if the softening length is smaller than the distance from orbit to corotation, the magnitude of these effects should strongly depend on this distance, which scales with the pressure gradient. If one regards the softening length as a proxy for the altitude in a three-dimensional disc, the extent of the disc vertical scale height concerned by these very small softening length issues should be small, however, since the distance from orbit to corotation is a fraction of $r_p h^2$. Nevertheless, it is of interest to investigate the behavior of the corotation torque in an adiabatic flow at very small softening length to assess the importance of such effects.

We present in this section preliminary results on this topic. We performed a series of calculations that are similar to the run of section 6.1.1, except that we vary the softening length from $0.05H(r_p)$ to $0.8H(r_p)$, hence from $2.5 \times 10^{-3} r_p$ to $4 \times 10^{-2} r_p$ ($H(r_p)$ remains fixed to $0.05r_p$). Note that the mesh resolution is the same for all values of ε . We stress that the customary value for ε is $\sim 0.6H(r_p)$, because the total torque obtained with two-dimensional isothermal calculations is found to be in good agreement with the three-dimensional analytical estimate of Tanaka et al. (2002). In the left panel of figure 6.10, we show as a function of $\varepsilon/H(r_p)$ the total torque exerted on the planet when the corotation torque is fully unsaturated. The results are displayed both with adiabatic and locally isothermal runs. The locally isothermal torque becomes more negative at smaller ε , suggesting an enhancement of the differential Lindblad torque. More quantitatively, the isothermal torque is increased by 2.5 when decreasing ε from $0.8H(r_p)$ to $0.2H(r_p)$. This is in very good agreement with the enhancement factor found by Masset (2002) for the differential Lindblad torque (see his figure 19). This confirms that an increase of the (positive) corotation torque is of negligible impact concerning the locally isothermal run. Note that for the smallest softening length reported, the trend seems to reverse. This

is not likely due to the differential Lindblad torque, since the latter converges as ε tends to zero (Masset 2002). For this run, we observed a strong accumulation of vortensity in the stagnation points close to the planet location (see Masset et al. (2006a) for the location of the stagnation points in two-dimensional isothermal calculations). After some time, this vortensity is released along the separatrices of the horseshoe region. These vortensity perturbations have same sign as those advected from the unperturbed vortensity gradient, and the (positive) corotation torque is therefore enhanced. This may explain why for this very small softening length the total torque gets a high, positive boost. The mechanism under which vortensity is accumulated in the stagnation points and then gets released is not fully understood yet. Presumably it is a non-linear effect since the Bondi radius to softening length ratio is ~ 0.8 . We will try to get more insight into this mechanism in section 6.1.7.

Contrary to the locally isothermal torque, the adiabatic torque becomes more positive when decreasing the softening length. This plays this time in favor of an increase of the (positive) contact discontinuity contribution to the torque. It also suggests that the latter increase be *stronger* than that of the differential Lindblad torque. To check this, we evaluated the fully unsaturated value of Γ_{cd} as a function of $\varepsilon/H(r_p)$. This is depicted in the right panel of figure 6.10. The dashed curve shows that Γ_{cd} scales with ε^{-1} , and confirms that it diverges when ε goes to zero. We point out that the scaling in ε^{-1} may be surprising. A hand-waving interpretation may be formulated as follows. In the limit of a cold isothermal disc, the corotation torque scales as the sum over m of $m\Phi_m(r_c)^2$, which turns in the end to scale as ε^{-2} (Masset, 2006, private communication). In the general isothermal case, the corotation torque involves the sum of $m|\Phi_m + \Psi_m|_{r_c}^2$, which is rather insensitive to ε , as shown above. In the adiabatic case now, given that $|\text{Im}[\Psi_m](r_c)| \lesssim |\text{Re}[\Psi_m](r_c)|$, Γ_{cd} , which accounts for the sum of $m\{\Phi_m[\Phi_m + \text{Re}(\Psi_m)]\}_{r_c}$, should *therefore* scale as ε^{-1} .

In the right panel of figure 6.10, we also superimposed the torque excess E for comparison. It shows that the ratio of the torque excess and of the contact discontinuity contribution is compatible with a factor of 2 at small softening length, in agreement with the analytic expectation (see section 6.1.2). However, we point out that this agreement may be fortuitous, for at least two reasons. First, we evaluate the torques when they are totally unsaturated, that is when the linear analysis is no longer valid. Moreover, we showed in the bottom panel of figure 6.1.4 that the relative difference of E and Γ_{cd} has a complex dependence with the entropy gradient. In particular, $|E|$ becomes smaller than $|\Gamma_{\text{cd}}|$ at large $|\mathcal{S}|$, contrary to what may be expected on analytical grounds. In this case, we believe that another non-linear effect is at work to explain the difference between E and Γ_{cd} . We will describe it in section 6.1.7.

6.1.6 Impact of the adiabatic index

Another parameter that may have a relevant impact on the torque excess is the adiabatic index γ . In particular, it is interesting to investigate what happens in the limit where γ tends to unity. In this limit, the pressure p and the thermal energy e evolve independently, and one would expect to recover the locally isothermal situation. To check this expectation, we performed an adiabatic calculation with $\gamma = 1.001$, another one with $\gamma = 1.4$, and a locally isothermal run. For these runs, the planet to primary mass ratio is $q = 2.2 \times 10^{-5}$, which corresponds to a $M_p \sim 7.3$ Earth-mass planet if the central object has a solar mass. The unperturbed surface density is taken *uniform* so that the unperturbed entropy profile be independent on γ . With this particular configuration, the gradients of the unperturbed temperature and entropy are therefore identical. We performed two series of runs:

- In the first series, whose results are displayed in the left panel of figure 6.11, the initial temperature and entropy are taken uniform ($\mathcal{S} = 0$). In this case, there is no entropy

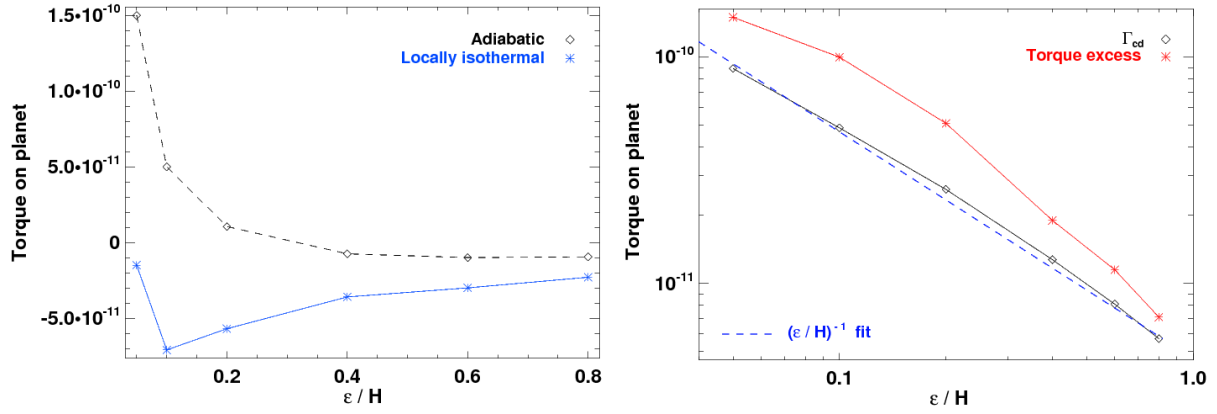


FIGURE 6.10: Left: Adiabatic and locally isothermal torques as a function of $\varepsilon/H(r_p)$, the softening length to disc scale height ratio. When decreasing the softening length, the adiabatic torque becomes more positive, the locally isothermal torque more negative. Right: torque excess and contact discontinuity contribution to the torque (Γ_{cd}) versus $\varepsilon/H(r_p)$. The dashed line corresponds to a $[\varepsilon/H(r_p)]^{-1}$ fit of Γ_{cd} .

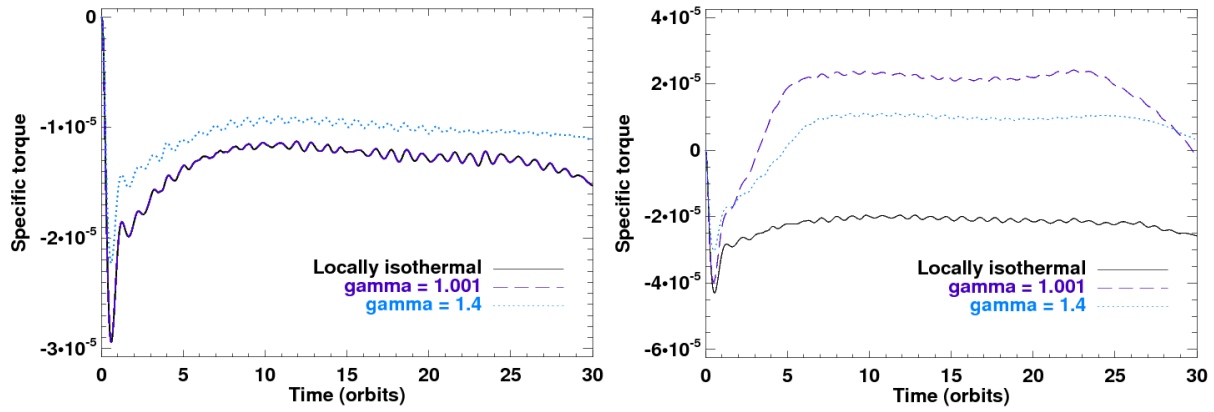


FIGURE 6.11: Specific torque for calculations having a $q = 2.2 \times 10^{-5}$ planet to primary mass ratio. We compare the time evolution of the torques obtained in the following situations: locally isothermal (solid line), adiabatic with $\gamma = 1.001$ (dashed line), and adiabatic with $\gamma = 1.4$ (as usually assumed, dotted line). All calculations have an unperturbed surface density profile that is uniform. On the left panel, the initial temperature is uniform. On the right panel, it decreases as r^{-1} .

perturbations in the planet's coorbital region, and the adiabatic torque only accounts for the differential Lindblad torque and for the contribution of the vortensity gradient to the corotation torque. When passing from the locally isothermal situation to the adiabatic one, both torques are divided by $\sim \gamma$ (see section 6.1.1). Not surprisingly, the torque of the adiabatic calculation with $\gamma = 1.001$, and that of the isothermal run are indistinguishable. This reference series confirms that the results of *isentropic* and of *isothermal* runs converge when the adiabatic index tends to unity (see section 3.3.1).

- In the second series, the temperature profile decreases as r^{-1} , and so does the entropy profile. The results are displayed in the right panel of figure 6.11. The torques obtained with the locally isothermal run, and with the adiabatic calculation with $\gamma = 1.001$ are totally different. Both adiabatic calculations display a positive excess of corotation torque due to the advection of entropy perturbations ($\mathcal{S} < 0$). The torque excess obtained with $\gamma = 1.001$ is even larger than the one with $\gamma = 1.4$. We note in passing that the fully unsaturated value of the total torque obtained with these two runs is positive. These results

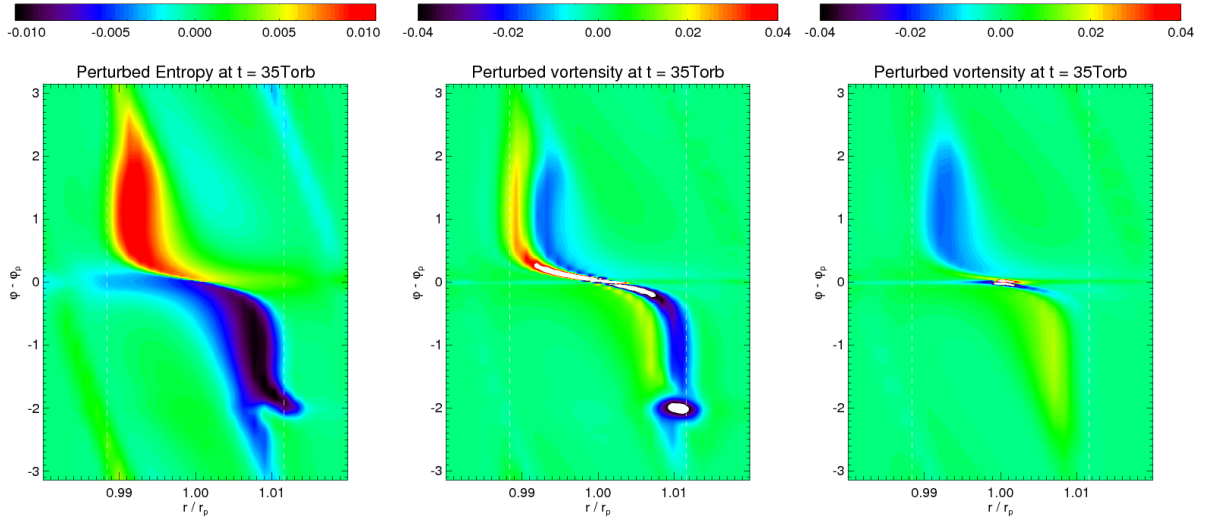


FIGURE 6.12: Results of a calculation with $S = 0.5$ and $\mathcal{V} = 1$. The left and middle panels show respectively the perturbations of the gas entropy and vortensity in the planet's horseshoe region. The vortensity perturbations obtained with a similar (locally) isothermal calculation are displayed in the right panel. The vertical dashed-lines represent the separatrices of the horseshoe region (those of the adiabatic calculation). The color scale in the two rightmost panel has been partially saturated to underline the primary and secondary advections (see text).

can be interpreted as follows. When the gradient of the unperturbed entropy profile does not vanish, the entropy conservation along element paths yields entropy perturbations in the horseshoe region, whatever the adiabatic index. Differently said, even when γ is very close to unity, the adiabatic configuration yields an excess of corotation torque that cannot exist in the locally isothermal situation, simply because in this case there is no entropy advection. This provides an example of hydrodynamic problem for which adiabatic and locally isothermal configurations give different results when the adiabatic index tends to unity. Furthermore, the larger the entropy difference on each side of the corotation radius, the larger the excess of corotation torque. The amplitude of the latter therefore increases with (i) the entropy gradient and (ii) the half-width x_s of the horseshoe region. For both adiabatic calculations, the unperturbed entropy profiles are identical. However, as already pointed out before, x_s scales with c_s^{-2} , hence with $\gamma^{-1/4}$ (this scaling shows that the corotation torque itself should scale with γ^{-1} , see section 6.1.1). This explains why the total torque obtained with $\gamma = 1.001$ is more positive than the one with $\gamma = 1.4$. Note however that the ratio of both torque is somewhat larger than 1.4. We mention that another side-effect of the reduction of γ is that both the horseshoe U-turn time and the libration time are reduced. This is clearly visible on the panel.

6.1.7 Vortensity - entropy coupling

Hitherto, we have stated that the vortensity perturbations in the adiabatic case should be similar to those of the locally isothermal situation, except that their amplitude should be smaller in the adiabatic case, because of the width reduction of the horseshoe region. However, from the vortensity equation given by equation (2.15), we expect the entropy perturbations to act as vortensity source terms.

To check the probable coupling between entropy and vortensity, we display in figure 6.12 the relative perturbations of the gas entropy (left panel) and vortensity (middle panel) for an

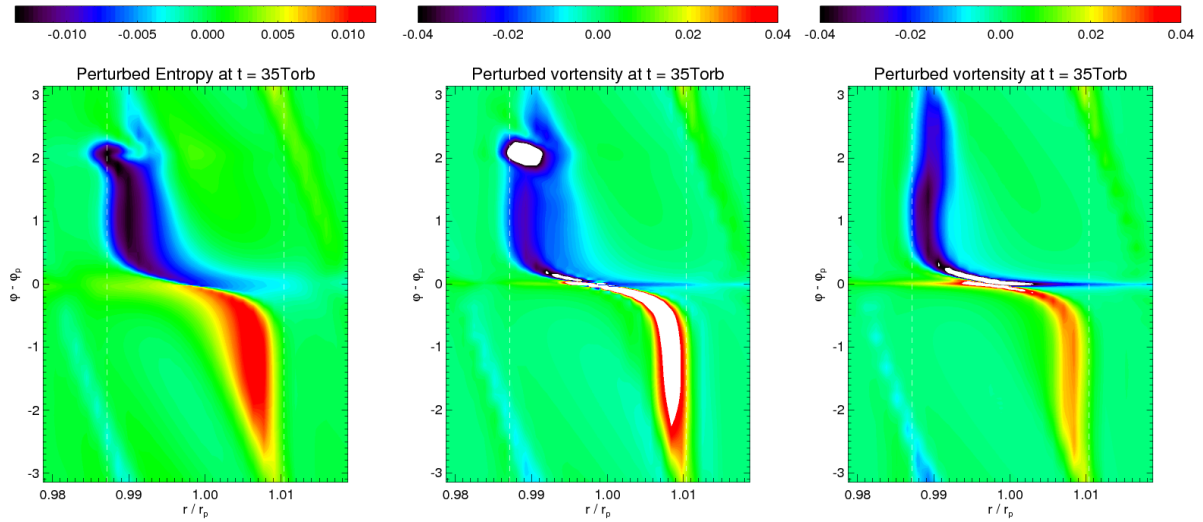


FIGURE 6.13: Same as figure 6.12, for calculations with $\mathcal{S} \approx -0.6$ and $\mathcal{V} = 1$.

adiabatic run with $\mathcal{S} = 0.5$ and $\mathcal{V} = 1$. The vortensity perturbation obtained with an equivalent locally isothermal run is depicted in the right panel. We see that the adiabatic perturbed vortensity presents a much more complicated structure than expected. We observe an additional advection of vortensity perturbations, at somewhat larger distance from corotation than the expected vortensity advection. The expected advection is now called "primary" advection, in contrast with the additional one, which we refer to as the "secondary advection". A closer look at the rightmost panel of figure 6.12 reveals an accumulation of vortensity very close to the planet location in the locally isothermal run. Although not reported here, we have checked that vortensity accumulates at the location of the fixed stagnation points identified by [Masset et al. \(2006a\)](#). For reasons that need to be clarified, the vortensity in the adiabatic case cannot accumulate at the stagnation points on the long term, and it is ultimately released in the flow, where it contributes to the secondary advection aforementioned. Note the asymmetry of the release process, which leads to the formation of a vortex at the outer separatrix of the horseshoe region. Regarding the impact on the torque, the primary and secondary advectations have opposite contributions. The vortensity contribution to the corotation torque is less positive than expected for the adiabatic run. This is taken into account by the torque excess, which is therefore larger (it is more negative) than expected from the entropy perturbations only.

We display in figure 6.13 the results obtained with $\mathcal{S} \approx -0.6$ and $\mathcal{V} = 1$. The vortensity of the locally isothermal run is qualitatively different from that of figure 6.12: the half-width of the horseshoe region is larger, and the accumulation in the stagnation points is less obvious. Presumably the secondary advection already appears in the locally isothermal run, but it is emphasized in the adiabatic case. Again, the additional vortensity perturbations render the torque excess larger (here it is more positive) than expected from the entropy perturbations only.

6.2 Desaturation of the corotation torque in a radiative disc

6.2.1 Saturation issues

In section 6.1, we have investigated the torque exerted on a low-mass planet by an adiabatic disc, and compared it to the torque obtained with a locally isothermal disc. In the adiabatic

case, we have found that the differential Lindblad torque is reduced by a factor of γ , and that the contribution of the vortensity perturbations to the corotation torque has essentially the same reduction, except at rather large entropy gradients, where additional vortensity perturbations may be triggered by entropy perturbations. We have found an additional contribution to the corotation torque, which originates from entropy perturbations due to entropy advection in the coorbital region. We have investigated in details the properties of the *fully unsaturated value* of this torque excess, in particular its dependence with the unperturbed entropy gradient. One key result is that the torque excess is positive for a negative entropy gradient, so type I migration should be slowed down. Nonetheless, due to libration in the coorbital region, the entropy perturbations start to mix up after about half the libration timescale, which is the time required for the perturbations sliding along the separatrices to perform a second horseshoe U-turn. Libration occurs on different timescales for the different streamlines of the corotation region, which tends to stir the entropy and to flatten out the entropy profile across the corotation region. This is similar to the behavior of the corotation torque in an isothermal disc, which tends to saturate as the vortensity profile is flattened out by libration. In the adiabatic case, both the entropy and the vortensity profiles are flattened out. This deserves some clarification. As the entropy becomes uniform over the libration region, the flow becomes barotropic. The source term $\nabla p \times \nabla \Sigma$ in the vortensity equation - see equation (2.15) - therefore cancels out, and the vortensity profile ultimately flattens out, as in the locally isothermal case. An illustration of the corotation torque saturation is displayed and commented in figure 6.14.

In the locally isothermal case, it is the *viscous diffusion* that can prevent the flattening out of the vortensity profile if it acts sufficiently rapidly to establish the large scale vortensity gradient before a libration time. This has been studied for an isolated resonance by Goldreich & Sari (2003) and Ogilvie & Lubow (2003), and by Balmforth & Korycansky (2001) and Masset (2001) for a planetary coorbital region. In both cases, the degree of saturation of the corotation torque in steady state depends on the ratio of the libration time and of the viscous time across the libration region. The corotation torque will keep its fully unsaturated value on the long term provided that the viscous time be (i) smaller than the libration time to minimize saturation, and (ii) larger than the horseshoe U-turn timescale, so that the corotation torque reaches its fully unsaturated value. The viscous time across the horseshoe region is $\tau_{\text{visc}} \sim x_s^2/3\nu_p$, with ν_p the kinematic viscosity at the planet location. Using equations (6.1), (6.21) (in the appendix), and $x_s \sim r_p \sqrt{q/h}$, we find that the α parameter³ at the planet location, $\alpha_p = \nu_p h^{-2} r_p^{-2} \Omega_p^{-1}$ - see equation (2.1) - should satisfy:

$$\frac{q^{3/2}}{8\pi h^{7/2}} \leq \alpha_p \leq \frac{q^{3/2}}{8\pi h^{9/2}}. \quad (6.16)$$

We display in figure 6.15 the range values of α_p that satisfy inequality (6.16) as a function of the planet to primary mass ratio, assuming $h = 0.05$. This range, for which the corotation torque will keep its fully unsaturated value, is indicated by the white area. Assuming for instance $q = 6 \times 10^{-6}$ (which corresponds to a two Earth mass planet if the central object has a solar mass), we read $2 \times 10^{-5} \leq \alpha_p \leq 4 \times 10^{-4}$. These range values are much smaller than the standard α values inferred from the numerical simulations of the Magneto-Rotational Instability (MRI), typically in between 10^{-3} and 10^{-1} - see section 2.2. From figure 6.15, we see that even with $\alpha_p \sim 10^{-3}$ τ_{visc} is likely to be much smaller than $\tau_{\text{u-turn}}$ for $q \lesssim 10^{-5}$, so the amplitude of the corotation torque should be very small compared to that of the differential Lindblad torque. Note however that inequality (6.16) is highly sensitive on the disc aspect ratio. If we take $h = 0.03$, the white area in figure 6.15 would correspond to values of α_p increased by an order of magnitude, and the corotation torque could keep its fully unsaturated value for $q \gtrsim 10^{-6}$.

³We now denote by α the so-called α parameter in the viscosity model of Shakura & Sunyaev (1973).

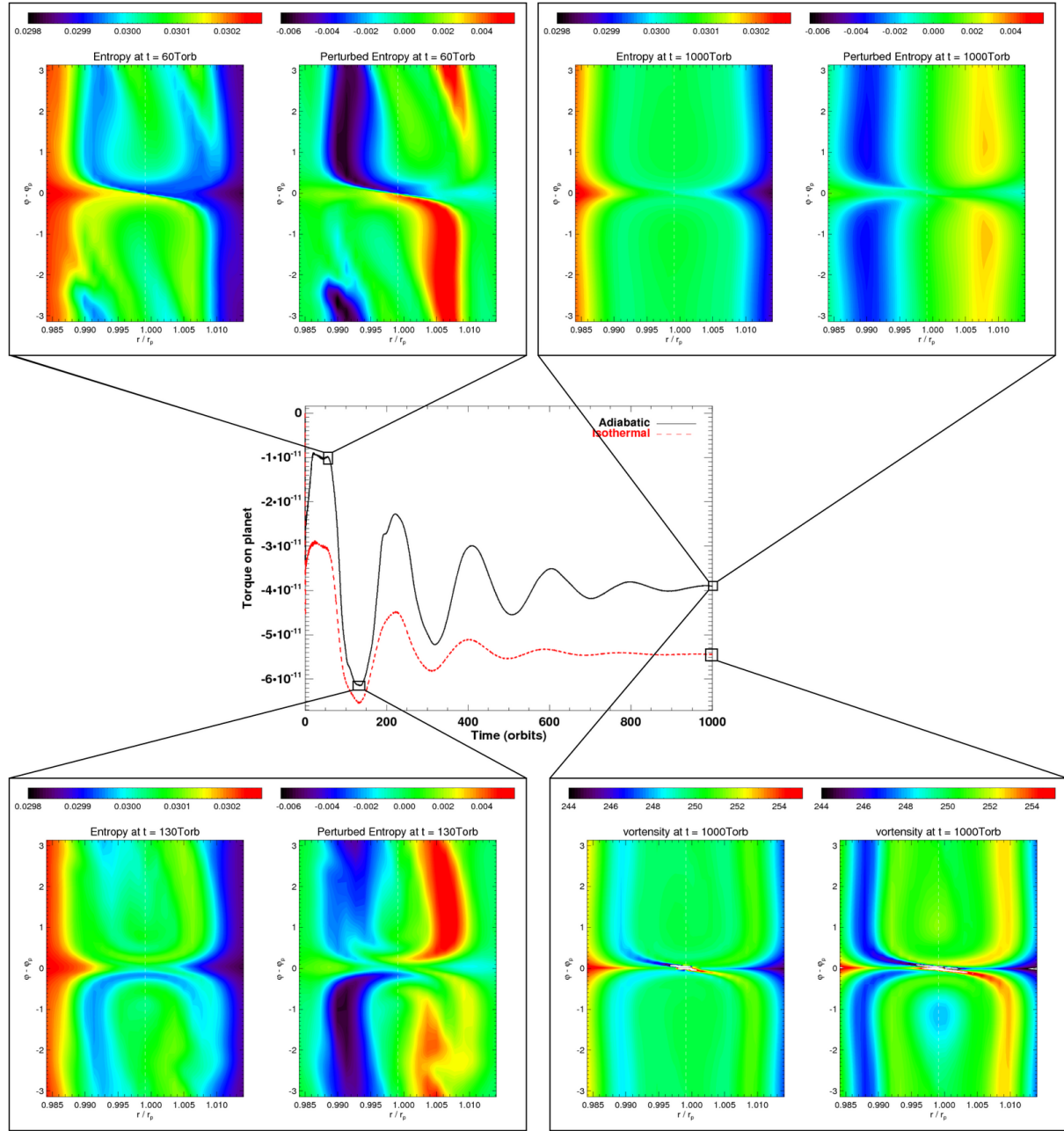


FIGURE 6.14: Illustration of the corotation torque saturation. The long-term evolution of the torque obtained with the illustrative run of section 6.1.1 is displayed in the middle row. The adiabatic torque (solid curve) and of the locally isothermal torque (dashed curve) oscillate with time, with an oscillation amplitude decreasing progressively with time, due to the saturation of the corotation torque. Both torques do not oscillate in phase, because the libration timescale, which is proportional to x_s^{-1} , is slightly larger in the adiabatic case. At about 1000 orbits, time oscillations are hardly distinguishable, which indicates that the corotation torque is fully saturated in both cases. At this time, the ratio of the isothermal torque and of the adiabatic one is very close to γ , as expected. In addition, the different boxes display screenshots of the entropy and of the perturbed entropy at several times: at about half the libration timescale, when the corotation torque starts to saturate (top-left box), at about the libration time, when the corotation torque is negative (bottom-left box), and at 1000 orbits, when the entropy inside the coorbital region is totally flat (top-right box). The bottom-right box displays the vortensity at 1000 orbits, for the adiabatic run (left panel) and for the locally isothermal one (right panel).

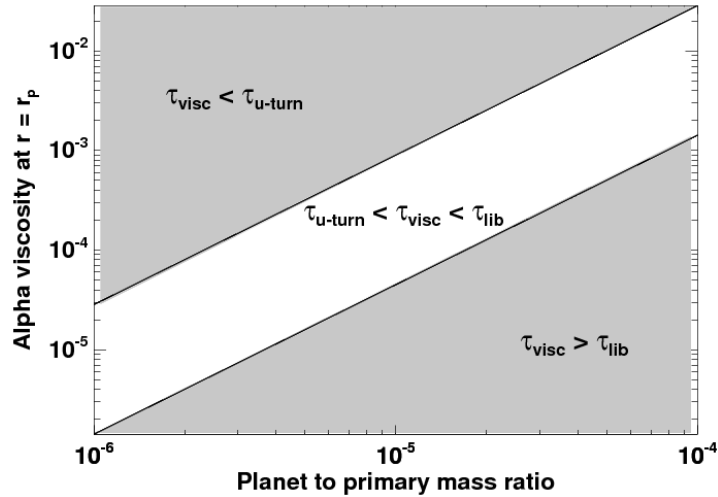


FIGURE 6.15: We display the range of α values at the planet location for which the isothermal corotation torque can be fully unsaturated (white area), as a function of the planet to primary mass ratio q . We assume that the disc aspect ratio at the planet location is $h(r_p) = 0.05$. In the upper shadowed area, the viscous timescale τ_{visc} is smaller than than the horseshoe U-turn time $\tau_{\text{u-turn}}$: the vortensity perturbations do not reach the separatrices, and the amplitude of the corotation torque is smaller than that of its fully unsaturated value. In the lower shadowed area, τ_{visc} is larger than the libration time τ_{lib} , so the corotation is partially saturated.

As stated above, the customary values of α aforementioned are associated with the turbulence generated by the MRI. The conditions under which this instability occurs have been described in section 2.2. Recall in particular that it is not clear whether the disc mid-plane, where planets build up and ultimately migrate, is magnetically active or not. Even if the planet is inside a dead zone, turbulence may be induced by the active layers, leading to an effective viscosity. The latter is however somewhat smaller than in the active layers, and an α value of $\sim 10^{-4}$ is generally considered as relevant for dead zones. From figure 6.15, we see that it may suffice to unsaturate the corotation torque for planet masses subject to type I migration.

Viscosity, which acts as a diffusive source term in the vortensity equation (see e.g. [Ogilvie & Lubow 2006](#)), will *also* be required in the adiabatic case to unsaturate the contribution of the vortensity perturbations to the corotation torque. The above discussion on the amount of viscosity required for unsaturation therefore holds for an adiabatic disc. By analogy, source terms in the energy equation will be required to unsaturate the contribution of the entropy perturbations to the corotation torque. Radiative processes (cooling and viscous heating) should be able to impose the large scale entropy gradient over the corotation region in less than a libration time. To maintain an unsaturated torque excess, these processes should occur on a timescale longer than a horseshoe U-turn (otherwise the flow can rather be considered as locally isothermal), but shorter than the libration time (otherwise the flow will rather be adiabatic, and the torque excess will saturate, at least partially). As already pointed out, there is at least an order of magnitude difference between the horseshoe U-turn time and the libration time in a thin disc. As for the viscous time, it should therefore be possible to find a location in the disc where the cooling time is much longer than the U-turn time and yet shorter than the libration time.

6.2.2 A simple temperature prescription

We study the desaturation properties of the corotation torque in radiative discs with a set of disc and planet parameters that is slightly different from that of section 6.1. The planet to primary mass ratio passes from $q = 5 \times 10^{-6}$ to $q = 6 \times 10^{-6}$. The initial temperature now decreases as r^{-1} instead of $r^{-0.6}$, so the unperturbed entropy gradient is twice that of the illustrative run of section 6.1.1. We adopt a uniform kinematic viscosity $\nu = 2 \times 10^{-7}$, which is equivalent to $\alpha = 8 \times 10^{-5}$ at the planet location. This low value is intended to represent the viscosity expected in the disc mid-plane inside a dead zone, as discussed in section 6.2.1. For the sake of simplicity, this low viscosity value is the only characteristic of the angular momentum transport we will aim at modeling. In particular, our model does not account for the velocity fluctuations induced by the hydrodynamic turbulence. The inclusion of turbulence, such as in the model proposed by Laughlin et al. (2004) to mimic the effect of the MRI, is certainly a promising extension of this work. We comment that the neglect of the stochastic effects of turbulence on migration is likely a reasonable assumption here, owing to the modest level of turbulence expected in the dead zone. The angular momentum transport is therefore still modeled in a *laminar way* with the usual Navier-Stokes viscosity tensor. We note in passing that, using figure 6.15, our value of α should maintain the corotation torque contribution from the vortensity perturbations to its fully unsaturated value.

Viscosity acts as a heating source term in the energy equation, and some additional cooling is required to reach a thermodynamic equilibrium. We neglect in this paragraph the thermal diffusion in the disc mid-plane (second term on the right-hand side of equation (3.56)). Instead of considering the energy flux radiated in the vertical direction, given by equation (3.58), we propose an equivalent formulation based on a simple temperature prescription with characteristic time τ_{presc} . This comes to substituting the cooling source term Q_- in the energy equation by:

$$Q_{\text{presc}} = \frac{T - T_0}{\tau_{\text{presc}}} \times \frac{e}{T} = \frac{e}{\tau_{\text{presc}}} - \frac{e_0}{\tau_{\text{presc}}} \frac{\Sigma}{\Sigma_0}, \quad (6.17)$$

where we recall that $e = \mathcal{R}\Sigma T/(\gamma - 1)$ denotes the thermal energy per unit area. Note that Q_{presc} may be positive or negative, depending on the sign of $T - T_0$. When $T > T_0$, Q_{presc} is positive and the gas temperature is reduced, whereas for $T < T_0$, $Q_{\text{presc}} < 0$ and the temperature is increased. When the disc is in thermodynamic equilibrium, the stationary profile of the temperature, T_{stat} , is given by $Q_+ = Q_{\text{presc}}$, with Q_+ the viscous heating flux, given by equation (3.59). This yields:

$$T_{\text{stat}}(r) = T_0(r) \left[1 + \frac{9}{8}(\gamma - 1)\nu \frac{\tau_{\text{presc}}}{H^2(r)} \right], \quad (6.18)$$

which reduces to $T_0(r)$ in absence of viscosity. To ensure that $T_{\text{stat}}(r)$ and $T_0(r)$ have the same large-scale radial gradient, we impose that τ_{presc} has the same radial dependence as H^2 , since ν is uniform. We thus take:

$$\tau_{\text{presc}}(r) = \tau_{\text{presc}}(r_p) \left(\frac{r}{r_p} \right)^{2+2f}, \quad (6.19)$$

with f the disc flaring index (see equation (3.3)). Let us assume that $\tau_{\text{presc}}(r_p)$ matches the viscous diffusion time across the horseshoe region, namely $\tau_{\text{presc}}(r_p) \approx 40 T_{\text{orb}}$. From equation (6.18), we find that $[T_{\text{stat}}(r) - T_0(r)]/T_0(r) \approx 0.9\%$, whatever r , so the temperature profile is hardly changed.

To illustrate the desaturation properties of the corotation torque, we display in the left panel of figure 6.16 the torque variation with time obtained with the following configurations:

- An adiabatic calculation (solid curve), for which the corotation torque saturates after ~ 50 orbits,

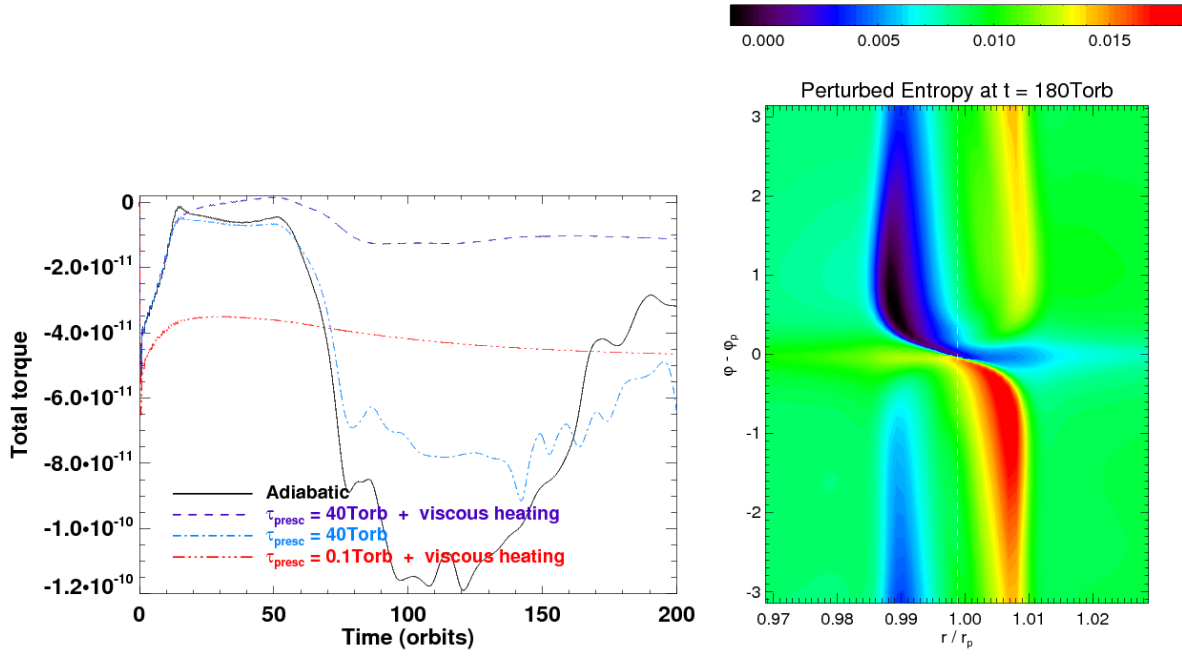


FIGURE 6.16: Left: torque variation with time obtained with the adiabatic and radiative calculations of section 6.2.2. The radiative calculations including viscous heating have a uniform kinematic viscosity $\nu = 2 \times 10^{-7}$, equivalent to $\alpha_p = 8 \times 10^{-5}$. All radiative calculations have a temperature prescription, the characteristic time being $\tau_{\text{presc}} = 40 T_{\text{orb}}$ or $\tau_{\text{presc}} = 0.1 T_{\text{orb}}$. Right: relative perturbation of the gas entropy at $t = 180 T_{\text{orb}}$ for the radiative calculation with viscous heating and $\tau_{\text{presc}} = 40 T_{\text{orb}}$ (its torque variation time corresponds to the dashed curve in the left-hand panel). The dashed line displays the location of the corotation radius.

- A radiative calculation with temperature prescription ($\tau_{\text{presc}} = 40 T_{\text{orb}}$), but no viscosity (dot-dashed curve). The torque average value is more positive than in the adiabatic run, as the torque contribution from the entropy perturbation is unsaturated.
- A radiative calculation with temperature prescription ($\tau_{\text{presc}} = 0.1 T_{\text{orb}}$) and viscosity (dot-dot-dot-dashed curve). As τ_{presc} is much smaller than the horseshoe U-turn time, there is no entropy perturbations advected in the horseshoe region. The corotation torque, which only includes the vortensity perturbations, is unsaturated due to the viscous diffusion across the horseshoe region.
- A radiative calculation with temperature prescription ($\tau_{\text{presc}} = 40 T_{\text{orb}}$) and viscosity (dashed curve). Here, both the torque contributions arising from the vortensity and the entropy perturbations are unsaturated. The total torque remains stationary in the long term, and it converges toward a value that is one order of magnitude smaller than the one obtained with a similar locally isothermal torque (not depicted here, its value is larger than the stationary value of the adiabatic torque by a factor of $\sim \gamma$).

These results confirm that both the viscosity and the radiative losses are required to unsaturate the corotation torque in radiative discs. In the right panel of figure 6.16, we show the relative perturbation of the gas entropy at $t = 180 T_{\text{orb}}$ for the radiative run with viscosity and $\tau_{\text{presc}} = 40 T_{\text{orb}}$. The global shape of the entropy perturbations, as well as that of the vortensity perturbations (not displayed here) hardly change after ~ 50 orbits, which explains the stationary value of the torque obtained after this date. This can be interpreted as follows. Let us consider a fluid element that has performed an inward horseshoe U-turn at the beginning of the simulation (e.g. at $t \sim \tau_{\text{u-turn}}$). While it slides along its streamline in the inner part of the horseshoe region, the fluid element does not conserve its specific entropy. The latter increases by the viscous heating, and it may increase or decrease through the temperature prescription. Here, the temperature prescription increases the entropy (and the temperature) of the fluid element until it reaches that of the background flow after a time comparable to the local prescription time τ_{presc} . The fluid element then performs an outward horseshoe U-turn, it propagates at the outer side of the coorbital region with a specific entropy larger than that of the local flow. This time, the entropy of the fluid element decreases so as to reach again the local entropy of after about τ_{presc} .

6.2.3 Heat diffusion in the disc mid-plane

We investigate in this paragraph the impact of the thermal diffusion on previous results. For this purpose, we performed two additional calculations with a uniform thermal diffusivity $\lambda = 2 \times 10^{-7}$. One corresponds to an inviscid disc, the other one has a uniform kinematic viscosity $\nu = 2 \times 10^{-7}$. Since thermal diffusion increases the entropy, a temperature prescription is used for these two runs. We took $\tau_{\text{presc}} = 40 T_{\text{orb}}$, as in section 6.2.2. We have checked that the stationary profile of the temperature is not altered by the thermal diffusion. Note also that the characteristic time for temperature relaxation, and the viscous and thermal diffusion timescales across the horseshoe region are approximately equal. All other disc and planet parameters are identical as those used in section 6.2.2. The left panel of figure 6.17 displays again the calculations results presented in the left panel of figure 6.16, to which we superimposed the results of the two additional runs with thermal diffusion. We see that the inclusion of thermal diffusion hardly alters the desaturation properties⁴, which has recently been confirmed by [Kley](#)

⁴Note however that it strongly depends on the characteristic times at play. The shortest timescale impacting on the radiative losses will dictate the desaturation of the corotation torque arising from the entropy perturbations in the horseshoe region.

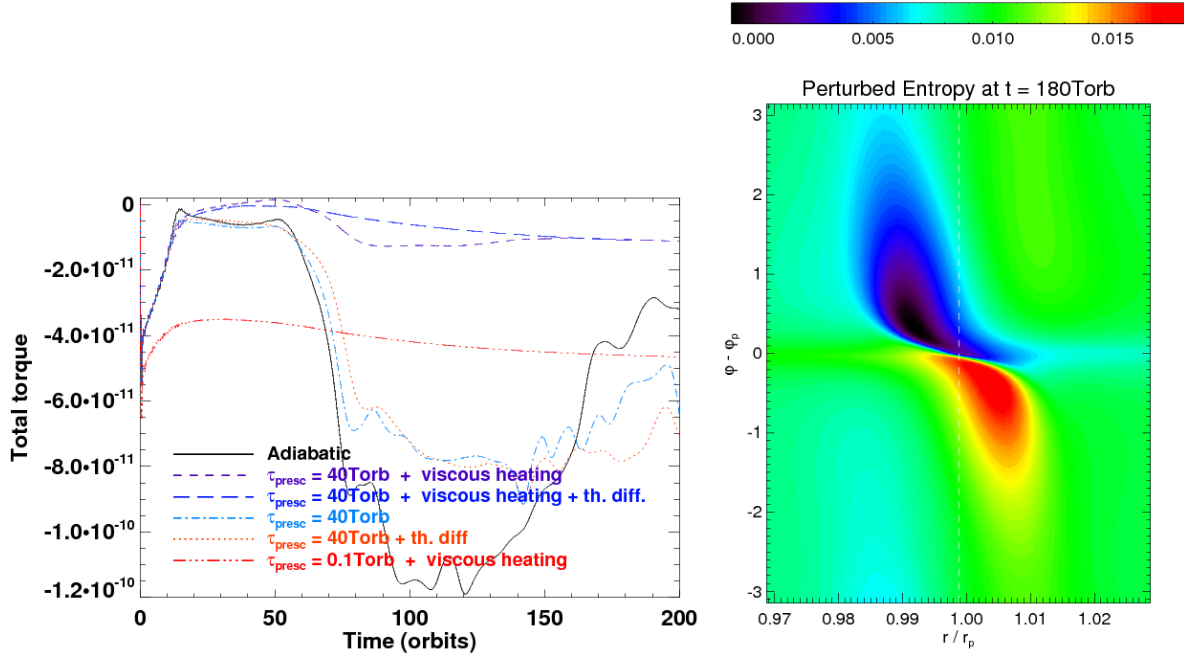


FIGURE 6.17: Left: same as the left panel of figure 6.16, except that the results of two calculations with thermal diffusion are superimposed. Both have a uniform thermal diffusivity $\lambda = 2 \times 10^{-7}$, one is inviscid (dotted curve), the other one has a uniform kinematic viscosity $\nu = 2 \times 10^{-7}$ (long-dashed curve). Right: same as the right panel of figure 6.16, but for the run including thermal diffusion.

& Crida (2008). This is illustrated by the right-hand panel in figure 6.17, where we show the entropy perturbation for the run with thermal diffusion, temperature prescription and viscosity. The comparison with the right panel of figure 6.16, where the thermal diffusion is discarded, reveals that the same large-scale entropy gradient is maintained.

6.3 Concluding remarks

We have investigated in this chapter the impact of the gas thermodynamics on type I migration. Our hydrodynamic calculations performed with an adiabatic disc have confirmed the main predictions made in chapter 5, in particular the scaling of the contact discontinuity contribution to the torque with the unperturbed entropy gradient. The numerical evaluation of this contribution is in very good agreement with the linear prediction for timescales smaller than the horseshoe U-turn time. However, the fully unsaturated value of this torque contribution is always underestimated by the linear analysis, by typically a 50% factor. Additional efforts are required to produce a predictive expression for the fully unsaturated corotation torque. We have finally shown that it is possible to unsaturate the corotation torque in radiative discs, provided that both viscosity and radiative losses are taken into account. When fully unsaturated, the torque exerted on a low-mass planet embedded in a radiative disc may be typically reduced by a factor of 10 with respect to a locally isothermal disc.

6.4 Appendix: estimate of the horseshoe U-turn time

We provide here an estimate of the horseshoe U-turn time and of the libration time for a small mass object embedded in a gaseous disc. The horseshoe half-width x_s is $\sim r_p \sqrt{q/h(r_p)}$. We

write a simplified Jacobi constant for a test particle near a horseshoe U-turn as

$$J = -\frac{\mathcal{G}M_p}{2Br_p|\varphi - \varphi_p|} + A(r - r_p)^2,$$

with A and B the Oort constants, given respectively by equations (5.1) and (5.2). We can thus estimate the distance of closest approach between the planet and a test particle flowing along a horseshoe separatrix, neglecting pressure effects. It reads:

$$r_p|\Delta\varphi|_s = \Omega_p^2 H(r_p)/2|AB| = \mathcal{O}(H(r_p)).$$

The time required to perform a horseshoe U-turn can be deduced using the radial drift velocity of the test particle when it crosses the orbit, at its closest approach from the planet:

$$\dot{x} = \frac{\mathcal{G}M_p}{2Br_p^2\Delta\varphi_s^2}.$$

We thus find:

$$\tau_{\text{U-turn}} = \frac{2x_s}{\dot{x}} = \frac{\Omega_p^2 h^{3/2}(r_p)}{q^{1/2} A^2 B} \approx \frac{4}{\Omega_p} \left(\frac{H(r_p)}{R_H} \right)^{3/2}, \quad (6.20)$$

where $R_H = r_p(q/3)^{1/3}$ is the Hill radius of the planet, and where the last equality holds for a Keplerian disc. When the planet emerges from the disc ($H(r_p) \sim R_H$), the horseshoe U-turn occurs on the dynamical timescale. When dealing with an embedded object however ($R_H < H(r_p)$), the horseshoe U-turn time can be substantially longer than the dynamical time (e.g. 10 times longer for an Earth mass object embedded in a disc with $h(r_p) = 0.05$). Using equation (6.1), we are led to

$$\tau_{\text{U-turn}} \approx h(r_p) \tau_{\text{lib}}. \quad (6.21)$$

Since $h \sim \mathcal{O}(10^{-1})$, there is at least an order of magnitude difference between the horseshoe U-turn time and the libration time in a thin disc.

Chapter 7

Conclusions and perspectives

Thirteen years have passed since the discovery of 51 Pegasus b, and studies of planetary formation and evolution keep providing lots of exciting results. The detection of the Hot Jupiters - see chapter 1 - has been the spearhead of a joint effort to produce coherent scenarios at each level of the planetary evolution. In particular, planetary migration has become an essential part of these scenarios. We have described in chapter 2 the different migration regimes a planet may encounter during its lifetime, depending on its mass and on the disc properties. The migration of low-mass planets - type I migration - has been particularly emphasized, since it enables analytic predictions that, together with models of planet formation and disc evolution, may be used to account for the great diversity of the exoplanets properties. When I started my thesis work, both analytic and numerical studies predicted that type I migration should occur on a timescale much shorter than the lifetime of the protoplanetary disc, rendering improbable the formation of giant planets far from their star. Many recent studies of disc-planet interactions have challenged to propose mechanisms slowing down, halting or even reversing migration, which underscore the particular sensitivity of migration on the underlying disc physics - see section 2.3.3. They have also stressed the important part played by hydrodynamic calculations to yield accurate estimates of the migration timescale. A detailed presentation of the hydrodynamic code we have used, and of the implementations we have made, has been described in chapter 3.

At the time of performing our first self-gravitating calculations, unexpected results were actually found *without* self-gravity. We have shown in chapter 4 that the usual practice of assuming a planet freely migrating in a disc without self-gravity can lead to a strong overestimate of the differential Lindblad torque, with respect to the analytical configuration where neither the planet nor the disc feel the disc gravity. We provide a simple way of evaluating this overestimate. It highlights the particular sensitivity of the differential Lindblad torque to any physical or unphysical processes that shift the resonances. The inclusion of the disc self-gravity in our calculations confirms that type I migration is slightly accelerated by the disc gravity. A simple determination of the torque relative difference with and without disc gravity is also given.

Studying the impact of the gas self-gravity beyond the linear regime will certainly contribute to refine our understanding of the migration processes. We have performed preliminary two-dimensional calculations showing that the self-gravity has generally a strong impact on the mass accumulation inside the circumplanetary disc, so the inertial mass of the planet can rapidly reach large values. A precise treatment of the gas thermodynamics will be required for such studies. Another point of interest is the outcome of passing to three-dimensional self-gravitating calculations. In the linear regime, we do not expect a change of the torque relative difference due to the disc gravity. However, it should be of considerable relevance for intermediate planet

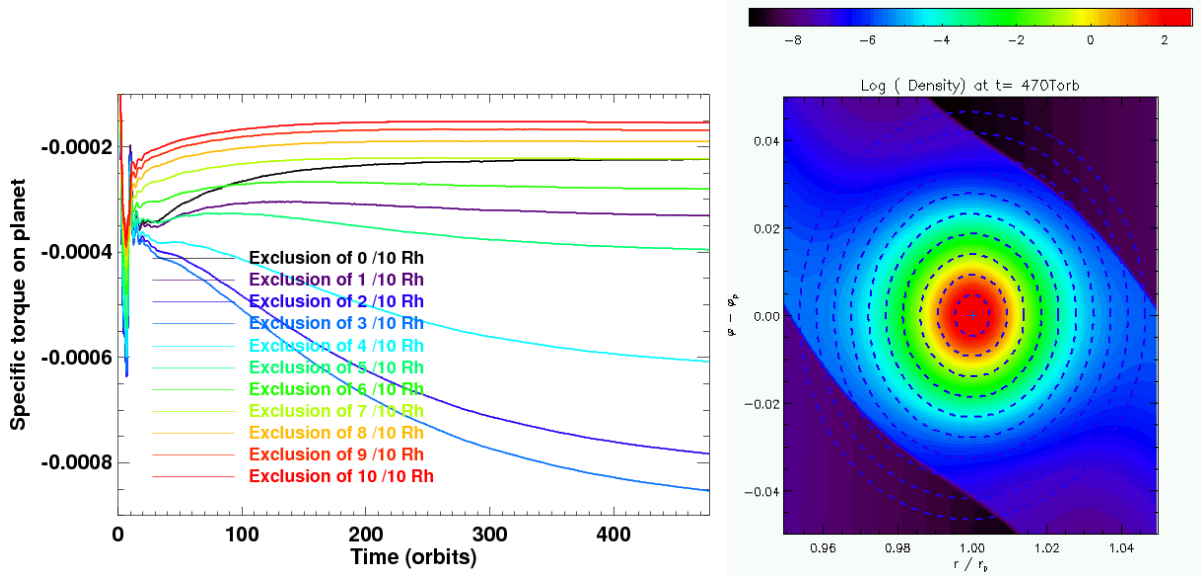


FIGURE 7.1: Results of a two-dimensional calculation with the hydrocode JUPITER, for a Saturn-mass planet ($M_p = 3 \times 10^{-4} M_\star$) in a massive disc ($M_{\text{disc}} = 2.4 \times 10^{-2} M_\star$). The planet is held on a fixed circular orbit for 477 orbits. The resolution near the planet is $\sim 4 \times 10^{-4} r_p$. On the left panel, we display the torque on the planet for different exclusion factors of the Hill Radius. For instance, exclusion of $3/10 R_H$ means that we discard the torque exerted on the planet by the fluid elements located within $0.3 R_H$ of the planet. On the right panel, we show the surface density near the planet location after 470 orbits. The ten dashed circles are centered on the planet, their radius goes from $0.1 R_H$ to R_H .

masses when a circumplanetary disc builds up, in particular to assess the frequency of type III migration. For planets harboring a circumplanetary disc, self-gravitating calculations may also bring a definitive answer to the debate on whether the circumplanetary disc should be excluded when evaluating the torque in absence of self-gravity. The relevance of this issue is illustrated in figure 7.1, where we show the results of a two-dimensional, non self-gravitating calculation obtained with the hydrocode JUPITER¹. The run, which involves a Saturn-mass planet in a massive disc, has the same parameters as the run 2DG6b of D’Angelo et al. (2005). The left panel shows that the torque on the planet can dramatically depend on the fraction of the planet’s Hill radius that is excluded on the torque evaluation. For instance, the torques obtained without exclusion and with exclusion of $0.3 R_H$ differ by a factor of ~ 4 ! The difference of these torques corresponds to the torque exerted on the planet by the material lying within $0.3 R_H$ of the planet. The surface density distribution near the planet location, depicted in the right panel of figure 7.1, however suggests that fluid elements within $\sim 0.6 R_H$ seem to be distributed axisymmetrically with respect to the planet. The origin of this large torque difference remains to be clarified.

Another aspect investigated in this thesis is the impact of the gas thermodynamic evolution on type I migration. We have first considered the interaction between a low-mass planet and an adiabatic two-dimensional disc. The linear analysis described in chapter 5 provides a generalized expression for the corotation torque. It features an additional contribution (torque excess) arising from the entropy advection in the coorbital region, and which scales with the (opposite of the) unperturbed entropy gradient. Hydrodynamic calculations performed with a low-mass planet have confirmed the main findings of our linear analysis, in particular the scaling of the fully unsaturated torque excess with the entropy gradient. This is described in chapter 6. Nonetheless, we have illustrated that the torque prediction of the linear analysis cannot fully

¹JUPITER is a multi-dimensional Godunov hydrocode (Masset, in prep.).

reproduce the unsaturated values of the torque excess obtained with the calculations. Presumably refined models of the horseshoe drag expression will provide a better agreement with the calculation results. In particular, the coupling of the gas entropy and vortensity deserves further investigations.

The saturation properties of the corotation torque in adiabatic discs have also been studied. We have shown that both the vortensity and the entropy large-scale gradients need to be restored to prevent saturation. The former require viscosity, the latter thermal cooling. We have demonstrated that the corotation torque can then be maintained to an unsaturated value, depending on the amount of viscosity and on the cooling efficiency. In this favorable case, the total torque in radiative discs may typically be an order of magnitude smaller than the one obtained in a locally isothermal calculation. This significant reduction of type I migration rate allows for predictive scenarios of planet formation and migration. The natural outcomes of these results are directed toward a more realistic treatment of the disc thermal properties, with three-dimensional calculations involving radiative transfer, and of the disc turbulence, with MHD calculations.

Bibliography

- Abramowitz, M. & Stegun, I. A. 1972, *Handbook of Mathematical Functions* (*Handbook of Mathematical Functions*, New York: Dover, 1972) 80
- Alibert, Y., Mordasini, C., Benz, W., & Winisdoerffer, C. 2005, *A&A*, 434, 343 12
- Artymowicz, P. 1993, *ApJ*, 419, 155 20
- Balbus, S. A. & Hawley, J. F. 1991, *ApJ*, 376, 214 17
- Balmforth, N. J. & Korycansky, D. G. 2001, *MNRAS*, 326, 833 134
- Baruteau, C. & Masset, F. 2008a, *ApJ*, 672, 1054 31
- . 2008b, *ApJ*, 678, 483 24
- Beaulieu, J.-P., Bennett, D. P., Fouqué, P., Williams, A., Dominik, M., Jørgensen, U. G., Kubas, D., Cassan, A., Coutures, C., Greenhill, J., Hill, K., Menzies, J., Sackett, P. D., Albrow, M., Brilliant, S., Caldwell, J. A. R., Calitz, J. J., Cook, K. H., Corrales, E., Desort, M., Dieters, S., Dominis, D., Donatowicz, J., Hoffman, M., Kane, S., Marquette, J.-B., Martin, R., Meintjes, P., Pollard, K., Sahu, K., Vinter, C., Wambsganss, J., Woller, K., Horne, K., Steele, I., Bramich, D. M., Burgdorf, M., Snodgrass, C., Bode, M., Udalski, A., Szymański, M. K., Kubiak, M., Więckowski, T., Pietrzyński, G., Soszyński, I., Szewczyk, O., Wyrzykowski, L., Paczyński, B., Abe, F., Bond, I. A., Britton, T. R., Gilmore, A. C., Hearnshaw, J. B., Itow, Y., Kamiya, K., Kilmartin, P. M., Korpela, A. V., Masuda, K., Matsubara, Y., Motomura, M., Muraki, Y., Nakamura, S., Okada, C., Ohnishi, K., Rattenbury, N. J., Sako, T., Sato, S., Sasaki, M., Sekiguchi, T., Sullivan, D. J., Tristram, P. J., Yock, P. C. M., & Yoshioka, T. 2006, *Nature*, 439, 437 8, 9
- Binney, J. & Tremaine, S. 1987, *Galactic dynamics* (Princeton, NJ, Princeton University Press, 1987, 747 p.) 52
- Boley, A. C., Durisen, R. H., Nordlund, Å., & Lord, J. 2007, *ApJ*, 665, 1254 14
- Boss, A. P. 1997, *Science*, 276, 1836 12, 13
- . 2005, *ApJ*, 629, 535 74
- . 2008, *ApJ*, 677, 607 13
- Brauer, F., Dullemond, C. P., & Henning, T. 2008, *A&A*, 480, 859 11
- Bryden, G., Chen, X., Lin, D. N. C., Nelson, R. P., & Papaloizou, J. C. B. 1999, *ApJ*, 514, 344 33
- Charbonneau, D., Brown, T. M., Latham, D. W., & Mayor, M. 2000, *ApJL*, 529, L45 7

- Charbonneau, D., Brown, T. M., Noyes, R. W., & Gilliland, R. L. 2002, *ApJ*, 568, 377–8
- Chauvin, G., Lagrange, A.-M., Dumas, C., Zuckerman, B., Mouillet, D., Song, I., Beuzit, J.-L., & Lowrance, P. 2004, *A&A*, 425, L29–5
- Cieza, L., Padgett, D. L., Stapelfeldt, K. R., Augereau, J.-C., Harvey, P., Evans, II, N. J., Merín, B., Koerner, D., Sargent, A., van Dishoeck, E. F., Allen, L., Blake, G., Brooke, T., Chapman, N., Huard, T., Lai, S.-P., Mundy, L., Myers, P. C., Spiesman, W., & Wahhaj, Z. 2007, *ApJ*, 667, 308–12
- Correia, A. C. M., Udry, S., Mayor, M., Laskar, J., Naef, D., Pepe, F., Queloz, D., & Santos, N. C. 2005, *A&A*, 440, 751–7
- Crida, A., Morbidelli, A., & Masset, F. 2006, *Icarus*, 181, 587–33, 76
- . 2007, *A&A*, 461, 1173–47
- D’Angelo, G., Bate, M. R., & Lubow, S. H. 2005, *MNRAS*, 358, 316–38, 144
- D’Angelo, G., Henning, T., & Kley, W. 2002, *A&A*, 385, 647–12, 47
- . 2003a, *ApJ*, 599, 548–62, 67, 68
- D’Angelo, G., Kley, W., & Henning, T. 2003b, *ApJ*, 586, 540–33, 35
- D’Angelo, G. & Lubow, S. H. 2008, *ArXiv e-prints*, 806–38
- de Val-Borro, M., Edgar, R. G., Artymowicz, P., Ciecielag, P., Cresswell, P., D’Angelo, G., Delgado-Donate, E. J., Dirksen, G., Fromang, S., Gawryszczak, A., Klahr, H., Kley, W., Lyra, W., Masset, F., Mellema, G., Nelson, R. P., Paardekooper, S.-J., Peplinski, A., Pierens, A., Plewa, T., Rice, K., Schäfer, C., & Speith, R. 2006, *MNRAS*, 695–65, 79, 107
- Durisen, R. H., Boss, A. P., Mayer, L., Nelson, A. F., Quinn, T., & Rice, W. K. M. 2007, in *Protostars and Planets V*, ed. B. Reipurth, D. Jewitt, & K. Keil, 607–622–13
- Edgar, R. G. 2007, *ApJ*, 663, 1325
- . 2008, *ArXiv e-prints*, 807
- Fleming, T. & Stone, J. M. 2003, *ApJ*, 585, 908–18
- Foglizzo, T. & Tagger, M. 2000, *A&A*, 363, 174–112
- Fromang, S. & Papaloizou, J. 2006, *A&A*, 452, 751–10
- . 2007, *A&A*, 476, 1113–18
- Gayon, J. & Bois, E. 2008, *A&A*, 482, 665–7
- Goldreich, P. & Sari, R. 2003, *ApJ*, 585, 1024–134
- Goldreich, P. & Tremaine, S. 1979, *ApJ*, 233, 857–19, 20, 22, 25, 29, 85, 100, 104
- . 1980, *ApJ*, 241, 425–21
- Gomes, R., Levison, H. F., Tsiganis, K., & Morbidelli, A. 2005, *Nature*, 435, 466–16
- Goodman, J. & Rafikov, R. R. 2001, *ApJ*, 552, 793–33

- Hillenbrand, L. A. 2008, ArXiv e-prints, 805 12
- Hubickyj, O., Bodenheimer, P., & Lissauer, J. J. 2005, *Icarus*, 179, 415 11
- Huré, J.-M., Hersant, F., Carreau, C., & Busset, J.-P. 2008, *A&A*, submitted 58
- Huré, J.-M. & Pierens, A. 2006, in SF2A-2006: Semaine de l'Astrophysique Française, ed. D. Barret, F. Casoli, G. Lagache, A. Lecavelier, & L. Pagani, 105–+ 76
- Ida, S. & Lin, D. N. C. 2004a, *ApJ*, 604, 388 11
- . 2004b, *ApJ*, 616, 567 13
- . 2008, *ApJ*, 673, 487 13
- Ilgner, M. & Nelson, R. P. 2008, *A&A*, 483, 815 18
- Johansen, A., Henning, T., & Klahr, H. 2006, *ApJ*, 643, 1219 17
- Johansen, A., Oishi, J. S., Low, M.-M. M., Klahr, H., Henning, T., & Youdin, A. 2007, *Nature*, 448, 1022 11
- Johnson, E. T., Goodman, J., & Menou, K. 2006, *ApJ*, 647, 1413 31
- Jorissen, A., Mayor, M., & Udry, S. 2001, *A&A*, 379, 992 6
- Klahr, H. 2004, *ApJ*, 606, 1070 64
- Klahr, H. H. & Bodenheimer, P. 2003, *ApJ*, 582, 869 17
- Kley, W. 1998, *A&A*, 338, L37 49
- Kley, W. & Crida, A. 2008, ArXiv e-prints, 806 139
- Korycansky, D. G. & Pollack, J. B. 1993, *Icarus*, 102, 150 25
- Landau, L. & Lifchitz, E. 1999, *Physique Théorique, mécanique des fluides* (Mir-Ellipses, third edition, 1994) 62
- Laskar, J., Joutel, F., & Robutel, P. 1993, *Nature*, 361, 615 2
- Laughlin, G., Steinacker, A., & Adams, F. C. 2004, *ApJ*, 608, 489 137
- LeVeque, R. J. 1998, *J. Comput. Phys.*, 146, 346 67
- Levison, H. 2006, "A Hand-Waving Derivation of Planethood", <http://www.boulder.swri.edu/~hal/planet/index.html> 4
- Levison, H. F. & Morbidelli, A. 2003, *Nature*, 426, 419 16
- Li, H., Colgate, S. A., Wendroff, B., & Liska, R. 2001, *ApJ*, 551, 874 17
- Li, H., Finn, J. M., Lovelace, R. V. E., & Colgate, S. A. 2000a, *ApJ*, 533, 1023 17
- . 2000b, *ApJ*, 533, 1023 100, 110
- Lin, D. N. C. & Papaloizou, J. 1979, *MNRAS*, 186, 799 33
- Lin, D. N. C. & Papaloizou, J. C. B. 1993, in *Protostars and Planets III*, ed. E. H. Levy & J. I. Lunine, 749–835 33

- Lovelace, R. V. E., Li, H., Colgate, S. A., & Nelson, A. F. 1999a, *ApJ*, 513, 805–17
- . 1999b, *ApJ*, 513, 805–110
- Lovis, C., Mayor, M., Bouchy, F., Pepe, F., Queloz, D., Santos, N. C., Udry, S., Benz, W., Bertaux, J.-L., Mordasini, C., & Sivan, J.-P. 2005, *A&A*, 437, 1121–6
- Lynden-Bell, D. & Pringle, J. E. 1974, *MNRAS*, 168, 603–36, 44
- Lyra, W., Johansen, A., Klahr, H., & Piskunov, N. 2008, *ArXiv e-prints*, 807–14
- Malhotra, R. 1995, *AJ*, 110, 420–16
- Marcy, G. W. & Butler, R. P. 1995, in *Bulletin of the American Astronomical Society*, Vol. 27, *Bulletin of the American Astronomical Society*, 1379–+ 4
- Marcy, G. W., Butler, R. P., Fischer, D., Vogt, S. S., Lissauer, J. J., & Rivera, E. J. 2001, *ApJ*, 556, 296–7
- Masset, F. 2000a, *A&AS*, 141, 165–43, 45, 49
- Masset, F. S. 2000b, in *Astronomical Society of the Pacific Conference Series*, Vol. 219, *Disks, Planetesimals, and Planets*, ed. G. Garzón, C. Eiroa, D. de Winter, & T. J. Mahoney, 75–+ 43, 45
- Masset, F. S. 2001, *ApJ*, 558, 453–28, 134
- . 2002, *A&A*, 387, 605–28, 29, 47, 129, 130
- Masset, F. S. 2008, in *EAS Publications Series*, Vol. 29, *EAS Publications Series*, 165–244–21, 37, 39
- Masset, F. S., D’Angelo, G., & Kley, W. 2006a, *ApJ*, 652, 730–27, 28, 35, 76, 92, 93, 125, 126, 130, 133
- Masset, F. S., Morbidelli, A., Crida, A., & Ferreira, J. 2006b, *ApJ*, 642, 478–31
- Masset, F. S. & Ogilvie, G. I. 2004, *ApJ*, 615, 1000–106, 107
- Masset, F. S. & Papaloizou, J. C. B. 2003, *ApJ*, 588, 494–37, 38
- Matsumura, S., Pudritz, R. E., & Thommes, E. W. 2007, *ApJ*, 660, 1609–30, 31
- Mayor, M., Pepe, F., Queloz, D., Bouchy, F., Rupprecht, G., Lo Curto, G., Avila, G., Benz, W., Bertaux, J.-L., Bonfils, X., dall, T., Dekker, H., Delabre, B., Eckert, W., Fleury, M., Gilliotte, A., Gojak, D., Guzman, J. C., Kohler, D., Lizon, J.-L., Longinotti, A., Lovis, C., Megevand, D., Pasquini, L., Reyes, J., Sivan, J.-P., Sosnowska, D., Soto, R., Udry, S., van Kesteren, A., Weber, L., & Weilenmann, U. 2003, *The Messenger*, 114, 20–7
- Mayor, M. & Queloz, D. 1995, *Nature*, 378, 355–4, 6
- Menou, K. & Goodman, J. 2004, *ApJ*, 606, 520–24
- Meyer-Vernet, N. & Sicardy, B. 1987, *Icarus*, 69, 157–20, 23
- Morohoshi, K. & Tanaka, H. 2003, *MNRAS*, 346, 915–31, 122
- Muto, T., Machida, M. N., & Inutsuka, S.-i. 2008, *ApJ*, 679, 813–24

- Narayan, R., Goldreich, P., & Goodman, J. 1987, *MNRAS*, 228, 1–80
- Nelson, A. F. & Benz, W. 2003a, *ApJ*, 589, 556–74, 86, 94
- . 2003b, *ApJ*, 589, 578–74, 86, 94
- Nelson, R. P. & Papaloizou, J. C. B. 2004, *MNRAS*, 350, 849–31, 32
- Ogilvie, G. I. & Lubow, S. H. 2002, *MNRAS*, 330, 950–21
- . 2003, *ApJ*, 587, 398–28, 109, 112, 134
- . 2006, *MNRAS*, 370, 784–136
- Paardekooper, S.-J. & Mellema, G. 2006, *A&A*, 459, L17–31, 32, 98, 106, 122, 124
- . 2008, *A&A*, 478, 245–127
- Paardekooper, S.-J. & Papaloizou, J. C. B. 2008, *A&A*, 485, 877–101, 123
- Papaloizou, J. C. B. & Terquem, C. 2006, *Reports of Progress in Physics*, 69, 119–39
- Pelat, D. & Huré, J.-M. 2002, *Modélisation numérique d'un disque d'accrétion autour d'un trou noir* 67, 68
- Pepliński, A., Artymowicz, P., & Mellema, G. 2008a, *MNRAS*, 386, 164–38
- . 2008b, *MNRAS*, 386, 179–38
- . 2008c, *MNRAS*, 387, 1063–38
- Pierens, A. & Huré, J.-M. 2005, *A&A*, 433, L37–24, 57, 74, 94
- Pollack, J. B., Hubickyj, O., Bodenheimer, P., Lissauer, J. J., Podolak, M., & Greenzweig, Y. 1996, *Icarus*, 124, 62–11, 12
- Rasio, F. A. & Ford, E. B. 1996, *Science*, 274, 954–16
- Santos, N. C. 2008, *New Astronomy Review*, 52, 154–9
- Sellwood, J. A. 1987, *ARA&A*, 25, 151–52
- Shakura, N. I. & Sunyaev, R. A. 1973, *A&A*, 24, 337–17, 44, 134
- Stone, J. M. & Norman, M. L. 1992, *ApJs*, 80, 753–45, 47, 49, 64
- Takeda, G. & Rasio, F. A. 2005, *ApJ*, 627, 1001–16
- Tanaka, H., Takeuchi, T., & Ward, W. R. 2002, *ApJ*, 565, 1257–12, 22, 23, 25, 28, 29, 32, 33, 35, 77, 78, 94, 104, 105, 108, 110, 123, 126, 129
- Tanigawa, T. & Lin, D. N. C. 2005, in *Protostars and Planets V*, 8466–+ 83
- Terquem, C. E. J. M. L. J. 2003, *MNRAS*, 341, 1157–24
- Toomre, A. 1964, *ApJ*, 139, 1217–87
- Toro, E. F. 1999, *Riemann Solvers and Numerical Methods for Fluid Dynamics* (Springer, second edition, 1999) 67

- Tremaine, S. 1993, in *Astronomical Society of the Pacific Conference Series*, Vol. 36, *Planets Around Pulsars*, ed. J. A. Phillips, S. E. Thorsett, & S. R. Kulkarni, 335–344 3
- Tsiganis, K., Gomes, R., Morbidelli, A., & Levison, H. F. 2005, *Nature*, 435, 459 16
- Udry, S., Mayor, M., Benz, W., Bertaux, J.-L., Bouchy, F., Lovis, C., Mordasini, C., Pepe, F., Queloz, D., & Sivan, J.-P. 2006, *A&A*, 447, 361 9
- van Leer, B. 1977, *Journal of Computational Physics*, 23, 276 49
- Varnière, P. & Tagger, M. 2006, *A&A*, 446, L13 14
- Vidal-Madjar, A., Désert, J.-M., Lecavelier des Etangs, A., Hébrard, G., Ballester, G. E., Ehrenreich, D., Ferlet, R., McConnell, J. C., Mayor, M., & Parkinson, C. D. 2004, *ApJL*, 604, L69 8
- Ward, W. R. 1991, in *Lunar and Planetary Institute Conference Abstracts*, 1463–+ 28, 29, 126
- Ward, W. R. 1997, *Icarus*, 126, 261 16, 20, 21, 22, 29, 30, 80, 91
- Wolszczan, A. & Frail, D. A. 1992, *Nature*, 355, 145 4
- Zhang, H. & Lai, D. 2006, *MNRAS*, 368, 917 104
- Zhang, H., Yuan, C., Lin, D. N. C., & Yen, D. C. C. 2008, *ApJ*, 676, 639 38

THE ASTROPHYSICAL JOURNAL, 672:1054–1067, 2008 January 10
 © 2008. The American Astronomical Society. All rights reserved. Printed in U.S.A.

ON THE COROTATION TORQUE IN A RADIATIVELY INEFFICIENT DISK

C. BARUTEAU¹ AND F. MASSET²

Laboratoire AIM, CEA/DSM-CNRS-Université Paris Diderot, DAPNIA/Service d'Astrophysique, CEA/Saclay,
 91191 Gif/Yvette Cedex, France; clement.baruteau@cea.fr, fmasset@cea.fr

Received 2007 July 19; accepted 2007 September 14

ABSTRACT

We consider the angular momentum exchange at the corotation resonance between a two-dimensional gaseous disk and a uniformly rotating external potential, assuming that the disk flow is adiabatic. We first consider the linear case for an isolated resonance, for which we give an expression of the corotation torque that involves the pressure perturbation and which reduces to the usual dependence on the vortensity gradient in the limit of a cold disk. Although this expression requires the solution of the hydrodynamic equations, it provides some insight into the dynamics of the corotation region. In the general case, we find an additional dependence on the entropy gradient at corotation. This dependence is associated with the advection of entropy perturbations. These are not associated with pressure perturbations. They remain confined to the corotation region, where they yield a singular contribution to the corotation torque. In a second part, we check our torque expression by means of customized two-dimensional hydrodynamical simulations. In a third part, we contemplate the case of a planet embedded in a Keplerian disk, assumed to be adiabatic. We find an excess of corotation torque that scales with the entropy gradient, and we check that the contribution of the entropy perturbation to the torque is in agreement with the expression obtained from the linear analysis. We finally discuss some implications of the corotation torque expression for the migration of low-mass planets in the regions of protoplanetary disks where the flow is radiatively inefficient on the timescale of the horseshoe U-turns.

Subject headings: accretion, accretion disks — hydrodynamics — methods: numerical — planetary systems: formation — planetary systems: protoplanetary disks

1. INTRODUCTION

It has been known since the early 1980s that low-mass planetary objects (that is, up to a few Earth masses) embedded in protoplanetary gaseous disks should undergo a fast decay toward their central object, on timescales much shorter than the lifetime of the disk. This process, known as type I migration, has constituted for a long time a critical stage for the theory of giant planet formation. While it may account for the discovery of close-in extrasolar planets, with orbital periods of a few days, it renders problematic the buildup of giant planet cores at distances from their central stars of several astronomical units. Most published studies of the tidal interaction of low-mass objects with their parent disk have used either a barotropic assumption (such as a polytropic equation of state) or a locally isothermal equation of state. All these studies, whether analytical or numerical, confirmed the vigorous tidal interaction of the planet with the disk, leading to its inward migration on short timescales.

There have been some exceptions to such assumptions. Morohoshi & Tanaka (2003) considered the case of a planet interacting with an optically thin disk, in the shearing sheet approximation, and found that radiative effects can significantly alter the one-sided torque between the planet and the disk. More recently, Paardekooper & Mellema (2006, hereafter PM06) have performed global, high-resolution three-dimensional calculations with nested grids that include radiative transfer. For the setup that they considered, they found that the total torque exerted by the disk on the planet increases with the disk opacity. For sufficiently large values of the opacity (and in the limit case of an adiabatic

flow, corresponding to an infinite opacity), they find that the total torque on the planet is positive. This result is of great importance, as it potentially solves the lingering problem of type I migration. PM06 identified the existence of a hot, underdense part of the co-orbital region lagging the planet, which accounted for the torque excess that they measured. The present work corresponds to an attempt to further investigate this topic, so as to identify the physical mechanism responsible for these effects. For this purpose, we consider a more restricted situation, namely, two-dimensional adiabatic flows.

This paper is organized as follows. In § 2 we set up the problem and define the notation. We then present an analysis of the corotation torque in an adiabatic disk in the linear regime, at an isolated resonance, in § 3. Our original motivation for the study of the linear regime was that PM06 found that the total torque reverses in a radiatively inefficient disk for both a $5 M_{\oplus}$ and a $0.5 M_{\oplus}$ planet, which pointed out that the effect is likely a linear one. In § 4 we check by means of customized two-dimensional hydrodynamical simulations involving an isolated resonance the torque expression found in § 3. In § 5 we turn to the case of a planet embedded in an adiabatic disk, for which we check that there is an excess of corotation torque that scales with the entropy gradient. We also check in this section that the torque excess corresponds to the sum of the linear contributions of all co-orbital corotation resonances, for a sufficiently small planet mass. We discuss the implications of the modified corotation torque expression for the issue of planet-disk tidal interactions, and we suggest further research on this topic in § 6. We sum up our results in § 7.

2. SETUP AND NOTATION

We consider an inviscid, radiatively inefficient (that is to say, for our purposes, adiabatic) two-dimensional disk. In order to

¹ Send offprint requests to clement.baruteau@cea.fr.

² Also at: IA-UNAM, Ciudad Universitaria, Apartado Postal 70-264, Mexico D.F. 04510, Mexico.

avoid corotation torque issues, we consider either a potential slowly turned on (§§ 3 and 4) or early stages after the introduction of a planet (§ 5). The unperturbed state of the disk corresponds to a rotational equilibrium between the gravitational force of the central object, the pressure gradient, and the centrifugal force. The unperturbed state is axisymmetric. The disk rotates with the angular speed $\Omega(r)$, where r is the distance to the central object. We denote by p the pressure, Σ denotes the surface density, u and v , respectively, are the radial and azimuthal velocities, and φ is the azimuthal angle. We denote by a “0” subscript the unperturbed quantities and with a “1” subscript the perturbed ones. For instance, $p(r, \varphi) = p_0(r) + p_1(r, \varphi)$. We essentially consider disks in which the unperturbed pressure and density are power laws of the radius, respectively, with index λ and σ ,

$$p_0(r) \propto r^{-\lambda}, \quad (1)$$

$$\Sigma_0(r) \propto r^{-\sigma}. \quad (2)$$

We make use of the two Oort’s constants,

$$A = \frac{1}{2} r \frac{d\Omega}{dr}, \quad (3)$$

which scales with the local shear in the flow, and

$$B = \frac{1}{2r} \frac{d(r^2\Omega)}{dr} = \Omega + A, \quad (4)$$

which is half the vertical component of the flow vorticity and which is also $(2r)^{-1}$ times the radial derivative of the specific angular momentum. We also use the epicyclic frequency $\kappa = (4\Omega B)^{1/2}$.

3. LINEAR ANALYSIS AT AN ISOLATED RESONANCE

3.1. Basic Equations

We study the linear response of the disk to a perturbing non-axisymmetric potential $\Phi(r, \varphi) = \Phi_m(r) \cos[m(\varphi - \Omega_p t)]$. The perturbing potential rotates at constant angular velocity Ω_p . In the inertial frame, the linearized Euler equations of the disk are

$$\frac{\partial u_1}{\partial t} + \Omega \frac{\partial u_1}{\partial \varphi} - 2\Omega v_1 = -\frac{\partial \Phi}{\partial r} - \frac{1}{\Sigma_0} \frac{\partial p_1}{\partial r} + \frac{\Sigma_1}{\Sigma_0^2} \frac{\partial p_0}{\partial r}, \quad (5)$$

$$\frac{\partial v_1}{\partial t} + \Omega \frac{\partial v_1}{\partial \varphi} + \frac{\kappa^2}{2\Omega} u_1 = -\frac{1}{r} \frac{\partial}{\partial \varphi} \left(\Phi + \frac{p_1}{\Sigma_0} \right). \quad (6)$$

The linearized continuity equation is

$$\frac{\partial \Sigma_1}{\partial t} + \Omega \frac{\partial \Sigma_1}{\partial \varphi} + \frac{1}{r} \frac{\partial}{\partial r} (r \Sigma_0 u_1) + \frac{1}{r} \frac{\partial}{\partial \varphi} (\Sigma_0 v_1) = 0. \quad (7)$$

We refer to the quantity $S = p \Sigma^{-\gamma}$ as the gas entropy, where γ is the adiabatic index. The energy equation is equivalent in our case to the conservation of the gas entropy. The linearized conservation of the entropy along a fluid element path reads

$$\frac{\partial S_1}{\partial t} + \Omega \frac{\partial S_1}{\partial \varphi} + u_1 \frac{\partial S_0}{\partial r} = 0, \quad (8)$$

where $S_1 = S_0(p_1/p_0 - \gamma \Sigma_1/\Sigma_0)$. We furthermore assume that the gas is described by an ideal equation of state so that p_0 and Σ_0 are connected by $p_0 = \Sigma_0 c_s^2 / \gamma$, c_s being the adiabatic sound speed.

We assume a perturbation of the form $x_{1,m}(r) \exp[im(\varphi - \Omega_p t)]$, where x_1 stands for any perturbed quantity of the flow.³ We note $\Delta\omega = m(\Omega_p - \Omega)$, and we use the prime notation to denote $\partial/\partial r$. Equation (8) can be recast as

$$\Sigma_1 = \frac{p_1}{c_s^2} + \frac{iS\Sigma_0 u_1}{r\Delta\omega}. \quad (9)$$

Combining equations (5), (6), and (9) we are led to

$$\Sigma_0 u_1 = i\mathcal{F} \left\{ \frac{\Delta\omega}{\Omega} \left[(\Phi + \Psi)' - \frac{S}{r} \Psi \right] - \frac{2m}{r} (\Phi + \Psi) \right\}, \quad (10)$$

$$\Sigma_0 v_1 = \mathcal{F} \left\{ \frac{\kappa^2}{2\Omega^2} \left[(\Phi + \Psi)' - \frac{S}{r} \Psi \right] - \frac{m}{r} \left(\frac{\Delta\omega}{\Omega} + \mathcal{S} \mathcal{P} \frac{c_s^2/r^2}{\Delta\omega\Omega} \right) (\Phi + \Psi) \right\}, \quad (11)$$

where \mathcal{S} and \mathcal{P} are given by

$$\mathcal{S} = \frac{1}{\gamma} \frac{d \ln S_0}{d \ln r} \quad (12)$$

$$\mathcal{P} = \frac{1}{\gamma} \frac{d \ln p_0}{d \ln r}, \quad (13)$$

Ψ is defined as

$$\Psi = p_1/\Sigma_0, \quad (14)$$

and \mathcal{F} is defined by

$$\mathcal{F} = \Sigma_0 \Omega / D, \quad (15)$$

with $D = \kappa^2 - \Delta\omega^2 - \mathcal{S} \mathcal{P} c_s^2 / r^2$.

Substituting equations (9), (10), and (11) into equation (7) leads to

$$r^2(\Phi + \Psi)'' + r(\mathcal{B} + \mathcal{S})(\Phi + \Psi)' - r\mathcal{S}\Psi' + \mathcal{C}\Psi + \mathcal{D}\Phi = 0, \quad (16)$$

where

$$\mathcal{B} = 1 + \mathcal{V} - \frac{d \ln \Omega}{d \ln r}, \quad (17)$$

$$\mathcal{C} = -\frac{D}{c_s^2/r^2} - 2m \frac{\Omega}{\Delta\omega} (\mathcal{V} + 2\mathcal{S}) - \mathcal{B}\mathcal{S} + \mathcal{S}^2 \left[\left(\frac{r}{S} \right)' - 1 \right] - m^2 \left(1 + \mathcal{S} \mathcal{P} \frac{c_s^2/r^2}{\Delta\omega^2} \right), \quad (18)$$

$$\mathcal{D} = -2m \frac{\Omega}{\Delta\omega} (\mathcal{V} + \mathcal{S}) - m^2 \left(1 + \mathcal{S} \mathcal{P} \frac{c_s^2/r^2}{\Delta\omega^2} \right), \quad (19)$$

$$\mathcal{V} = \frac{d \ln \mathcal{F}}{d \ln r}. \quad (20)$$

Equation (16) reduces to equation (15) of Li et al. (2000) if one considers the propagation of free waves ($\Phi = 0$), while it

³ We drop the subscript m in $x_{1,m}(r)$ to improve legibility.

reduces to equation (13) of Goldreich & Tremaine (1979) in the case of a homentropic ($S = 0$) flow.

3.2. Corotation Torque

We now estimate the rate of angular momentum exchanged between the perturber and the radiatively inefficient disk described in § 3.1. This rate therefore corresponds to the disk torque, which we denote by Γ and which we define as the torque exerted by the disk on the perturber (unless otherwise stated). It reads

$$\Gamma = \int_{\text{disk}} \Sigma_1(r, \varphi) \frac{\partial \Phi}{\partial \varphi} r dr d\varphi. \quad (21)$$

We limit ourselves to the torque exerted by the disk material lying in the vicinity of corotation, hence to the corotation torque, which we denote by Γ_c . In a linear analysis, this torque can be expressed as a series of contributions at each azimuthal wave-number, $\Gamma_c = \sum_m \Gamma_{c,m}$. Each individual torque can be expressed, assuming that Φ is real, as

$$\Gamma_{c,m} = m\pi r_c^2 \Phi(r_c) \int_{-\infty}^{\infty} dx \text{Im}[\Sigma_1(x)], \quad (22)$$

where Im denotes the imaginary part, r_c is the corotation radius, and $x = (r - r_c)/r_c$. We substitute $\Sigma_0 u_1$ in equation (9) by the expression given by equation (10), and we keep only the terms which are large in the vicinity of corotation. As in Goldreich & Tremaine (1979) we assume that the disk responds to a slowly increasing perturbation and take $\Delta\omega$ to have a small, positive imaginary part α ,

$$\Delta\omega = m(\Omega_p - \Omega) + i\alpha \approx -mr_c\Omega'(r_c)(x + i\epsilon), \quad (23)$$

where $\epsilon = -\alpha/[mr_c\Omega'(r_c)] > 0$. In the vicinity of corotation, we can finally write

$$\Sigma_1(x) = \Psi(x) \left(\frac{\Sigma_0}{c_s^2} \right)_{r_c} - \frac{(\Phi + \Psi)(x)}{x + i\epsilon} \left(\frac{2\mathcal{F}\mathcal{S}}{r^3\Omega'} \right)_{r_c}. \quad (24)$$

We are primarily interested in the imaginary part of Σ_1 . In the limit $\epsilon \rightarrow 0$, we can write the terms that yield a nonvanishing contribution to the torque as

$$\begin{aligned} \text{Im}[\Sigma_1(x)] &= \text{Im}[\Psi(x)] \left(\frac{\Sigma_0}{c_s^2} \right)_{r_c} + \pi\delta(x) \\ &\times \left\{ \frac{2\mathcal{F}\mathcal{S}[\Phi + \text{Re}(\Psi)]}{r^3\Omega'} \right\}_{r_c} - \frac{\text{Im}[\Psi(x)]}{x} \left(\frac{2\mathcal{F}\mathcal{S}}{r^3\Omega'} \right)_{r_c}, \end{aligned} \quad (25)$$

where $\delta(x)$ is the Dirac delta function. The first two terms of the right-hand side of equation (25) yield, respectively, the following contributions to the corotation torque:

$$\Gamma_{c,m,1} = \left(\frac{m\pi\Sigma_0 r^2 \Phi}{c_s^2} \right)_{r_c} \int_{-\infty}^{\infty} dx \text{Im}[\Psi(x)] \quad (26)$$

$$\Gamma_{c,m,2} = \left\{ \frac{2m\pi^2 \mathcal{F}\mathcal{S}\Phi[\Phi + \text{Re}(\Psi)]}{r\Omega'} \right\}_{r_c}. \quad (27)$$

The third term of equation (25) yields a contribution that can be shown to be negligible, in the planetary context, compared to $\Gamma_{c,m,2}$. This is shown in the Appendix.

The first term, $\Gamma_{c,m,1}$, is the contribution of the function Ψ , such as in the barotropic case. The second term, $\Gamma_{c,m,2}$, corre-

sponds to a singularity at corotation, associated with a nonvanishing entropy gradient. It corresponds to the torque arising from the advection of entropy in the corotation region, which results in a surface density perturbation if the entropy is not uniform. The perturbation is singular for the surface density and the entropy, but not for the pressure (see § 3.2.2). It remains confined to corotation, where it yields a singular contribution to the torque. Some further insight into the dynamics of this perturbation are given in § 4.3. We provide in § 3.2.1 an expression for the corotation torque in the limit of a cold disk, then we turn to the general case.

3.2.1. Limit of a Cold Disk

We contemplate here the case for which $|\Psi| \ll |\Phi|$, which we refer to as a cold case. This condition depends on the strength of the perturbing potential, its radial scale, and on the disk temperature. In particular, in the planetary context some corotation resonances may correspond to a cold situation, while others have $|\Psi| \sim |\Phi|$. Nevertheless, a given resonance eventually satisfies the cold case condition as the disk temperature tends to zero.

The evaluation of equation (26) requires an explicit expression for Ψ , obtained by solving the differential equation (16) in the vicinity of corotation. This has been done by Goldreich & Tremaine (1979) for a cold barotropic disk. An explicit solution can also be obtained for a cold adiabatic disk within the same level of approximation. Note, however, that some additional difficulties arise, in particular the existence of a double pole (term proportional to $\Delta\omega^{-2}$) in the coefficients \mathcal{C} and \mathcal{D} , defined, respectively, by equations (18) and (19).

We discard the double pole for the following reasons:

1. Unlike the simple pole, it scales with c_s^2 , which indicates that when the disk aspect ratio tends to zero, it becomes negligible; differently stated, there should be a critical disk thickness under which it is safe to neglect this term.
2. This term is the only one that depends both on the entropy and on the pressure gradients. As we see in § 5.2.2, our results of numerical simulations for a planet embedded in a disk with aspect ratio $h = 0.05$ show that the torque excess with respect to an isothermal situation essentially depends on \mathcal{S} , the gradient of entropy, which indicates that already for $h = 0.05$ the double pole term is negligible.
3. The double pole is regularized with a very small amount of dissipation. Even the molecular viscosity suffices to render it negligible in the disks that we consider (S.-J. Paardekooper 2007, private communication).

Discarding the double pole and within the same level of approximation as Goldreich & Tremaine (1979), equation (16) can be recast, in the vicinity of the corotation, as

$$\frac{d^2\Psi}{dx^2} - q^2\Psi = -\frac{P_1\Phi(r_c)}{x + i\epsilon}, \quad (28)$$

where

$$P_1 = \left[\frac{2\Omega}{r\Omega'} (\mathcal{V} + \mathcal{S}) \right]_{r_c}, \quad q = \left(\frac{Dr}{c_s} \right)_{r_c} \approx \left(\frac{\kappa r}{c_s} \right)_{r_c}.$$

The general solution of equation (28) reads

$$\begin{aligned} \Psi(x) &= \frac{P_1}{2q} \Phi(r_c) \left(e^{qx} \int_x^\infty \frac{dt}{t + i\epsilon} e^{-qt} \right. \\ &\quad \left. + e^{-qx} \int_{-\infty}^x \frac{dt}{t + i\epsilon} e^{qt} \right), \end{aligned} \quad (29)$$

which reduces to the equation (53) of Goldreich & Tremaine (1979) when $\mathcal{S} = 0$. Combining equations (26) and (29) yields the contribution $\Gamma_{c,m,1}$ to the corotation torque,

$$\Gamma_{c,m,1} = \Gamma_0 [(\mathcal{V} + \mathcal{S})\Phi^2]_{r_c}, \quad (30)$$

where $\Gamma_0 = -(m\pi^2\Sigma_0)/(2Br\Omega')$ is to be evaluated at the corotation radius. It can be approximated as $(4m\pi^2\Sigma_0/3\Omega^2)_{r_c}$ in a Keplerian disk.

The second contribution to the corotation torque, given by equation (27), is specific to the adiabatic case and involves the singularity arising from the entropy advection. Using equation (27) and noting that $|\text{Re}(\Psi)| \ll |\Phi|$, this contribution to the corotation torque reads

$$\Gamma_{c,m,2} = -\Gamma_0 (\mathcal{S}\Phi^2)_{r_c}. \quad (31)$$

From equations (30) and (31), we infer the corotation torque for a cold, adiabatic disk, which reads

$$\Gamma_{c,m} = \Gamma_0 (\mathcal{V}\Phi^2)_{r_c}. \quad (32)$$

This expression does not depend on \mathcal{S} . We note from equations (15) and (20) that \mathcal{V} can be approximated as

$$\mathcal{V} = \frac{d \ln \Sigma_0 / B}{d \ln r}, \quad (33)$$

since the disk aspect ratio at corotation $h(r_c) = c_s(r_c)/[r_c\Omega(r_c)]$ satisfies $h(r_c) \ll 1$. Equation (32) therefore corresponds to the corotation torque expression⁴ of Goldreich & Tremaine (1979). This argues that the corotation torque for a cold case does not depend on whether the disk can radiate energy efficiently (assuming a locally isothermal equation of state) or not (assuming an adiabatic energy equation). This can be expected on general grounds. In the cold disk limit, the internal energy of the fluid is negligible with respect to its mechanical energy; hence, the power and the torque of the tidal force correspond to the case of noninteracting test particles, for which the expression of Goldreich & Tremaine (1979) prevails.

3.2.2. General Case

We consider in this section the general case where we cannot neglect Ψ with respect to Φ in equations (26) and (27), as we have done in § 3.2.1. Instead of resorting to a solution of equation (16), we use a method similar to the method used by Tanaka et al. (2002) based on the jump of angular momentum flux at corotation. In the case of Tanaka et al. (2002), this eventually yields a torque expression similar to the expression of Goldreich & Tremaine (1979) except that Φ has to be substituted by $\Phi + \eta$ (where η is the enthalpy perturbation). The drawback of this method is that it provides a torque expression that depends on the (unknown) solution of the differential equation. Nevertheless, it gives some insight into the dynamics of the corotation region and allows us to draw the general trends of the corotation torque in an adiabatic disk. In our case, the torque expression features $\Psi = p_1/\Sigma_0$. We note that in the isothermal case, Zhang & Lai (2006) have provided an explicit solution for the perturbed enthalpy at corotation, which leads to a corotation torque expression that only depends on the forcing potential.

⁴ They have a negative sign because they consider the torque exerted by the perturber on the disk.

We note that the jump of angular momentum flux at corotation misses the singular contribution of the entropy perturbation at corotation and as such leads only to an evaluation of $\Gamma_{c,m,1}$. The contribution $\Gamma_{c,m,2}$ of the entropy perturbation to the corotation torque needs to be calculated similarly to that in equation (31). The angular momentum flux F_A is given by

$$F_A = \Sigma_0 r^2 \int_0^{2\pi} \text{Re}(u)\text{Re}(v)d\varphi = \pi\Sigma_0 r^2 \text{Re}(uv^*), \quad (34)$$

where Re stands for the real part and the asterisk superscript denotes the complex conjugate. Equation (34) can be written as $F_A = \sum_m F_{A,m}$ with

$$F_{A,m} = \pi\Sigma_0 r^2 [\text{Re}(u_1)\text{Re}(v_1) + \text{Im}(u_1)\text{Im}(v_1)]. \quad (35)$$

Combining equations (10), (11), and (35), we obtain

$$F_{A,m} = \frac{m\pi\Sigma_0 r}{D} \left\{ \text{Im}(\Phi + \Psi) \frac{d\text{Re}(\Phi + \Psi)}{dr} - \text{Re}(\Phi + \Psi) \times \frac{d\text{Im}(\Phi + \Psi)}{dr} + \frac{\mathcal{S}}{r} [\text{Re}(\Phi)\text{Im}(\Psi) - \text{Im}(\Phi)\text{Re}(\Psi)] \right\}. \quad (36)$$

In the homentropic ($\mathcal{S} = 0$) case, equation (36) reduces to the expression used by Tanaka et al. (2002). The contribution $\Gamma_{c,m,1}$ to the corotation torque is then given by

$$\Gamma_{c,m,1} = \lim_{r_c^+ \rightarrow r_c^-} [F_{A,m}(r_c^+) - F_{A,m}(r_c^-)], \quad (37)$$

where $r_c^+ > r_c$ and $r_c^- < r_c$ are the radii of locations, respectively, beyond and before corotation, and where we evaluate the flux of advected angular momentum.

Tanaka et al. (2002) showed that $\Phi + \eta$ is continuous at corotation. Here, since equation (16) cannot be recast as an ordinary differential equation involving only $\Phi + \Psi$, we have to consider more stringent albeit reasonable assumptions, namely, that both Φ and Ψ are continuous at corotation. The fact that Φ is continuous at corotation can be realized with an arbitrarily small softening length of the potential, in the case of an embedded pointlike mass (for which the potential components would diverge logarithmically at corotation, in the absence of any softening). Assuming that Φ is continuous at corotation, equation (16) imposes that Ψ is also continuous at corotation [we would otherwise have a null linear combination of $\delta(x)$ and $\delta'(x)$ functions with nonvanishing coefficients, which is impossible].

Our continuity assumption implies that the terms proportional to \mathcal{S} on the right-hand side of equation (36) do not contribute to the torque. The jump in the advected flux therefore comes from the jump in $d(\Phi + \Psi)/dr$.

We integrate equation (16) over an infinitesimal interval containing $r = r_c$. All finite terms in this equation yield a vanishing contribution; hence, we are left only with the jump of $d(\Phi + \Psi)/dr$ stemming from the second derivative term of equation (16) and the poles of the terms $\mathcal{C}\Psi$ and $\mathcal{D}\Phi$. This reads

$$\begin{aligned} & \frac{d(\Phi + \Psi)}{dr}(r_c^+) - \frac{d(\Phi + \Psi)}{dr}(r_c^-) \\ &= \frac{i\pi}{r_c} [P_2(\Phi + \Psi)(r_c) - Q\Phi(r_c)], \end{aligned} \quad (38)$$

where

$$P_2 = \left[\frac{2\Omega}{r\Omega'} (\mathcal{V} + 2\mathcal{S}) \right]_{r_c}, \quad Q = \left(\frac{2\Omega}{r\Omega'} \mathcal{S} \right)_{r_c}.$$

1058

BARUTEAU & MASSET

Vol. 672

Using equations (36), (37), and (38) and $2B = \kappa^2/2\Omega$, we find that

$$\Gamma_{c,m,1} = \Gamma_0 \left[(\mathcal{V} + 2S)|\Phi + \Psi|^2 - S\Phi \text{Re}(\Phi + \Psi) \right]_{r_c}. \quad (39)$$

Equation (39) reduces to equation (30) in the cold disk limit.

We now come to the contribution $\Gamma_{c,m,2}$ of the entropy perturbation to the corotation torque. Equation (27) yields

$$\Gamma_{c,m,2} = -\Gamma_0 [S\Phi \text{Re}(\Phi + \Psi)]_{r_c}. \quad (40)$$

Equation (40) reduces to equation (31) in the cold disk limit.

The general expression for the corotation torque is obtained by accounting for the contribution given by equation (39) and that of the entropy perturbation given by equation (40),

$$\Gamma_{c,m} = \Gamma_0 \left[(\mathcal{V} + 2S)|\Phi + \Psi|^2 - 2S\Phi \text{Re}(\Phi + \Psi) \right]_{r_c}. \quad (41)$$

Equation (41) reduces to the expression of Tanaka et al. (2002) when $S = 0$, while it reduces to that of Goldreich & Tremaine (1979) for a cold disk.

A case of interest is that of a disk perturbed by a peaked potential (that of an embedded protoplanet for instance), for which $|\Phi + \text{Re}(\Psi)| \ll |\Phi|$ and $|\Phi + \text{Re}(\Psi)| \ll |\text{Re}(\Psi)|$ at corotation. For such a case, $|\Phi \text{Re}(\Phi + \Psi)|_{r_c} \gg |\Phi + \Psi|_{r_c}^2$; hence, the corotation torque may be approximated as $\Gamma_{c,m} \approx -2\Gamma_0 [S\Phi \text{Re}(\Phi + \Psi)]_{r_c}$. The corotation torque may therefore be much larger in the nonhomentropic case ($S \neq 0$) than in the homentropic case ($S = 0$). Furthermore, its sign is given by that of S rather than that of \mathcal{V} . This enhancement of the corotation torque in an adiabatic flow may have a dramatic impact on the type I migration of an embedded protoplanet, as was noted by PM06.

4. NUMERICAL STUDY OF AN ISOLATED COROTATION RESONANCE

We check in this section the analytical predictions of § 3 by means of numerical simulations involving an isolated corotation resonance (CR).

4.1. Numerical Issues

Our setup offers a number of similarities with the setup of Masset & Ogilvie (2004) for the case of an isothermal disk. The hydrodynamics equations for the disk described in § 3.1 are solved using the code FARGO. A description of the properties of this code is deferred to § 5.1, in which the code is used to simulate an embedded planet. As in Masset & Ogilvie (2004) we deal with the $m = 3$ CR. The disk is therefore torqued by an $m = 3$ external potential Φ that reads

$$\Phi(r, \varphi, t) = T(t/\tau)\phi(r) \cos[3(\varphi - \Omega_p t)], \quad (42)$$

where $\phi(r)$ denotes the radial profile of the potential, Ω_p is its pattern speed (note that we work in the corotating frame), t is the time, and

$$T(x) = \begin{cases} \sin^2(\pi x/2), & x < 1, \\ 1, & \text{otherwise,} \end{cases}$$

is a temporal tapering that turns on the potential on the time-scale τ .

The total torque Γ_c exerted by the disk on the perturber, given by equation (21), is evaluated by

$$\Gamma_c = \sum_{i=0}^{N_r-1} \sum_{j=0}^{N_s-1} \frac{\Phi_{i,j+1} - \Phi_{i,j-1}}{2\Delta\varphi} \Sigma_{i,j} S_{i,j}, \quad (43)$$

where N_r (N_s) is the radial (azimuthal) number of zones of the mesh, $S_{i,j}$ is the surface area of zone (i,j) , $\Phi_{i,j}$ and $\Sigma_{i,j}$ are the external potential and surface density at the center of this zone, and $\Delta\varphi = 2\pi/N_s$ is the azimuthal resolution. Furthermore, the contribution $\Gamma_{c,1}$ of the function Ψ to the torque is obtained by substituting Σ_1 by p_1/c_s^2 in equation (21). It is therefore evaluated by

$$\Gamma_{c,1} = \sum_{i=0}^{N_r-1} \sum_{j=0}^{N_s-1} \frac{\Phi_{i,j+1} - \Phi_{i,j-1}}{2\Delta\varphi} \frac{p_{i,j}}{c_{si,j}^2} S_{i,j}, \quad (44)$$

where $p_{i,j}$ and $c_{si,j}$ are the pressure and sound speed at the center of zone (i,j) . The contribution $\Gamma_{c,2}$ of the entropy perturbation to the torque is eventually estimated as

$$\Gamma_{c,2} = \Gamma_c - \Gamma_{c,1}. \quad (45)$$

The radial computational domain is narrow enough to avoid the location of the $m = 3$ inner and outer Lindblad resonances (see Masset & Ogilvie 2004). Despite this precaution, wave killing zones next to the boundaries were implemented to minimize unphysical wave reflections (de Val-Borro et al. 2006). Furthermore, the torque evaluation is performed by summing only on a domain of the grid that does not contain the wave killing zones, and the summation includes a spatial tapering on the edges of that domain.

The disk surface density and temperature are initially axisymmetric with power-law profiles,

$$\Sigma(r) = \Sigma_c (r/r_c)^{-\sigma} \quad (46)$$

$$T(r) = T_c (r/r_c)^{-1+2f}, \quad (47)$$

where Σ_c and T_c are the surface density and temperature at the corotation radius r_c , respectively, and f is the flaring index of the disk. The disk aspect ratio is given by $h(r) = H(r)/r = h(r_c)(r/r_c)^f$, where $H(r)$ is the disk scale height at radius r . A vanishing value of the flaring index f therefore corresponds to a uniform disk aspect ratio. The functions \mathcal{V} and S are constant and read

$$\mathcal{V} = 3/2 - \sigma, \quad (48)$$

$$S = \sigma - (\sigma + 1 - 2f)/\gamma. \quad (49)$$

The main numerical parameters are those taken by Masset & Ogilvie (2004), namely, a $h(r_c) = 0.01$ disk aspect ratio at corotation and $\Sigma_c = 1$. Our disk is inviscid. The libration islands are resolved by 30 zones azimuthally. As the potential increases, the radial width of the islands also increases. Their maximal radial width W spans approximately 20 zones.

The results presented in § 4.2 have the following units: the mass of the central object M_* is the mass unit, the corotation radius r_c of our $m = 3$ CR is the distance unit, and the Keplerian orbital period T_{orb} at $r = r_c$ is 2π times the time unit.

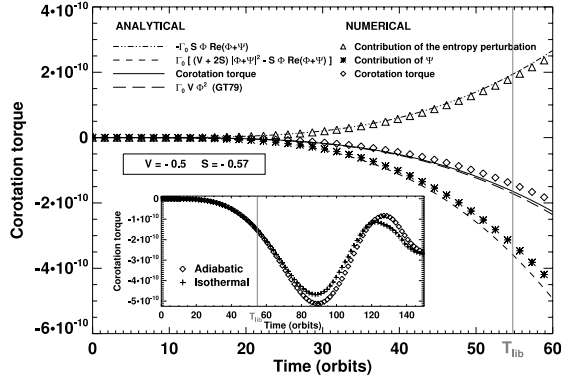


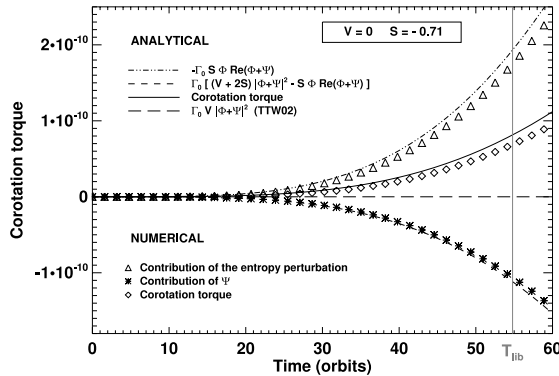
FIG. 1.—Corotation torque exerted by the disk on the perturber, as a function of time, assuming a flat radial profile of the potential. The results shown are obtained with an adiabatic calculation, except in the close-up, where we compare the isothermal and adiabatic corotation torques over the whole duration of the calculations. Numerical results are displayed with a symbol, while the theoretical expectations are displayed with curves. We plot as a function of time the adiabatic corotation torque (diamonds and solid curve), the contribution of the function Ψ to the torque (stars and dashed curve), and the contribution of the entropy perturbation (triangles and dot-dot-dashed curve). The long-dashed curve, which is nearly superimposed on the solid curve, displays the corotation torque expression of Goldreich & Tremaine (1979). The vertical solid line gives an estimate of the final libration time (see text).

4.2. Results

We consider three cases, corresponding, respectively, to Figures 1, 2a, and 2b:

1. An external potential with a flat profile $\phi(r) = -10^{-5}$, as in Masset & Ogilvie (2004). This case, which we call the “flat potential case,” has the following parameters: $\sigma = 2$ and $f = -0.3$, which implies, from equations (48) and (49), that $\mathcal{V} = -0.5$ and $\mathcal{S} \approx -0.57$.

2. A potential profile that corresponds to the $m = 3$ Fourier component of the smoothed potential of a $M = 3.1 \times 10^{-6} M_*$ pointlike object. The softening length is $\varepsilon = H(r_c)$, which is approximately equal to W . The object rotates at speed Ω_p , with orbital radius r_c . This neglects the pressure gradient effects, as we do not resolve the distance from orbit to corotation, but this distance is much smaller than the potential softening length, so this is not a concern in the present case. By contrast to the previous case, we call this situation the “peaked potential case.”



The value of M was chosen so that $\phi(r_c) = -10^{-5}$, as in the flat potential case. For this calculation we have $\sigma = 1.5$ and $f = -0.3$, so that $\mathcal{V} = 0$ and $\mathcal{S} \approx -0.71$. The results are depicted in Figure 2a.

3. A calculation similar to the previous one, except that $\sigma = 0.5$ and $f = -0.1$, so that $\mathcal{V} = 1$ and $\mathcal{S} \approx -0.71$. The results are depicted in Figure 2b.

For the three pairs $(\mathcal{V}, \mathcal{S})$ quoted above, the tapering timescale value is $\tau = 150 T_{\text{orb}}$, which corresponds to the duration of the calculations. This is about 3 times larger than the final libration time, estimated as

$$T_{\text{lib}} \sim \frac{1}{m} \left[\frac{3|\phi(r_c)|}{32} \right]^{-1/2} \approx 55 T_{\text{orb}}. \quad (50)$$

In each case we evaluate:

1. The total corotation torque (diamonds) with equation (43), to be compared to the analytical expression (solid curve) given by equation (41). In our units, $\Gamma_0 \approx 39.5$.
2. The contribution of the function Ψ to the corotation torque (stars) obtained with equation (44), the expected expression of which (dashed curve) is calculated using equation (39).
3. The contribution of the entropy perturbation to the torque (triangles) using equation (45), which is to compare to the prediction of equation (40), represented by the dot-dot-dashed curve.

In these figures, the corotation torque first increases with time, since the potential is progressively turned on until it reaches its final value at the end of the calculation. After some time it starts to oscillate. This oscillation corresponds to the saturation of the CR, as the ratio t/T_{lib} tends to unity (Ogilvie & Lubow 2003). Figures 1, 2a, and 2b therefore argue that our numerical simulations succeed in reproducing the results of our analytical study as long as $t \lesssim T_{\text{lib}}$, which is when a linear analysis is grounded (which requires that the time of the calculation be much smaller than the libration time).

The examination of the results of these calculations leads to the following comments:

1. In the flat potential case, depicted in Figure 1, we have $\text{Re}[\psi(r_c)] \approx -0.02\phi(r_c)$ throughout the calculation, where $\psi(r)$ denotes the radial profile of Ψ . This situation therefore corresponds to a cold case. As expected from equation (32), the analytical corotation torque and the expression of Goldreich & Tremaine (1979) almost coincide. The close-up shows the torque evolution over

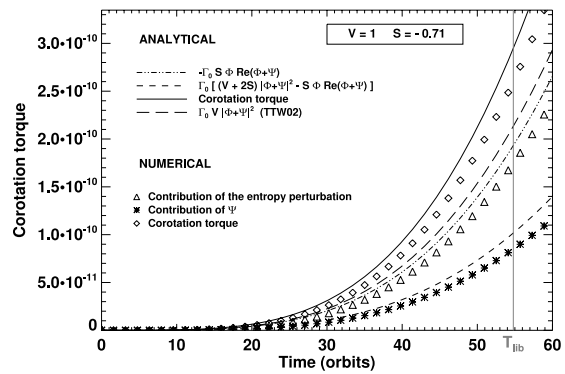


FIG. 2.—Same as Fig. 1, except that the results are obtained with a peaked potential, with $\mathcal{V} = 0$ ($\mathcal{V} = 1$) in the left (right) panel. The long-dashed curve in both panels shows the expectation from the corotation torque expression of Tanaka et al. (2002) denoted by TTW02.

1060

BARUTEAU & MASSET

Vol. 672

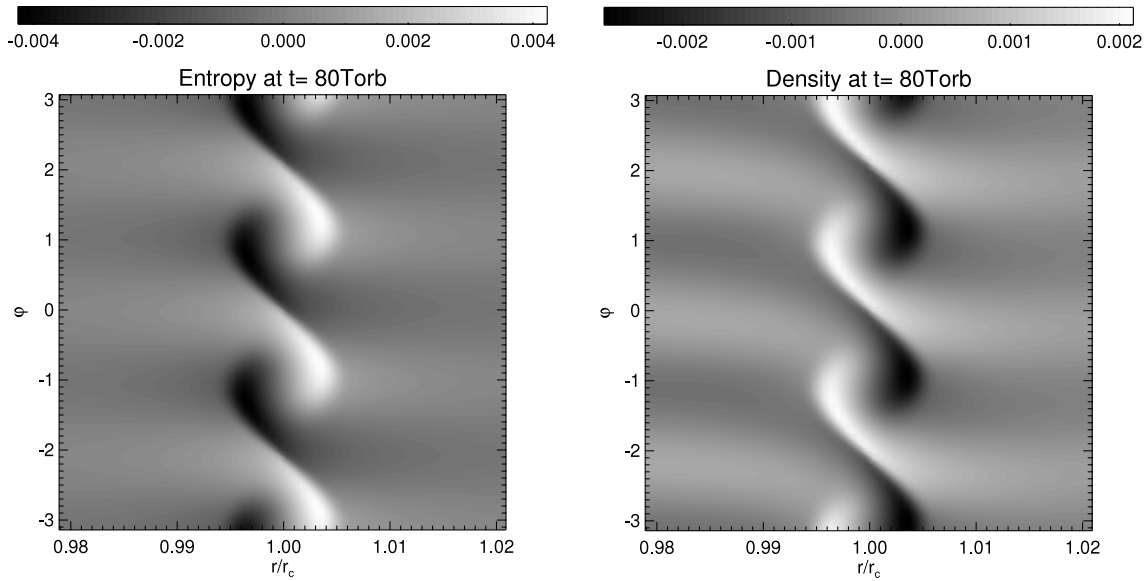


FIG. 3.—Relative perturbation of entropy (left) and surface density (right) for an isolated resonance, at $t \approx 1.5T_{\text{lib}}$. Libration is clockwise.

the whole extent of the calculation, up to $t = \tau$. The torque obtained with a locally isothermal equation of state is also depicted. Our isothermal runs have the same radial temperature dependence as the adiabatic runs (see eq. [47]). Although there is an entropy gradient in these isothermal calculations, it does not contribute to the corotation torque as it would in an adiabatic disk: the appearance of the singular contribution at corotation in the adiabatic case is linked (1) to the advection of entropy and (2) to the appearance of a singularity in the perturbed density and temperature fields. In the isothermal situation, neither the entropy is conserved along a fluid element path nor is a temperature singularity allowed to appear. The comparison of isothermal and adiabatic calculations shows that, as expected for a cold case, the adiabatic and isothermal torques coincide, as long as we are in the linear regime. We note that both torques do not oscillate about 0, since the potential reaches a stationary value only at the end of the calculation.

2. For the two calculations of the peaked potential case, depicted in Figure 2, we find that $\text{Re}[\psi(r_c)] \approx -0.2\phi(r_c)$. Thus, the term $|\Phi \text{Re}(\Phi + \Psi)|$ slightly dominates the term $|\Phi + \Psi|^2$ in equation (41). Because $S < 0$ for these calculations, the corotation torque in the adiabatic case (*diamonds and solid curve*) is larger than the corotation torque in an isothermal disk (*long-dashed curve*) with the same parameters, as predicted by Tanaka et al. (2002). In particular, in the case for which $\mathcal{V} = 0$, the isothermal corotation torque vanishes, while we find a net positive corotation torque for an adiabatic flow, in agreement with the analytical expression.

4.3. Dynamics of the Corotation Region

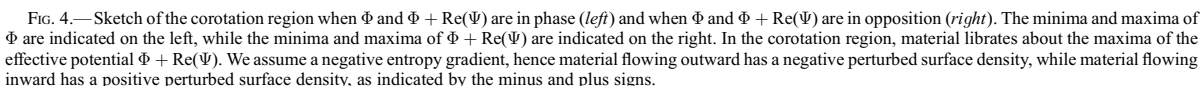
We discuss in this section the dynamics of the CR of an adiabatic disk and give some comments about the corotation torque expression of equation (41). In the isothermal case, the corotation torque expression involves the product of the gradient of vortensity and the square of the effective potential ($\Phi + \eta$; see, e.g., Tanaka et al. 2002). The torque is then given by the angular momentum budget between material flowing outward and material flowing inward at corotation, regardless of the sign of $\Phi + \eta$.

Equation (41) displays a term that has a similar behavior, except that it does not feature the vortensity gradient only, but rather $\mathcal{V} + 2S$. This factor scales with the (logarithmic) gradient of $(\Sigma_0/B)S^{2/\gamma}$, which is a key quantity considered by Li et al. (2000) and by Lovelace et al. (1999), who pointed out that vortensity is not conserved in a two-dimensional adiabatic flow.

In addition to this term, equation (41) contains a term that scales with $\Phi[\Phi + \text{Re}(\Psi)]$. The sign of this term therefore depends on the relative signs of Φ and $\Phi + \text{Re}(\Psi)$. In order to get some insight into the physical meaning of this term, we show in Figure 3 the response of the disk in the corotation region, for the entropy and the surface density. These fields correspond to the calculation with the flat potential profile considered in § 4.2. The disk has a negative radial entropy gradient. Therefore, libration brings the (larger) inner entropy to the outer part of the libration islands, yielding a positive perturbed entropy (*brighter areas*), while it brings the (smaller) outer entropy to the inner part of the libration islands, yielding a negative perturbed entropy (*darker areas*). An opposite behavior is observed for the perturbed density, since the relative pressure perturbation (*not represented*) is much smaller.

The sign of this torque component can be understood as follows. Figure 4 depicts the situation in two cases: Φ and $\Phi + \text{Re}(\Psi)$ have the same sign (*left*) and Φ and $\Phi + \text{Re}(\Psi)$ have opposite signs (*right*). In the left case, the negative perturbed surface density on the outside of corotation is located in the region where $\partial\varphi\Phi < 0$; hence, the perturbation yields a positive torque on the perturber. A similar conclusion applies to the material flowing inward which has positive perturbation of surface density. The torque on the perturber is therefore positive, in agreement with the sign of $-S\Phi[\Phi + \text{Re}(\Psi)]$. An opposite conclusion holds for the case where $\Phi[\Phi + \text{Re}(\Psi)] < 0$.

The order of magnitude and functional dependence of this torque component can be justified as follows. As the sign has been justified in the previous paragraph, we give here an estimate of the absolute value. The perturbed surface density on the outside of corotation is $\sim |\Sigma_0 \delta / r_c|$, where $\delta = ([\Phi + \text{Re}(\Psi)] / (-8AB))^{1/2}$ is an order of magnitude of the width of the libration islands. The specific torque in the region of surface density perturbation is



It is worth noting that only half of the second term of equation (41) comes from equation (40). Equation (39), which is obtained from the momentum flux jump and which as such captures effects occurring at a finite (albeit small) distance from corotation, also displays a term similar to that of equation (40). The advection of entropy perturbations is not a silent process; it triggers the emission of pressure waves (Foglizzo & Tagger 2000). Our torque expression indicates that half of the energy required to advect entropy in the libration islands is evacuated through pressure waves.

In § 3 we derived an expression for the corotation torque between a radiatively inefficient disk and an external rotating potential. This expression is successfully reproduced by local numerical simulations of an isolated CR, in the linear regime. We now contemplate the case of an embedded protoplanet in a radiatively inefficient two-dimensional disk, for which all co-orbital CRs are simultaneously active.

Our numerical simulations are performed with the code FARGO. It is a staggered mesh hydrocode that solves the Navier-Stokes, continuity, and energy equations on a polar grid. It uses an upwind transport scheme with a harmonic, second-order slope limiter (van Leer 1977). Its particularity is to use a change of rotating frame on each ring of the polar grid, which increases the

In this work, the disk is taken to be inviscid so $Q = 0$. There is no radiative transfer either, since the disk is assumed to be radiatively inefficient. Furthermore, p and e are connected by an ideal equation of state $p = (\gamma - 1)e$, where the adiabatic index γ is set to 1.4. This equation of state can be expressed in terms of the disk temperature T and surface density Σ as $p = \Sigma T$. The adiabatic sound speed reads $c_s = (\gamma T)^{1/2}$, hence $c_s = \sqrt{\gamma} c_{s,\text{iso}}$, where $c_{s,\text{iso}}$ refers to the isothermal sound speed. We comment that the Lindblad torque, which scales as c_s^{-2} (Ward 1997), is therefore weakened by a factor of γ in an adiabatic disk. The same is true of the corotation torque, when there is no entropy gradient. We checked both effects with appropriate calculations, not reproduced here. This plays in favor of a total torque reversal in adiabatic disks with a negative entropy gradient. The disk is initially slightly sub-Keplerian (the pressure gradient is accounted for in the centrifugal balance) and axisymmetric, with power-law profiles for the surface density and temperature given by equations (46) and (47).

The disk is perturbed by the smoothed potential of a protoplanet. We adopt a Plummer potential, with a softening length $\varepsilon = 0.6H(r_p)$ (unless otherwise stated), r_p being the planet orbital radius. This fiducial value is quite substantial for our purposes, but investigating the disk response at much smaller softening lengths, where the adiabatic effects on the corotation torque are increasingly

TABLE 1
REFERENCE PARAMETERS

Parameter	Notation	Reference Value
Aspect ratio at $r = r_p$	$h(r_p)$	0.05
Surface density at $r = r_p$	Σ_p	2×10^{-3}
Softening length	ε	0.03
Adiabatic index	γ	1.4
Mesh inner radius	r_{\min}	0.4
Mesh outer radius	r_{\max}	1.8
Radial zones number	N_r	512
Azimuthal zones number	N_s	2048

NOTE.—The disk is inviscid.

important, requires a very large resolution. A high-resolution systematic study at small softening length will be presented in a forthcoming work.

The protoplanet is held on a fixed circular orbit, at $r = r_p$. The disk parameters are summed up in Table 1, where they are expressed in the following unit system: r_p is the length unit, the mass of the central object M_* is the mass unit, and $(GM_*/r_p^3)^{-1/2}$ is the time unit, G being the gravitational constant ($G = 1$ in our unit system). We denote by T_{orb} the planet orbital period, M_p the planet mass, and $q = M_p/M_*$ the planet to primary mass ratio.

5.2. Results

5.2.1. An Illustrative Example

We show the results of an illustrative calculation with a $q = 2.2 \times 10^{-5}$ planet to primary mass ratio (corresponding to $M_p = 7.3 M_{\oplus}$ if the central object has a solar mass). The horseshoe libration time is

$$\tau_{\text{lib}} = \frac{8\pi r_p}{3\Omega_p x_s}, \quad (52)$$

where Ω_p is the protoplanet angular velocity and x_s denotes the half-width of the horseshoe region. Masset et al. (2006) have given an estimate of x_s in the isothermal case that reads $x_s \approx 1.16 r_p [q/h(r_p)]^{1/2}$. A streamline analysis was performed and confirmed that this estimate holds for an adiabatic disk, if one substitutes $h(r_p)$ with $\sqrt{\gamma}h(r_p)$. We find therefore $\tau_{\text{lib}} \approx 60T_{\text{orb}}$. Numerical diffusion eventually alters the conservation of entropy. Nevertheless, the horseshoe region spans 20 zones radially, which is sufficient to follow the horseshoe dynamics over several libration times. Since we are concerned here with a fraction of the libration time, the entropy is conserved with a good level of accuracy over the duration of our runs, and it can be regarded as a Lagrangian tracer of the flow.

Two calculations were performed, an adiabatic and an isothermal one. Both lasted 30 orbital periods, hence half the horseshoe libration time. These calculations have $\sigma = 0.5$ and $f = 0$, as in PM06. This gives $\mathcal{S} \approx -0.57$.

Figure 5 displays the gas entropy, surface density, and pressure obtained in the adiabatic calculation, after $15T_{\text{orb}}$. Each field represents the relative perturbation of the corresponding quantity with respect to the unperturbed state. For instance, the top right panel shows $[\Sigma(r, \varphi) - \Sigma_0(r)]/\Sigma_0(r)$. While the azimuthal range spans the whole $[0, 2\pi]$ interval, the radial range depicted is restricted to a band of width $2.5x_s$ around the corotation radius r_c . We overplot streamlines on the entropy panel to give an idea of the extent of the horseshoe region. The vertical dashed line represents the corotation radius. Whereas the pressure panel does not display any significant perturbation, the entropy and density pan-

els show the propagation of a perturbation inside the horseshoe region, which slides along the separatrices. This is reminiscent of the behavior commented on the case of an isolated resonance in § 4.3.

The interpretation of this dynamics is as follows. The entropy of the fluid elements is conserved as they perform a horseshoe U-turn in the co-orbital region. When there is initially an entropy gradient at corotation, the co-orbital dynamics yields an entropy perturbation that has a sign opposite of that of the entropy gradient on the outward U-turns and the sign of the entropy gradient on the inward U-turns. Since the pressure field is only weakly perturbed, the entropy perturbation is related to a density perturbation of opposite sign and, in relative value, of the same order of magnitude. Therefore, if there is a negative entropy gradient at corotation ($\mathcal{S} < 0$, as in the example shown here), the co-orbital dynamics yields a negative density perturbation at $\varphi < \varphi_p$ and a positive density perturbation at $\varphi > \varphi_p$, with straightforward consequences for the corotation torque. Using an expression inherited from the terminology of Riemann solvers, we call this perturbation a contact discontinuity. A contact discontinuity is characterized by a discontinuity in the density and temperature fields, while the pressure and velocity fields are continuous. A contact discontinuity is simply advected by the flow. Here it follows the horseshoe dynamics, and it remains confined to the horseshoe region.

We give hereafter a simple estimate of the relative perturbation of the disk surface density due to the advection of entropy. We consider a fluid element that performs a horseshoe U-turn from the inner part of the horseshoe region (where we assume that there is no entropy perturbation, which is true as long as $t < \tau_{\text{lib}}/2$) to the outer part. All physical quantities at the inner (outer) leg of the horseshoe streamline are denoted by a minus (plus) subscript. A first-order expansion yields, assuming no pressure perturbation,

$$p_{\pm} = p_0(r_c)(1 \mp \lambda x/r_c), \quad (53)$$

where $0 < x < x_s$ is the distance of the streamline to corotation, and

$$\Sigma_{\pm} = \Sigma_0(r_c)(1 \pm \sigma x/r_c). \quad (54)$$

On the outer horseshoe leg, the disk surface density is perturbed according to the entropy perturbation and reads

$$\Sigma_{+} = \Sigma_0(r_c)(1 + R - \sigma x/r_c), \quad (55)$$

where R is the relative perturbation of surface density at $r = r_c + x$ (we assume a symmetric horseshoe U-turn), due to the entropy advection. Entropy conservation along the fluid element path ($\mathcal{S}_{-} = \mathcal{S}_{+}$) leads to

$$R = 2 \frac{x}{r_c} \left(\sigma - \frac{\lambda}{\gamma} \right) = 2 \frac{x}{r_c} \mathcal{S}. \quad (56)$$

The horseshoe U-turn that we have considered lags the planet ($\varphi < \varphi_p$). A similar conclusion holds for a horseshoe U-turn that switches from the outer leg to the inner one (at $\varphi > \varphi_p$); hence, we finally have

$$R(x) = 2x\mathcal{S}/r_c, \quad \forall x \in [-x_s, +x_s]. \quad (57)$$

The bottom right panel of Figure 5 displays the slices of the perturbed density field at $t = 15T_{\text{orb}}$, for $\varphi - \varphi_p = 1$ (diamonds) and -1 (stars). The two horizontal dashed lines display the values

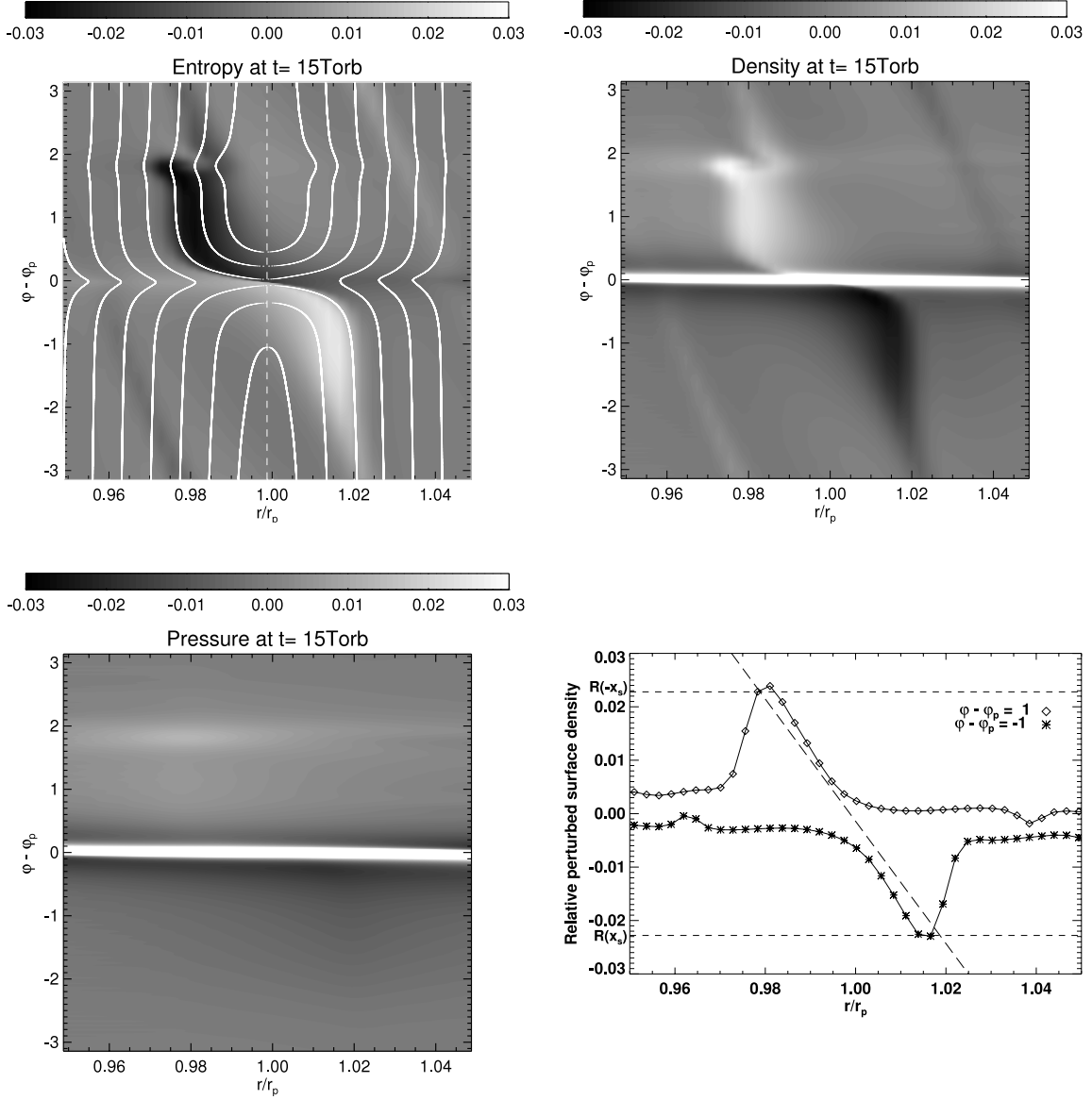


FIG. 5.— *Top row and bottom left:* Relative perturbations of the gas entropy, surface density, and pressure, at $t = 15T_{\text{orb}} \approx \tau_{\text{lib}}/4$. The protoplanet is located in $r = r_p$, $\phi = \phi_p$. In the top left panel, streamlines are overplotted and the vertical dashed line stands for the corotation radius r_c . In the top right and bottom left panels, the color scale is adjusted to highlight the advection of the entropy perturbation (see text). The nearly horizontal overdensity structure at $\phi = \phi_p$ is the protoplanet's wake. *Bottom right:* Slices of the relative perturbed density field at the same time, at $\phi - \phi_p = 1$ (diamonds) and $\phi - \phi_p = -1$ (stars). The two horizontal dashed lines refer to the values of $R(-x_s)$ and $R(x_s)$, while the long-dashed curve displays the quantity $2(r - r_c)S/r_c$ (see text and eq. [57]).

of $R(-x_s)$ and $R(x_s)$, where x_s is estimated through a streamline analysis. Similarly, the long-dashed curve shows $R(x) = 2xS/r_c$, which is in agreement with the calculation results. The surface density structure in the horseshoe region is therefore dictated by the sign of S . In particular, we do not expect any contact discontinuity in the homentropic case ($S = 0$). We have checked this prediction with a numerical simulation (not presented here).

5.2.2. Excess of Corotation Torque and Entropy Gradient

An order of magnitude of the excess of corotation torque arising from the perturbation of the surface density field can be given

by estimating how the standard horseshoe drag expression (Ward 1991; Masset 2001) is modified by the perturbation of surface density $R(x)\Sigma_0(r_c)$. We consider the outward horseshoe U-turns that occur at $\phi < \phi_p$. Assuming, in this order-of-magnitude estimate, that the rotation profile of the disk is unperturbed, we evaluate the variation of angular momentum flux of the horseshoe disk material after the U-turn attributable to the change of the disk's surface density,

$$\Delta\Gamma_{\text{hs}^-} = \int_0^{x_s} (-2Ax)\Sigma_0 R(x)(j_c + 2Br_c x)dx, \quad (58)$$

1064

BARUTEAU & MASSET

Vol. 672

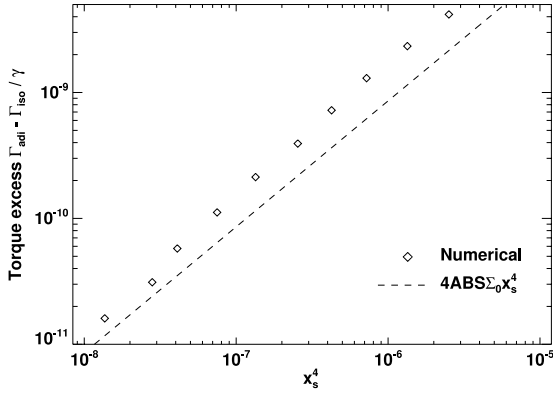


FIG. 6.—Torque excess (see text) as a function of the half-width of the horseshoe region.

where j_c is the specific angular momentum of the material at corotation. The first factor of the integrand of equation (58) represents the material velocity in the corotating frame due to the shear. The last factor is the material specific angular momentum obtained from a first-order expansion at corotation. Similarly, we obtain the change of angular momentum flux due to the perturbation of surface density on inward horseshoe U-turns,

$$\Delta\Gamma_{\text{hs}^+} = \int_0^{x_s} (-2Ax)\Sigma_0 R(-x)(j_c - 2Br_c x)dx. \quad (59)$$

Adding equations (58) and (59), we are left with

$$\Delta\Gamma_{\text{hs}} = 2 \int_0^{x_s} (-2Ax)\Sigma_0 R(x)2Br_c x dx = -4AB\Sigma_0 S x_s^4. \quad (60)$$

Figure 6 shows the excess of corotation torque between an adiabatic and isothermal calculation with the same parameters as a function of the half-width of the horseshoe region. This excess is obtained by subtracting the total torque of an adiabatic and an isothermal calculation (the isothermal torque being rescaled by a factor γ^{-1} , since $c_s = \sqrt{\gamma}c_{s,\text{iso}}$). We call this difference the torque excess for further reference. Each data point corresponds to a calculation with a given planet mass, for which we determine x_s through a streamline analysis. We find that the torque excess

approximately scales as x_s^4 and that it is within a factor 2 of our order-of-magnitude estimate, given by $-\Delta\Gamma_{\text{hs}}$.

The torque expression of equation (41) as well as the horseshoe drag expression of equation (60) suggest that the torque excess scales with S , hence with the entropy gradient. In order to check that, we have undertaken a number of calculations with different values of S . These calculations have $q = 2.2 \times 10^{-5}$, and the disk parameters are those of Table 1. Each entropy gradient is realized with different combinations of the indices of the pressure and surface density power laws. Adiabatic effects on the torque are assessed in two different ways:

1. By calculating the torque excess, as in Figure 6.
2. By evaluating the integral

$$\Gamma_{\text{cd}} = \int_{\text{disk}} \left(\Sigma - \frac{P}{c_s^2} \right) \frac{\partial \Phi}{\partial \varphi} r dr d\varphi, \quad (61)$$

which provides an estimate of the torque due to the contact discontinuity (this contribution arises from perturbations of Σ which do not have a pressure counterpart). In the linear regime, equation (61) amounts to a summation over m of the last term of equation (24). We check this statement in § 5.2.3.

These two estimates of adiabatic effects on the torque value are shown, respectively, in Figures 7a and 7b. Remarkably, they coincide within $\sim 25\%$. We comment further on this coincidence in § 5.2.3.

The main conclusion that can be drawn from the results of Figure 7 is that the torque excess (or the contact discontinuity contribution) essentially depends on the entropy gradient, as expected. The excess is positive for a negative entropy gradient; hence, we may expect the total torque exerted on a planet embedded in a radiatively inefficient disk to be a positive quantity if the radial entropy gradient is sufficiently negative.

5.2.3. Connection to the Analytical Expression

We have given in equation (40) an estimate of the singular torque contribution from the contact discontinuity at an isolated resonance, while we have estimated the total contribution in the planetary case of the contact discontinuity using equation (61) in § 5.2.2. We check in the present section that this total contribution corresponds to the sum over m of the torque expression of equation (40). For this purpose, we have adopted a planet to primary mass ratio $q = 5 \times 10^{-6}$, as the one adopted in the previous sections ($q = 2.2 \times 10^{-5}$) led to poor agreement, presumably

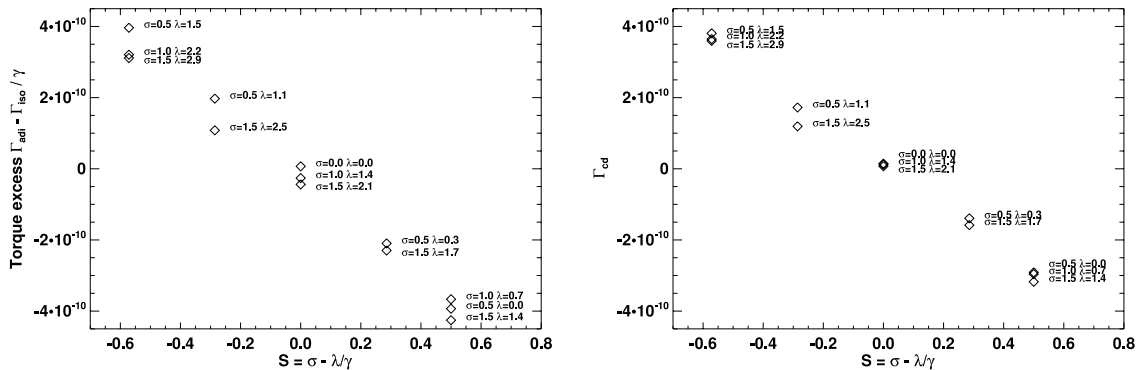


FIG. 7.—Torque excess (left) and contact discontinuity contribution to the torque (right) as a function of S . Although the calculations display some scatter for a given value of S , the different points can be considered as aligned within a good level of approximation. The slope of the dependence is negative.

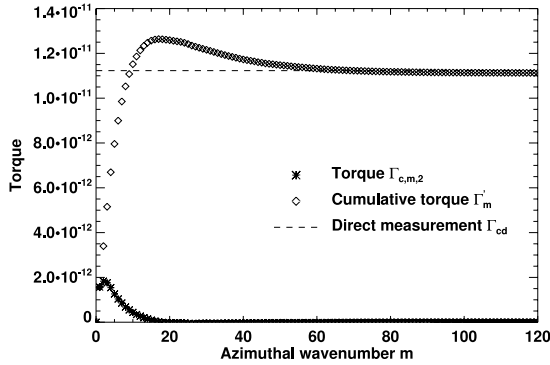


FIG. 8.—Partial sums of the torque series given by eq. (63) (diamonds) and direct estimate of the contact discontinuity contribution given by eq. (61) (dashed line). The asymptotic value of the partial sum almost coincides with the direct estimate (i.e., the diamonds almost lie on the dashed line at large m); hence, with a very good accuracy we have $\Gamma_\infty = \Gamma_{cd}$ (see text).

because of the onset of nonlinear effects. For each azimuthal wavenumber m , we measure $\text{Re}(\Psi_m)$ from the calculation output (at $t = 5T_{\text{orb}}$), and we evaluate the sum over m of the torque $\Gamma_{c,m,2}$,

$$\Gamma_\infty = \lim_{k \rightarrow +\infty} \Gamma'_k, \quad (62)$$

where

$$\Gamma'_k = -\frac{4\pi^2}{3} \left(\frac{S\Sigma_0}{\Omega^2} \right) \sum_{m=1}^k m \Phi_m [\Phi_m + \text{Re}(\Psi_m)] \quad (63)$$

is the partial sum of $\Gamma_{c,m,2}$. We compare the torque contribution given by equation (61) to Γ_∞ . The results are presented in Figure 8. The agreement between the direct torque measurement and the linear estimate is excellent.

This confirms what we anticipated in § 3.2 and what is shown in the Appendix, that the contribution of the last term of equation (25) to the torque is negligible in the planetary context. Also of interest is the torque density associated, respectively, with p/c_s^2 and $\Sigma - p/c_s^2$. The sum of these two torque densities is the total torque density. They are represented in Figure 9. The total torque density displays a smooth profile and a narrow peak at corotation. This is reminiscent of the torque density found by PM06 (their

Fig. 2) or by Morohoshi & Tanaka (2003, their Fig. 3). The decomposition above splits this total torque density into a smooth component arising from p/c_s^2 , which reminds one of the torque density in an isothermal disk, and a sharp, localized torque density arising from $\Sigma - p/c_s^2$. This corresponds to the torque density of the contact discontinuity contribution given by equation (61). Figure 9 shows that this contribution (which is singular at corotation in the linear case for an isolated resonance) is here bounded by the extent of the horseshoe region.

We comment on the surprising agreement found in § 5.2.2 between the torque excess and the contribution of the contact discontinuity. The linear analysis suggests that the former should be the sum of $\Gamma_{0,m}(2S|\Phi_m + \Psi_m|^2 - 2S\Phi_m[\Phi_m + \text{Re}(\Psi_m)])$, which, in the limit where $|\Phi_m + \text{Re}(\Psi_m)| \ll |\text{Re}(\Psi_m)|$ and $|\Phi_m + \text{Re}(\Psi_m)| \ll |\Phi_m|$, should reduce to $-2\Gamma_{0,m}S\Phi_m[\Phi_m + \text{Re}(\Psi_m)]$, which is twice the contribution of the contact discontinuity (see § 3.2.2). Nevertheless, for the calculations presented here, we can check that $2 \sum_m m |\Phi_m + \Psi_m|^2$ is almost exactly compensated by $\sum_m m \Phi_m [\Phi_m + \text{Re}(\Psi_m)]$. Namely, the ratio of the former to the latter quantity is found to be 1.07, which explains why the full excess expression essentially amounts to the contact discontinuity contribution. Presumably, this coincidence is fortuitous and linked to the relatively large softening length that we use. At smaller softening lengths, the term in $\Phi_m[\Phi_m + \text{Re}(\Psi_m)]$ should largely dominate, yielding a ratio of 2 between the torque excess and the contribution of the contact discontinuity. We note that PM06 also quote that the torque estimate given by their equation (1) accounts for the total torque within 25% (this equation can also be seen as an estimate of the contact discontinuity contribution). This seems to suggest that the softening length of $0.6H(r_p)$ that we adopted is a correct choice to reproduce the magnitude of the corotational effects in adiabatic three-dimensional disks.

6. DISCUSSION

6.1. Softening Length

In an isothermal disk, the corotation torque scales with $|\Phi + \eta|^2$ (Tanaka et al. 2002). Even if Φ diverges at corotation, $\Phi + \eta$ remains finite, which makes the isothermal corotation torque a quantity relatively insensitive to the softening length. The situation is quite different for the effects linked to the entropy advection that we present here; they involve the product $\Phi(\Phi + \Psi)$, which diverges when Φ does. Adiabatic effects on the corotation torque should acquire a very large magnitude at small softening lengths. In particular, if the softening length is smaller than the

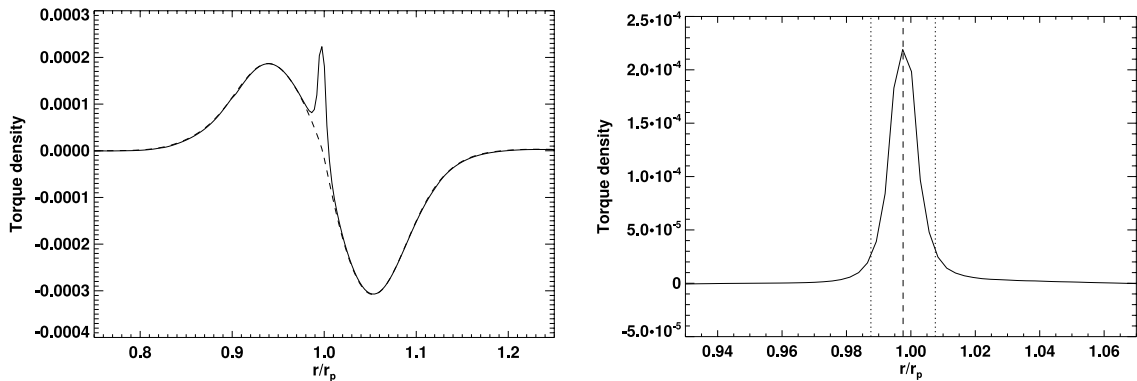


FIG. 9.—Left: Total torque density (solid curve) and torque density of p/c_s^2 (dashed curve). Right: Torque density of $\Sigma - p/c_s^2$. The vertical dashed line shows the corotation radius, while the two vertical dotted lines show the extent of the horseshoe region.

distance from orbit to corotation, the magnitude of these effects should strongly depend on this distance, which scales with the pressure gradient. If one regards the softening length as a proxy for the altitude in a three-dimensional disk, the extent of the disk vertical scale height concerned by these very small softening length issues should be small, however, since the distance from orbit to corotation is a fraction of $r_p h^2$. Nevertheless, it is of interest to investigate the behavior of the corotation torque in an adiabatic flow at very small softening lengths to assess the importance of such effects. Owing to the very large resolution required to investigate this problem, we defer this investigation to a forthcoming work.

6.2. Saturation

The origin of the effects presented here is the advection of entropy in the corotation region, which triggers an entropy perturbation (and therefore a density perturbation) whenever there is an entropy gradient in the equilibrium profile. Libration occurs on different timescales for the different streamlines of the corotation region, which tends to stir the entropy and to flatten out the entropy profile across the corotation region (be it the horseshoe region in the planetary case or a libration island in the isolated resonance case). This is quite similar to the behavior of the corotation torque in an isothermal disk, which tends to saturate because the vortensity profile is flattened out by libration. In this case, it is the viscous diffusion which can prevent the flattening out of the profile if it acts sufficiently rapidly to establish the large-scale gradients before a libration time. This has been studied for an isolated resonance by Goldreich & Sari (2003) and Ogilvie & Lubow (2003) and by Balmforth & Korycansky (2001) and Masset (2001) for a planetary co-orbital region. In both cases, the degree of saturation of the corotation torque in steady state depends on the ratio of the libration time and of the viscous time across the libration region. The dissipative processes required to prevent the torque saturation in the situation presented here should be able to impose the large-scale entropy gradient over the corotation region in less than a libration time. Radiative processes (cooling and heating) should therefore occur on a timescale longer than a horseshoe U-turn (otherwise the flow can rather be considered as locally isothermal), but they should act on a timescale shorter than the libration time. We provide an estimate of the horseshoe U-turn time and of the libration time for a small-mass object embedded in a gaseous disk. The horseshoe half-width x_s is $\sim r_p [q/h(r_p)]^{1/2}$. Neglecting pressure effects and writing a simplified Jacobi constant for a test particle near a horseshoe U-turn as $J = -GM_p/(2Br_p|\varphi - \varphi_p|) + A(r - r_p)^2$, we can estimate the distance of closest approach between the planet and a test particle flowing along a horseshoe separatrix as $r_p|\Delta\varphi|_s = \Omega_p^2 H(r_p)/2|AB| = O(H(r_p))$. The time required to perform a horseshoe U-turn can be deduced using the radial drift velocity of the test particle when it crosses the orbit, at its closest approach from the planet $\dot{x} = GM_p/(2Br_p^2\Delta\varphi_s^2)$. That yields

$$\tau_{U\text{-turn}} = \frac{2x_s}{\dot{x}} = \frac{\Omega_p^2 h(r_p)^{3/2} q^{-1/2}}{A^2 B} \approx \frac{4}{\Omega_p} \left[\frac{H(r_p)}{R_H} \right]^{3/2}, \quad (64)$$

where $R_H = r_p(q/3)^{1/3}$ is the Hill radius of the planet and where the last equality holds for a Keplerian disk. When the planet emerges from the disk [$H(r_p) \sim R_H$], the horseshoe U-turn occurs on the dynamical timescale. When dealing with an embedded object however [$R_H < H(r_p)$], the horseshoe U-turn time can be substantially longer than the dynamical time [e.g., 10 times longer for an Earth mass object embedded in a disk with $h(r_p) = 0.05$].

Using equation (52), we are led to

$$\frac{\tau_{\text{lib}}}{\tau_{U\text{-turn}}} \approx h(r_p)^{-1}. \quad (65)$$

There is at least an order of magnitude difference between the horseshoe U-turn time and the libration time in a thin disk; hence, it should be possible to find a location in the disk where the cooling time is much longer than the U-turn time and yet shorter than the libration time, so as to maintain an unsaturated corotation torque.

6.3. Entropy Gradient and Baroclinic Instability

The effect that we present in this two-dimensional analysis is of particular interest when there is a negative entropy gradient at corotation, since this may suffice to halt type I migration. It would be of interest to generalize the present analysis to the case of a three-dimensional baroclinic disk. We comment also that in such systems, a negative entropy gradient may render the disk unstable to a baroclinic instability (Klahr 2004; Klahr & Bodenheimer 2003). It is certainly important to examine the interplay of the baroclinic instability and of the corotational effects presented here. The turbulence generated by the baroclinic instability, in particular, could provide a mechanism to prevent the saturation of the corotation torque, much like the turbulence arising from the magnetorotational instability can prevent the corotation torque saturation in an isothermal disk.

7. CONCLUSIONS

We evaluate the corotation torque between an adiabatic gaseous disk and a uniformly rotating external potential. In the linear case for an isolated resonance, we find a singular contribution at corotation which scales with the entropy gradient and which arises from the advection of entropy within the libration region. This effect neither exists in isothermal or locally isothermal flows nor does it exist for barotropic fluids (such as fluids described by a polytropic equation of state). We provide a torque expression at an isolated resonance which involves the pressure perturbation at corotation. We then check the torque expression by two-dimensional adiabatic calculations that involve an isolated resonance. In particular, we exhibit a case with a flat vortensity profile, for which the corotation torque does not cancel out and is in agreement with the analytical expression. We then turn to the case of an embedded planet, for which we find an excess of corotation torque in the adiabatic case, which scales with the entropy gradient. For a sufficiently small planet mass, we check that this excess can be accounted for by a summation over the resonances of the torque excess that we found in the first part. This confirms that this effect is essentially a linear effect. We finally discuss in § 6 some open questions linked to the softening length, to the saturation, to the case of a three-dimensional baroclinic disk, and to the interplay with the baroclinic instability, on to which theoretical efforts should focus in a nearby future.

We wish to thank Sijme-Jan Paardekooper and John C. B. Papaloizou for interesting discussions on the topics covered in this manuscript. We also thank Alessandro Morbidelli for a thorough reading of a first version of this manuscript and an anonymous referee for comments that led to an improvement of the paper.

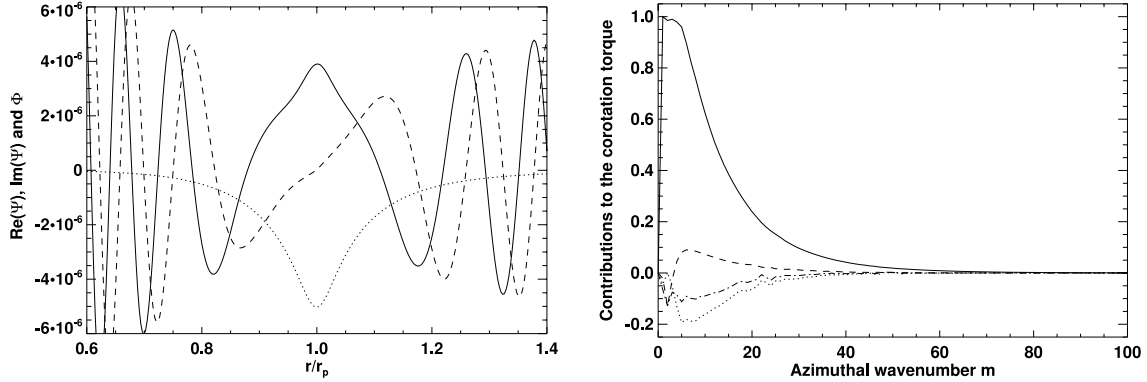


FIG. 10.—*Left:* The $m = 8$ azimuthal component of $\Psi = p/\Sigma_0$ (the real part is shown by a solid curve, the imaginary part is shown by a dashed curve). The dotted line shows the $m = 8$ component of the potential (which is purely real). *Right:* Singular contribution of Ψ at corotation (solid curve), contribution of the extra term in $\text{Im}[\Psi(x)]/x$ of eq. (25) (dotted curve), contribution of the first term of eq. (10) (dashed curve), and total contribution of these extra terms (dash-dotted curve). Each contribution is normalized to the maximum value of the singular contribution of Ψ at corotation.

APPENDIX

ADDITIONAL CONTRIBUTION TO THE COROTATION TORQUE

We check hereafter that the contribution of the last term of equation (25) is negligible for an embedded planet. For this purpose, we compare $G = \int dx \text{Im}[\Psi(x)]\Phi(x)/x$ to $-\pi[\text{Re}(\Psi)\Phi]_{r_c}$. Figure 10a shows the $m = 8$ component of $\Psi = p/\Sigma_0$ for the calculation presented in § 5.2.3. We clearly see that the behavior of $\text{Im}(\Psi)$ in the vicinity of corotation comes from the overlap of the behavior arising at the inner and outer Lindblad resonances. Between its outermost inner minimum at $r_- \sim 0.87$ and its innermost outer maximum at $r_+ \sim 1.12$, $\text{Im}(\Psi)$ can be considered as having a linear dependence in x . Notwithstanding the decrease of Φ as one recedes from corotation, the main contribution to G will come from $\text{Im}[\Psi(x)]/x$ between these two radii, as it exhibits a flat behavior over this range. This yields $G \sim 2\Phi(r_c)|\text{Im}[\Psi(r_{\pm})]|$, that is to say a result comparable in order of magnitude to $-\pi[\text{Re}(\Psi)\Phi]_{r_c}$. Nevertheless, the final contribution of the extra term is much smaller than the singular one at corotation for the following reasons:

1. The potential decreases sharply as one recedes from corotation, which provides a cutoff to the extra term, which is not localized at corotation.
2. The extra term is partially compensated for by the first term of equation (10), which we have neglected in writing equation (24) and which yields another term in equation (25) that reads $-(\mathcal{FS}/r^2\Omega)_{r_c} d\text{Im}[\Psi(x)]/dx$. Adding this additional term and the last term of equation (25), we are left with

$$-\frac{d\text{Im}[\Psi(x)]}{dx} \left(\frac{\mathcal{FS}}{r^2\Omega} \right)_{r_c} - \frac{\text{Im}[\Psi(x)]}{x} \left(\frac{2\mathcal{FS}}{r^3\Omega'} \right)_{r_c} \sim -\frac{\text{Im}[\Psi(x)]}{x} \left(\frac{r\Omega'}{2\Omega} + 1 \right) \left(\frac{2\mathcal{FS}}{r^3\Omega'} \right)_{r_c} \sim -\frac{\text{Im}[\Psi(x)]}{x} \left(\frac{\mathcal{FS}}{2r^3\Omega'} \right)_{r_c},$$

which shows that, in addition to the potential cutoff, the last term of equation (25) should be decreased by a factor of 4 [we neglect, at this level of accuracy, the jump in $\text{Im}(\Psi')$ at corotation].

We have checked on the calculation presented in § 5.2.3 that the contribution of these extra terms is indeed small compared to the singular contribution at corotation at all m . This is shown in Figure 10b, from which we can conclude that the total contribution of the extra terms is about an order of magnitude smaller than the singular contribution. The agreement that we found in § 5.2.3 between the numerical simulation of an embedded planet and the torque series, which was of the order of a percent, might then be fortuitous. Nevertheless, we expect an agreement of the order of 10%, which is still very satisfactory. These findings are also compatible with the fact that we hardly see any diffuse torque density outside of the horseshoe region in Figure 9b.

REFERENCES

- Balmforth, N. J., & Korycansky, D. G. 2001, MNRAS, 326, 833
D'Angelo, G., Henning, T., & Kley, W. 2003, ApJ, 599, 548
de Val-Borro, M., et al. 2006, MNRAS, 370, 529
Fogizzo, T., & Tagger, M. 2000, A&A, 363, 174
Goldreich, P., & Sari, R. 2003, ApJ, 585, 1024
Goldreich, P., & Tremaine, S. 1979, ApJ, 233, 857
Klahr, H. 2004, ApJ, 606, 1070
Klahr, H. H., & Bodenheimer, P. 2003, ApJ, 582, 869
Li, H., Finn, J. M., Lovelace, R. V. E., & Colgate, S. A. 2000, ApJ, 533, 1023
Lovelace, R. V. E., Li, H., Colgate, S. A., & Nelson, A. F. 1999, ApJ, 513, 805
Masset, F. 2000a, A&AS, 141, 165
———. 2000b, in ASP Conf. Ser. 219, Disks, Planetesimals, and Planets, ed. G. Garzón et al. (San Francisco: ASP), 75
Masset, F. 2001, ApJ, 558, 453
Masset, F. S., D'Angelo, G., & Kley, W. 2006, ApJ, 652, 730
Masset, F. S., & Ogilvie, G. I. 2004, ApJ, 615, 1000
Morohoshi, K., & Tanaka, H. 2003, MNRAS, 346, 915
Ogilvie, G. I., & Lubow, S. H. 2003, ApJ, 587, 398
Paardekooper, S.-J., & Mellema, G. 2006, A&A, 459, L17
Stone, J. M., & Norman, M. L. 1992, ApJS, 80, 753
Tanaka, H., Takeuchi, T., & Ward, W. R. 2002, ApJ, 565, 1257
van Leer, B. 1977, J. Comput. Phys., 23, 276
Ward, W. R. 1991, in Lunar Planetary Science Conf., 22, 1463
———. 1997, Icarus, 126, 261
Zhang, H., & Lai, D. 2006, MNRAS, 368, 917

THE ASTROPHYSICAL JOURNAL, 678:483–497, 2008 May 1

© 2008. The American Astronomical Society. All rights reserved. Printed in U.S.A.

TYPE I PLANETARY MIGRATION IN A SELF-GRAVITATING DISK

C. BARUTEAU AND F. MASSET¹Laboratoire AIM, CEA/DSM-CNRS-Université Paris Diderot, DAPNIA/Service d'Astrophysique, CEA-Saclay,
91191 Gif/Yvette Cedex, France; clement.baruteau@cea.fr, fmasset@cea.fr

Received 2007 September 20; accepted 2008 January 9

ABSTRACT

We investigate the tidal interaction between a low-mass planet and a self-gravitating protoplanetary disk by means of two-dimensional hydrodynamic simulations. We first show that considering a planet as freely migrating in a disk without self-gravity leads to a significant overestimate of the migration rate. The overestimate can reach a factor of 2 for a disk having 3 times the surface density of the minimum mass solar nebula. Unbiased drift rates may be obtained only by considering a planet and a disk orbiting within the same gravitational potential. In the second part, the disk self-gravity is taken into account. We confirm that the disk gravity enhances the differential Lindblad torque with respect to the situation where neither the planet nor the disk feels the disk gravity. This enhancement only depends on the Toomre parameter at the planet location. It is typically 1 order of magnitude smaller than the spurious one induced by assuming a planet migrating in a disk without self-gravity. We confirm that the torque enhancement due to the disk gravity can be entirely accounted for by a shift of Lindblad resonances and can be reproduced by the use of an anisotropic pressure tensor. We do not find any significant impact of the disk gravity on the corotation torque.

Subject headings: accretion, accretion disks — hydrodynamics — methods: numerical —
planetary systems: formation — planetary systems: protoplanetary disks

1. INTRODUCTION

Since the discovery of the first exoplanet (Mayor & Queloz 1995), theories of planet-disk interaction have received renewed attention. Using the analytic torque expression of Goldreich & Tremaine (1979) at Lindblad and corotation resonances, Ward (1997, and references therein) has elaborated a theory of planet-disk tidal interaction which shows that a planet embedded in a protoplanetary disk should experience an orbital decay toward the central object. For low-mass protoplanets, the timescale of this inward migration (usually known as type I planetary migration) is much smaller than the disk lifetime, by typically 1 or 2 orders of magnitude (Ward 1997). This is a challenge to current theories of planetary formation, since it seems very unlikely that a giant planet can be built up before its protoplanetary core has reached the vicinity of the central star.

Most of recent works dealing with planet-disk interactions have therefore proposed mechanisms that could slow down or stop type I migration. Menou & Goodman (2004) considered realistic models of T Tauri α -disks instead of the customary power-law models and found that type I migration can be significantly slowed down at opacity transitions in the disk. Masset et al. (2006b) showed that surface density jumps in the disk can trap low-mass protoplanets, thereby reducing the type I migration rate to the disk's accretion rate. Paardekooper & Mellema (2006) found that the migration may even be reversed in disks of large opacity. More recently, Baruteau & Masset (2008) have shown that, in a radiatively inefficient disk, there is an excess of corotation torque that scales with the initial entropy gradient at corotation. If the latter is sufficiently negative, the excess of corotation torque can be positive enough to reverse type I migration.

A common challenge is in any case to yield precise estimates of the migration timescale. Nevertheless, a very common simplification of numerical algorithms consists of discarding the disk

self-gravity. Apart from a considerable gain in computational cost, this is justified by the fact that protoplanetary disks have large Toomre parameters, so that the disk self-gravity should be unimportant. Even in disks that are not subject to the gravitational instability, neglecting the self-gravity may have important consequences on planetary migration, as we shall see.

Thus far, a very limited number of works have taken the disk self-gravity into account in numerical simulations of planet-disk interactions. Boss (2005) performed a large number of disk simulations in which the self-gravity induces giant planet formation by gravitational instability. His calculations are therefore short, running for a few dynamical times, and involve only very massive objects. The planets formed in these simulations excite a strongly nonlinear response by the disk, and any migration effects are probably marginal or negligible. Furthermore, Nelson & Benz (2003a, 2003b) included the disk self-gravity in their two-dimensional simulations of planet-disk interactions. The authors find that the migration rate of a planet that does not open a gap is slowed down by at least a factor of 2 in a self-gravitating disk. Nonetheless, Pierens & Hure (2005, hereafter PH05) reported an analytical expression for the shifts of Lindblad resonances due to the disk gravity, and found that the disk gravity accelerates type I planetary migration. The apparent contradiction between these findings motivated our investigation.

This work is the first part of a series of studies dedicated to the role of self-gravity on planetary migration. In the present paper, we focus on the impact of self-gravity on the migration of low-mass objects, that is, on type I migration. This study will be extended beyond the linear regime in a future publication.

The paper is organized as follows. The numerical setup used in our calculations is described in § 2. We study in § 3 the dependence of the differential Lindblad torque on the disk surface density, without and with disk self-gravity. We confirm in this section that the disk gravity accelerates type I migration, and check that this acceleration can be exclusively accounted for by a shift of Lindblad resonances. In § 4, we show that the increase of the differential Lindblad torque due to the disk gravity can be reproduced

¹ Also at IA-UNAM, Ciudad Universitaria, Apartado Postal 70-264, Mexico D. F. 04510, Mexico.

with an anisotropic pressure tensor. We investigate in § 5 the impact of the disk self-gravity on the corotation torque. We sum up our results in § 6.

2. NUMERICAL SETUP

We study the impact of the disk self-gravity on the planet-disk tidal interaction by performing a large number of two-dimensional hydrodynamic simulations. Notwithstanding the need for a gravitational softening length, the two-dimensional restriction provides a direct comparison with the analytical findings of PH05 and enables us to achieve a wide exploration of the parameter space (mainly in terms of disk surface density, disk thickness, and planet mass).

2.1. Units

As usual in numerical simulations of planet-disk interactions, we adopt the initial orbital radius r_p of the planet as the length unit, the mass of the central object M_* as the mass unit and $(GM_*/r_p^3)^{-1/2}$ as the time unit, G being the gravitational constant ($G = 1$ in our unit system). We denote M_p as the planet mass and q as the planet to primary mass ratio.

2.2. A Poisson Equation Solver for the Code FARGO

Our numerical simulations are performed with the code FARGO. It is a staggered mesh hydrocode that solves the Navier-Stokes and continuity equations on a polar grid. It uses an upwind transport scheme with a harmonic, second-order slope limiter (van Leer 1977). Its particularity is to use a change of rotating frame on each ring of the polar grid, which increases the time step significantly (Masset 2000a, 2000b), thereby lowering the computational cost of a given calculation.

2.2.1. Implementation

We implemented a Poisson equation solver in FARGO as follows. Using the variables $(u = \log r, \varphi)$, where r and φ denote the polar coordinates, the potential V of the disk, as well as the radial and azimuthal accelerations g_r and g_φ derived from it, involves convolution products (Binney & Tremaine 1987). They can therefore be calculated at low computational cost using fast Fourier transforms (FFTs), provided that a grid with a logarithmic radial spacing is used. Our Poisson equation solver calculates g_r and g_φ with FFTs.

To avoid the well-known alias issue, the calculation of the FFTs is done on a grid whose radial zones number is twice that of the hydrodynamics grid, the additional cells being left empty of mass. Thus, the mass distribution of the hydrodynamics mesh cannot interact tidally with its adjacent replications in Fourier space (Sellwood 1987), and it remains isolated. Because of the 2π periodicity, such a precaution is not required in the azimuthal direction.

Furthermore, a softening parameter ε_{SG} is adopted to avoid numerical divergences, the same way as the planet potential is smoothed. We point out that ε_{SG} must scale with r so that the expressions of g_r and g_φ , smoothed over the softening length ε_{SG} , indeed involve convolution products. The expressions of g_r and g_φ are given in Appendix A.

Finally, we present a test problem. For a two-dimensional disk with a uniform surface density Σ , g_r reads

$$g_r(r) = 4G\Sigma \left[\frac{E(v_{\max}) - K(v_{\max})}{v_{\max}} + K(u_{\min}) - E(u_{\min}) \right], \quad (1)$$

where K and E denote the complete elliptic integrals of the first and second kinds, respectively, where $u_{\min} = r_{\min}/r$ and $v_{\max} = r/r_{\max}$, and r_{\min} (r_{\max}) denote the disk inner (outer) edge (see

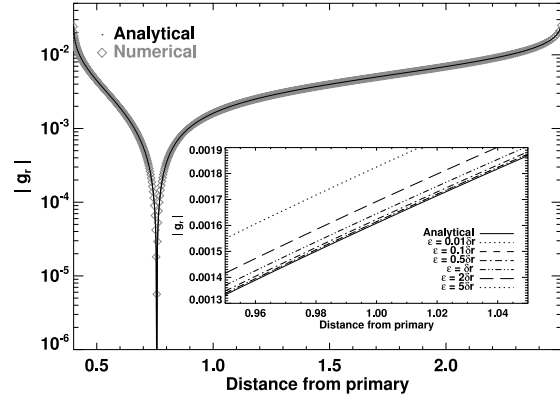


FIG. 1.—Radial self-gravitating acceleration $g_r(r)$, in absolute value, for a uniform surface density field. The analytical expression of g_r (see eq. [1]) is compared with the result of a self-gravitating calculation with a small softening length (see text). We point out that $g_r(r)$ is positive at the inner edge, then it becomes negative (here from $r \gtrsim 0.75$). The close-up reveals the influence of the softening length on the agreement between the numerical calculation and the analytical expectation (see text).

PH05). We performed a self-gravitating calculation with $\Sigma = 2 \times 10^{-3}$, $r_{\min} = 0.4r_p$, and $r_{\max} = 2.5r_p$. The radial zones number is $N_r = 512$, and we took a very small softening length [$\varepsilon_{SG}(r_p)$ is 100 times smaller than the grid radial spacing at $r = r_p$]. Figure 1 shows the agreement between the result of our calculation and the analytical expression of equation (1). The close-up displays g_r around $r = r_p$, for different softening length to mesh resolution ratios, $\varepsilon/\delta r$, at $r = r_p$. This shows the good convergence of our numerical calculation toward the analytical expectation when the softening length tends to zero.

2.2.2. Numerical Issues

The implementation of the disk self-gravity addresses two issues. The first one concerns the convergence properties of our results. We performed preliminary runs to check the torque convergence, without and with self-gravity. The computational domain is covered with N_r zones radially between $r_{\min} = 0.4r_p$ and $r_{\max} = 2.5r_p$, and N_φ zones azimuthally between $\varphi = 0$ and 2π . For a comparative purpose, a logarithmic radial spacing is also used for the calculations without self-gravity. We adopted disk parameters and a planet mass that are representative of our study, namely, a $Q = 8$ Toomre parameter at the planet location, and a $M_p = 5 \times 10^{-6} M_*$ planet mass. A complete description of our model parameters is deferred to § 2.3. We evaluate the torque obtained without self-gravity (Γ_{NOG}) and with self-gravity (Γ_{FSG}) for several pairs (N_r, N_φ) . The relative difference of these torques is displayed in Figure 2a. We see in particular that the torque convergence is already achieved for $N_r = 512$ and $N_\varphi = 1536$, values that we adopted for all the calculations of this paper.

Furthermore, since the softening length ε_{SG} varies from one ring to another, the FFT algorithm does not ensure an exact action-reaction reciprocity. Thus, the disk self-gravity may worsen the conservation of the total angular momentum (that of the system {gas+planet}). To investigate this issue, we performed calculations with a planet migrating in a disk without and with self-gravity. For these calculations only, the disk is inviscid, and reflecting boundaries are adopted. As for the above convergence study, we adopted a $M_p = 5 \times 10^{-6} M_*$ planet mass, and a $Q = 8$ Toomre parameter at the planet location. The value of $\varepsilon_{SG}(r_p)$ is the one used in our calculations hereafter (see § 2.3). We display in

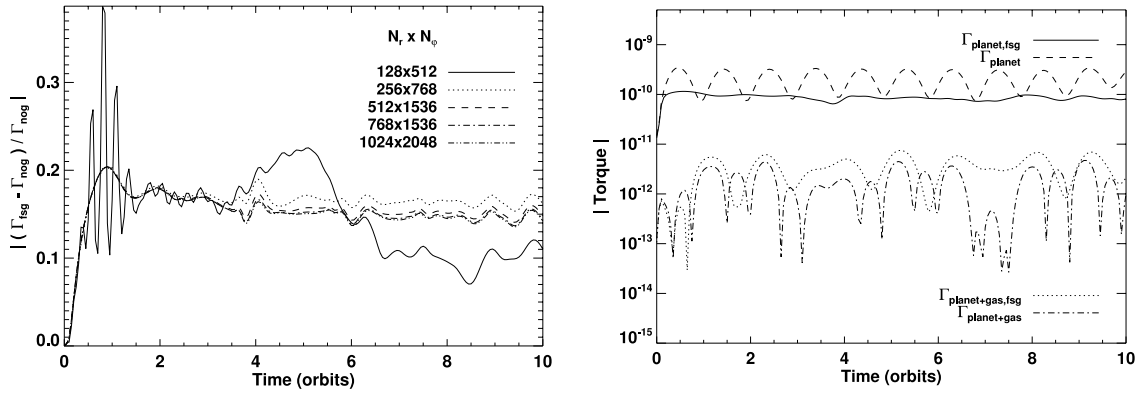


FIG. 2.—*Left*: Relative difference of the torques obtained without self-gravity (Γ_{NOG}), and with self-gravity (Γ_{FSG}), for different grid resolutions (see text). *Right*: Torque exerted on a $M_p = 5 \times 10^{-6} M_*$ planet mass, and on the system {gas+planet}. Torques are depicted for a calculation without self-gravity (long-dashed and dash-dotted curves) and with self-gravity (solid and dotted curves).

Figure 2b the torques on the planet (Γ_{planet}) and on the whole system ($\Gamma_{\text{planet+gas}}$), for both calculations. If the code were perfectly conservative, the ratio $\Gamma_{\text{planet+gas}}/\Gamma_{\text{planet}}$ would cancel out, to within machine precision. This ratio is typically $\sim 0.5\%$ without self-gravity, and $\sim 3\%$ with self-gravity. Although, as expected, the conservation of the total angular momentum is worse with self-gravity, it remains highly satisfactory.

2.3. Model Parameters

In the runs presented hereafter, the disk surface density Σ is initially axisymmetric with a power-law profile, $\Sigma(r) = \Sigma_p(r/r_p)^{-\sigma}$, where Σ_p is the surface density at the planet's orbital radius. The reference value of σ is $3/2$. We therefore expect the corotation torque, which scales with the gradient of (the inverse of) the disk vortensity, to cancel out for a non-self-gravitating disk (Ward 1991; Masset 2001).

The vertically integrated pressure p and Σ are connected by an isothermal equation of state, $p = \Sigma c_s^2$, where c_s is the local isothermal sound speed. The disk aspect ratio is $h(r) = H(r)/r = c_s(r)/r\Omega_K(r)$, where $H(r)$ is the disk scale height at radius r , and Ω_K denotes the Keplerian angular velocity. We take h to be uniform, ranging from $h = 0.03$ to 0.05 , depending on the calculations. We use a uniform kinematic viscosity ν , which is 10^{-5} in our unit system.

The gravitational forces exerted on the disk include

1. The gravity of the central star.
2. The gravity of an embedded planet, whose potential is a Plummer one with softening parameter $\varepsilon = 0.3H(r_p)$.
3. The disk self-gravity, whenever it is mentioned. The self-gravity softening length ε_{SG} is chosen to scale with r , and to be equal to ε at the planet's orbital radius, which yields $\varepsilon_{\text{SG}}(r) = \varepsilon(r/r_p)$. Since h is taken to be uniform, $H(r)$ scales with r , and $\varepsilon_{\text{SG}}(r) = 0.3H(r)$. We comment that $\varepsilon_{\text{SG}}(r_p)$ is very close to the recent prescription of Huré & Pierens (2006) for the softening length of a flat, axisymmetric self-gravitating disk. From now on, whenever we mention the softening length, we will refer to it as ε .

The disk's initial rotation profile $\Omega(r)$ is slightly sub-Keplerian, the pressure gradient being accounted for in the centrifugal balance. When the disk self-gravity is taken into account, it reads

$$\Omega(r) = \left\{ \Omega_K^2(r) \left[1 - (1 + \sigma)h^2 \right] - \frac{g_r(r)}{r} \right\}^{1/2}. \quad (2)$$

We comment that $g_r(r)$ is not necessarily a negative quantity. When it is so, the disk rotates slightly faster with self-gravity than without. In a two-dimensional truncated disk, g_r is positive at the inner edge and becomes negative at a distance from the inner edge that depends on σ . We checked that, whatever the values of σ used in this paper, g_r is always negative in a radial range around the planet's orbital radius that is large enough to embrace all Lindblad resonances (except the inner Lindblad resonance of $m = 1$ for $\sigma = 0$, as can be inferred from Fig. 1).

As stated in § 2.2.2, our calculations are performed on a grid with a logarithmic radial spacing, even when the disk self-gravity is not taken into account. The resolution is therefore the same in all our calculations. The computational domain is covered with $N_r = 512$ zones radially between $r_{\text{min}} = 0.4r_p$ and $r_{\text{max}} = 2.5r_p$, and $N_\phi = 1536$ zones azimuthally between $\phi = 0$ and 2π .

3. DEPENDENCE OF THE DIFFERENTIAL LINDBLAD TORQUE ON THE DISK SURFACE DENSITY

Our study is restricted to the linear regime, which enables us to compare the results of our calculations with analytical predictions. For this purpose, we consider a $q = 5 \times 10^{-6}$ planet to primary mass ratio. According to Masset et al. (2006a) for a two-dimensional calculation, the flow in the planet vicinity remains linear as long as

$$r_B \ll \varepsilon, \quad (3)$$

where $r_B = GM_p/c_s^2(r_p)$ is the planet's Bondi radius and ε is the softening length. Equation (3) translates into $q \ll q_{\text{lin}}$, with $q_{\text{lin}} = 0.3h^3$ in our units. For a $h = 5\%$ disk aspect ratio, $q_{\text{lin}} \approx 4 \times 10^{-5}$ so that our planet mass is well inside the linear regime. For a $h = 3\%$ disk aspect ratio, $q_{\text{lin}} \approx 8 \times 10^{-6}$, and our planet mass approximately fulfills the linearity condition. Note that the linearity criterion given by equation (3) ensures that the torque Γ exerted by the disk on the planet scales with q^2 . We focus in this section on the scaling of Γ with Σ_p , scaling that is expected, for a non-self-gravitating disk, as long as the planet does not open a gap. The gap clearance criterion, recently revisited by Crida et al. (2006) reads in our unit system as

$$\frac{3}{4}h\left(\frac{q}{3}\right)^{-1/3} + 50\frac{\nu}{q} \leq 1. \quad (4)$$

TABLE 1
PLANET'S ANGULAR VELOCITY $\Omega_p(r_p)$ AND DISK'S ROTATION
PROFILE $\Omega(r)$ FOR A NON-SELF-GRAVITATING DISK

Parameter	Fixed Case	Free Case
$\Omega_p(r_p)$	$\Omega_K(r_p)$	$\left[\Omega_K^2(r_p) - \frac{g_r(r_p)}{r_p} \right]^{1/2}$
$\Omega(r)$	$\Omega_K(r)[1 - (1 + \sigma)h^2]^{1/2}$	$\Omega_K(r)[1 - (1 + \sigma)h^2]^{1/2}$

NOTE.—In both cases, the initial planet's angular velocity is strictly Keplerian. For all the runs presented here, $g_r(r_p) < 0$, so that $\Omega_p(r_p)$ is slightly greater in the free case than in the fixed case.

The left-hand side of equation (4) is ~ 100 , hence we expect to check $\Gamma \propto \Sigma_p$ in our calculations without self-gravity.

The runs presented hereafter lasted for 20 orbits, which was long enough to get stationary values of the torque. For the calculations without self-gravity, the torque evaluation takes all the disk into account, it does not exclude the content of the planet's Hill sphere. We checked that excluding it or not makes no difference in the torque measurement. This is consistent with the fact that, for the planet mass considered here, we do not find any material trapped in libration around the planet, be it inside a circumplanetary disk (a fraction of the planet's Hill radius) or inside a Bondi sphere.

3.1. Case of a Non-Self-Gravitating Disk

We first tackle the case of a non-self-gravitating disk. We measure the specific torque $\gamma = \Gamma/q$ on the planet for six different values of Σ_p , ranging from $\Sigma_p = 2 \times 10^{-4}$ to 2×10^{-3} . This corresponds to varying the initial disk surface density at the planet's orbital radius from one to 10 times the surface density of the minimum mass solar nebula (MMSN). Two situations are considered (see also Table 1):

1. On the one hand, the planet does not feel the disk gravity; it is held on a fixed circular orbit, with a strictly Keplerian orbital velocity. In this case, referred to as the fixed case, both the planet and the disk feel the star gravity but do not feel the disk gravity. The disk non-Keplerianity is exclusively accounted for by the radial pressure gradient. This is the configuration that has been contemplated in analytical torque estimates (see, e.g., Tanaka et al. 2002).

2. On the other hand, the planet feels the disk gravity. In other words, we let the planet evolve freely in the disk, so its angular velocity, which reads

$$\Omega_p(r_p) = [\Omega_K^2(r_p) - g_r(r_p)/r_p]^{1/2}, \quad (5)$$

is slightly greater than Keplerian. In this case, which we call the free case, the planet feels the gravity of the star and of the disk while, as previously stated, the disk does not feel its own gravity. Contrary to the fixed case, the free case is not a self-consistent configuration since the planet and the disk do not orbit under the same gravitational potential. Nevertheless, this situation is of interest as it corresponds to the standard scheme of all simulations dealing with the planet-disk tidal interaction.

We show in Figure 3 the specific torques (in absolute value) obtained with the fixed and free cases, for a $h = 0.05$ disk aspect ratio. In the fixed situation, there is an excellent agreement with the expectation $\gamma \propto \Sigma_p$, and, not surprisingly, the torques are bounded by the two- and three-dimensional analytical estimates of Tanaka et al. (2002). Nonetheless, the free case reveals two unexpected results. For a given surface density, the absolute value

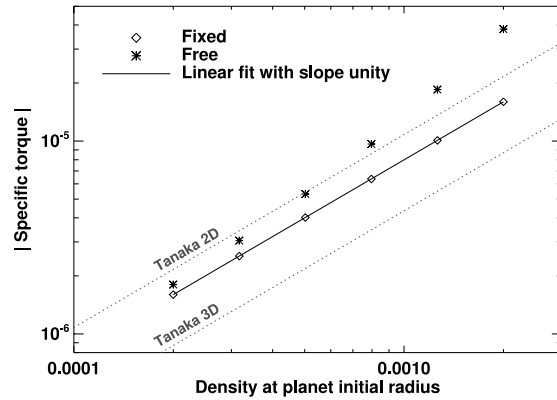


FIG. 3.—Specific torque γ exerted on a $M_p = 5 \times 10^{-6} M_*$ planet mass by a non-self-gravitating disk, with a $h = 5\%$ aspect ratio. Diamonds refer to the fixed case (the planet is held on a fixed circular orbit, with a strictly Keplerian angular velocity), while asterisks refer to the free case (the planet freely evolves in the disk, the planet's angular velocity is greater than Keplerian). The solid line corresponds to a proportional fit of the fixed case data, and shows the excellent agreement between our results of calculations and the expectation $\gamma \propto \Sigma_p$ in the fixed case. The two dotted lines depict the two- and three-dimensional analytical estimates of Tanaka et al. (2002).

of the torque is larger than expected from the fixed case. Moreover, it increases faster than linearly with the disk surface density.

The two latter results can be explained with the relative positions of the Lindblad resonances (hereafter LRs) in the fixed and free cases. We display in Figure 4a the locations r_{ILR} (r_{OLR}) of an inner (outer) LR, when the planet is on a fixed orbit. They are given by $r_{\text{ILR}} = \Omega^{-1}(\Omega_{\text{ILR}})$ and $r_{\text{OLR}} = \Omega^{-1}(\Omega_{\text{OLR}})$, with $\Omega(r)$ being the disk's rotation profile (solid curve), and Ω_{ILR} (Ω_{OLR}) being the frequency of the ILR (OLR), simply deduced from the planet frequency Ω_p .

When the planet is on a free orbit (Fig. 4b), its frequency is slightly larger than in the fixed case. Thus, the frequencies of the LRs are also larger in the free case, which induces a spurious inward shift of all the resonances. The OLRs get closer to the orbit, which increases the (negative) outer Lindblad torque. The ILRs are shifted away from the orbit, which reduces the (positive) inner Lindblad torque. Thus, the (negative) differential Lindblad torque is artificially larger in the free case.

The inward shift of the LR, which we denote by δR , has been evaluated analytically by PH05. A simple estimate can be obtained as follows. We denote by R_* the nominal position of the resonances without disk gravity. We assume that the disk's rotation profile is strictly Keplerian. The shift δR being induced by the increase of the planet frequency, we have $\delta R/R_* = -2\delta\Omega_p(r_p)/3\Omega_K(r_p)$, where $\delta\Omega_p(r_p)$ is the difference of the planet frequencies between the free and fixed cases. Using equation (5) and a first-order expansion, we are left with

$$\frac{\delta R}{R_*} = \frac{g_r(r_p)}{3r_p\Omega_K^2(r_p)}. \quad (6)$$

A more accurate expression for $\delta R/R_*$ is given by PH05 (see their eq. [7c]). Equation (6) shows that the shift of the LR scales with $g_r(r_p)$, and hence with Σ_p . This explains why the torque in the free case increases faster than linearly with the disk surface density. The relative shift of the resonances $\delta R/R_*$ typically amounts from -3×10^{-4} to -3×10^{-3} for our range value

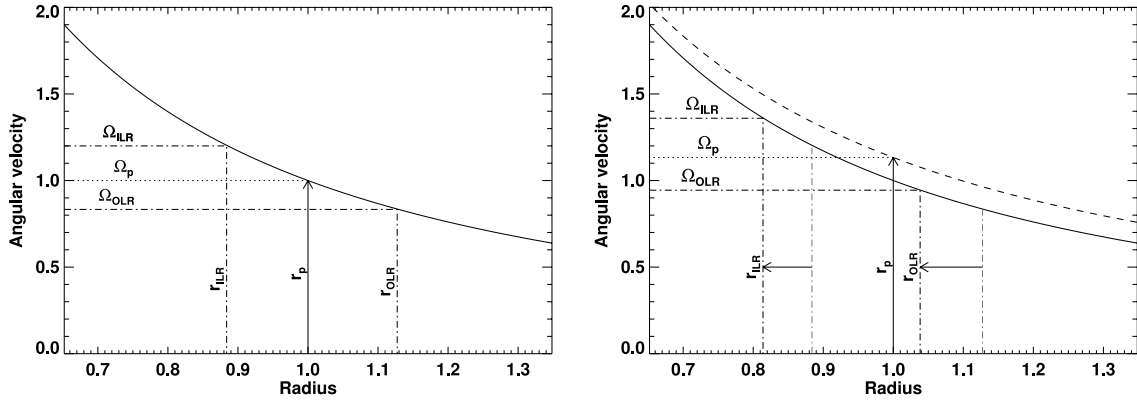


FIG. 4.—Location of two Lindblad resonances in the fixed case (*left*) and in the free case (*right*): the ILR of $m = 6$ ($\Omega_{\text{ILR}} = (6/5)\Omega_p$), and the OLR of $m = 5$ ($\Omega_{\text{OLR}} = (5/6)\Omega_p$). The disk's rotation profile $\Omega(r)$ is depicted without self-gravity (*solid curve*) and with self-gravity (*dashed curve, right*). In the latter case, $g_r(r)$ is given by a calculation with $\Sigma_p = 5 \times 10^{-2}$, a value exaggerated to improve legibility. Note also that the pressure buffer has been discarded in both profiles, for the sake of simplicity. The vertical arrow at $r = 1$ indicates the planet location, it reaches the upper curve in the free case (*right*), since the planet feels the disk gravity. The ILR and OLR are located, respectively, at $r_{\text{ILR}} = \Omega^{-1}(\Omega_{\text{ILR}})$ and $r_{\text{OLR}} = \Omega^{-1}(\Omega_{\text{OLR}})$. The nominal position of the resonances (that of the fixed case) is indicated by light gray dash-dotted lines on the right panel to appreciate their shift, highlighted by a horizontal arrow.

of surface densities, corresponding, however, to a torque relative discrepancy between $\sim 12\%$ and $\sim 120\%$ (see Fig. 3).

We are primarily interested in a quantitative comparison of the torques in the fixed and free cases. Nonetheless, since the shift of the LR scales with $g_r(r_p)$, it depends on the mass distribution of the whole disk. Thus, the torque discrepancy between the fixed and free cases also depends on $g_r(r_p)$, and hence on Σ_p , σ , r_{min} , and r_{max} . In particular, we point out that if the planet is close enough to the disk's inner edge, then $g_r(r_p)$ can be positive (see Fig. 1, for $\sigma = 0$). This shifts all the LR outward (instead of inward) and reduces the torque. We have checked this prediction with an appropriate calculation (not presented here).

In our study, only Σ_p is a free parameter. The index of the unperturbed surface density profile, σ , is fixed indeed to $3/2$, as explained in § 2.3. Our values of r_{min} and r_{max} are those customarily used in numerical simulations of planet-disk interactions (see, e.g., de Val-Borro et al. 2006). Thus, a useful quantitative comparison of the torques between the free and fixed cases can be provided just by varying Σ_p . In particular, one may think the torque discrepancy to be significant only for high values of Σ_p . Nevertheless, such a discrepancy depends both on the surface density Σ_p and on the disk aspect ratio h . As explained in Appendix B, we expect the relative difference of the torques between the free and fixed situations to scale with $(Qh)^{-1}$, where Q is the Toomre parameter at the planet's orbital radius,

$$Q = \left[\frac{c_s \kappa}{\pi G \Sigma} \right]_{r_p} \equiv h/m_D, \quad (7)$$

where κ is the horizontal epicyclic frequency, defined as $\kappa = \{2\Omega r^{-1} [d(r^2\Omega)/dr]\}^{1/2}$, and $m_D = \pi r_p^2 \Sigma_p / M_*$. Equation (7) can be recast as $Q = h/\pi \Sigma_p$ in our units.

To study the impact of h on previous results, we performed another set of calculations with $h = 0.03$. Figure 5 confirms that the relative difference of the torques scales with the inverse of Qh . It yields an estimate of the error done on the torque evaluation when involving the strongly biased free situation rather than the self-consistent fixed situation. For instance, for a $h = 3\%$ disk aspect ratio, the free situation can overestimate the torque by as much as a factor of 2 in a disk that has only ~ 3 times the disk surface density of the MMSN. Moreover, the torque relative dif-

ference is less than 20% as long as $Qh \gtrsim 2.5$, and hence as long as the Toomre parameter at the planet location is approximately greater than 50 if $h = 0.05$, or 80 if $h = 0.03$. Remember that these estimates depend on the precise value of $g_r(r_p)$, and hence on the mass distribution of the whole disk. They are provided with fixed, but customarily used values of σ , r_{min} , and r_{max} .

To avoid the above torque discrepancy, one must ensure that the planet and the disk feel the same gravitational potential. The workaround depends on whether the disk is self-gravitating or not, and whether the planet freely migrates in the disk or not:

1. The disk is not self-gravitating. The planet's angular velocity should therefore be strictly Keplerian:

- A. The planet evolves freely in the disk. Thus, its angular velocity, given by equation (5), is slightly greater than Keplerian. A workaround could be to subtract the axisymmetric component of the disk surface density to the surface density before calculating the force exerted on the planet by the disk. This would cancel out $g_r(r_p)$, and the planet's angular velocity would remain strictly Keplerian.

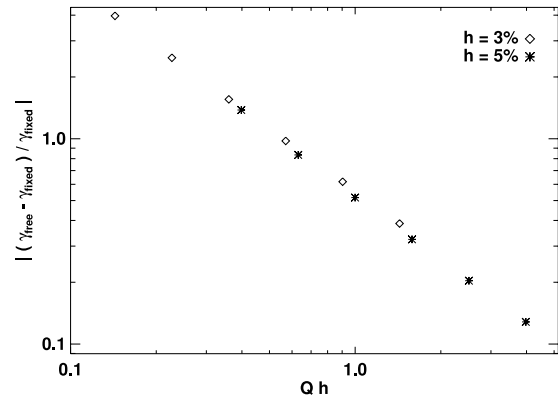


FIG. 5.—Relative difference of the torques between the free and fixed situations, as a function of Qh (see text and eq. [7]).

TABLE 2
PLANET'S ANGULAR VELOCITY $\Omega_p(r_p)$ AND DISK'S ROTATION PROFILE $\Omega(r)$,
WITHOUT AND WITH DISK GRAVITY

Parameter	Without Disk Gravity	With Disk Gravity
$\Omega_p(r_p) \dots$	$\Omega_K(r_p)$	$\left[\Omega_K^2(r_p) - \frac{g_p(r_p)}{r_p} \right]^{1/2}$
$\Omega(r) \dots\dots$	$\Omega_K(r)[1 - (1 + \sigma)h^2]^{1/2}$	$\left\{ \Omega_K^2(r)[1 - (1 + \sigma)h^2] - \frac{g_p(r)}{r} \right\}^{1/2}$

B. The planet is held on a fixed circular orbit, with necessarily a Keplerian angular velocity. This is a self-consistent situation.

2. The disk is self-gravitating. The planet's angular velocity should therefore be given by equation (5):

A. The planet evolves freely in the disk. This is a self-consistent situation.

B. The planet is held on a fixed circular orbit. This situation is self-consistent only if the planet's *fixed* angular velocity is given by equation (5).

From now on, whenever calculations without disk gravity are mentioned, they refer to the fixed situation. We call them the NOG calculations.

3.2. Case of a Self-Gravitating Disk

We study how the results of § 3.1 differ when the disk gravity is felt both by the planet and the disk. The planet is still held on a fixed circular orbit at $r = r_p$; its angular velocity is given by equation (5). As in the situation without disk gravity, the planet's initial velocity is that of a fluid element that would not be subject to the radial pressure gradient (see Table 2).

Taking the disk self-gravity into account induces two shifts of Lindblad resonances (PH05): (i) a shift arising from the axisymmetric component of the disk self-gravity, and (ii) a shift stemming from the nonaxisymmetric component of the disk self-gravity. We therefore performed two series of calculations:

1. Calculations that involve only the axisymmetric part of the disk self-gravity. We will call these the axisymmetric self-gravitating calculations (ASG calculations). Their computational cost is the same as that of a calculation without disk gravity since only one-dimensional FFTs are performed. The results of these calculations are presented in § 3.2.1.

2. Fully self-gravitating calculations (FSG calculations), which are more computationally expensive as they involve two-dimensional FFTs. Their results are presented in § 3.2.2.

3.2.1. Axisymmetric Self-Gravitating Calculations

We display in Figure 6 the torques obtained with the NOG, ASG, and FSG calculations, when varying Σ_p . We will comment the results of the FSG calculations in § 3.2.2. The torques obtained in the ASG situation, which we denote by γ_{ASG} , are hardly distinguishable from the torques without disk gravity, denoted γ_{NOG} . A straightforward consequence is that γ_{ASG} scales with Σ_p with a good level of accuracy. We point out however that the torque difference $|\gamma_{ASG}| - |\gamma_{NOG}|$ is slightly negative and decreases with Σ_p (not displayed here). The relative difference $||\gamma_{ASG}| - |\gamma_{NOG}||/|\gamma_{NOG}|$ varies from $\sim 0.2\%$ for $\Sigma_p = 2 \times 10^{-4}$, to $\sim 2\%$ for $\Sigma_p = 2 \times 10^{-3}$.

The interpretation of these results is as follows. In the ASG situation, the positions of the LR related to the Fourier component

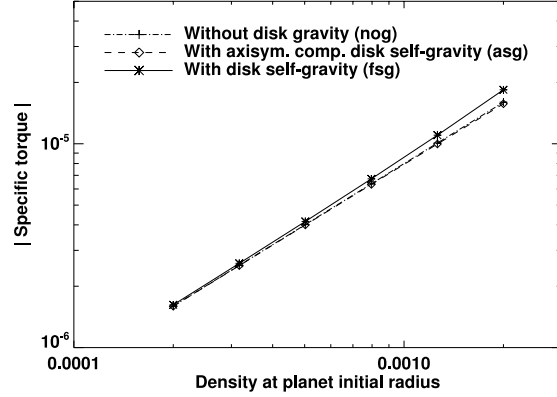


FIG. 6.—Specific torque on a $M_p = 5 \times 10^{-6} M_*$ planet mass, obtained with axisymmetric and fully self-gravitating calculations, with a $h = 5\%$ disk aspect ratio. Torques achieved without disk gravity (see § 3.1) are also displayed, for comparison.

with wavenumber m are the roots of equation (see PH05, and references therein)

$$D_{ASG}(r) = \kappa^2(r) - m^2[\Omega(r) - \Omega_p]^2 + m^2 c_s^2(r)/r^2 = 0, \quad (8)$$

where, contrary to the NOG situation, $\Omega(r)$ and Ω_p depend on g_r (see Table 2). As in § 3.1, the increase of the planet frequency implies an inward shift of the LR, which increases the differential Lindblad torque (see Fig. 4b). Furthermore, as pointed out in Figure 7a, the increase of the disk frequency causes an outward shift of all LR, which reduces the differential Lindblad torque. Accounting for the axisymmetric component of the disk gravity therefore leads to two shifts of the resonances, acting in opposite ways. Figure 7b shows that both shifts do not compensate exactly: the LR are slightly² moved away from corotation with respect to their nominal position without disk gravity. This is in qualitative agreement with PH05, who found a resulting shift which is negative for inward resonances, and positive for outward resonances (see their $\delta R_1 + \delta R_3$ expression). The sign of the shift results from the fact that the disk's rotation profile decreases more slowly with self-gravity than without,³ and explains why $|\gamma_{ASG}| - |\gamma_{NOG}|$ is negative. The absolute value of this shift increases with Σ_p , which means that $||\gamma_{ASG}| - |\gamma_{NOG}||$ increases with Σ_p .

3.2.2. Fully Self-Gravitating Calculations

We now come to the results of the FSG calculations depicted in Figure 6. The torques obtained with the FSG calculations, denoted by γ_{FSG} , are larger than γ_{ASG} and γ_{NOG} . Moreover, $|\gamma_{FSG}|$ grows faster than linearly with the disk surface density, a result already mentioned by Tanigawa & Lin (2005).

These results can be understood again in terms of shifts of the LR. Besides the shift due to the slight increase of the planet and of the disk frequency, the FSG situation triggers another shift stemming from the additional nonaxisymmetric term $-2\pi G \Sigma m/r$ in the dispersion relation of density waves (in the WKB approximation,

² To improve the legibility of Figs. 4 and 7, the disk's rotation profile with self-gravity is depicted with a value of Σ_p that is 25 times greater than the maximal value of our set of calculations.

³ We comment that this statement is not straightforward since it involves both the sign and the variations of function g_r ; here again we checked that this statement is valid in a radial range around the orbit that is large enough to concern all LR.

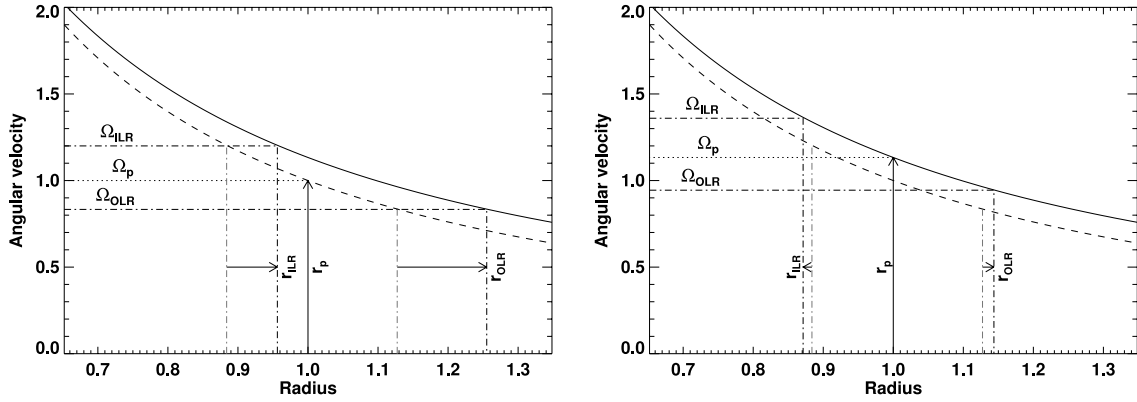


FIG. 7.—Same as Fig. 4, except that we examine the shift of the LR when the disk is self-gravitating (its rotation profile is now the solid, top curve). *Left*: The planet does not feel the disk gravity; the frequency of the planet, and therefore that of the LR, is the same as in Fig. 4a. *Right*: Both the planet and the disk feel the disk gravity; the frequencies of the planet and of the LR are those of Fig. 4b.

see PH05). The positions of the LR associated with wavenumber m are this time the roots of equation

$$D_{\text{FSG}}(r) = D_{\text{ASG}}(r) - 2\pi G \Sigma(r) m/r = 0, \quad (9)$$

where D_{ASG} is given by equation (8). PH05 showed that

1. This nonaxisymmetric contribution moves inner and outer LRs toward the orbit, with respect to their location in the ASG situation. This explains why $|\gamma_{\text{FSG}}| > |\gamma_{\text{ASG}}|$ and implies that the torque variations at inner and outer resonances have opposite signs.
2. The shift induced by the nonaxisymmetric part of the disk self-gravity dominates that of its axisymmetric component. Therefore, it approximately accounts for the total shift due to the disk gravity, and explains why $|\gamma_{\text{FSG}}| > |\gamma_{\text{NOG}}| \approx |\gamma_{\text{ASG}}|$.
3. This shift increases with Σ_p , so that $|\gamma_{\text{FSG}}|$ increases faster than linearly with Σ_p .

Our results of calculations are in qualitative agreement with the analytical work of PH05. Before coming to a quantitative comparison in § 3.3.2, we focus on the relative difference of the torques between the FSG and NOG situations. From previous results, we assume that the only shift of the LR is due to the nonaxisymmetric part of the disk gravity. Interestingly, this shift does not feature g_r , so it does not depend on the mass distribution of the whole disk. It only depends on the surface density at the planet location. Since the torque variations at inner and outer resonances are of opposite sign, we expect the relative difference of the torques to scale with Q^{-1} , for high to moderate values of Q . This is shown in Appendix C. It differs from the $(Qh)^{-1}$ scaling obtained in Figure 5, where the torque variations at inner and outer resonances were of identical sign.

In Figure 8, we plot this relative difference as a function of Q for previous results and for another series of runs performed with a $h = 0.03$ disk aspect ratio. The departure from the expected scaling occurs for $Q \lesssim 6$. The behavior at low Q will be tackled in § 3.3.2. Figure 8 yields a useful estimate of the torque increase due to the disk gravity, or, differently stated, of the torque underestimate if one discards the disk gravity. Such an estimate depends only on the Toomre parameter at the planet location, whatever the global mass distribution of the disk. The torques' relative difference is typically 1 order of magnitude smaller than in the situation of a planet freely migrating in a non-self-gravitating disk (Fig. 5).

It amounts typically to 10% for $Q \approx 10$. For $Q \gtrsim 50$, accounting for the disk gravity or not has no significant impact on the torque measurement.

Our results confirm that the disk *gravity* accelerates type I migration. This might sound contradictory with the results of Nelson & Benz (2003a, 2003b), who found that the disk *self-gravity* slows down migration for a planet that does not open a gap. The authors compared, however, the results of their self-gravitating calculations (where both the planet and the disk feel the disk gravity) to those obtained with the misleading situation of a planet freely migrating in a disk without self-gravity. As shown by Figure 9, or as can be inferred from Figures 3 and 6, comparing both situations would lead us to the same conclusion. There is therefore no contradiction between their findings and ours. From now on, we do not distinguish the *gravity* and *self-gravity* designations, since the planet and the disk orbit within the same potential in our calculations. Whenever calculations with disk gravity are mentioned, they refer to the FSG situation.

3.3. Comparison with Analytical Results

3.3.1. An Analytical Estimate

We propose in this section a simple analytical estimate of the relative difference of the torques between the FSG and NOG

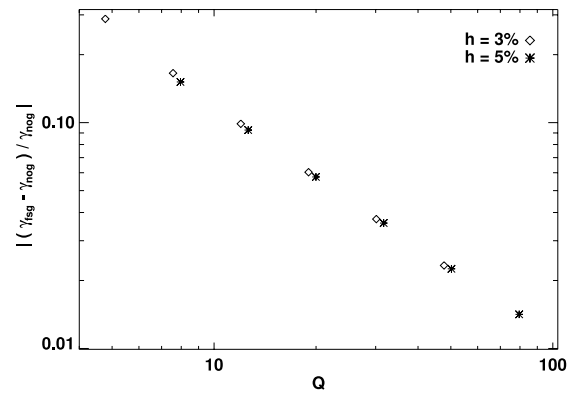


FIG. 8.—Relative difference of the torques obtained with the fully self-gravitating calculations (γ_{FSG}) and the calculations without disk gravity (γ_{NOG}), as a function of the Toomre parameter Q at the planet location.

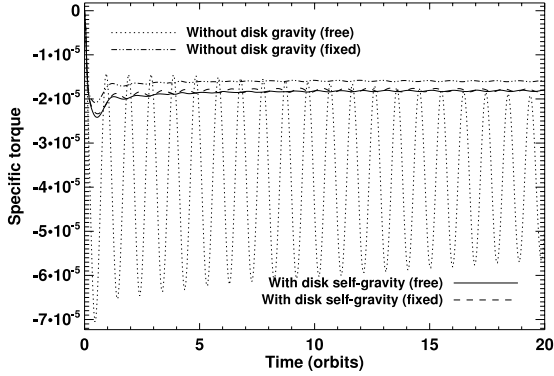


FIG. 9.—Specific torque variation with time, with and without disk gravity. In each case, two situations are depicted: the fixed case (the planet is on a fixed orbit with the appropriate angular velocity, see Table 2) and the free case (the planet is free to migrate in the disk). Except the self-gravitating calculation with a free planet, the calculations are those of Figs. 3 and 6 for $\Sigma_p = 2 \times 10^{-3}$. When the planet is on a free orbit without self-gravity, the torque oscillates with a large amplitude. This is due to the slight increase of the planet frequency: $\Omega_p(r_p)$, which is initially strictly Keplerian, is given by eq. (5) during its time evolution.

situations. This estimate concerns high to moderate values of the Toomre parameter at the planet location. We assume that the only shift of the LR in the FSG situation arises from its non-axisymmetric contribution. This comes to approximating the NOG and ASG situations, which is a reasonable assumption from Figure 6. Furthermore, since this shift has same order of magnitude at inner and outer LR (PH05), we focus on the one-sided Lindblad torque and use a local shearing sheet approximation. We set up local Cartesian coordinates (x, y) with origin at the planet position, with the x - and y -axes pointing toward the radial and azimuthal directions. Our x -coordinate is taken to be normalized:

$$x = \frac{r - r_p}{H(r_p)} = \frac{r - r_p}{hr_p}. \quad (10)$$

As is usually done in the shearing sheet framework, we discard the radial dependence of the disk surface density and scale height (Narayan et al. 1987). In a nongravitating disk, the LR associated with wavenumber m are therefore located at

$$x_{\text{NOG}} = \frac{2}{3} \epsilon \frac{\sqrt{1 + \xi^2}}{\xi}, \quad (11)$$

where $\xi = mh$, $\epsilon = +1$ for outer resonances, and $\epsilon = -1$ for inner resonances. In the FSG situation, LRs are located at $x_{\text{NOG}} + \delta x_{\text{FSG}}$, where the shift δx_{FSG} is evaluated by $D_{\text{FSG}}(x_{\text{NOG}} + \delta x_{\text{FSG}}) = 0$. Using equations (8), (9), and (11), a first-order expansion yields

$$\delta x_{\text{FSG}} = -\frac{2}{3\epsilon Q} \frac{1}{\sqrt{1 + \xi^2}}. \quad (12)$$

We comment that equation (7b) of PH05 reduces to our equation (12) for a surface density profile decreasing as $r^{-3/2}$.

In the linear regime, the one-sided Lindblad torque Γ amounts to a summation over m of the Fourier components Γ_m . In the shearing sheet approximation, since all quantities depend on m

through ξ , the summation over m is approximated as an integral over ξ ,

$$\Gamma = \frac{1}{h} \int_0^\infty T(x = x_L, \xi) d\xi, \quad (13)$$

where x_L denotes the positions of the LR and T is the m th Fourier component of the one-sided Lindblad torque, given by (see e.g., Ward 1997)

$$T(x, \xi) = K \frac{\xi^2 \Psi^2(x, \xi)}{\sqrt{1 + \xi^2}(1 + 4\xi^2)}, \quad (14)$$

where K is a constant. We assume that equation (14) can be used whether the disk is self-gravitating or not (Goldreich & Tremaine 1979). The forcing function Ψ in equation (14) is approximated in a standard way as a function of the Bessel K_0 and K_1 functions,

$$\Psi(x, \xi) = K_1(|x|\xi) + 2\sqrt{1 + \xi^2} K_0(|x|\xi). \quad (15)$$

We furthermore approximate $\Psi(x, \xi)$ as $(|x|\xi)^{-1}$, to within a numerical factor of order unity (Abramowitz & Stegun 1972). This approximation is valid when $\xi \lesssim 1$, and hence for low m -values.

With a first-order expansion in Q^{-1} , the difference of the one-sided Lindblad torques between the FSG and NOG situations reads

$$\Gamma_{\text{FSG}} - \Gamma_{\text{NOG}} \approx \frac{1}{h} \int_0^\infty \left(\frac{\partial T}{\partial x} \right)_{x=x_{\text{NOG}}, \xi} \delta x_{\text{FSG}} d\xi. \quad (16)$$

Combining equation (11) and (16), we are left with

$$\left| \frac{\Gamma_{\text{FSG}} - \Gamma_{\text{NOG}}}{\Gamma_{\text{NOG}}} \right| = \frac{2I}{3Q}, \quad (17)$$

where

$$\begin{aligned} I &= 3 \frac{\int_0^\infty \xi^3 / \left[(1 + \xi^2)^{5/2} (1 + 4\xi^2) \right] d\xi}{\int_0^\infty \xi^2 / \left[(1 + \xi^2)^{3/2} (1 + 4\xi^2) \right] d\xi} \\ &= \frac{2\sqrt{3} - \log(7 + 4\sqrt{3})}{\sqrt{3} - \pi/3} \approx 1.21. \end{aligned} \quad (18)$$

Not surprisingly, the relative difference of the one-sided Lindblad torques scales with the inverse of Q . This is the same scaling as for the relative difference of the differential Lindblad torques, assuming high to moderate values of Q (see Appendix C and Fig. 8). Note that, unlike the analysis of PH05, the present analysis, which is restricted to the shearing-sheet framework, enables one to exhibit the Q^{-1} scaling given by equation (17).

3.3.2. Results

We come to a quantitative comparison of our results of calculations with our analytical estimate, given by equation (17), and the analytical results of PH05, who estimated the dependence of the differential Lindblad torque on the disk mass for a fully self-gravitating disk (see their Fig. 4b). Another series of FSG calculations was performed with disk parameters similar to those of PH05, namely, a $h = 5\%$ disk aspect ratio and a planet mass corresponding to the linear regime (its value is precise hereafter). We vary the disk surface density at the planet's orbital radius from $\Sigma_p = 4 \times 10^{-4}$ to 10^{-2} . This corresponds to varying Q from 40

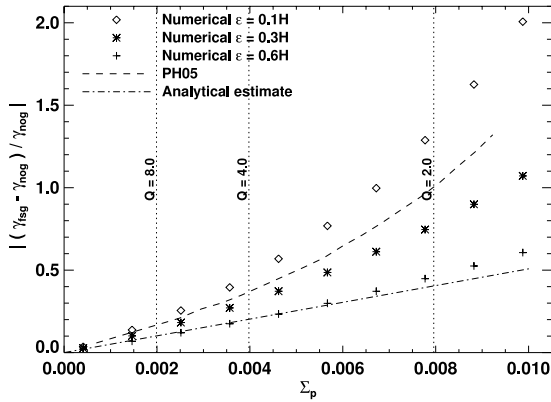


FIG. 10.—Relative difference of the torques between with the FSG situation (γ_{FSG}) and the NOG situation (γ_{NOG}) as a function of the disk surface density Σ_p . We compare the results of our calculations (each symbol refers to a different value of the softening length ϵ) with the analytical results of PH05 (dashed curve), and our analytical estimate (dash-dotted curve, see text and eq. [17]). The vertical dotted lines display different values of the Toomre parameter at the planet location.

to 1.6. The runs lasted for 10 planet's orbital periods, which was long enough to get stationary torques for the largest values of Q , but short enough to avoid a significant growth of nonaxisymmetric perturbations for the lowest values of Q , probably due to swing amplification (Toomre 1964).

As we aim at comparing the results of two-dimensional calculations with analytical expectations (for which there is no softening parameter), we investigated how much our calculation results depend on the softening length. For this purpose, the calculations were performed with three values of ϵ : 0.1, 0.3, and 0.6 $H(r_p)$. The planet mass is $M_p = 4.4 \times 10^{-6} M_*$ for $\epsilon = 0.3$ and 0.6 $H(r_p)$, whereas $M_p = 10^{-6} M_*$ for $\epsilon = 0.1 H(r_p)$. This choice ensures that the Bondi radius to softening length ratio does not exceed $\sim 10\%$ for each value of ϵ .

Each calculation was performed with and without disk gravity, so as to compute the relative difference of the torques between both situations. The reason why we compute this relative difference is that it does not depend on the details of the torque normalization, be it for the numerical or the analytical results. Nonetheless, PH05 only calculated the normalized torque in the FSG situation as a function of the disk mass. We then evaluated their normalized torque without disk gravity by extrapolating their torque with disk gravity in the limit where the disk mass tends to zero.

Figure 10 displays the relative difference of the torques between the FSG situation (γ_{FSG}) and the NOG situation (γ_{NOG}), obtained with our calculations, the analytical expectation of PH05 and our analytical estimate. This relative difference grows faster than linearly with Σ_p , although a linear approximation is valid at low surface density, as already stated in § 3.2.2. Our linear estimate is in agreement with the results of calculations with $\epsilon = 0.6 H(r_p)$ up to $Q \sim 3$, where it leads to a torque enhancement that is typically half the one estimated by PH05. Furthermore, our calculation results depend heavily on ϵ , especially at high Σ_p . For a given value of Σ_p , the relative difference of the torques decreases as ϵ increases. Differently stated, increasing the softening length reduces γ_{FSG} more significantly than γ_{NOG} .

We finally comment that our calculation results with $\epsilon = 0.1 H(r_p)$, which matches the mesh resolution in the planet vicinity, are in quite good agreement with the analytical prediction

of PH05. Surprisingly, the relative differences obtained with our calculations are greater than their analytical expectation. We checked that doubling the mesh resolution in each direction does not alter the relative differences measured with our calculations, as already pointed out in § 2.2.2 (see Fig. 2a). We show in Appendix D that this result can be explained by the failure of the WKB approximation for low values of the azimuthal wave-number. The relative difference between the results of our calculations and the predictions of PH05 is $\sim 15\%$ for $Q \sim 8$, and does not exceed $\sim 30\%$ for $Q \leq 2$. This satisfactory agreement confirms that the impact of the disk gravity on the differential Lindblad torque may be exclusively accounted for by a shift of Lindblad resonances.

4. MODELING THE NONAXISYMMETRIC CONTRIBUTION OF THE DISK SELF-GRAVITY WITH AN ANISOTROPIC PRESSURE TENSOR

In § 3, we investigated the impact of the disk gravity on the differential Lindblad torque for low-mass planets. The torque of an ASG calculation (where only the axisymmetric component of the disk self-gravity is taken into account) is close to that of a NOG calculation (without disk gravity). However, a FSG calculation (which also involves the nonaxisymmetric contribution of the self-gravity) displays a significant increase of the torque, which can be exclusively accounted for by a shift of the LR.

We propose in this section to model this torque enhancement for low-mass planets. Our model aims at calculating only the axisymmetric part of the disk self-gravity, and applying an additional shift of the LR that mimics the one of its nonaxisymmetric part. Altering the location of the LR amounts to modifying the dispersion relation of the density waves. The dispersion relations of the ASG and FSG cases differ only by the $-2\pi G \Sigma m/r$ term (in the WKB approximation, see equations [8] and [9]). There is however no straightforward way to add an extra term proportional to m in the dispersion relation D_{ASG} of the ASG situation. We propose to multiply the $m^2 c_s^2/r^2$ term of D_{ASG} by a constant, positive factor $1 - \alpha$, with $\alpha > 0$ to ensure that LRs are shifted toward the orbit. This can be achieved by multiplying the azimuthal pressure gradient $\partial_\phi P$ by $1 - \alpha$ in the Navier-Stokes equation or, differently stated, by assuming an anisotropic pressure tensor, for which the pressure in the azimuthal direction reads $P_\phi = (1 - \alpha)P_r$, where P_r , the pressure in the radial direction, is given by $P_r = \Sigma c_s^2$. We call α the anisotropy coefficient. When an ASG calculation includes the anisotropic pressure model, we will call it an ASG+AP calculation. We comment that the rotational equilibrium of the disk, which involves the radial pressure gradient, is not altered by this model.

We now explain how to take the adequate value for the anisotropy coefficient. As in § 3, we assume an initial surface density profile that scales with $r^{-3/2}$, which induces a negligible⁴ vortensity gradient, and hence a negligible corotation torque. Thus, the torques obtained with our calculations only include the differential Lindblad torque. We denote by Γ_{FSG} , Γ_{ASG} , and Γ_{ASG+AP} the differential Lindblad torques obtained with the FSG, ASG, and ASG+AP calculations. Our model aims at imposing

$$\Gamma_{ASG+AP} - \Gamma_{ASG} = \Gamma_{FSG} - \Gamma_{ASG}. \quad (19)$$

⁴ With a uniform disk aspect ratio, the vortensity gradient vanishes for a non-self-gravitating disk while it is negligible, but does not cancel out, for a self-gravitating disk.

TABLE 3
CALCULATION OF ANISOTROPY COEFFICIENT:
VALUES OF β FOR DIFFERENT VALUES OF η

$\eta = \varepsilon/H$	β
0.1.....	0.32
0.3.....	0.61
0.6.....	0.94

A first-order expansion of the left-hand side of equation (19) with α , and of its right-hand side with Q^{-1} leads to

$$\alpha = \beta Q^{-1}, \quad (20)$$

where

$$\beta = \frac{(\partial \Gamma_{\text{FSG}} / \partial Q^{-1})_{Q^{-1}=0}}{(\partial \Gamma_{\text{ASG+AP}} / \partial \alpha)_{\alpha=0}}. \quad (21)$$

The parameter β depends only on the softening length to disk scale height ratio $\eta = \varepsilon/H$. We calculated it for $\eta = 0.1, 0.3$, and 0.6 for small, fixed values of α and Q^{-1} , which we denote with a zero subscript. For each value of η , we performed an ASG, an ASG+AP, and a FSG calculation with $q = 10^{-6}$ and $h = 5\%$, corresponding to a Bondi radius to softening length ratio of $\sim 2.7\%$. Furthermore, we adopted $\Sigma_p = 5 \times 10^{-4}$, yielding $Q_0^{-1} \sim 0.03$. The ASG+AP calculation had $\alpha_0 = 0.01$. Using equation (21), the parameter β was therefore calculated by

$$\beta = \alpha_0 Q_0 \frac{\Gamma_{\text{FSG}} - \Gamma_{\text{ASG}}}{\Gamma_{\text{ASG+AP}} - \Gamma_{\text{ASG}}}. \quad (22)$$

We display in Table 3 the values of β for $\eta = 0.1, 0.3$, and 0.6 . We note that our anisotropic pressure model should be applied only when $Q > \beta$, to satisfy the constraint $1 - \alpha > 0$. This is not a stringent constraint, since $\beta < 1$ for these values of η .

We comment that the value of m for which the resonance shifts induced by the self-gravity and by the anisotropic pressure are equal is beyond the torque cutoff. Several reasons may conspire for that:

1. For a given shift, the relative torque variation is larger for resonances that lie closer to the orbit, which gives more weight to the high- m component.
2. The shifts estimated by a WKB analysis may dramatically differ from the real shifts (see Appendix D), especially at low- m , where significant torque is exerted.
3. The torque expression for an anisotropic pressure has not been worked out in the literature, and may differ from the standard expression (Ward 1997), with the consequence that equal shifts will not yield equal torque variations.

4.1. Validity of the Anisotropic Pressure Model

We first test the validity of our model by performing a series of calculations with Q ranging from 1.5 to 8. From equation (7), Q can be set by varying either h or Σ_p . Varying h however alters the ratio r_B/ε , which controls the flow linearity in the planet vicinity. We therefore fixed $h = 0.05$ and varied Σ_p . The planet to primary mass ratio is $q = 10^{-6}$, the softening length is $\varepsilon = 0.3H(r_p)$. For each value of Q , we performed a FSG, an ASG, and an ASG+AP calculation, for which the anisotropy coefficient is $\alpha = \beta/Q$, with $\beta = 0.61$ (see Table 3). The results are displayed in Figure 11. As expected from the first-order expansion in Q^{-1} used to derive

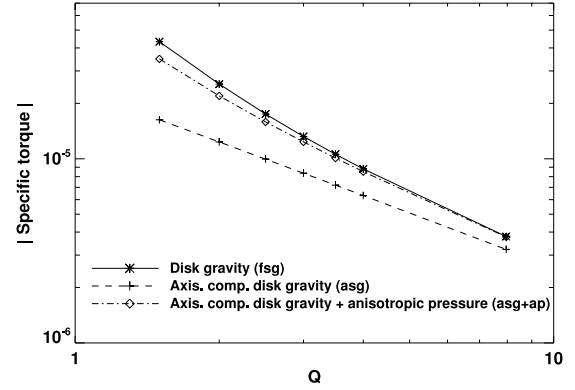


FIG. 11.—Specific torque exerted on a $M_p = 10^{-6} M_*$ planet mass, as a function of the Toomre parameter Q at the planet location. We display the torques obtained with ASG calculations (plus signs), FSG calculations (asterisks), and ASG+AP calculations (diamonds).

equation (20), the difference between the torques of the FSG and ASG+AP calculations increases when Q decreases. The relative difference is $\sim 0.4\%$ for $Q = 8$, $\sim 10\%$ for $Q = 2.5$, and reaches $\sim 25\%$ for $Q = 1.5$. The anisotropic pressure model therefore reproduces the torque of a FSG calculation with a good level of accuracy up to $Q \sim 4$.

The robustness of our model is furthermore tested against the onset of nonlinearities, by varying the planet to primary mass ratio q . The Toomre parameter at the planet location is fixed at $Q = 8$. A series of ASG, ASG+AP, and FSG calculations was performed with q ranging from 10^{-6} to 7×10^{-6} , and hence with r_B/ε ranging from $\sim 2.7\%$ to $\sim 18.7\%$. Figure 12 displays the specific torque as a function of q for each calculation. The torques obtained with the FSG and ASG+AP agree with a good level of accuracy. Their relative difference, shown in the close-up, increases almost linearly from $\sim 0.4\%$ to $\sim 4\%$, due to the onset of nonlinearities.

These results indicate that the anisotropic pressure model succeeds in reproducing the total torque obtained with a fully self-gravitating disk, as far as a low-mass planet, a high to moderate

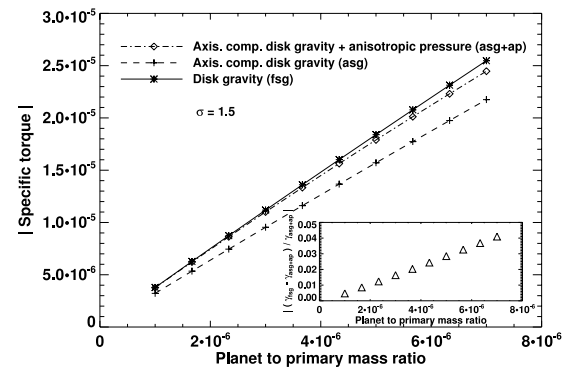


FIG. 12.—Specific torque as a function of the planet to primary mass ratio. Calculations obtained with the anisotropic pressure model (ASG+AP) are compared with axisymmetric self-gravitating calculations (ASG) and fully self-gravitating calculations (FSG). The close-up displays the relative difference of the torques between the FSG and ASG+AP situations. For all these calculations, $Q = 8$ at the planet location (the disk mass is $\sim 0.024 M_*$).

Toomre parameter, and a surface density profile scaling with $r^{-3/2}$ are considered. With these limitations, these results present another confirmation that the impact of the disk gravity on the differential Lindblad torque can be entirely accounted for by a shift of the LR. We suggest that in the restricted cases mentioned above, the anisotropic pressure model could be used as a low-computational cost method to model the contribution of the disk gravity. We finally comment that, not surprisingly, these results do not differ if the planet freely migrates in the disk, which we checked with long-term FSG and ASG+AP calculations (not presented here).

5. COROTATION TORQUE ISSUES

Hitherto, we have considered an initial surface density profile that scales with $r^{-3/2}$, which induces a negligible vortensity gradient, and hence a negligible corotation torque. This assumption ensured that the torques derived from our calculations accounted only for the differential Lindblad torque. It enabled a direct comparison with analytical expectations focusing on the differential Lindblad torque. We release this assumption and evaluate the impact of the disk self-gravity on the corotation torque Γ_C , in the linear regime. For a disk without self-gravity, Γ_C can be estimated by the horseshoe drag expression (Masset et al. 2006a), which reads (Ward 1991, 1992; Masset 2001)

$$\Gamma_C = \frac{3}{4} x_s^4 \Omega^2 (r_c) \Sigma(r_c) \left[\frac{d \ln(\Sigma/B)}{d \ln r} \right]_{r=r_c}, \quad (23)$$

where x_s is the half-width of the horseshoe region, r_c denotes the corotation radius, and $B = (2r)^{-1} d(r^2 \Omega)/dr$ is half the vertical component of the flow vorticity. We denote by $\Gamma_{C,ASG}$, $\Gamma_{C,ASG+AP}$, and $\Gamma_{C,FSG}$ the corotation torques in the ASG, ASG+AP, and FSG situations. The same quantities without the “C” subscript refer to the total torque in the corresponding situation.

We performed the same set of ASG, ASG+AP, and FSG calculations as in § 4.1, but with a flat initial surface density profile (we vary the planet to primary mass ratio q , for $Q = 8$). An additional NOG calculation was also performed for $q = 5 \times 10^{-6}$. The results of these calculations are displayed in Figure 13. The torques of the NOG and ASG calculations are hardly distinguishable, their relative difference being $\sim 2\%$, similarly as in § 3.2.1, where $\sigma = 1.5$. This difference should therefore be attributed to the differential Lindblad torque rather than to the corotation torque. It confirms that the corotation torque is not altered by the axisymmetric component of the disk gravity.

Furthermore, the torques of the FSG runs are significantly larger than those of the ASG+AP runs. Their relative difference varies from $\sim 11\%$ to $\sim 17\%$. We do not expect this difference to arise from the differential Lindblad torque, despite the change of σ . The differential Lindblad torques should therefore differ from $\sim 0.4\%$ to $\sim 4\%$, as for $\sigma = 1.5$ (close-up of Fig. 12). This reveals that the FSG situation, or the ASG+AP situation, or both, boosts the (positive) corotation torque.

We expect in fact the ASG+AP situation to enhance the corotation torque. Masset et al. (2006a) have estimated x_s for a disk without self-gravity, in the linear regime. Their estimate reads $x_s \approx 1.16 r_p (q/h)^{1/2}$. In the limit where the planet mass vanishes, a fluid element on a horseshoe separatrix has a circular trajectory and is only sensitive to the azimuthal gradient of the disk pressure. The above estimate of x_s therefore holds for an ASG+AP calculation if one substitutes h with $(1 - \alpha)^{1/2} h$, which we checked by a streamline analysis. Thus, we expect the anisotropic pressure

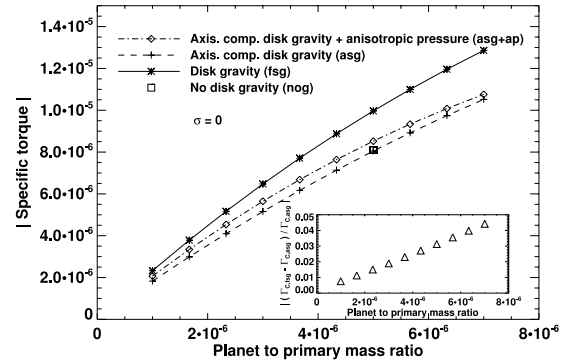


FIG. 13.— Specific torque as a function of the planet to primary mass ratio, for a flat initial surface density profile. The square corresponds to an additional NOG calculation performed with $q = 5 \times 10^{-6}$. The close-up displays the relative difference of the corotation torques between the ASG and FSG situations (see text and eq. [26]).

model to slightly increase the half-width of the horseshoe zone, thereby increasing the corotation torque as

$$\Gamma_{C,ASG+AP} = \frac{\Gamma_{C,ASG}}{1 - \alpha}, \quad (24)$$

with $\Gamma_{C,ASG}$ given by equation (23), and $\alpha = \beta/Q$.

To investigate whether the FSG situation also increases the corotation torque, we evaluate the quantity $(\Gamma_{C,FSG} - \Gamma_{C,ASG})/\Gamma_{C,ASG}$, which can be recast as

$$\frac{\Gamma_{C,FSG} - \Gamma_{C,ASG}}{\Gamma_{C,ASG}} = \frac{\Gamma_{C,FSG} - \Gamma_{C,ASG+AP}}{\Gamma_{C,ASG}} + \frac{\Gamma_{C,ASG+AP} - \Gamma_{C,ASG}}{\Gamma_{C,ASG}}. \quad (25)$$

Using equation (24), the second term on the right-hand side of equation (25) reads $\alpha/(1 - \alpha)$, and is $\sim 8.4\%$. Moreover, for the sake of simplicity, we neglect the relative change of the differential Lindblad torques. This assumption is grounded for the smallest planet masses that we consider, for which, as stated above, this change does not exceed $\sim 1\%$. The first term on the right-hand side of equation (25) therefore reads $(\Gamma_{FSG} - \Gamma_{ASG+AP})/\Gamma_{C,ASG}$. The quantity $\Gamma_{C,ASG}$ can be connected with Γ_{ASG} , using the estimate of Tanaka et al. (2002) for a flat surface density profile. This connection is motivated by the fact that both the differential Lindblad torque, and the corotation torque are almost identical in the NOG and ASG situations. This leads to $\Gamma_{C,ASG} \approx -1.56 \Gamma_{ASG}$. Equation (25) finally reads

$$\frac{\Gamma_{C,FSG} - \Gamma_{C,ASG}}{\Gamma_{C,ASG}} = -\frac{\Gamma_{FSG} - \Gamma_{ASG+AP}}{1.56 \Gamma_{ASG}} + \frac{\alpha}{1 - \alpha}. \quad (26)$$

This ratio is displayed in the close-up of Figure 13. It shows that the FSG situation slightly enhances the corotation torque, but this enhancement does not exceed $\sim 4.5\%$ for the highest planet mass that we consider. For the smallest planet masses, it is negligible with respect to the increase of the corotation torque triggered by the ASG+AP situation. Thus, the large difference between the torques of the ASG+AP and FSG calculations can be exclusively accounted for by the boost of the corotation torque in the ASG+AP situation.

The slight increase of the corotation torque in the FSG calculations should be compared to that of the differential Lindblad torque, which typically amounts to $\sim 17\%$ (for $\sigma = 1.5$, see Fig. 12). This comparison indicates that the disk self-gravity hardly changes, if at all, the corotation torque.

6. CONCLUDING REMARKS

The present work investigates the impact of the disk self-gravity on the type I migration. We show that the assumption customarily used in planet-disk calculations, namely, a planet freely migrating in a disk without self-gravity, can lead to a strong overestimate of the migration rate. We provide a simple evaluation of this overestimate (Fig. 5). The drift rate can be overestimated by as much as a factor of 2. Such a factor is inappropriate for the accurate calculation of migration rates, which is the main motivation of many recent studies of planet-disk interactions. The planet and the disk must therefore orbit within the same potential to yield unbiased estimates of the drift rate. Avoiding a spurious shift of resonances may be even more crucial in a nonbarotropic situation. In this case, the corotation torque depends strongly on the distance between orbit and corotation (Baruteau & Masset 2008), so that an ill-located corotation would yield meaningless drift rates.

The inclusion of the disk self-gravity in our calculations confirms that the disk gravity accelerates type I migration. We solve the contradiction between the statements of Nelson & Benz (2003a, 2003b) and Pierens & H ur e (2005) regarding the impact of the disk self-gravity on the migration rate. The increase of the differ-

ential Lindblad torque due to the disk gravity is typically 1 order of magnitude smaller than the spurious one induced by a planet freely migrating in a non-self-gravitating disk. We provide a simple evaluation of this torque increase (Fig. 8), which depends only on the Toomre parameter at the planet location, whatever the mass distribution of the whole disk. Furthermore, we argue that it can be entirely accounted for by a shift of the Lindblad resonances and be modeled with an anisotropic pressure tensor. This model succeeds in reproducing the differential Lindblad torque of a self-gravitating calculation, but increases the corotation torque. This model enables us to conclude that there is no significant impact of the disk self-gravity on the corotation torque, in the linear regime.

In a future work, we will extend our study beyond the linear regime. Preliminary calculations show that, regardless of the planet mass, the disk gravity speeds up migration. It would also be of interest to extend this study in three dimensions. In the linear regime, we do not expect the torque relative increase due to the disk gravity to be altered in three dimensions. However, three-dimensional calculations, involving the gas self-gravity, should be of considerable relevance for intermediate planet masses when a circumplanetary disk builds up, in particular to assess the frequency of type III migration.

We thank the anonymous referee for a careful and insightful report.

APPENDIX A

EXPRESSIONS OF g_r AND g_φ

In this section, we give the expressions of the radial and azimuthal self-gravitating accelerations g_r and g_φ , smoothed over the softening length ε_{SG} . We use the variables ($u = \log(r/r_{\min})$, φ), where r_{\min} denotes the inner edge radius of the grid. With this set of coordinates, $g_r(u, \varphi)$ reads

$$g_r(u, \varphi) = -Ge^{-u/2} \int_0^{u_{\max}} \int_0^{2\pi} S_r(u', \varphi') K_r(u - u', \varphi - \varphi') du' d\varphi' + G\Sigma(u, \varphi) K_r(0, 0) \Delta u \Delta \varphi, \quad (A1)$$

where S_r and K_r are defined as

$$S_r(u, \varphi) = \Sigma(u, \varphi) e^{u/2} \quad \text{and} \quad K_r(u, \varphi) = \frac{1 + B^2 - e^{-u} \cos(\varphi)}{\{2[\cosh(u) - \cos(\varphi)] + B^2 e^u\}^{3/2}}. \quad (A2)$$

In equations (A1) and (A2), G denotes the gravitational constant, $u_{\max} = \log(r_{\max}/r_{\min})$ with r_{\max} being the outer edge radius of the grid, Σ is the disk surface density, Δu and $\Delta \varphi$ are the mesh sizes, $K_r(0, 0) = 1/B$, and $B = \varepsilon_{SG}/r$. Since $\varepsilon_{SG} \propto r$ (see § 2.2.1), B is uniform over the grid. The second term on the right-hand side of equation (A1) is an additional corrective term that ensures the absence of radial self-force. Similarly, $g_\varphi(u, \varphi)$ reads

$$g_\varphi(u, \varphi) = -Ge^{-3u/2} \int_0^{u_{\max}} \int_0^{2\pi} S_\varphi(u', \varphi') K_\varphi(u - u', \varphi - \varphi') du' d\varphi', \quad (A3)$$

where S_φ and K_φ are given by

$$S_\varphi(u, \varphi) = \Sigma(u, \varphi) e^{3u/2} \quad \text{and} \quad K_\varphi(u, \varphi) = \frac{\sin(\varphi)}{\{2[\cosh(u) - \cos(\varphi)] + B^2 e^u\}^{3/2}}. \quad (A4)$$

In the particular case where only the axisymmetric component of the disk self-gravity is accounted for, which involves the axisymmetric component of the disk surface density $\bar{\Sigma}(u) = (2\pi)^{-1} \int_0^{2\pi} \Sigma(u, \varphi) d\varphi$, g_φ cancels out and

$$g_r(u) = -Ge^{-u/2} \int_0^{u_{\max}} \bar{S}_r(u') \bar{K}_r(u - u') du' + G\bar{\Sigma}(u) \Delta u \bar{K}_r(0), \quad (A5)$$

where $\bar{S}_r(u) = (2\pi)^{-1} \int_0^{2\pi} S_r(u, \varphi) d\varphi$ and $\bar{K}_r(u) = \int_0^{2\pi} K_r(u, \varphi) d\varphi$.

APPENDIX B

RELATIVE DIFFERENCE OF THE TORQUES BETWEEN THE FREE AND FIXED SITUATIONS
(WITHOUT DISK GRAVITY)

We denote by $\delta\Gamma$ the difference of the one-sided Lindblad torques between the free and fixed cases. This difference can be written as

$$\delta\Gamma = \sum_m \left(\frac{\partial T}{\partial x} \right)_{x_L} \delta x, \quad (\text{B1})$$

where $x = r - r_p$, δx is the shift of the Lindblad resonances induced by the free case, T is the m th Fourier component of the one-sided Lindblad torque (see e.g., Ward 1997, or eq. [14]), and x_L is the location of the Lindblad resonances in the fixed situation:

$$x_L = \frac{2}{3} \epsilon \frac{\sqrt{1 + \xi^2}}{\xi} h r_p, \quad (\text{B2})$$

where $\xi = mh$, $\epsilon = +1$ for outer resonances, and $\epsilon = -1$ for inner resonances. Approximating the summation over m as an integral over ξ , equation (B1) can be recast as

$$\delta\Gamma = \int (\partial_x T / T) T \delta x d\xi. \quad (\text{B3})$$

In equation (B3), T depends on x through the square of the forcing function Ψ , which is usually approximated as a function of the Bessel functions K_0 and K_1 (see, e.g., Ward 1997, or eq. [15]). Furthermore, $\Psi(x, \xi)$ can be approximated as $h r_p / |x| \xi$, to within a numerical factor of order unity (Abramowitz & Stegun 1972). Thus, $T \propto x^{-2}$ and $\partial_x T / T \propto x^{-1}$. At the location of Lindblad resonances, given by equation (B2), this yields $\partial_x T / T \propto \epsilon h^{-1}$. Moreover, $T \propto \epsilon \Sigma_p h^{-3}$. The shift δx , which has same sign for inner and outer Lindblad resonances, scales with Σ_p . The difference of the differential Lindblad torques is eventually obtained by summing equation (B3) at inner and outer Lindblad resonances,

$$\delta\Gamma_{\text{ILR}} + \delta\Gamma_{\text{OLR}} \propto \Sigma_p h^{-1} \int (T_{\text{OLR}} - T_{\text{ILR}}) d\xi \propto \Sigma_p h^{-1} \Sigma_p h^{-3} \propto \Sigma_p^2 h^{-4}. \quad (\text{B4})$$

Since the differential Lindblad torque scales with $\Sigma_p h^{-2}$, the relative difference of the differential Lindblad torques between the free and fixed cases scales with $\Sigma_p h^{-2}$, and hence with $(Qh)^{-1}$.

APPENDIX C

RELATIVE DIFFERENCE OF THE TORQUES WITH AND WITHOUT DISK GRAVITY

The calculation of the difference $\delta\Gamma$ of the one-sided Lindblad torques between the fully self-gravitating and nongravitating situations is similar to the one derived in Appendix B. The difference $\delta\Gamma$ is given again by equation (B3), where δx is this time the shift induced by the FSG situation. This shift has an opposite sign at inner and outer Lindblad resonances: $\delta x \propto \epsilon \Sigma_p$ [see the δR_2 expression of PH05, or skip to equation (12), where, however, $x = (r - r_p)/h r_p$]. Furthermore, assuming that the expression of T given by equation (14) can be applied for a self-gravitating disk (Goldreich & Tremaine 1979), we still have $\partial_x T / T \propto \epsilon h^{-1}$. Since the differential Lindblad torque scales with $\Sigma_p h^{-2}$, we find

$$\delta\Gamma_{\text{ILR}} + \delta\Gamma_{\text{OLR}} \propto \Sigma_p h^{-1} \int (T_{\text{OLR}} + T_{\text{ILR}}) d\xi \propto \Sigma_p h^{-1} \Sigma_p h^{-2} \propto \Sigma_p^2 h^{-3}. \quad (\text{C1})$$

The relative difference of the differential Lindblad torques between the FSG and NOG cases therefore scales with $\Sigma_p h^{-1}$, and hence with Q^{-1} .

APPENDIX D

NUMERICAL AND ANALYTICAL SHIFTS OF LINDBLAD RESONANCES INDUCED BY THE DISK SELF-GRAVITY

We studied in § 3.3.2 the relative difference of the torques between the FSG and NOG situations. In particular, we find that our calculations with $\varepsilon = 0.1H(r_p)$, which matches the mesh resolution in the planet vicinity, display a relative difference that is stronger than the one obtained with the estimate of PH05, which however does not involve a softening parameter. We give hereafter more insight into this result.

We propose to evaluate for each azimuthal wavenumber m the shift of the Lindblad resonances induced by our FSG calculations, and compare it with its theoretical expression given by equation (12). This theoretical expression predicts that the shifts at inner and outer resonances are of opposite sign, their absolute value, which we denote by $\delta x_{\text{th},m}$, being identical. We furthermore denote by $\delta x_{\text{num},m}$ the shift (in absolute value) inferred from our calculations, and $\Gamma_{\text{FSG},m}^i$ ($\Gamma_{\text{FSG},m}^o$) the m th Fourier component of the inner (outer)

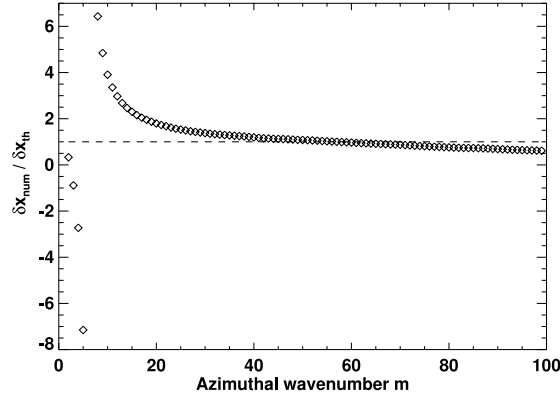


FIG. 14.—Ratio of δx_{num} , the shift of Lindblad resonances obtained with our FSG calculations (see eq. [D3]), and of δx_{th} , its analytically expected value (see eq. [12]).

Lindblad torque of a FSG calculation. We use similar notations for a NOG calculation, and we drop hereafter the m subscripts for the sake of legibility. A first-order expansion yields

$$\Gamma_{\text{FSG}}^i = \Gamma_{\text{NOG}}^i + \partial_x \Gamma_{\text{NOG}}^i \delta x_{\text{num}} \quad \text{and} \quad \Gamma_{\text{FSG}}^o = \Gamma_{\text{NOG}}^o - \partial_x \Gamma_{\text{NOG}}^o \delta x_{\text{num}}. \quad (\text{D1})$$

To estimate the quantities $\partial_x \Gamma_{\text{NOG}}^i$ and $\partial_x \Gamma_{\text{NOG}}^o$, we performed an additional NOG calculation, which we call the NOGO calculation, for which we imposed a slight, known shift of the resonances. This was done by fixing the planet's angular velocity at $\Omega_p - \delta\Omega_p$, with $\delta\Omega_p = 10^{-5}\Omega_p$. This slight decrease of the planet's angular velocity, with respect to the NOG situation implies an outward shift of inner and outer Lindblad resonances that reads $\delta x_0 = (2\delta\Omega_p)/(3h\Omega_p)$, an expression that is independent of m . With similar notations as before for the NOGO calculation, and using again a first-order expansion, we have

$$\Gamma_{\text{NOGO}}^i = \Gamma_{\text{NOG}}^i + \partial_x \Gamma_{\text{NOG}}^i \delta x_0 \quad \text{and} \quad \Gamma_{\text{NOGO}}^o = \Gamma_{\text{NOG}}^o + \partial_x \Gamma_{\text{NOG}}^o \delta x_0. \quad (\text{D2})$$

Combining equations (D1) and (D2), we are finally left with

$$\delta x_{\text{num}} = \frac{(\Gamma_{\text{FSG}}^i - \Gamma_{\text{FSG}}^o) - (\Gamma_{\text{NOG}}^i - \Gamma_{\text{NOG}}^o)}{(\Gamma_{\text{NOGO}}^i + \Gamma_{\text{NOGO}}^o) - (\Gamma_{\text{NOG}}^i + \Gamma_{\text{NOG}}^o)} \delta x_0. \quad (\text{D3})$$

We plot in Figure 14 the ratio $\delta x_{\text{num}}/\delta x_{\text{th}}$ as a function of the azimuthal wavenumber m , for $\Sigma_p = 2 \times 10^{-3}$ ($Q \sim 8$). We first comment that the ratio is negative for $m \leq 6$, positive beyond, with a divergent behavior at the transition. We checked that this behavior is caused by a change of sign of the denominator⁵ of equation (D3), which is negative for $m \leq 6$ and positive beyond. Furthermore, the ratio $\delta x_{\text{num}}/\delta x_{\text{th}}$ is significantly greater than unity for m ranging from ~ 7 to ~ 20 , that is for the dominant Lindblad resonances. Differently stated, the dominant Lindblad resonances are more shifted by our calculations than analytically expected by PH05, which explains why the torque enhancement is more important with our calculations.

Beyond, the ratio is close to unity for a rather large range of high m -values. This confirms that for high values of m the WKB approximation yields analytical estimates that are in good agreement with the results of numerical simulations. However, since our calculations involve a softening parameter, the ratio does not converge when increasing m , and slowly tends to zero. We checked that the value of m for which the ratio becomes lower than unity increases when decreasing the softening length. This explains why the torque enhancement is increasingly important at smaller softening length, as inferred from Figure 10.

⁵ This denominator corresponds to the difference of the differential Lindblad torques between the NOG and NOGO situations, expected to be positive for all m .

REFERENCES

- Abramowitz, M., & Stegun, I. A. 1972, *Handbook of Mathematical Functions* (New York: Dover)
- Baruteau, C., & Masset, F. 2008, *ApJ*, 672, 1054
- Binney, J., & Tremaine, S. 1987, *Galactic Dynamics* (Princeton: Princeton Univ. Press)
- Boss, A. P. 2005, *ApJ*, 629, 535
- Crida, A., Morbidelli, A., & Masset, F. 2006, *Icarus*, 181, 587
- de Val-Borro, M., et al. 2006, *MNRAS*, 370, 529
- Goldreich, P., & Tremaine, S. 1979, *ApJ*, 233, 857
- Hur , J.-M., & Pierens, A. 2006, in *Proc. Annu. Meeting of the French Soc. of Astron. and Astrophys.*, ed. D. Barret et al., 105
- Masset, F. 2000a, *A&AS*, 141, 165
- Masset, F. S. 2000b, in *ASP Conf. Ser. 219, Disks, Planetesimals, and Planets*, ed. G. Garz n et al. (San Francisco: ASP), 75
- . 2001, *ApJ*, 558, 453
- Masset, F. S., D'Angelo, G., & Kley, W. 2006a, *ApJ*, 652, 730
- Masset, F. S., Morbidelli, A., Crida, A., & Ferreira, J. 2006b, *ApJ*, 642, 478
- Mayor, M., & Queloz, D. 1995, *Nature*, 378, 355
- Menou, K., & Goodman, J. 2004, *ApJ*, 606, 520
- Narayan, R., Goldreich, P., & Goodman, J. 1987, *MNRAS*, 228, 1
- Nelson, A. F., & Benz, W. 2003a, *ApJ*, 589, 556
- . 2003b, *ApJ*, 589, 578
- Paardekooper, S.-J., & Mellema, G. 2006, *A&A*, 459, L17
- Pierens, A., & Hur , J.-M. 2005, *A&A*, 433, L37 (PH05)

No. 1, 2008

TYPE I MIGRATION IN SELF-GRAVITATING DISK

497

Sellwood, J. A. 1987, ARA&A, 25, 151

Tanaka, H., Takeuchi, T., & Ward, W. R. 2002, ApJ, 565, 1257

Tanigawa, T., & Lin, D. N. C. 2005, in Protostars and Planets V, ed. V. Mannings
et al. (Tucson: Univ. Arizona Press), 8466

Toomre, A. 1964, ApJ, 139, 1217

van Leer, B. 1977, J. Comput. Phys., 23, 276

Ward, W. R. 1991, in LPI Conf. Abs. 22, 1463

———. 1992, in LPI Conf. Abs. 23, 1491

———. 1997, Icarus, 126, 261

Curriculum Vitæ

Name: Clément Baruteau
 Birth: July 08, 1982 (France)
 Nationality: French
 Address: Service d'Astrophysique, bâtiment 709
 CE-Saclay 91191 Gif-sur-Yvette Cedex France
 Phone: +33 1 6908 1886
 Fax: +33 1 6908 6577
 e-mail: clement.baruteau@cea.fr
 Web: <http://clement.baruteau.free.fr/work>

Research Experience:

Doctoral Research:

Type I Migration in an Adiabatic Disk, with F. Masset (CE-Saclay, 2007).

With two-dimensional calculations, we found an excess of corotation torque that scales with the unperturbed entropy gradient at the planet's corotation radius. This torque excess can be large enough to reverse type I migration.

Corotation Torque in Adiabatic Flows, with F. Masset (CE-Saclay, 2007).

We derived a generalized expression for the corotation torque between a rotating potential and a two-dimensional gaseous disk, assuming an adiabatic flow.

Planetary Migration and Disk Self-Gravity, with F. Masset (CE-Saclay, 2006).

By means of two-dimensional calculations, we confirmed that the disk gravity accelerates type I migration. We showed that the impact of the disk self-gravity on the differential Lindblad torque can be reproduced with an anisotropic pressure tensor.

Predoctoral Research:

Runaway Migration, with F. Masset (CE-Saclay, 2005).

We investigated the occurrence of runaway planetary migration (type III migration) with three-dimensional calculations.

N-body calculations, with B. Sémelin (Observatoire de Paris, 2005).

I developed a parallelized N-body code to study (i) the formation of a galactic bar and (ii) Pluto's capture in mean-motion resonance.

Dynamics methods, with J. Laskar (Observatoire de Paris, 2004).

I studied the perturbed pendulum-like Hamiltonian system with dynamics methods: symplectic integrators, Poincaré map, frequency analysis.

Accretion Disk, with D. Pelat and J.-M. Huré (Observatoire de Meudon, 2004).

With a group of students, we developed a one-dimensional code to model an accretion disk around a black hole.

Classical Novae, with M. Hernanz (Institut d'Estudis Espacials de Catalunya, Spain, 2003).

I investigated the detectability of classical novae with the INTEGRAL mission.

X-Ray Flashes, with R. Mochkovitch (Institut d'Astrophysique de Paris, 2002).

We compared the properties of X-Ray Flashes and of Gamma-Ray Bursts with the internal shocks model.

Publications:

Refereed articles:

- **Type I planetary migration in a self-gravitating disk**, Baruteau, C. & Masset, F. 2008, ApJ, 678, 483
- **On the corotation torque in a radiatively inefficient disk**, Baruteau, C. & Masset, F. 2008, ApJ, 672, 1054

Conference proceedings:

- **On type I planetary migration in adiabatic disks**, Baruteau, C. & Masset, F. 2007, Proceedings of the 249th Symposium of the IAU, 2007, 397
- **Type I planetary migration in a self-gravitating disk**, Baruteau, C. & Masset, F. 2007, Proceedings of the 249th Symposium of the IAU, 2007, 393
- **On type I planetary migration in an adiabatic disk**, Baruteau, C. & Masset, F. 2007, SF2A Proceedings, 437
- **On the impact of disk gravity on planetary migration**, Baruteau, C. & Masset, F. 2006, SF2A Proceedings, 569

Conferences attended:

- *Origin and Evolution of Planets 2008*, June 30 - July 04 2008, Ascona, Switzerland (poster)
- *Division on Dynamical Astronomy*, April 28 - May 01 2008, Boulder, USA (talk)
- IAU Symposium No. 249, *Exoplanets: Detection, Formation and Dynamics*, October 22-26 2007, Suzhou, China (talk and poster)
- *Semaine de l'Astrophysique Française* (SF2A), July 2-6 2007, Grenoble, France (talk)
- *Extreme Solar Systems*, June 25-29 2007, Santorini, Greece (poster)
- *Stars, Disks and Planets: The Many Worlds of John Papaloizou*, June 11-13 2007, Paris, France
- *Semaine de l'Astrophysique Française* (SF2A), June 26-30 2006, Paris, France (talk)
- 4th Planet Formation Workshop, *Planet Formation and Evolution Studies: Various Approaches - One Goal*, March 1-3 2006, Heidelberg, Germany

Seminars given:

- *Type I planetary migration: impact of the disc thermodynamics*, June 09 2008, IAAT, Tübingen, Germany

- *Planetary migration in protoplanetary discs*, April 14 2008, MPIA, Heidelberg, Germany
- *Migration planétaire dans un disque protoplanétaire*, April 03 2008, LAB, Bordeaux, France
- *Migration planétaire dans un disque protoplanétaire*, April 01 2008, OCA, Nice, France
- *Planetary migration in non-isothermal discs*, March 18 2008, IAP, Paris, France
- *Sobreviviendo la migración planetaria de tipo I*, February 06 2008, UNAM, México D.F., México
- *Migration planétaire dans un disque adiabatique*, July 12 2007, GRAAL, Montpellier, France

Teaching Experience:

Teaching Assistant at Université Paris VI (2006-2008): lectures in Mechanics and Hydrodynamics to first-year undergraduate students (64h per year). Instructor: Dr F. Daigne.

Teaching Assistant at Lycée Jacques Decour (2004-2006): oral examinations in Physics and Chemistry to students in second year of Classes Préparatoires (50h per year).

Teaching Assistant at Lycée Descartes, Antony (2002-2003): 12th Grade Physics and Chemistry courses (2h per week).

Statistical Mechanics: I wrote a set of lecture notes (139 pages) for third-year undergraduate students (2002).

Public outreach:

Fête de la Science, October 14 2006, Extrasolar planets.

Education:

- 2005-2008 PhD, Astrophysics, Observatoire de Paris (defense day: October 02 2008). Dissertation: *Toward predictive scenarios of planetary migration*. Advisor: Dr. Frédéric Masset (CE-Saclay)
- 2005 Master II, Astronomy and Astrophysics (equivalent to a Master's Degree - first year of PhD in Astrophysics), Observatoire de Paris, rank: 2/42
- 2004 Agrégation (competitive examination for the recruitment of secondary school teachers in France), Physics and Chemistry, rank: 37/170
- 2001-2005 Undergraduate studies at Ecole Normale Supérieure de Cachan, and at Université Paris XI (equivalent to the preparation of a MSc, Physics, Minor, Astrophysics), highest distinction
- 2001 Admitted to Ecole Normale Supérieure de Cachan
- 1999-2001 Classes Préparatoires, Lycée Descartes, Tours (a two-year intensive course in advanced maths and physics to prepare the admission to French *Grandes Ecoles*)

Awards:

Student Stipend Award of the American Astronomical Society to attend the Division on Dynamical Astronomy meeting in Boulder, Colorado (April 2008)

Agrégation in Physics and Chemistry

Student fellowship at Ecole Normale Supérieure de Cachan

Skills:

Computing: very good working knowledge in C, parallel computing (MPI, OPENMP), IDL and LaTeX, good working knowledge in C++, perl, CVS, PBS, bash and F90.

Languages: French (native speaker), English (fluent), Spanish (fluent), Italian (basics), Russian (basics).

Vers des scénarios prédictifs de la migration planétaire

La détection récente des exoplanètes a fourni un formidable laboratoire d'expérimentation des théories de formation et d'évolution planétaire. Un résultat troublant est la proportion de planètes géantes situées plus près de leur étoile que ne l'est Mercure de notre Soleil! Si, comme il est admis, ces planètes se sont formées à plus grande distance de l'étoile dans le disque protoplanétaire, il reste à expliquer comment elles ont pu s'en rapprocher. Remarquablement, une telle théorie est apparue bien avant la découverte de la première exoplanète. Elle explique que sous l'interaction avec le disque protoplanétaire, les planètes se rapprochent de leur étoile en spiralant. On parle de migration planétaire. De nombreuses études ont montré que le temps de migration des planètes de faible masse est bien plus court que le temps de dissipation du disque. Toutes les planètes devraient avoir migré jusqu'à leur étoile! Ce qui est déjà remis en cause par notre Système Solaire. Afin d'inscrire la migration planétaire dans un scénario prédictif de formation et d'évolution planétaire, il est primordial d'affiner notre compréhension de l'interaction disque-planète. La prise en compte de l'auto-gravité du disque est un exemple de progrès en ce sens. Je montre que négliger l'auto-gravité conduit à surestimer significativement le couple différentiel de Lindblad. Une autre branche explorée dans cette thèse est l'impact des processus thermiques sur la migration. Je montre que l'évolution thermodynamique du disque génère une contribution supplémentaire au couple de corotation, capable de ralentir considérablement, voire de renverser, la migration des planètes de faible masse.

Mots clé : migration planétaire, disques protoplanétaires, hydrodynamique, analyse linéaire, simulations numériques

Toward predictive scenarios of planetary migration

The recent detection of extrasolar planets has provided an exciting opportunity to test our theories of planet formation and evolution. An impressive result is the significant proportion of giant planets located much closer to their star than Mercury is from our own Sun! These planets should have formed further out in the protoplanetary disc, thus one needs to explain how they could move closer to their host star. Remarkably enough, such an explanation was proposed well before the discovery of the first exoplanet. It considered the interaction between a planet and the protoplanetary disc, which leads to a decrease of the planet's semi-major axis. This is known as planetary migration. Many studies have shown that the migration timescale of low-mass planets is much shorter than the lifetime of the disc. All planets should therefore have migrated to the vicinity of their host star! This is at least in contradiction with the locations of the planets in our Solar System. In order to elaborate predictive scenarios of planet formation and evolution, it is of primary interest to refine our understanding of disc-planet interactions. The inclusion of the disc self-gravity is an illustration of this. With analytical and numerical arguments, I show that discarding the self-gravity leads to a significant overestimate of the differential Lindblad torque for migrating low-mass planets. Another aspect explored in this thesis is the impact of the gas thermodynamics on migration. I show that the thermodynamic evolution of the disc induces an additional contribution to the corotation torque, which may dramatically slow down or even reverse the migration of low-mass planets.

Keywords: planetary migration, protoplanetary discs, hydrodynamics, linear analysis, numerical simulations